Guided waves in rectangular integrated magnetooptic devices

Dissertation
zur Erlangung des Grades eines
Doktors der Naturwissenschaften
von

Manfred Lohmeyer

Fachbereich Physik der Universität Osnabrück
Osnabrück, im Juni 1999

Berichterstatter: Prof. Dr. Peter Hertel
Prof. Dr. Horst Dötsch

Eingereicht am 08.06.1999
Mündliche Prüfung am 22.07.1999

Contents

Introduction

The present rapid development of global communications and computer science demands for constantly increasing capacities of data transmission and data processing. For a number of reasons, ranging from a higher bandwith to the inexpensiveness of optical fiber materials, the conventional technologies based on electric currents are more and more complemented or replaced by a technology on the basis of light. As in electronics, there is a trend towards integration in optics. Components with diverse functionalities are to be combined into single monolithic chips, denoted by the shorthands PIC or OIC for photonic or optical integrated circuits. Consequently, the field is called 'integrated optics' [148, 62, 91, 60], as a subdivision of 'photonics'.

Dielectric waveguides constitute the integrated optical analogon to the conductor paths of microelectronics. Frequently, these are small ribs or strips with cross section dimensions in the order of micrometers, fabricated by various etching techniques from stacks of transparent dielectric films. Similar to optical fibers, the structures are able to confine, to 'guide' light via the mechanism of total internal reflection. This thesis aims at improvements in the understanding of light propagation in dielectric waveguides and devices composed of them, by means of numerical simulations.

Transparent materials with specific optical properties are of particular interest for general as well as for integrated optics. For this thesis, special emphasis lies on waveguides made of epitaxially grown rare earth iron garnet films [163]. Along with low losses in the relevant wavelength regions around $1.3\ \mu$m and $1.5\ \mu$m, a window of transparency of optical fibers, these materials show comparably large magnetooptic effects of first order (Faraday effect) and second order (Cotton-Mouton-effect) [174]. Garnet films are thus well qualified for integrated optics, where their pronounced Faraday effect enables the design of nonreciprocal devices. These are intended to distinguish between optical waves propagating in opposite directions. In the current framework, a device with two ports A and B that establishes a connection from A to B, but blocks all power transmission from B to A, is called an 'isolator'. A more sophisticated 'circulator' comprises more ports, three at least, which are connected in a circular manner. In fact, magnetooptic garnets seem to be the only materials available for the realization of these components.

Numerical simulation of light propagation in dielectric waveguides [136, 157] amounts to solving the Maxwell equations for the waveguide domain. Besides other small contributions, the optical properties of garnet waveguides are described by a locally isotropic permittivity profile that causes the light guiding and an additional small magnetooptic part. The numerical model includes the first part rigorously, while the magnetooptic contribution to the permittivity is considered as a perturbation. Thus Chapters 1–5 of this thesis deal with waveguides made from isotropic materials.

Chapter 1 surveys the theoretical (analytical) foundations which are relevant for the following numerical simulations. For this thesis, emphasis is on waveguides with a rectangular, piecewise constant permittivity profile, as they typically emerge from fabrication processes employing wet-chemical or ion-beam etching. Here peculiarities of the garnet refractive index parameters demand to be very strict in the treatment of the resulting dielectric interfaces. This feature already distinguishes the numerical analysis of the magnetooptic structures from other simulations dealing e.g. with semiconductor materials, glasses, or polymers.

Nonreciprocal devices typically comprise long longititudinally homogeneous waveguide segments to accumulate the small magnetooptic effects. Hence the discussion shall be kept in the framework of guided waves, the so called 'modes'. For reasons explained in Section 1.2, calculating the guided mode interference must be preferred to alternative modeling e.g. by means of beam propagation techniques [179, 57]. We

consider only the simplest type of longitudinal inhomogenities, i.e. junctions of waveguides with different cross sections. The subsequent chapters illustrate that even these junctions lead to complex and interesting devices.

The remaining parts of Chapter 1 describe fundamental perturbational techniques. Single modes may be perturbed by small permittivity variations, uniformly on an area of the waveguide cross section. This is the subject of Section 1.3, which includes a simple model for waveguides made of absorbing materials. We have argued that adequate recognition of the dielectric boundaries is indispensable. Consequently, one has to expect a strong influence of the interface positions on the light propagation. Interferometric devices made of garnet waveguides usually have very strict fabrication tolerances with respect to the waveguide geometry. Section 1.4 provides the basic expressions for a perturbational geometry tolerancing of waveguides with a rectangular cross section.

Anisotropic permittivity contributions may lead to polarization coupling. The proper modeling tool is coupled mode theory [45, 59] as sketched in Section 1.5, which allows to incorporate the magnetooptic effects. The same basic coupled mode formalism can be applied for the analysis of multiwaveguide couplers, which are the subject of the last chapter. Therefore, the last section of Chapter 1 contains remarks on coupled modes of different polarization as well as on coupled modes of different waveguides.

Chapter 2 summarizes mode properties and perturbational expressions for the much simpler case of planar waveguides where the waveguide cross section is restricted to one relevant dimension. Section 2.2 recalls the transfer matrix strategy for the numerical or quasi-analytical calculation of the modes of isotropic planar multilayer waveguides. It establishes the numerical basis for the planar device designs in Chapter 7.

While the exact mode analysis of slab waveguides with piecewise constant permittivity is fairly easy, for waveguides with twodimensional cross section this task is far more involved. Apart from circular geometries there are no known analytical solutions; an overview over the various numerical techniques can be found e.g. in Refs. [23, 159]. The procedure proposed in Chapter 3, published as 'wave matching method' (WMM), may be viewed as a more or less direct extension of the planar technique to channel waveguides. While Chapter 3 states the background for the mode solving algorithm, Chapters 4 focuses on WMM results for a number of common benchmark structures, for both the semivectorial (Section 4.1) and the fully vectorial program versions (Section 4.2). The current implementation allows for quite general cross section shapes, and we have tested the mode solver on several composite geometries (Section 4.3) as well.

Previously to the later application of the perturbational techniques from Chapter 1 for concrete designs, Chapter 5 attempts a numerical assessment of their practical behaviour. The chapter contains sections on mode attenuation, geometry tolerancing, and coupled mode theory.

Single magnetooptic waveguides are the subject of Chapter 6. With the magnetooptic permittivity contribution considered as a perturbation, we describe light propagation in the framework of coupled mode theory. A classification of the magnetooptic effects in Section 6.1 for waveguides of definite symmetry is followed by Section 6.2 on nonreciprocal phase shifters for modes of both polarizations and by Section 6.3 on nonreciprocal polarization converters. Each of these applications corresponds to a configuration, where the bias magnetic field is oriented along one of the cartesian coordinate axes. Section 6.4 investigates a setup with inclined magnetization, leading to a combination of nonreciprocal phase shift and polarization conversion. This enables the design of unidirectional polarization converters, i.e. waveguides that switch between orthogonal polarizations in one direction of light propagation, but keep the polarization state for light propagating in the opposite direction.

Chapter 7 reports on our proposals for complete isolator or circulator devices, respectively, and polarization splitters. The structures are based on three waveguide couplers with broad and multimode central waveguides, for which the term 'radiatively coupled waveguides' was coined in Ref. [85]. Following an overview of the typical coupling characteristics, the simulations of this chapter combine many of the tools and methods from the previous parts, ranging from the planar and three-dimensional mode solvers over the perturbational formalisms for geometry tolerancing and coupled mode theory to the properties of magnetooptic

waveguides. The simulation of a polarization independent four port circulator, composed of radiatively coupled polarization splitters and of two magnetooptic unidirectional polarization converters, completes the last chapter.

Work on this thesis was accompanied by the following publications:

- M. Lohmeyer, N. Bahlmann, O. Zhuromskyy, H. Dötsch, and P. Hertel. Unidirectional magnetooptic polarization converters. *Journal of Lightwave Technology*, 1999. Submitted.
- M. Lohmeyer, N. Bahlmann, O. Zhuromskyy, and P. Hertel. Wave-matching-simulations of integrated optical coupler structures. *Fiber and integrated optics*, 1999. Submitted (invited).
- M. Lohmeyer, N. Bahlmann, O. Zhuromskyy, and P. Hertel. Radiatively coupled waveguide polarization splitter simulated by wave-matching based coupled mode theory. *Optical and Quantum Electronics*, 1999. Accepted for publication.
- M. Lohmeyer, N. Bahlmann, and P. Hertel. Geometry tolerance estimation for rectangular dielectric waveguide devices by means of perturbation theory. *Optics Communications*, 163(1-3):86–94, 1999.
- M. Fehndrich, A. Josef, L. Wilkens, J. Kleine-Börger, N. Bahlmann, M. Lohmeyer, P. Hertel, and H. Dötsch. Experimental Investigation of the Nonreciprocal Phase Shift of a TE-Mode in a Magneto-Optic Rib Waveguide. *Applied Physics Letters*, 74(20):2918–2920, 1999.
- O. Zhuromskyy, M. Lohmeyer, N. Bahlmann, H. Dötsch, and P. Hertel. Analysis of Polarization Independent Mach-Zehnder Type Integrated Optical Isolator. *Journal of Lightwave Technology*, 17(7):1200–1205, 1999.
- N. Bahlmann, M. Lohmeyer, H. Dötsch, and P. Hertel. Finite-Element Analysis of Nonreciprocal Phase Shift for TE Modes in Magnetooptic Rib Waveguides with a Compensation Wall. *IEEE Journal of Quantum Electronics*, 35(2):250–253, 1999.
- M. Lohmeyer, N. Bahlmann, O. Zhuromskyy, and P. Hertel. Wave-matching-simulations of integrated optical coupler structures. In G. C. Righini and S. I. Najafi, editors, *Integrated Optics Devices III*, volume 3620 of SPIE Proceedings, pages 68–78, 1999.
- M. Lohmeyer, N. Bahlmann, O. Zhuromskyy, and P. Hertel. Perturbational estimation of geometry tolerances for rectangular integrated optics devices. In G. C. Righini and S. I. Najafi, editors, *Integrated Optics Devices III*, volume 3620 of SPIE Proceedings, pages 311–319, 1999.
- N. Bahlmann, M. Lohmeyer, O. Zhuromskyy, H. Dötsch, and P. Hertel. Nonreciprocal coupled waveguides for integrated optical isolators and circulators for TM-modes. *Optics Communications*, 161(4-6):330–337, 1999.
- N. Bahlmann, M. Lohmeyer, H. Dötsch, and P. Hertel. Integrated magneto-optic Mach-Zehnder interferometer isolator for TE-modes. *Electronics Letters*, 34(22):2122–2123, 1998.
- A. F. Popkov, M. Fehndrich, M. Lohmeyer, and H. Dötsch. Nonreciprocal TE-mode phase shift by domain walls in magnetooptic rib waveguides. *Applied Physics Letters*, 72(20):2508–2510, 1998.
- M. Lohmeyer. Vectorial wave-matching mode analysis of integrated optical waveguides. *Optical and Quantum Electronics*, 30:385–396, 1998.
- M. Wallenhorst, V. Backherms, A. Josef, N. Bahlmann, M. Lohmeyer, H. Dötsch, and P. Hertel. Optimized nonreciprocal rib waveguides for integrated magneto-optic isolators. In K. Rubin, J. A. Bain, T. Nolan, D. Bogy, B. J. H. Stadler, M. Levy, J. P. Lorenzo, M. Mansuripur, Y. Okamura, and R. Wolfe, editors, *High-Density Magnetic Recording and Integrated Magneto-Optics: Materials and Devices*, volume 517 of MRS Symposium Proceedings Series, pages 463–468, 1998.

- M. Lohmeyer, M. Shamonin, N. Bahlmann, P. Hertel, and H. Dötsch. Radiatively coupled waveguide concept for an integrated magneto-optic circulator. In K. Rubin, J. A. Bain, T. Nolan, D. Bogy, B. J. H. Stadler, M. Levy, J. P. Lorenzo, M. Mansuripur, Y. Okamura, and R. Wolfe, editors, *High-Density Magnetic Recording and Integrated Magneto-Optics: Materials and Devices*, volume 517 of MRS Symposium Proceedings Series, pages 519–524, 1998.

- N. Bahlmann, M. Lohmeyer, M. Wallenhorst, H. Dötsch, and P. Hertel. A comparison of an improved design for two integrated optical isolators based on nonreciprocal Mach-Zehnder interferometry. In K. Rubin, J. A. Bain, T. Nolan, D. Bogy, B. J. H. Stadler, M. Levy, J. P. Lorenzo, M. Mansuripur, Y. Okamura, and R. Wolfe, editors, *High-Density Magnetic Recording and Integrated Magneto-Optics: Materials and Devices*, volume 517 of MRS Symposium Proceedings Series, pages 513–518, 1998.

- M. Lohmeyer, N. Bahlmann, O. Zhuromskyy, H. Dötsch, and P. Hertel. Phase-matched rectangular magnetooptic waveguides for applications in integrated optics isolators: numerical assessment. *Optics Communications*, 158:189–200, 1998.

- N. Bahlmann, M. Lohmeyer, M. Wallenhorst, H. Dötsch, and P. Hertel. An improved design of an integrated optical isolator based on nonreciprocal Mach-Zehnder interferometry. *Optical and Quantum Electronics*, 30:323–334, 1998.

- M. Lohmeyer. Wave-matching method for mode analysis of dielectric waveguides. *Optical and Quantum Electronics*, 29:907–922, 1997.

- M. Lohmeyer, M. Shamonin, and P. Hertel. Integrated Optical Circulator based on Radiatively Coupled Waveguides. *Optical Engineering*, 36(3):889–895, 1997.

- M. Shamonin, M. Lohmeyer, and P. Hertel. Directional coupler based on radiatively coupled waveguides. *Applied Optics*, 36(3):635–641, 1997.

- M. Shamonin, M. Lohmeyer, and P. Hertel. Analysis of Power-Dependent Switching Between Radiatively Coupled Planar Waveguides. *Journal of Lightwave Technology*, 15(6):983–989, 1997.

- M. Lohmeyer, M. Shamonin, and P. Hertel. Boundary Conditions for the Finite Difference Beam Propagation Method Based on Plane Wave Solutions of the Fresnel Equation. *IEEE Journal of Quantum Electronics*, 33(2):279–285, 1997.

- M. Shamonin, M. Lohmeyer, and P. Hertel. Radiatively coupled magneto-optic waveguides. In S. I. Najafi and M. N. Armenise, editors, *Functional Photonic and Fiber Devices*, volume 2695 of SPIE Proceedings, pages 355–361, 1996.

- M. Shamonin, M. Lohmeyer, P. Hertel, and H. Dötsch. Magneto-optic waveguides: modeling and applications. In S. I. Najafi and M. N. Armenise, editors, *Functional Photonic and Fiber Devices*, volume 2695 of SPIE Proceedings, pages 344–354, 1996.

- M. Shamonin, M. Lohmeyer, P. Hertel, and H. Dötsch. Optimization of a nonreciprocal phase shifter comprising a magneto-optic slab waveguide. *Optics Communications*, 131:37–40, 1996.

1 Optical waveguide theory

The following sections provide the theoretical basis for the numerical simulations considered in the subsequent chapters. Section 1.1 introduces the notation and lists fundamental equations. Although frequently a more compact notation would have been possible, relations which enter the numerical simulations directly or may serve for immediate inspection are written explicitely in components. Naturally, in distinct formulations most of the material of Section 1.1 is the subject of standard texts on optical waveguide theory, e.g. of Refs. [136, 157, 62, 91]; here explicit references are not included.

With the garnet waveguides in mind, one has to be very strict in the treatment of dielectric interfaces. Roughly this can be realized as follows. The discontinuities may be less significant for two reasons: Either the refractive index contrast itself is small, or it is high enough, such that the strength of the guided electromagnetic field at the interface becomes negligible. For a waveguide made of semiconductor material with typical substrate, film, and cover permittivities of 11.7, 11.8, 1.0, the first reason applies to the substrate-film interface with a permittivity contrast of 1%, the second one to the film-cover boundary with a contrast of 92% (these are parameters of common mode solver benchmark problems). In contrast, an air covered Yttrium-Iron-Garnet (YIG) film on a Gallium-Gadolinium-Garnet (GGG) substrate corresponds to a permittivity profile of 3.6, 5.3, 1.0, apart from the magnetooptic properties. Here permittivity contrasts of 32% and 81% require explicit consideration of the dielectric boundaries for all modeling attempts.

The somewhat exotic parameters have specific consequences for the field profiles as well. For an illustration, we refer to the basic ray model for the planar three layer dielectric waveguide. The guided field may be viewed to be composed from constructively interfering rays in the film region, which propagate at a certain angle with respect to the film plane. For the above example of semiconductor parameters, the condition of total reflection at the film boundaries leads to a small maximum propagation angle of 5°. In contrast, the garnet waveguide permits angles up to 34°. Guided fields in these waveguides have large components in the direction of propagation, the fields are no longer transversal. There is a pronounced dependence on the orientation of polarization, even for waveguides made of isotropic material. The familiar viewpoint of propagating plane waves should be completely abandoned. The term 'polarization' is to be associated with mode amplitudes, rather than with the electric field vector, which varies in size and orientation over the waveguide cross section.

1.1 Properties of guided modes

The further reasoning of this thesis is based on the macroscopic Maxwell equations of electrodynamics for the electric field $\boldsymbol{\mathcal{E}}$, magnetic induction $\boldsymbol{\mathcal{B}}$, dielectric displacement $\boldsymbol{\mathcal{D}}$, and the magnetic field $\boldsymbol{\mathcal{H}}$. We are interested in stationary optical fields, i.e. fields with a harmonic time dependence at angular frequency ω. With the space and time coordinates denoted x, y, z, and t, the electric field can be written

$$\boldsymbol{\mathcal{E}}(x,y,z,t) = \frac{1}{2}\bar{\boldsymbol{E}}(x,y,z)\,\mathrm{e}^{\mathrm{i}\omega t} + \frac{1}{2}\bar{\boldsymbol{E}}^*(x,y,z)\,\mathrm{e}^{-\mathrm{i}\omega t}\,. \tag{1.1}$$

Analogous relations combine the time dependent quantities $\boldsymbol{\mathcal{B}}$, $\boldsymbol{\mathcal{D}}$, $\boldsymbol{\mathcal{H}}$, and the complex amplitude fields $\bar{\boldsymbol{B}}$, $\bar{\boldsymbol{D}}$, $\bar{\boldsymbol{H}}$. The Maxwell equations have to be supplemented by suitable material relationships. Assuming a linear dielectric medium with the magnetic susceptibility vanishing [106, 123] at optical frequencies, these

are

$$\bar{\boldsymbol{B}} = \mu_0 \bar{\boldsymbol{H}} \quad \text{and} \quad \bar{\boldsymbol{D}} = \epsilon_0 \hat{\epsilon} \bar{\boldsymbol{E}}\,, \tag{1.2}$$

with vacuum permittivity ϵ_0 and permeability μ_0. For the modeling of waveguiding phenomena, the relative permittivity $\hat{\epsilon}$ is to be considered depending on the space coordinates. Now the Maxwell equations for the frequency domain in an uncharged medium, with the magnetic induction and the dielectric displacement eliminated, read

$$\operatorname{curl} \bar{\boldsymbol{E}} = -\mathrm{i}\omega\mu_0 \bar{\boldsymbol{H}}\,, \quad \operatorname{curl} \bar{\boldsymbol{H}} = \mathrm{i}\omega\epsilon_0 \hat{\epsilon} \bar{\boldsymbol{E}}\,, \quad \operatorname{div} \hat{\epsilon} \bar{\boldsymbol{E}} = 0\,, \quad \operatorname{div} \bar{\boldsymbol{H}} = 0\,. \tag{1.3}$$

The curl equations can be combined to form the wave equations

$$\operatorname{curl}\operatorname{curl} \bar{\boldsymbol{E}} = k^2 \hat{\epsilon} \bar{\boldsymbol{E}}\,, \quad \text{or} \quad \operatorname{curl} \hat{\epsilon}^{-1} \operatorname{curl} \bar{\boldsymbol{H}} = k^2 \bar{\boldsymbol{H}}\,, \tag{1.4}$$

where $k = \omega/c = 2\pi/\lambda$ is the vacuum wavenumber, given by the frequency ω and the speed of light $c = 1/\sqrt{\epsilon_0\mu_0}$, or alternatively by the vacuum wavelength parameter λ.

Although many applications in integrated optics rely on crystalline materials, frequently the deviation of the permittivity from isotropy is small. Therefore we focus on waveguiding structures made of isotropic lossless media first. Anisotropic contributions are included in Sections 1.3, 1.5 by means of perturbation theory. Note that a change of coordinates aiming at a diagonalization of the permittivity tensor is usually not an option in the current framework. The waveguide geometry dictates the proper coordinate system. Otherwise a description of the guided wave propagation in slanted coordinates would be required.

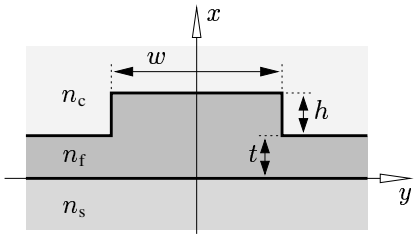

Figure 1.1: Rib waveguide cross section. n_s, n_f, and n_c denote the refractive indices of the substrate, the film, and the cover layers. w and h are the width and height of the rib, t is the thickness of the remaining film outside the rib. As suggested by the figure, throughout this thesis the directions of the transverse coordinate axes y and x will be referred to by the terms horizontal *and* vertical. *The z-axis denotes the* longitudinal *direction, the direction of light propagation.*

Figure 1.1 shows a typical example for a longitudinally homogeneous dielectric waveguide, assumed to be made of isotropic lossless material with refractive index n. It is prescribed by a real diagonal permittivity profile $\epsilon = n^2$ that depends on the transverse coordinates x and y only.

We are interested in solutions of Eqs. (1.3) or (1.4), respectively, in the form

$$\bar{\boldsymbol{E}}(x,y,z) = \boldsymbol{E}(x,y)\,\mathrm{e}^{-\mathrm{i}\beta z}, \quad \bar{\boldsymbol{H}}(x,y,z) = \boldsymbol{H}(x,y)\,\mathrm{e}^{-\mathrm{i}\beta z}, \tag{1.5}$$

i.e. modes with harmonic dependence on the propagation coordinate z. A mode is defined by its propagation constant β and by the electric part $\boldsymbol{E}$ and magnetic part $\boldsymbol{H}$ of the mode profile. Frequently, β is referred to in terms of the effective mode index $n_{\text{eff}} = \beta/k$ or the effective permittivity $\epsilon_{\text{eff}} = n_{\text{eff}}^2$.

With ansatz (1.5) inserted into Eqs. (1.3), these split into a first set combining the real parts of the transverse electric and magnetic components with the imaginary parts of the longitudinal components, and a second identical set that includes the imaginary parts of the transverse and the real parts of the longitudinal components. Solutions of both systems for the same parameter β and for identical boundary conditions of integrable fields should coincide up to a real constant. Therefore, without loss of generality, the mode profile can be written $\boldsymbol{E} = (E_x, E_y, \mathrm{i}E_z)$, $\boldsymbol{H} = (H_x, H_y, \mathrm{i}H_z)$ where the component functions E_x, E_y, E_z, H_x, H_y, H_z are *real*. Note that the longitudinal components of $\boldsymbol{E}$ and $\boldsymbol{H}$ are $\mathrm{i}E_z$ and $\mathrm{i}H_z$.

To summarize the notation, the electric and magnetic field associated with a mode of propagation constant β has the form

$$\boldsymbol{\mathcal{E}}(x,y,z,t) = \begin{pmatrix} E_x \\ E_y \\ \mathrm{i}E_z \end{pmatrix}(x,y)\ \mathrm{e}^{\mathrm{i}(\omega t - \beta z)}, \quad \boldsymbol{\mathcal{H}}(x,y,z,t) = \begin{pmatrix} H_x \\ H_y \\ \mathrm{i}H_z \end{pmatrix}(x,y)\ \mathrm{e}^{\mathrm{i}(\omega t - \beta z)}. \tag{1.6}$$

In general it must be assumed to be hybrid, i.e. none of the components vanish. Adhering to common notational rules, the second term and the factors $1/2$ from Eq. (1.1) are suppressed in Eq. (1.6) and in related following equations.

With ansatz Eq. (1.6), Eqs. (1.3) reduce to a real system of first order differential equations for the mode components

$$\begin{array}{lll} \beta E_x = \omega\mu_0 H_y - \partial_x E_z, & \beta H_x = -\omega\epsilon_0\epsilon E_y - \partial_x H_z, & \omega\epsilon_0\epsilon E_z = \partial_y H_x - \partial_x H_y, \\ \beta E_y = -\omega\mu_0 H_x - \partial_y E_z, & \beta H_y = \omega\epsilon_0\epsilon E_x - \partial_y H_z, & \omega\mu_0 H_z = \partial_x E_y - \partial_y E_x, \\ \epsilon\beta E_z = -\partial_x\epsilon E_x - \partial_y\epsilon E_y, & \beta H_z = -\partial_x H_x - \partial_y H_y, & \end{array} \tag{1.7}$$

where the curl equations (the first two rows) imply the two divergence relations.

1.1.1 Vectorial mode equations

Eqs. (1.7) allow us to eliminate four of the six component fields. Alternatively, the two transverse electric, the two transverse magnetic, or the two longitudinal components may be retained. Using the abbreviations $X = \epsilon^{-1}(\partial_x\epsilon)$, $Y = \epsilon^{-1}(\partial_y\epsilon)$, and $B = 1/(\beta^2 - k^2\epsilon)$, the vectorial mode equations read

$$\begin{array}{l} (\partial_x^2 + \partial_y^2 + k^2\epsilon - \beta^2)E_x + \partial_x X E_x + \partial_x Y E_y = 0 \\ (\partial_x^2 + \partial_y^2 + k^2\epsilon - \beta^2)E_y + \partial_y X E_x + \partial_y Y E_y = 0 \end{array} , \tag{1.8}$$

$$\begin{array}{l} (\partial_x^2 + \partial_y^2 + k^2\epsilon - \beta^2)H_x - Y\partial_y H_x + Y\partial_x H_y = 0 \\ (\partial_x^2 + \partial_y^2 + k^2\epsilon - \beta^2)H_y + X\partial_y H_x - X\partial_x H_y = 0 \end{array} , \tag{1.9}$$

$$\begin{array}{l} (\partial_x B\epsilon\partial_x + \partial_y B\epsilon\partial_y - \epsilon)\sqrt{\epsilon_0}E_z + \beta k^{-1}(\partial_x B\partial_y - \partial_y B\partial_x)\sqrt{\mu_0}H_z = 0 \\ (\partial_x B\partial_x + \partial_y B\partial_y - 1)\sqrt{\mu_0}H_z + \beta k^{-1}(\partial_y B\partial_x - \partial_x B\partial_y)\sqrt{\epsilon_0}E_z = 0 \end{array} . \tag{1.10}$$

While these three formulations should be equivalent, the second one is usually preferred for numerical simulations: In contrast to E_x and E_y in Eq. (1.8), the basic fields of Eq. (1.9) are continuous at dielectric interfaces. For common waveguides, at least one of H_x and H_y is a large component, thus evaluation of the remaining fields is considered less error prone than subtracting derivatives of the small longitudinal components in Eq. (1.10).

1.1.2 Semivectorial approximation

Frequently, waveguide simulations are performed in semivectorial approximation as introduced in Refs. [139, 140]. The assumption that one of the transverse electric or magnetic components vanishes reduces the vectorial mode problem to a scalar wave equation.

For semivectorial TE modes, or quasi TE modes, E_x is set to zero. The dominant electric component E_y satisfies the semivectorial TE wave equation

$$(\partial_x^2 + \partial_y^2 + k^2\epsilon - \beta^2)E_y = 0\,. \tag{1.11}$$

Semivectorial TM modes or quasi TM modes are characterized by vanishing H_x. For the dominant magnetic component H_y the semivectorial TM wave equation

$$(\epsilon\partial_x\frac{1}{\epsilon}\partial_x + \partial_y^2 + k^2\epsilon - \beta^2)H_y = 0 \tag{1.12}$$

holds. Both equations follow immediately from the vectorial formulations (1.8), (1.9) with the approximation of small horizontal permittivity variations, i.e. for $\partial_y\epsilon = \epsilon\partial_y$. Without this assumption, the first rows

of Eqs. (1.8), (1.9) would be violated. Typically, y is along the substrate surface, the direction in which the field is less tightly confined. Note that the transverse directions are no longer treated alike, as they are in the fully vectorial formalism.

A number of arguments supports this approximation:

- For planar waveguides (cf. Chapter 2) the mode set exactly splits into a subset with transverse electric components only (TE modes) and another subset with transverse magnetic components only (TM modes). If a planar waveguide is laterally bounded, i.e. transformed to a broad rib waveguide, $(\partial_y \epsilon)$ is still small, and the qualitative features of the mode fields should be retained. Consequently, the modes of the rib waveguides also split into a subset with large E_y, H_x components and small E_x, H_y fields, and another subset with large E_x, H_y and small E_y, H_x. Although all modes have both small longitudinal electric and magnetic components, the former are commonly called TE modes, the latter are named TM modes. As in the planar case, E_y and H_y serve as basic fields for the semivectorial modes.

- Leading to mode fields with five nonvanishing components, the semivectorial approximation as formulated above is self consistent: The entire set of Eqs. (1.7) is fulfilled, provided that Eqs. (1.11), (1.12) hold, and that the assumption $\partial_y \epsilon \approx \epsilon \partial_y$ is valid.

  Note that with an alternative ansatz of vanishing E_y for TM modes or vanishing H_y for TE polarization (cf. Refs. [139, 140]), this self consistency property would be violated, as can be shown by inspection of Eqs. (1.8), (1.9).

- Regarding the corrections of scalar modes in weakly guiding structures due to increased refractive index contrast, a perturbation formalism [157, 123] can be applied. It predicts vanishing lowest order polarization correction for the basic scalar modes polarized along one of the coordinate axes, provided that the waveguide has a mirror symmetry (see Section 1.1.3). This supports the assumptions of one negligible transverse component.

- In most cases, the approximation yields correct results, at least if only the propagation constants are compared with data from fully vectorial simulations. For rectangular rib or raised strip waveguides, usually one of the transverse electric or magnetic mode components turns out to be significantly larger than the other one, and the main assumption for semivectorial modeling is fulfilled. On standard benchmark problems [159], semivectorial and vectorial mode solvers achieve an equal level of accuracy.

Strictly speaking the first two arguments are not applicable to a waveguide with a discontinuous permittivity profile, or to a waveguide with a profile that does not distinguish between the x and y axes. The only way to assure reliability of the semivectorial approximation is to compare it with a fully vectorial calculation on the same problem, or with experimental data, if available.

However, there are applications that require the extended accuracy of fully vectorial calculations (cf. e.g. Section 6.3), even if one of the transverse mode components is still small. Additionally, certain configurations yield modes with both transverse electric components of the same order of magnitude [95]. This occurs if two modes of the same symmetry (see Section 1.1.3) are degenerate or almost degenerate. There are even applications relying on such structures [96, 94], where semivectorial analysis is obviously insufficient.

1.1.3 Symmetric waveguides

Frequently, waveguides are mirror symmetric with respect to the transformation $y \to -y$. Figure 1.1 is an example; in fact, all basic structures discussed in this thesis fall into this class. Their guided modes have a definite parity. As can be realized by inspection of Eqs. (1.7), the Maxwell equations demand equal parity for H_x, E_y, and H_z, and reversed parity for E_x, H_y, and E_z. Throughout this thesis, we call a hybrid mode with even H_x, E_y, and H_z *symmetric* (s), one with these components odd will be denoted *antisymmetric* (a).

Commonly, modes of rectangular waveguides are classified by their dominant transverse components, where the naming conventions TE and TM of Section 1.1.2 transfer to truly hybrid modes. A lower index indicates the number of nodal lines parallel to the x axis in the dominant electric and magnetic component, respectively (with the exception of Chapter 2 and Section 4.3.3, only vertical nodal lines occur). Consequently, for a waveguide with mirror symmetry, all TE modes with even index and TM modes with odd index are symmetric. The corresponding semivectorial fields approximate symmetric hybrid modes. This is summarized in Table 1.1. Immediate consequences of these statements are discussed e.g. in Section 6.1.

	E_x	E_y	E_z	H_x	H_y	H_z	
(s)	$-$	$+$	$-$	$+$	$-$	$+$	$\mathrm{TE}_0, \mathrm{TM}_1, \mathrm{TE}_2, \mathrm{TM}_3, \ldots$
(a)	$+$	$-$	$+$	$-$	$+$	$-$	$\mathrm{TM}_0, \mathrm{TE}_1, \mathrm{TM}_2, \mathrm{TE}_3, \ldots$

Table 1.1: Naming conventions (s)/(a), TE/TM, and signs $\pm$ of the mode components under the reflection $y \to -y$, for waveguides with mirror symmetry with respect to the x-z-plane.

The above convention is to be applied if the hybrid character of modes is important, or if multiple modes of undefined polarization come into play. However, frequently one deals with multimode waveguides, and only one polarization is considered. Note that in this context the symmetry property usually indicates the symmetry of the basic field component of the relevant polarization, i.e. TE_0, TM_0, TE_2, TM_2, ... modes are named symmetric, modes with odd index are called antisymmetric.

Additionally, longitudinal homogeneous waveguides are symmetric with respect to $z \to -z$. From each field of the form (1.5) a mode with inverted propagation constant $-\beta$ can be constructed. Inspection of Eqs. (1.7) shows that the profile has the form $(E_x, E_y, -\mathrm{i}E_z)$, $(-H_x, -H_y, \mathrm{i}H_z)$. According to Eq. (1.13), this operation reverses the direction of the power flux, thus the mode propagates at the same frequency in the negative z direction. These backward traveling modes will be relevant for the discussion of orthogonality properties in the following section.

1.1.4 Power flux and mode orthogonality

A mode is called guided, if the time averaged Poynting vector $\boldsymbol{S} = \mathrm{Re}(\boldsymbol{E} \times \boldsymbol{H}^*)/2$ associated with the field (1.5) can be integrated over the waveguide cross section plane. Due to ansatz (1.6) of real component fields, $\boldsymbol{S}$ has a longitudinal component $S_z = (E_x\, H_y - E_y\, H_x)/2$ only. A general hybrid guided mode carries the power

$$P = \frac{1}{2} \iint (E_x\, H_y - E_y\, H_x)\, \mathrm{d}x\, \mathrm{d}y\,. \tag{1.13}$$

In the semivectorial approximation, this expression evaluates to

$$P = \frac{\beta}{2\omega\mu_0} \iint \left(E_y^2 - \beta^{-2} E_y \partial_y^2 E_y\right)\, \mathrm{d}x\, \mathrm{d}y \approx \frac{\beta}{2\omega\mu_0} \iint E_y^2\, \mathrm{d}x\, \mathrm{d}y \tag{1.14}$$

for TE, and

$$P = \frac{\beta}{2\omega\epsilon_0} \iint \frac{1}{\epsilon} \left(H_y^2 - \beta^{-2} H_y \partial_y^2 H_y\right)\, \mathrm{d}x\, \mathrm{d}y \approx \frac{\beta}{2\omega\epsilon_0} \iint \frac{1}{\epsilon} H_y^2\, \mathrm{d}x\, \mathrm{d}y \tag{1.15}$$

for TM polarized modes, where for the last terms in Eqs. (1.14), (1.15) the profiles are assumed only weakly guiding in the y-direction, such that terms $\beta^{-2}\partial_y^2$ are small, if compared to the basic fields.

Closely related is the topic of mode orthogonality. Let $\bar{\boldsymbol{E}}_m$, $\bar{\boldsymbol{H}}_m$ and β_m denote mode profiles of the form (1.5), (1.6) and their propagation constants that correspond to the same lossless dielectric waveguide. Eqs. (1.3) directly lead to the identity

$$\mathrm{div}\,(\bar{\boldsymbol{E}}_l \times \bar{\boldsymbol{H}}_m^* + \bar{\boldsymbol{E}}_m^* \times \bar{\boldsymbol{H}}_l) = 0. \tag{1.16}$$

By integrating over the cross section and inserting ansatz (1.5), one arrives at the orthogonality property

$$(\boldsymbol{E}_l, \boldsymbol{H}_l; \boldsymbol{E}_m, \boldsymbol{H}_m) = \delta_{lm} P_m \,, \tag{1.17}$$

where P_m denotes the power (1.13) assigned to mode m, and $\delta_{lm} = 1$ for $l = m$, $\delta_{lm} = 0$ otherwise. It is valid for $\beta_l \neq \beta_m$, i.e. for nondegenerate hybrid modes, with the bilinear product defined as

$$(\boldsymbol{E}_l, \boldsymbol{H}_l; \boldsymbol{E}_m, \boldsymbol{H}_m) = \frac{1}{4} \iint (E_{lx} H_{my} - E_{ly} H_{mx} + E_{mx} H_{ly} - E_{my} H_{lx}) \,\mathrm{d}x \,\mathrm{d}y \,. \tag{1.18}$$

This form will be used e.g. in the framework of coupled mode theory in Section 1.5. Obviously hybrid modes of opposite symmetry (cf. Section 1.1.3) are orthogonal with respect to this product.

Subtracting the corresponding relation for one backward traveling mode (propagation constant $-\beta_m$) leads to a more familiar and simpler, but nonsymmetric form

$$\frac{1}{2} \iint (E_{lx} H_{my} - E_{ly} H_{mx}) \,\mathrm{d}x \,\mathrm{d}y = \delta_{lm} P_m, \tag{1.19}$$

which requires $|\beta_l| \neq |\beta_m|$.

Analogous expressions hold for semivectorial fields. Assuming terms $\sim \beta^{-2} \partial_y^2$ to be negligible again, with two TE modes inserted, Eq. (1.19) reads

$$\frac{\beta_m}{2\omega\mu_0} \iint E_{ly} E_{my} \,\mathrm{d}x \,\mathrm{d}y = \delta_{lm} P_m, \tag{1.20}$$

while two nondegenerate TM modes satisfy the relation

$$\frac{\beta_m}{2\omega\epsilon_0} \iint \frac{1}{\epsilon} H_{ly} H_{my} \,\mathrm{d}x \,\mathrm{d}y = \delta_{lm} P_m. \tag{1.21}$$

Semivectorial modes are strictly orthogonal with respect to the product (1.18), if they belong to different symmetry classes of Table 1.1. In particular, this applies to the fundamental modes of both polarizations in a symmetric waveguide. For general nondegenerate semivectorial modes, approximate orthogonality (1.17) may be expected, since this relation holds for the corresponding hybrid fields. In contrast to the planar case (see Eq. (2.8)), arbitrary three-dimensional quasi TE modes are not a priori strictly orthogonal to quasi TM modes.

Note that the general form (1.18) is not positive definite, while its restrictions on semivectorial fields, i.e. the left hand sides of Eqs. (1.20), (1.21), define scalar products for the single basic field components E_y and H_y. However, the definiteness property will not be needed throughout this thesis, since we do not employ Hilbert space methods.

1.1.5 Piecewise constant permittivity

The profile of our example waveguide in Figure 1.1 can be divided into regions of constant permittivity. With vanishing transverse derivatives of the permittivity, the various formulations of the mode problem (1.8)–(1.12) shrink to the single Helmholtz equation

$$\partial_x^2 \Phi + \partial_y^2 \Phi = (\beta^2 - k^2 \epsilon) \Phi \,, \tag{1.22}$$

uniformly for the six mode components $\Phi \in \{E_x, E_y, E_z, H_x, H_y, H_z\}$. It applies for all points on the waveguide cross section except on the boundary lines, where appropriate boundary conditions have to be implemented. Abandoning the sets of globally valid differential equations, this formulation emphasizes the viewpoint that guiding effects as well as polarization coupling arise from the permittivity discontinuity lines

only, while in between (i.e. locally) the fields satisfy the equation for electromagnetic waves in an infinite homogeneous medium.

We further specialize to structures with the dielectric boundary lines parallel to the transverse coordinate axes, as in Figure 1.1. This class includes the majority of waveguides investigated in the cited references, the standard benchmark problems, and the magnetooptic waveguides discussed for isolator applications. Especially for the latter, inclusion of suitable boundary conditions becomes important, since typical permittivity contrasts are such that the fields are neither negligible on the interfaces, nor are the contrasts low enough to allow disregarding the permittivity jump.

Hybrid modes

General hybrid modes are still described by two basic fields. They satisfy the wave equation (1.22) separately, i.e. the fields are decoupled. Expressing the remaining components in terms of the two directly computed fields leads to the following alternative formulations, corresponding to Eqs. (1.8)–(1.10):

$$\begin{pmatrix} E_x \\ E_y \\ \mathrm{i}E_z \end{pmatrix} = \begin{pmatrix} E_x \\ E_y \\ -\mathrm{i}\beta^{-1}(\partial_x E_x + \partial_y E_y) \end{pmatrix}, \quad \begin{pmatrix} H_x \\ H_y \\ \mathrm{i}H_z \end{pmatrix} = \frac{1}{\omega\mu_0} \begin{pmatrix} -\beta E_y + \beta^{-1}(\partial_{xy} E_x + \partial_y^2 E_y) \\ \beta E_x - \beta^{-1}(\partial_x^2 E_x + \partial_{xy} E_y) \\ \mathrm{i}(\partial_x E_y - \partial_y E_x) \end{pmatrix}, \tag{1.23}$$

$$\begin{pmatrix} E_x \\ E_y \\ \mathrm{i}E_z \end{pmatrix} = \frac{1}{\omega\epsilon_0\epsilon} \begin{pmatrix} \beta H_y - \beta^{-1}(\partial_{xy} H_x + \partial_y^2 H_y) \\ -\beta H_x + \beta^{-1}(\partial_x^2 H_x + \partial_{xy} H_y) \\ \mathrm{i}(\partial_y H_x - \partial_x H_y) \end{pmatrix}, \quad \begin{pmatrix} H_x \\ H_y \\ \mathrm{i}H_z \end{pmatrix} = \begin{pmatrix} H_x \\ H_y \\ -\mathrm{i}\beta^{-1}(\partial_x H_x + \partial_y H_y) \end{pmatrix}, \tag{1.24}$$

$$\begin{pmatrix} E_x \\ E_y \\ \mathrm{i}E_z \end{pmatrix} = \frac{1}{\sqrt{\epsilon_0}} \begin{pmatrix} B(-k\partial_y h - \beta\partial_x e) \\ B(k\partial_x h - \beta\partial_y e) \\ \mathrm{i}e \end{pmatrix}, \quad \begin{pmatrix} H_x \\ H_y \\ \mathrm{i}H_z \end{pmatrix} = \frac{1}{\sqrt{\mu_0}} \begin{pmatrix} B(k\epsilon\partial_y e - \beta\partial_x h) \\ B(-k\epsilon\partial_x e - \beta\partial_y h) \\ \mathrm{i}h \end{pmatrix}, \tag{1.25}$$

with $B = 1/(\beta^2 - k^2\epsilon)$ and basic fields $e = \sqrt{\epsilon_0}E_z$, $h = \sqrt{\mu_0}H_z$ of the same dimension. Note that the above expressions are valid at points with constant and isotropic permittivity only.

The boundaries considered here are uncharged interfaces. The tangential components of the electric and magnetic fields and the normal components of the dielectric displacement and the magnetic induction are continuous on the plane that divides the two dielectric media. Hence the electric and magnetic mode components are subject to the following boundary conditions: On horizontal boundaries (parallel to the y axis) the quantities ϵE_x, E_y, E_z, H_x, H_y, H_z are continuous, while on vertical boundaries (parallel to the x axis) continuity is required for E_x, ϵE_y, E_z, H_x, H_y, H_z. These conditions connect the two basic unknown fields according to Eqs. (1.23)–(1.25).

Particular problems arise from the corners in a piecewise constant profile. Consider e.g. the corner of the rib flank and the outer film surface at $x = t$, $y = w/2$ in the rib waveguide profile of Figure 1.1. On a horizontal line through this point, E_x has to be continuous inside the rib for $y < w/2$. Outside the rib, for $y > w/2$, E_x jumps by a factor of n_f^2 at $x = t$. At the same time, on the entire vertical line through the corner, E_x is required to be continuous. Obviously, the conditions are contradictory for finite functions, and the mode profiles are known to be divergent at such corner points [8, 144, 20].

The derivations of the relations regarding mode orthogonality (Section 1.1.4), perturbation theory (Section 1.3), or coupled mode theory (Section 1.5), are formulated in terms of $\boldsymbol{E}$ and $\boldsymbol{H}$. Partial integration with respect to the transverse coordinates involves derivatives of the form $\mathrm{div}\,(\boldsymbol{E} \times \boldsymbol{H})$ only. Thus these results are compatible with the discontinuous mode fields of waveguides with piecewise constant permittivity.

A number of perturbational expressions, e.g. for geometry variations (Section 1.4), for the TE phase shift in a magnetooptic waveguide (Section 6.2.2), or for roughness scattering [55, 104] are based on integrals of the squared electric mode profile along vertical dielectric interfaces, typically the sidewalls of a rib waveguide.

In that case it is usually not adequate to neglect the discontinuities in E_y, since one would have to admit an uncertainty in the order of the squared permittivity ratio. For an interface between a magnetic garnet (refractive index 2) and air, this is a factor of 16.

Semivectorial modes

For modeling under the semivectorial approximation, merely one scalar field must be calculated directly. The components E_y for TE and H_y for TM polarization are the basis for five component approximations to the mode profiles.

TE:

$$\begin{pmatrix} E_x \\ E_y \\ \mathrm{i}E_z \end{pmatrix} = \begin{pmatrix} 0 \\ E_y \\ -\mathrm{i}\beta^{-1}\partial_y E_y \end{pmatrix}, \quad \begin{pmatrix} H_x \\ H_y \\ \mathrm{i}H_z \end{pmatrix} = \frac{1}{\omega\mu_0} \begin{pmatrix} -\beta E_y + \beta^{-1}\partial_y^2 E_y \\ -\beta^{-1}\partial_{xy} E_y \\ \mathrm{i}\partial_x E_y \end{pmatrix}, \tag{1.26}$$

TM:

$$\begin{pmatrix} E_x \\ E_y \\ \mathrm{i}E_z \end{pmatrix} = \frac{1}{\omega\epsilon_0\epsilon} \begin{pmatrix} \beta H_y - \beta^{-1}\partial_y^2 H_y \\ \beta^{-1}\partial_{xy} H_y \\ -\mathrm{i}\partial_x H_y \end{pmatrix}, \quad \begin{pmatrix} H_x \\ H_y \\ \mathrm{i}H_z \end{pmatrix} = \begin{pmatrix} 0 \\ H_y \\ -\mathrm{i}\beta^{-1}\partial_y H_y \end{pmatrix}. \tag{1.27}$$

We demand the following boundary conditions for the E_y component of quasi TE modes to hold: On horizontal boundaries, E_y and its normal derivative $\partial_x E_y$ ($\sim H_z$) must be continuous. On vertical boundaries, continuity is required for the product ϵE_y (the normal component of the dielectric displacement) and the derivative $\partial_y E_y$ ($\sim E_z$). In general there is a discontinuity in E_y on the vertical boundary lines.

For quasi TM modes, continuity conditions should be formulated in terms of H_y. On horizontal boundaries, H_y and the product $\epsilon^{-1}\partial_x H_y$ ($\sim E_z$) must be continuous, while on vertical boundaries both the field H_y and its normal derivative $\partial_y H_y$ ($\sim H_z$) have to be continuous.

While this choice of boundary conditions for the semivectorial approximation is common [113], it is not compelling [139, 140]. Obviously the conditions do not follow from Eqs. (1.11)–(1.12), since otherwise horizontal and vertical boundaries would be treated alike (the second term in Eq. (1.12) reads $\epsilon\partial_y\epsilon^{-1}\partial_y$ alternatively). Inspection of Eqs. (1.26), (1.27) shows that the semivectorial modes of both polarizations satisfy the boundary conditions on horizontal discontinuities exactly. On vertical boundaries, quasi TE modes violate the continuity requirements for H_x and H_z. Likewise, quasi TM modes do not satisfy the conditions for E_x and E_z. Note that this is the only approximation in the semivectorial ansatz for piecewise constant permittivity, provided the wave equation (1.22) is obeyed exactly.

1.1.6 Interval for effective mode indices

Usually, a mode analysis program needs an interval n_b, n_t to be supplied, which the algorithm searches for the effective indices of guided modes. A tight estimate is desirable, since the computational effort grows with increasing interval length. For planar multilayer waveguides as investigated in Chapter 2, outwards exponential field decays and a harmonic field shape on at least one inner layer are necessary to satisfy the conditions of square integrable fields and of suitable continuity at the dielectric interfaces. Thus appropriate interval boundaries n_b, n_t are given by the maximum of the refractive indices of the outermost layers, and by the refractive index maximum on the inner layers, respectively. Analogous limits apply to radially symmetric profiles.

However, in case of the vectorial modes of a raised strip or rib waveguide, determining a suitable interval is more complicated. Consider the rib waveguide of Figure 1.1. Straightforward extension of the above rule to the regions of constant permittivity is not possible, since this would obviously yield an empty interval.

From the numerical method employed in this thesis (Chapter 3), the following practical recipe emerges. Effective mode indices are never found above the level of the refractive index maximum, therefore this maximum constitutes the top boundary n_t of the search interval. The ansatz (3.3) for the mode field fails on unbounded corner regions (cf. Figure 3.1), if the trial value for the propagation constant is below kn, where n is the local refractive index. Thus, the bottom limit n_b is given by the maximum of the refractive indices of the corner regions.

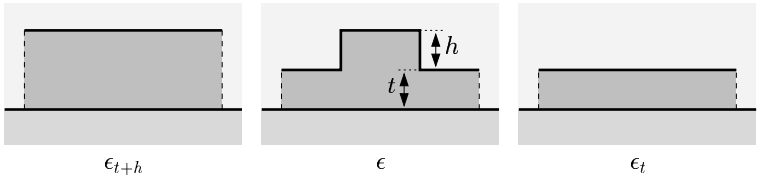

Figure 1.2: Planar structures limiting a rib waveguide.

The interval can be narrowed if one accepts the approximation of scalar fields. A scalar mode corresponding to the permittivity profile ϵ is a continuously differentiable field ϕ satisfying the wave equation (1.22). For such fields, the effective mode indices of layered, but laterally bounded structures are limited by the effective indices of the planar waveguides corresponding to the smallest and largest thickness of the guiding film (provided these support guided modes). Roughly, this can be seen as follows. We refer to the rib waveguide of Figure 1.1. Defining a linear operator $L_\epsilon = \partial_x^2 + \partial_y^2 + k^2\epsilon$, the wave equation (1.22) becomes an eigenvalue problem $L_\epsilon\phi = \beta\phi$. Analogously, operators L_{ϵ_t} and $L_{\epsilon_{t+h}}$ shall describe permittivity profiles of broad (in the sense of appropriate limits) raised strip waveguides with thicknesses t and $t+h$, see Figure 1.2. Employing standard Hilbert space theory [169], the operators can be shown to satisfy the inequality $L_{\epsilon_{t+h}} \geq L_\epsilon \geq L_{\epsilon_t}$. Each has a number of discrete eigenvalues $\beta_j^{\epsilon_{t+h}}$, β_j^{ϵ}, $\beta_j^{\epsilon_h}$ at the top of the spectrum. Assuming these to be in descending order, the operator inequality transfers to the eigenvalues: $\beta_j^{\epsilon_{t+h}} \geq \beta_j^{\epsilon} \geq \beta_j^{\epsilon_h}$. With increasing strip width, the waveguides with profiles ϵ_t and ϵ_{t+h} support a growing number of guided modes, while the lowest order propagation constants approach the levels of the fundamental propagation constants $\beta_\mathrm{pl}^{\epsilon_{t+h}}$, $\beta_\mathrm{pl}^{\epsilon_t}$ of the corresponding planar waveguides (three layer waveguides with refractive indices n_s, n_f, n_c and guiding film thickness t or $t+h$, respectively). Thus, in the limit of large strip width, the effective mode indices β_j^{ϵ}/k of the waveguide in question are limited by

$$\beta_\mathrm{pl}^{\epsilon_{t+h}} \geq \beta_j^{\epsilon} \geq \beta_\mathrm{pl}^{\epsilon_t} \,. \tag{1.28}$$

Note that this argument does not apply to the semivectorial or fully vectorial mode problem, since suitable Hilbert space formulations seem to be not available. Nevertheless, frequently the approximation $n_\mathrm{b} = \beta_\mathrm{pl}^{\epsilon_t}$, $n_\mathrm{t} = \beta_\mathrm{pl}^{\epsilon_h+t}$ from Eq. (1.28) is helpful for a mode analysis algorithm.

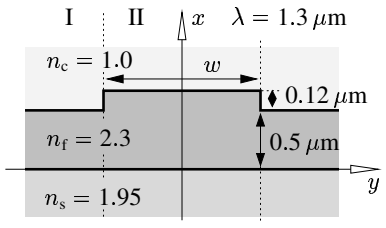

Figure 1.3: Leaky for TM polarization?
For this rib waveguide, the planar propagation constants of the layer stacks corresponding to sections I and II are $\beta_{TE}^{I}/k = 2.1474$, $\beta_{TM}^{I}/k = 2.0923$, $\beta_{TE}^{II}/k = 2.1846$, $\beta_{TM}^{II}/k = 2.1466$, thus $\beta_{TE}^{I} > \beta_{TM}^{II}$.

While for semivectorial calculations replacing the scalar values $\beta_\mathrm{pl}^{\epsilon_t}$, $\beta_\mathrm{pl}^{\epsilon_h+t}$ by planar propagation constants of appropriate polarization is reasonable, it is unclear, whether this extension remains correct in the fully vectorial, i.e. the physically relevant case. Consider e.g. an only slightly etched rib waveguide. The limiting planar waveguides as sketched in Figure 1.2 may be such that the TM effective index level of the thicker one is below the TE effective index of the thinner guide. Figure 1.3 shows an example. Does this rib waveguide support a losslessly propagating, hybrid antisymmetic (dominantly TM polarized) mode? It would comprise a small E_y field at a propagation constant below the TE level of the outer slabs. Corresponding remarks in Ref. [159] and the investigation of Refs. [105, 103] indicate that for such waveguides the fundamental TM

mode must be assumed to be leaky. This amounts to the existence of a minimum etching depth, which has to be exceeded for TM waves to propagate losslessly.

However, for the waveguides investigated in this thesis, there is no experimental evidence that the leakage, if present, should be significant when compared to other effects causing power loss, even if some structures (e.g. some ribs of Section 6.2.2 or a benchmark waveguide of Section 4.1.2, for $t = 0.9\,\mu$m) fall into the class where leakage may occur.

1.2 Waveguide junctions

Some interesting devices consist of a number of longitudinally homogeneous waveguide segments only. Examples are the radiatively coupled waveguide structures of Chapter 7, or multimode interference couplers with a basic element as investigated in Section 4.1.4. These devices consist of one or more well separated input waveguides, followed by a usually multimode coupling section of definite length L, and by a number of output waveguides. Light is inserted via a single mode of one of the input ports. At the first junction the power gets distributed among the modes of the coupling segment. At its end, the interfering modes excite one or more modes of the output waveguides.

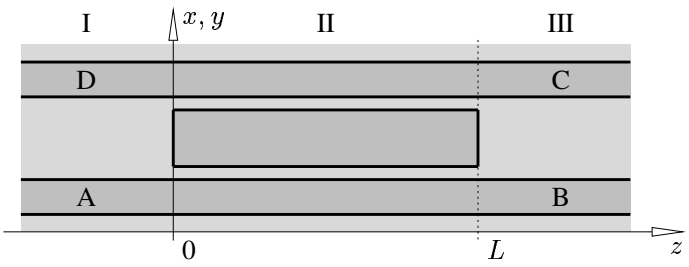

Figure 1.4: Composite device comprising three longitudinal homogeneous waveguide sections I – III, and input and output waveguides A to D. Guiding regions are indicated by darker shading.

Consider a junction between two waveguide segments I and II as sketched in Figure 1.4, located at $z = 0$. Both profiles support a number of guided modes with propagation constants β_l^{I}, β_m^{II}, and mode profiles $\phi_l^{\mathrm{I}} = (\boldsymbol{E}_l^{\mathrm{I}}, \boldsymbol{H}_l^{\mathrm{I}})$, $\phi_m^{\mathrm{II}} = (\boldsymbol{E}_m^{\mathrm{II}}, \boldsymbol{H}_m^{\mathrm{II}})$. For several well separated waveguides as in segment I, the mode set consists of the modes of the isolated waveguides (A and D in Figure 1.4), while for a profile like segment II the modes of the entire structure are relevant. Modes belonging to the same profile are orthogonal with respect to the product (1.18), $(\phi_l^{\mathrm{I}}; \phi_m^{\mathrm{I}}) = P_m^{\mathrm{I}} \delta_{lm}$, and $(\phi_l^{\mathrm{II}}; \phi_m^{\mathrm{II}}) = P_m^{\mathrm{II}} \delta_{lm}$, due to either an exact orthogonality, as for the modes of segment II, or due to the large waveguide distance, as for segment I.

The permittivity profiles ϵ^{I}, ϵ^{II} shall be such that the reflections due to a mode ϕ_i^{I} incident on the junction at $z = 0$ can be neglected. This approximation is justified e.g. if ϕ_i^{I} is small at abrupt longitudinal permittivity discontinuities, as in Figure 1.4. Then the incident mode profile may be assumed to be a reasonable initial field for the further light propagation at the beginning of segment II.

Inside segment II, apart from a remainder ρ^{II}, the electromagnetic field is a superposition of guided modes

$$(\boldsymbol{\mathcal{E}}, \boldsymbol{\mathcal{H}})(x, y, z, t) = \sum_m A_m^{\mathrm{II}} \frac{1}{\sqrt{P_m^{\mathrm{II}}}} \phi_m^{\mathrm{II}}(x, y)\, \mathrm{e}^{\mathrm{i}\omega t - \mathrm{i}\beta_m^{\mathrm{II}} z} + \rho^{\mathrm{II}}(x, y, z)\, \mathrm{e}^{\mathrm{i}\omega t}\,, \tag{1.29}$$

with x,y,z-independent amplitudes A_m^{II}. At the junction, the superposition matches the initial field ϕ_i^{I}, scaled to an input power P_i^{in}:

$$\sqrt{\frac{P_i^{\mathrm{in}}}{P_i^{\mathrm{I}}}} \phi_i^{\mathrm{I}}(x, y) = \sum_m A_m^{\mathrm{II}} \frac{1}{\sqrt{P_m^{\mathrm{II}}}} \phi_m^{\mathrm{II}}(x, y) + \rho^{\mathrm{II}}(x, y, 0). \tag{1.30}$$

Assuming $(\rho^{\mathrm{II}}; \phi_m^{\mathrm{II}}) = 0$ for all m, the (real) propagating mode amplitudes are determined by the overlap

between the incident mode of segment I and the modes of segment II. Projection of Eq. (1.30) on ϕ_m^{II} yields

$$A_m^{\mathrm{II}} = \sqrt{\frac{P_i^{\mathrm{in}}}{P_i^{\mathrm{I}} P_m^{\mathrm{II}}}} (\phi_m^{\mathrm{II}}; \phi_i^{\mathrm{I}}) \,. \tag{1.31}$$

For a similar treatment of the junction between segments II and III, at $z = L$, the unknown remaining field ρ^{II} must be assumed to be negligible. ρ^{II} is made up of the unguided part of the electromagnetic field in section II, the forward propagating radiating fields emerging from an excitation at $z = 0$. At $z = L$ it is small, if either it is initially small, i.e. if the superposition (1.30) approximates the incident mode well, or if segment II is of sufficient length such that the radiated power has left the relevant region at the junction. The applications discussed in Section 4.3.4 and Chapter 7 usually meet both prerequisites.

Thus, neglecting reflections again, as with the first junction the field at the second junction can be written

$$\begin{aligned} (\boldsymbol{\mathcal{E}}, \boldsymbol{\mathcal{H}})(x, y, L, t) &= \sum_m A_m^{\mathrm{II}} \frac{1}{\sqrt{P_m^{\mathrm{II}}}} \phi_m^{\mathrm{II}}(x, y)\, \mathrm{e}^{\mathrm{i}\omega t - \mathrm{i}\beta_m^{\mathrm{II}} L} \\ &= \sum_l A_l^{\mathrm{III}} \frac{1}{\sqrt{P_l^{\mathrm{III}}}} \phi_l^{\mathrm{III}}(x, y)\, \mathrm{e}^{\mathrm{i}\omega t} + \rho^{\mathrm{III}}(x, y, L)\, \mathrm{e}^{\mathrm{i}\omega t}, \end{aligned} \tag{1.32}$$

where an extension of the notation to segment III is obvious. Projection of Eq. (1.32) on ϕ_o^{III} leads to the complex amplitude for output mode number o

$$A_o^{\mathrm{III}} = \sqrt{P_i^{\mathrm{in}}} \sum_m w_{oi}^m\, \mathrm{e}^{-\mathrm{i}\beta_m^{\mathrm{II}} L} \quad \text{with real weights} \quad w_{oi}^m = \frac{1}{\sqrt{P_o^{\mathrm{III}} P_m^{\mathrm{II}} P_m^{\mathrm{II}} P_i^{\mathrm{I}}}} (\phi_o^{\mathrm{III}}; \phi_m^{\mathrm{II}})(\phi_m^{\mathrm{II}}; \phi_i^{\mathrm{I}}) \tag{1.33}$$

that are given by the overlaps of the normalized modes at the two junctions. As for segment I, we assume orthogonality for the modes of segment III. Then the power transferred to output mode o after excitation in input mode i is

$$P_o^{\mathrm{out}} = P_i^{\mathrm{in}} \left| \sum_m w_{oi}^m\, \mathrm{e}^{-\mathrm{i}\beta_m^{\mathrm{II}} L} \right|^2, \quad \text{or} \quad P_o^{\mathrm{out}} = P_i^{\mathrm{in}} \sum_{l,m} w_{oi}^l w_{oi}^m \cos(\beta_l^{\mathrm{II}} - \beta_m^{\mathrm{II}}) L \,. \tag{1.34}$$

If extended to a larger number of waveguide segments this kind of modeling may be referred to as Propagating Mode Analysis (PMA) [65, 173]. Regarding the treatment of the waveguide junctions, we have employed the simplest model only. If radiation and reflection are less negligible, i.e. if significant field intensities are to pass large longitudinal refractive index discontinuities, advanced simulations should be based on more sophisticated overlap techniques [157] or least squares approaches as described in [116], which include reflections as well. These are to be applied also if e.g. the light propagation through an end facet of a waveguide is to be simulated [21, 122, 162]. A few remarks on the problem of end-fire coupling light into and out of a waveguide follow in Section 6.3.2.

Use of beam propagation techniques [179, 57] would be an alternative to the PMA approach. The majority of the vast number of proposed propagation schemes are unidirectional, they neglect reflections. While the beam propagation method (BPM) yields approximations to both the radiated and the guided field after a junction, frequently one is interested in the guided part only, provided that the waveguide segments are long enough, and such that the radiated field does not reenter the guiding structures.

Most BPM algorithms are based on the paraxial approximation or higher order, wide angle variants. Usually for the longitudinal direction a slowly varying envelope approximation is employed, which requires a reference refractive index parameter to be supplied. Guided modes are propagated at a wavenumber the deviation of which from the exact value grows with the deviation from the reference refractive index. With a paraxial BPM algorithm, propagation of one mode may be modeled exactly. Setting the reference parameter to the average effective mode index allows us to simulate the correct beat length for two modes [72]. But for

more than two modes, the simulation will always introduce phase errors which accumulate with increasing propagation distance, leading to an erroneous interference pattern. These considerations become important if the interval allowed for propagation constants is large [158], e.g. for the deeply etched garnet waveguides of Chapters 6, 7. Therefore for the rectangular structures investigated in this thesis the propagating mode analysis must be considered less approximative than beam propagation modeling, provided that sufficiently accurate mode profiles and propagation constants for the single and composite waveguides are available.

1.2.1 Two coupled parallel waveguides

Two coupled parallel waveguides constitute the simplest variant of a directional coupler. This is the result of omitting the central guiding region of segment II in Figure 1.4. Additionally, according to the desired light path, only one of guides A and D and one of B and C shall be present in segment I and III, respectively. Usually the waveguides are meant to be single-moded, only one polarization is considered, and both waveguides are assumed to be identical. Depending on the permittivity contrast, they are to be placed in close proximity.

Then the coupling segment II supports two modes, one of even symmetry (index s) and one of odd symmetry (index a), and the power Eq. (1.34) transferred from input port $i = \mathrm{A}, \mathrm{D}$ to output port $o = \mathrm{B}, \mathrm{C}$ is

$$P_o^{\mathrm{out}} = P_i^{\mathrm{in}} \left((w_{oi}^{\mathrm{s}})^2 + (w_{oi}^{\mathrm{a}})^2 + 2 w_{oi}^{\mathrm{s}} w_{oi}^{\mathrm{a}} \cos(\beta_{\mathrm{s}}^{\mathrm{II}} - \beta_{\mathrm{a}}^{\mathrm{II}}) L \right) . \tag{1.35}$$

The two mode interference results in a strictly harmonic beating pattern with half-beat-length, or coupling length,

$$L_{\mathrm{c}} = \frac{\pi}{\beta_{\mathrm{s}}^{\mathrm{II}} - \beta_{\mathrm{a}}^{\mathrm{II}}} . \tag{1.36}$$

In the limit of weakly coupled waveguides, i.e. for large gap width or large refractive index contrast, one can assume $|w_{oi}^{\mathrm{s}}| \approx |w_{oi}^{\mathrm{a}}| \approx 1/2$. For the straight path A $\rightarrow$ B or D $\rightarrow$ C the transmission reads

$$P_{\mathrm{B}}^{\mathrm{out}} = P_{\mathrm{A}}^{\mathrm{in}} \frac{1}{2} \left(1 + \cos(\beta_{\mathrm{s}}^{\mathrm{II}} - \beta_{\mathrm{a}}^{\mathrm{II}}) L \right) , \tag{1.37}$$

while one obtaines

$$P_{\mathrm{C}}^{\mathrm{out}} = P_{\mathrm{A}}^{\mathrm{in}} \frac{1}{2} \left(1 - \cos(\beta_{\mathrm{s}}^{\mathrm{II}} - \beta_{\mathrm{a}}^{\mathrm{II}}) L \right) \tag{1.38}$$

for the cross light path A $\rightarrow$ C or D $\rightarrow$ B.

In this thesis, symmetrical two waveguide couplers will be employed as test structures for the mode solver characterization (Sections 4.1.3, 4.3.1), for an assessment of the coupled mode theory (Section 5.3), and for a demonstration of geometry tolerancing (Section 5.2). The simulation is restricted to piecewise longitudinally homogeneous structures. However, real devices are usually designed as four port couplers with branches comprising waveguide bends (X-couplers). Analysis can be kept in the framework of guided modes with a kind of quasistatic approximation [156, 62, 16]. In that case, the device length L in Eq. (1.35) must be replaced by a value between the actual length of the coupling section and a length beyond which the overlap of the modes in the diverging waveguides becomes negligible.

1.3 Single mode perturbations

For many integrated optical waveguides, the permittivity profile $\hat{\epsilon} = \epsilon + \delta\hat{\epsilon}$ can be split into the contribution $\epsilon = n^2$ of an isotropic lossless refractive index n and a residual $\delta\hat{\epsilon}$, a perturbation. Assuming the mode profiles and the propagation constants corresponding to the original permittivity ϵ to be known, in this section we are interested in the influence of the perturbation profile $\delta\hat{\epsilon}$ on the propagation constants.

The curl equations (1.3) for the mode profiles can be written as

$$(\mathrm{C} + \mathrm{i}\beta\mathrm{R})\boldsymbol{E} = -\mathrm{i}\omega\mu_0\boldsymbol{H}, \quad (\mathrm{C} + \mathrm{i}\beta\mathrm{R})\boldsymbol{H} = \mathrm{i}\omega\epsilon_0\hat{\epsilon}\boldsymbol{E}, \tag{1.39}$$

where the curl operator has been split into a longitudinal part $\beta\mathrm{R}$ and a part C acting on the transverse coordinates only,

$$\mathrm{R} = \begin{pmatrix} 0 & 1 & 0 \\ -1 & 0 & 0 \\ 0 & 0 & 0 \end{pmatrix}, \qquad \mathrm{C} = \begin{pmatrix} 0 & 0 & \partial_y \\ 0 & 0 & -\partial_x \\ -\partial_y & \partial_x & 0 \end{pmatrix}. \tag{1.40}$$

With these two operators and standard scalar product notation $\langle \boldsymbol{F}, \boldsymbol{G} \rangle = \iint \boldsymbol{F}^* \boldsymbol{G} \,\mathrm{d}x\,\mathrm{d}y$, one can define [157] the following functional $\mathrm{B}_{\hat{\epsilon}}$ in terms of the six independent mode components $E_x, \ldots, H_z$:

$$\mathrm{B}_{\hat{\epsilon}}(\boldsymbol{E}, \boldsymbol{H}) = \frac{\omega\epsilon_0 \langle \boldsymbol{E}, \hat{\epsilon}\boldsymbol{E} \rangle + \omega\mu_0 \langle \boldsymbol{H}, \boldsymbol{H} \rangle + \mathrm{i}\langle \boldsymbol{E}, \mathrm{C}\boldsymbol{H} \rangle - \mathrm{i}\langle \boldsymbol{H}, \mathrm{C}\boldsymbol{E} \rangle}{\langle \boldsymbol{E}, \mathrm{R}\,\boldsymbol{H} \rangle - \langle \boldsymbol{H}, \mathrm{R}\,\boldsymbol{E} \rangle}. \tag{1.41}$$

If a valid mode field is inserted, i.e. for $\boldsymbol{E}$ and $\boldsymbol{H}$ satisfying Eqs. (1.39), the functional evaluates to the propagation constant

$$\beta = \mathrm{B}_{\hat{\epsilon}}(\boldsymbol{E}, \boldsymbol{H}). \tag{1.42}$$

Using the identity $\langle \boldsymbol{F}, (\mathrm{C} + \mathrm{i}\beta\mathrm{R})\boldsymbol{G} \rangle = \langle (\mathrm{C} + \mathrm{i}\beta\mathrm{R})\boldsymbol{F}, \boldsymbol{G} \rangle$, one can show that $\mathrm{B}_{\hat{\epsilon}}$ is stationary at a mode field in the sense of $\partial_s \mathrm{B}_{\hat{\epsilon}}(\boldsymbol{E} + s\boldsymbol{F}, \boldsymbol{H} + s\boldsymbol{G})|_{s=0} = 0$ for arbitrary $\boldsymbol{F}$, $\boldsymbol{G}$. While the stationarity property holds for a Hermitian permittivity tensor only, the functional satisfies Eq. (1.42) for arbitrary $\hat{\epsilon}$.

Now let β, $\boldsymbol{E}$, $\boldsymbol{H}$ denote the propagation constants and the mode field corresponding to the unperturbed permittivity profile ϵ. Along with the permittivity, the modes properties change by small amounts $\delta\beta$, $\delta\boldsymbol{E}$, $\delta\boldsymbol{H}$, and the modified quantities are connected by the modified functional

$$\beta + \delta\beta = \mathrm{B}_{\epsilon+\delta\hat{\epsilon}}(\boldsymbol{E} + \delta\boldsymbol{E}, \boldsymbol{H} + \delta\boldsymbol{H}). \tag{1.43}$$

Since B_ϵ is stationary at $\boldsymbol{E}$, $\boldsymbol{H}$, substituting $\mathrm{B}_\epsilon(\boldsymbol{E} + \delta\boldsymbol{E}, \boldsymbol{H} + \delta\boldsymbol{H})$ by $\mathrm{B}_\epsilon(\boldsymbol{E}, \boldsymbol{H})$ and expanding the remainder of the right hand side of Eq. (1.43) gives directly the first order correction of the propagation constant $\delta\beta = \omega\epsilon_0 \langle \boldsymbol{E}, \delta\hat{\epsilon}\boldsymbol{E} \rangle \left(\langle \boldsymbol{E}, \mathrm{R}\boldsymbol{H} \rangle - \langle \boldsymbol{H}, \mathrm{R}\boldsymbol{E} \rangle\right)^{-1}$ or

$$\delta\beta = \frac{\omega\epsilon_0}{2} \frac{\displaystyle\iint \boldsymbol{E}^* \,\delta\hat{\epsilon}\boldsymbol{E} \,\mathrm{d}x\,\mathrm{d}y}{\displaystyle\iint (E_x H_y - E_y H_x) \,\mathrm{d}x\,\mathrm{d}y}. \tag{1.44}$$

This expression can be arrived at by numerous other approaches as well, as shown e.g. in Refs. [157, 123, 42] or in Section 1.5. In the form (1.44) it holds for arbitrary reasonable permittivity perturbations, but for unperturbed modes as discussed in Section 1.1 only. Applications in this thesis include the nonreciprocal phase shift of magnetooptic waveguides (Chapters 6, 7), linear birefringence (Section 6.3.1) and absorption (Sections 1.3.1, 5.1, 6.3.1).

1.3.1 Absorption

Eq. (1.44) is valid for non-Hermitian permittivity contributions as well. Assume a region $\square$ on the waveguide section to be made of an absorbing material with refractive index n that attenuates the intensity of a plane wave according to $\sim \exp(-\alpha z)$ with a small attenuation constant α. Its effect is described by an isotropic but imaginary permittivity perturbation $\delta\epsilon_{\text{abs}} = -\mathrm{i}n\alpha/k$. According to Eq. (1.44), the propagation constant of a mode with profile $\boldsymbol{E}$, $\boldsymbol{H}$ gets an additional imaginary part

$$\delta\beta_{\text{abs}} = -\mathrm{i}\alpha_{\text{m}}/2\,, \quad \text{with} \quad \alpha_{\text{m}} = \alpha\, n \sqrt{\frac{\epsilon_0}{\mu_0}} \frac{\iint_{\square} |\boldsymbol{E}|^2 \mathrm{d}x\,\mathrm{d}y}{\iint (E_x\, H_y - E_y\, H_x)\,\mathrm{d}x\,\mathrm{d}y}\,. \tag{1.45}$$

Thus the power carried by this mode is attenuated according to $\sim \exp(-\alpha_{\text{m}} z)$. Note that the mode power attenuation α_{m} usually differs from the bulk value α, and that it depends on the mode field, i.e. on the polarization, if only a part of the waveguiding structure is absorbing.

1.4 Geometry variations

Frequently, integrated optical devices rely on the interference of guided modes propagating along homogeneous waveguide sections. In first order perturbation theory, a slight alteration of a dimensional parameter influences the mode wavenumbers only, while the mode amplitudes are almost unaffected. To estimate the deviation of the power transmission, it should be sufficient to consider only the propagation constant alteration, which amounts to calculating wavenumber gradients with respect to geometry variables.

For a waveguide with piecewise constant permittivity profile, alteration of a dimensional parameter can be regarded as changing the refractive index in a thin layer along a dielectric discontinuity line. While expressions for the wavenumber shift due to such thin layer perturbations are known but rarely applied [157], in this section we investigate their interpretation as geometry modifications. The section covers material of Refs. [75, 78]. An example of an analogous treatment for the scalar modes of weakly guiding circular step index fibers can be found in [136].

Following the reasoning of [157], the expressions for thin layer perturbations are applied in the first parts of this section to derive wavenumber gradients due to the displacement of boundaries between regions of different permittivity. The remainder comments on the tight connection between the geometry parameters and the wavelength as the defining dimensional variable.

As an alternative to the derivation below, one might think of directly employing the general perturbational expression (1.44) with a thin layer perturbation expressed by step functions. Taking the derivative with respect to the location of a layer boundary leads to integrals involving the Dirac-distribution. However, evaluation of the distribution runs into problems, since some of the test functions (the mode components) are discontinuous at the relevant boundaries.

1.4.1 Thin layer perturbations

Suppose the propagation constant β and the field $\boldsymbol{E}$, $\boldsymbol{H}$ to be known, which correspond to the piecewise constant isotropic and lossless permittivity profile ϵ. We consider a part of the waveguide cross section containing a dielectric boundary, as sketched in Figure 1.5.

Shifting the horizontal boundary changes the permittivity to $\epsilon + \delta\epsilon$ with

$$\delta\epsilon(x,y) = \begin{cases} \epsilon^- - \epsilon^+ & \text{for } (x,y) \in \square \\ 0 & \text{otherwise} \end{cases}\,, \tag{1.46}$$

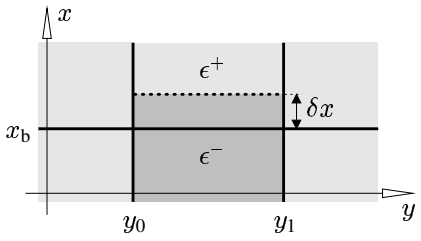

Figure 1.5: Horizontal boundary variation. For $y_0 < y < y_1$, the boundary separating permittivities ϵ^- below and ϵ^+ above is shifted from its original position x_b to the new position $x_b + \delta x$.

where the box symbol $\square$ indicates the rectangular region $x_\mathrm{b} < x < x_\mathrm{b} + \delta x$, $y_0 < y < y_1$. Both the propagation constant and the mode fields change by small amounts $\delta\beta$, $\delta\boldsymbol{E}$, $\delta\boldsymbol{H}$, such that

$$\beta + \delta\beta = \mathrm{B}_{\epsilon+\delta\epsilon}(\boldsymbol{E} + \delta\boldsymbol{E}, \boldsymbol{H} + \delta\boldsymbol{H}), \tag{1.47}$$

where B is the functional (1.41). $\mathrm{B}_{\epsilon+\delta\epsilon}$ is stationary at $\boldsymbol{E} + \delta\boldsymbol{E}$, $\boldsymbol{H} + \delta\boldsymbol{H}$. Thus, inserting plausible expressions for the variations of the mode profiles should be sufficient for calculating the propagation constant shift $\delta\beta$. Fortunately, most of the components are continuous on the boundary, and one can simply choose the original fields as good estimates for the perturbed profiles: $\delta H_x = \delta H_y = \delta H_z = 0$, $\delta E_y = \delta E_z = 0$. In contrast, the normal component of the dielectric displacement ϵE_x must be continuous, and E_x jumps in x_b, from a level E_x^- to E_x^+, where field superscripts $+$, $-$ denote appropriate limits on the horizontal boundary line. While $E_x + \delta E_x$ must be continuous in x_b, this new field has the jump displaced to $x_\mathrm{b} + \delta x$, thus E_x is to be modified by

$$\delta E_x(x,y) = \begin{cases} \dfrac{\epsilon^+ - \epsilon^-}{\epsilon^-} E_x(x,y) & \text{for } (x,y) \in \square \\ 0 & \text{otherwise} \end{cases} . \tag{1.48}$$

This is illustrated in Figure 1.6.

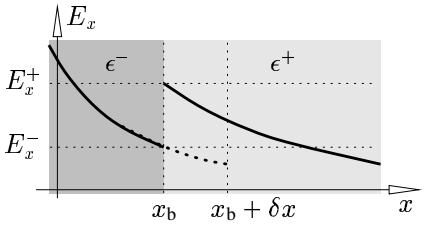

Figure 1.6: Boundary shift from x_b to $x_b + \delta x$. E_x changes from the continuous to the dotted curve.

With these quantities substituted into functional (1.47), terms $\sim \delta\beta\delta\boldsymbol{E}$ neglected, and with help of Eqs. (1.39) one arrives at

$$\delta\beta = \omega\epsilon_0 \frac{\langle \delta\boldsymbol{E}, \epsilon\delta\boldsymbol{E}\rangle + \langle \boldsymbol{E} + \delta\boldsymbol{E}, \delta\epsilon(\boldsymbol{E} + \delta\boldsymbol{E})\rangle}{\langle \boldsymbol{E}, \mathrm{R}\boldsymbol{H}\rangle - \langle \boldsymbol{H}, \mathrm{R}\boldsymbol{E}\rangle} . \tag{1.49}$$

Using Eqs. (1.46), (1.48), the above becomes an expression for the propagation constant change due to a thin layer perturbation [157]:

$$\delta\beta = \frac{\omega\epsilon_0}{2} \frac{(\epsilon^- - \epsilon^+) \iint_\square \left(\dfrac{\epsilon^+}{\epsilon^-} E_x^2 + E_y^2 + E_z^2 \right) \mathrm{d}x\,\mathrm{d}y}{\iint (E_x H_y - E_y H_x)\ \mathrm{d}x\,\mathrm{d}y} . \tag{1.50}$$

1.4.2 Geometry perturbation formulas

For small δx the surface integration over the box region can be replaced by a line integral along the dielectric boundary. Now the equation gives directly the derivative of the propagation constant with respect to the

boundary location

$$\delta\beta = \frac{\omega\epsilon_0}{2} \frac{(\epsilon^- - \epsilon^+) \int_{y_0}^{y_1} \left(E_x^+ E_x^- + E_y^2 + E_z^2 \right)(x_\mathrm{b}, y)\,\mathrm{d}y}{\iint (E_x H_y - E_y H_x)\,\mathrm{d}x\,\mathrm{d}y} \delta x\,. \tag{1.51}$$

This is a plausible expression. The propagation constant is influenced only if there is a discontinuity in the permittivity, and if the mode field does not vanish on the boundary. Only well defined quantities enter, there are no ambiguities regarding the discontinuity of E_x (the first term in the numerator is alternatively $E_x^+ E_x^- = \epsilon^+ (E_x^+)^2/\epsilon^- = \epsilon^- (E_x^-)^2/\epsilon^+ = (\epsilon E_x)^2/(\epsilon^-\epsilon^+)$). Fortunately, the result remains the same if one starts with a downwards shifted boundary and rewrites Eqs. (1.46) and (1.48) accordingly.

With ansatz (1.26) for semivectorial TE polarized modes inserted, Eq. (1.51) reads

$$\delta\beta = \frac{k_0^2}{2\beta} \frac{(\epsilon^- - \epsilon^+) \int_{y_0}^{y_1} \left(E_y^2 + \frac{1}{\beta^2} (\partial_y E_y)^2 \right)(x_\mathrm{b}, y)\,\mathrm{d}y}{\iint \left(E_y^2 - \frac{1}{\beta^2} E_y \partial_y^2 E_y \right) \mathrm{d}x\,\mathrm{d}y} \delta x\,. \tag{1.52}$$

If one neglects the derivative $\beta^{-1}\partial_y E_y$ on the relevant horizontal boundary and the second order y-derivative in the denominator (cf. Section 1.1.4), Eq. (1.52) simplifies to

$$\delta\beta = \frac{k_0^2}{2\beta} \frac{(\epsilon^- - \epsilon^+) \int_{y_0}^{y_1} E_y^2(x_\mathrm{b}, y)\,\mathrm{d}y}{\iint E_y^2\,\mathrm{d}x\,\mathrm{d}y} \delta x\,. \tag{1.53}$$

For the waveguides considered in Section 5.2, we have found this approximation to be adequate.

In case of quasi TM polarization, usually all components are expressed by the dominant magnetic component H_y. Now Eq. (1.51) yields

$$\delta\beta = \frac{\beta}{2} \frac{(\epsilon^- - \epsilon^+) \int_{y_0}^{y_1} \left(\frac{1}{\epsilon^-\epsilon^+} (H_y - \frac{1}{\beta^2}\partial_y^2 H_y)^2 + \frac{1}{\beta^4} (\partial_y \frac{1}{\epsilon} \partial_x H_y)^2 + \frac{1}{\beta^2} (\frac{1}{\epsilon} \partial_x H_y)^2 \right)(x_\mathrm{b}, y)\,\mathrm{d}y}{\iint \frac{1}{\epsilon} \left(H_y - \frac{1}{\beta^2}\partial_y^2 H_y \right) H_y\,\mathrm{d}x\,\mathrm{d}y} \delta x \tag{1.54}$$

for the propagation constant shift of a quasi TM mode due to a horizontal boundary displacement. Again all quantities in the denominator are well defined, since the inverse permittivity times the normal derivative of H_y is continuous on the horizontal boundary. As in the TE case, the derivatives ∂_y can be dropped in Eq. (1.54) without noticeably affecting the results given in Section 5.2.

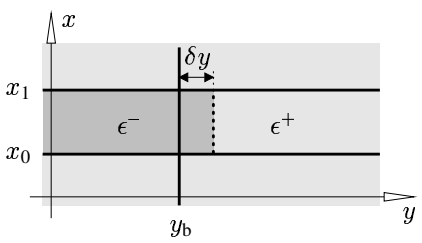

Figure 1.7: Shift of a vertical boundary.

Analogous equations hold for shifting vertical boundaries. Figure 1.7 illustrates the relevant geometry. Moving the boundary between permittivities ϵ^- on the left and ϵ^+ on the right from y_b to $y_\mathrm{b} + \delta y$ changes

the propagation constant of a hybrid, arbitrarily polarized mode by

$$\delta\beta = \frac{\omega\epsilon_0}{2} \frac{(\epsilon^- - \epsilon^+) \int_{x_0}^{x_1} \left(E_x^2 + E_y^+ E_y^- + E_z^2\right)(x, y_\mathrm{b})\,\mathrm{d}x}{\iint (E_x H_y - E_y H_x)\,\mathrm{d}x\,\mathrm{d}y}\,\delta y\,. \tag{1.55}$$

For semivectorial TE-polarized fields, it is usually no longer possible to skip the y-derivative, since the maxima of the longitudinal electric component $E_z = -\beta^{-1}\partial_y E_y$ are located at the rib flanks. The expression for the wavenumber shift of a quasi TE mode reads

$$\delta\beta = \frac{k_0^2}{2\beta} \frac{(\epsilon^- - \epsilon^+) \int_{x_0}^{x_1} \left(E_y^+ E_y^- + \frac{1}{\beta^2}(\partial_y E_y)^2\right)(x, y_\mathrm{b})\,\mathrm{d}x}{\iint \left(E_y^2 - \frac{1}{\beta^2} E_y \partial_y^2 E_y\right)\mathrm{d}x\,\mathrm{d}y}\,\delta y\,. \tag{1.56}$$

While quasi TM modes satisfy the continuity requirements for H_y and H_z on vertical boundaries exactly, the continuity requirements for E_x and E_z are significantly violated. Thus Eq. (1.55) can hardly be expected to give satisfying results with a quasi TM field inserted. A way out is the observation that the TM problem, if restricted to vertical boundaries, should be equivalent to the TE problem with horizontal boundaries. Therefore a plausible expression for the TM wavenumber shift due to the displacement of a vertical boundary is Eq. (1.52), with E_y substituted by H_y and x and y exchanged:

$$\delta\beta = \frac{k_0^2}{2\beta} \frac{(\epsilon^- - \epsilon^+) \int_{x_0}^{x_1} H_y^2(x, y_\mathrm{b})\,\mathrm{d}x}{\iint H_y^2\,\mathrm{d}x\,\mathrm{d}y}\,\delta y\,. \tag{1.57}$$

Maybe in an alternative way this equation or a modified version can be rigorously derived. At least for the structures considered in Section 5.2, we have found Eq. (1.57) to be correct up to the same accuracy as the expressions for TE and hybrid modes. The problem does not arise with quasi TE modes. For the component E_y entering the numerator of Eq. (1.56), the correct continuity requirements on vertical boundaries are enforced by definition.

The standard rib waveguide as sketched in Figure 1.1 is defined by three geometry variables: the rib width w, its height h and the thickness t of the remaining film besides the rib. We are interested in the partial derivatives $\partial_h\beta$, $\partial_t\beta$, and $\partial_w\beta$. The two former ones are obtained by applying one of Eqs. (1.51), (1.52), (1.53), (1.54) to the top of the rib or to the rib baseline, respectively. Using Eqs. (1.55), (1.56), or (1.57) with one of the rib flanks yields $\partial_w\beta$. This approach extends in an obvious way to the coupler structures discussed in the following section and to other, more complex geometries. Usually, the perturbational expressions must be applied to more than one boundary section to compute the derivatives with respect to a general model variable.

1.4.3 Wavelength

For the rib waveguide of Figure 1.1, the relevant dimensional parameters are w, h, t, and the wavelength λ. The propagation constant is a homogeneous function of degree -1 in these parameters, i.e. for an arbitrary factor a the equality $\beta(a\lambda, ah, aw, at) = \beta(\lambda, h, w, t)/a$ holds. Thus the partial derivatives are related by

$$\partial_\lambda\beta = -\frac{1}{\lambda}\left(\beta + h\partial_h\beta + w\partial_w\beta + t\partial_t\beta\right). \tag{1.58}$$

Therefore, the perturbational expressions (1.51)–(1.57) give direct access to the derivative with respect to the wavelength as well. Note that Eq. (1.58) assumes all material parameters to be fixed. A pronounced wavelength dependence e.g. of one of the refractive indices (dispersion) must be taken into account by a combination of perturbation formulas or by explicit numerical evaluation.

1.5 Coupled mode theory

Commonly, the term 'mode coupling' adresses one of at least three different means of power transfer. These include coupling modes of distinct waveguides by evanescent fields, coupling modes in the same waveguide by longitudinally homogeneous perturbations, and co- and contradirectional coupling by longitudinally inhomogeneous, usually periodical perturbations. The first two versions of coupled mode theory will be applied in Chapter 6 to magnetooptic polarization conversion and in Chapter 7 to a number of radiatively coupled waveguide structures. Overviews over the variety of related publications can be found in [59, 45]. The formulation given in this section [48, 157] is the theoretical basis of Refs. [76, 79, 77].

Suppose a composite waveguide is to be simulated. Its profile $\hat{\epsilon}$ (in general a tensor) shall be such that the propagating light $\boldsymbol{\mathcal{E}}$, $\boldsymbol{\mathcal{H}}$ may be reasonably assumed to be a superposition of a number of known guided mode profiles, $\boldsymbol{E}_m$, $\boldsymbol{H}_m$, with longitudinally varying amplitudes C_m:

$$\boldsymbol{\mathcal{E}}(x,y,z,t) = \sum_m \frac{C_m(z)}{\sqrt{P_m}} \boldsymbol{E}_m(x,y)\,\mathrm{e}^{\mathrm{i}\omega t}, \quad \boldsymbol{\mathcal{H}}(x,y,z,t) = \sum_m \frac{C_m(z)}{\sqrt{P_m}} \boldsymbol{H}_m(x,y)\,\mathrm{e}^{\mathrm{i}\omega t}\,. \tag{1.59}$$

The amplitudes C_m include the harmonic dependence on the propagation distance. $\sqrt{P_m}$ are normalization factors computed for mode profiles m according to Eq. (1.13).

Each mode is assigned the difference $\delta\hat{\epsilon}_m = \hat{\epsilon} - \epsilon_m$ between the permittivity profile $\hat{\epsilon}$ describing the entire structure and the permittivity ϵ_m with which mode number m was calculated. We restrict the basic fields to lossless isotropic waveguides, i.e. ϵ_m is real, with equal diagonal elements. Let β_m denote the propagation constant corresponding to the mode profile $\boldsymbol{E}_m$, $\boldsymbol{H}_m$, in the waveguide described by ϵ_m.

From the Maxwell equations the following reciprocity identity can be derived straightforwardly [157]:

$$\mathrm{div}\,(\bar{\boldsymbol{H}} \times \bar{\boldsymbol{E}}_m^* - \bar{\boldsymbol{E}} \times \bar{\boldsymbol{H}}_m^*) = \mathrm{i}\omega\epsilon_0 \bar{\boldsymbol{E}}_m^*\,\delta\hat{\epsilon}_m \bar{\boldsymbol{E}}\,. \tag{1.60}$$

$\bar{\boldsymbol{E}}_m$ and $\bar{\boldsymbol{H}}_m$ are the mode profiles $\boldsymbol{E}_m$, $\boldsymbol{H}_m$ multiplied by the appropriate space dependence $\exp(-\mathrm{i}\beta_m z)$. Integration over the x-y-plane and insertion of Eq. (1.59) yields

$$\sum_l \sigma_{ml}(\partial_z C_l + \mathrm{i}\beta_m C_l) = -\mathrm{i}\sum_l \alpha^{\mathrm{I}}_{ml} C_l\,, \tag{1.61}$$

with the power coupling coefficients σ_{lm} defined as

$$\sigma_{lm} = \frac{1}{4\sqrt{P_l P_m}} \iint (E_{l,x}H_{m,y} - E_{l,y}H_{m,x} + E_{m,x}H_{l,y} - E_{m,y}H_{l,x})\,\mathrm{d}x\,\mathrm{d}y \tag{1.62}$$

and for

$$\alpha^{\mathrm{I}}_{lm} = \frac{\omega\epsilon_0}{4\sqrt{P_l P_m}} \iint \boldsymbol{E}_l^*\,\delta\hat{\epsilon}_l \boldsymbol{E}_m\,\mathrm{d}x\,\mathrm{d}y\,. \tag{1.63}$$

Obviously $\sigma_{lm} = \sigma_{ml}$ holds, but in general the coupling coefficients α^{I}_{lm} are not symmetric. One can invoke the reciprocity theorem a second time [157], now in the form

$$\mathrm{div}\,(\bar{\boldsymbol{H}}_l \times \bar{\boldsymbol{E}}_m^* - \bar{\boldsymbol{E}}_l \times \bar{\boldsymbol{H}}_m^*) = \mathrm{i}\omega\epsilon_0 \bar{\boldsymbol{E}}_m^*\,(\hat{\epsilon}_l - \hat{\epsilon}_m)\bar{\boldsymbol{E}}_l\,, \tag{1.64}$$

in order to show the identity

$$(\beta_l - \beta_m)\sigma_{lm} = \alpha^{\mathrm{II}}_{lm} - \alpha^{\mathrm{I}}_{lm} \quad \text{with} \quad \alpha^{\mathrm{II}}_{lm} = \frac{\omega\epsilon_0}{4\sqrt{P_l P_m}} \iint \boldsymbol{E}_l^*\,\delta\hat{\epsilon}_m \boldsymbol{E}_m\,\mathrm{d}x\,\mathrm{d}y\,. \tag{1.65}$$

If inserted into Eq. (1.61), this leads to

$$\sum_l \sigma_{ml}(\partial_z C_l + \mathrm{i}\beta_l C_l) = -\mathrm{i}\sum_l \alpha^{\mathrm{II}}_{ml} C_l\,. \tag{1.66}$$

Combination of Eqs. (1.61) and (1.66) yields coupled mode equations with symmetrical coupling matrices

$$\sum_l \sigma_{ml}\partial_z C_l = -\mathrm{i}\frac{1}{2}\sum_l \sigma_{ml}(\beta_m + \beta_l)C_l - \mathrm{i}\sum_l \kappa_{ml} C_l\,, \tag{1.67}$$

where the coupling coefficients κ_{lm} are defined as

$$\kappa_{lm} = \frac{\omega\epsilon_0}{8\sqrt{P_l P_m}}\iint \boldsymbol{E}_l^*\,(\delta\hat{\epsilon}_l + \delta\hat{\epsilon}_m)\boldsymbol{E}_m\,\mathrm{d}x\,\mathrm{d}y\,. \tag{1.68}$$

For lossless materials, $\hat{\epsilon}$, $\hat{\epsilon}_m$ are Hermitian, thus $\kappa^*_{ml} = \kappa_{lm}$. In matrix form the coupled mode equations read

$$\mathsf{S}\partial_z \boldsymbol{C} = -\mathrm{i}(\mathsf{B} + \mathsf{K})\boldsymbol{C}\,, \tag{1.69}$$

with real symmetric matrices $\mathsf{S} = (\sigma_{lm})$, $\mathsf{B} = (\sigma_{lm}(\beta_l + \beta_m)/2)$, and Hermitian $\mathsf{K} = (\kappa_{lm})$, acting on the vector $\boldsymbol{C} = (C_l)$ of mode amplitudes.

The total guided power $P = \mathrm{Re}\iint(\boldsymbol{\mathcal{E}}\times\boldsymbol{\mathcal{H}}^*)_z\,\mathrm{d}x\,\mathrm{d}y/2$ evaluates to $P = \boldsymbol{C}^\dagger\mathsf{S}\boldsymbol{C}$, where † denotes the adjoint. Its vanishing derivative $\partial_z P = \mathrm{i}\boldsymbol{C}^\dagger\Big((\mathsf{B}+\mathsf{K})^\dagger - (\mathsf{B}+\mathsf{K})\Big)\boldsymbol{C}$ indicates that Eqs. (1.67) conserve power.

Note that alternatively ansatz (1.59) may be formulated in terms of the transverse components only [46, 25] (for isotropic $\hat{\epsilon}$), leading to slightly different expressions for the coupling coefficients Eqs. (1.63), (1.65), (1.68). However, in Ref. [156] the difference has been shown to be of second order in the permittivity differences, thus to be small. The formulation employed for this thesis is compatible with the variational expressions of Section 1.3 (see below) and immediately applicable to anisotropic perturbations.

1.5.1 Polarization conversion

Consider a single waveguide made of anisotropic material. Its permittivity tensor $\hat{\epsilon} = n^2 + \delta\hat{\epsilon}$ shall deviate by a perturbation $\delta\hat{\epsilon}$ from that of isotropic lossless media with refractive index profile n. The modes of the corresponding isotropic structure are assumed to be known, while the perturbation will be included via coupled mode theory.

In this case all permittivity differences from above are equal, $\delta\hat{\epsilon}_m = \delta\hat{\epsilon}$. The basic modes are orthogonal according to Eq. (1.19), thus $\sigma_{lm} = \delta_{lm}$. This reduces Eqs. (1.67) to the simpler form

$$\partial_z C_m = -\mathrm{i}\beta_m C_m - \mathrm{i}\sum_l \kappa_{ml} C_l, \tag{1.70}$$

where the coupling coefficients κ_{lm} are given by

$$\kappa_{lm} = \frac{\omega\epsilon_0}{4\sqrt{P_l P_m}}\iint \boldsymbol{E}_l^*\,\delta\hat{\epsilon}\boldsymbol{E}_m\,\mathrm{d}x\,\mathrm{d}y\,. \tag{1.71}$$

Note that in general the diagonal coefficients κ_{mm} do not vanish. In fact, Eq. (1.71) resembles the perturbational expression (1.44) for the propagation constant shift due to a permittivity variation.

We now specialize to the case of only two coupled modes (indices 1, 2), typically the fundamental hybrid symmetric (TE) and antisymmetric mode (TM), as in Section 6.3. This is justified if either the waveguide

supports these two modes only, or if the initial amplitudes of the remaining ones and their coupling to the fundamental modes is negligible. For Hermitian $\delta\epsilon$ the coupled mode equations reduce to

$$\partial_z C_1 = -\mathrm{i}\beta_1' C_1 - \mathrm{i}\kappa C_2\,, \qquad \partial_z C_2 = -\mathrm{i}\beta_2' C_2 - \mathrm{i}\kappa^* C_1\,, \tag{1.72}$$

with $\beta_m' = \beta_m + \kappa_{mm}$ and $\kappa = \kappa_{12}$. Their solution is

$$\begin{pmatrix} C_1 \\ C_2 \end{pmatrix}(z) = \exp(-\mathrm{i}\frac{\beta_1' + \beta_2'}{2} z) \begin{pmatrix} \cos\rho z - \mathrm{i}\dfrac{\Delta\beta'}{2\rho}\sin\rho z & -\mathrm{i}\dfrac{\kappa}{\rho}\sin\rho z \\ -\mathrm{i}\dfrac{\kappa^*}{\rho}\sin\rho z & \cos\rho z + \mathrm{i}\dfrac{\Delta\beta'}{2\rho}\sin\rho z \end{pmatrix} \begin{pmatrix} C_{10} \\ C_{20} \end{pmatrix}, \tag{1.73}$$

where ρ is defined as $\rho = \sqrt{(\Delta\beta'/2)^2 + |\kappa|^2}$, with $\Delta\beta' = \beta_1' - \beta_2'$. Projection (cf. Section 1.2) on an initial field $(\boldsymbol{E}_{\mathrm{in}}, \boldsymbol{H}_{\mathrm{in}})(x,y)\exp(-\mathrm{i}\omega t)$ gives the amplitudes C_{m0} at $z = 0$:

$$C_{m0} = \frac{1}{2\sqrt{P_m}} \iint (E_{mx} H_{\mathrm{in},y}^* - E_{my} H_{\mathrm{in},x}^*)\,\mathrm{d}x\,\mathrm{d}y\,. \tag{1.74}$$

We are interested in the polarization conversion. Starting at $z = 0$ with all power concentrated in mode 1, after a distance z the relative power $\eta(z) = |C_2(z)/C_{10}|^2$ carried by mode 2 is

$$\eta(z) = \eta_{\max}\sin^2\rho z \quad \text{with} \quad \eta_{\max} = \frac{|\kappa|^2}{(\Delta\beta'/2)^2 + |\kappa|^2}\,. \tag{1.75}$$

The power transfer ratio η reaches its maximum $\eta_{\max}$ at the position of the conversion length $L_{\mathrm{c}} = \pi/(2\rho)$. Note that the mismatch $\Delta\beta' = \beta_1' - \beta_2'$ between the phase-shifted propagation constants determines the upper limit of the polarization conversion.

1.5.2 Supermode propagation

The most common application of coupled mode theory is the simulation of composite structures which can be reasonably (usually ambiguously [48]) divided into a number of separate waveguides. Figure 1.8 shows an example.

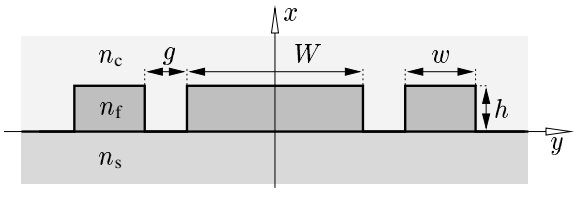

Figure 1.8: Cross section of a three waveguide coupler from Chapter 7.

For simulation in the framework of coupled mode theory, we suppose the guided modes of the single isotropic lossless waveguides to be known. In the example of Figure 1.8, for fixed polarization, these are the two single modes of the outer waveguides, and the set of modes of the central guide. For purely real permittivities, the coupling coefficients are real, thus symmetric $\kappa_{ml} = \kappa_{lm}$.

Eq. (1.69) is readily solved by an ansatz of harmonic dependence on the propagation distance, $\boldsymbol{C}(z) = \boldsymbol{a}\,\mathrm{e}^{-\mathrm{i}\beta z}$, where $\boldsymbol{a}$ is a constant weighting vector and β is the supermode propagation constant. This ansatz leads to the real generalized eigenvalue problem

$$(\mathsf{B} + \mathsf{K})\boldsymbol{a} = \beta\mathsf{S}\boldsymbol{a}\,. \tag{1.76}$$

If only forward propagating modes are included in Eq. (1.59), a positive S permits convenient numerical solution of Eq. (1.76) via Cholesky-decomposition of S [112]. The solution consists of a number of supermode propagation constants β^s and corresponding real vectors $\boldsymbol{a}^s$ which constitute the supermode field profiles

$$\boldsymbol{E}^s = \sum_m a_m^s \frac{1}{\sqrt{P_m}} \boldsymbol{E}_m, \quad \boldsymbol{H}^s = \sum_m a_m^s \frac{1}{\sqrt{P_m}} \boldsymbol{H}_m. \tag{1.77}$$

For nondegenerate propagation constants, the orthogonality property $(\boldsymbol{a}^r)^{\mathsf{T}} \mathsf{S} \boldsymbol{a}^s = \delta_{rs} P^s$ holds, where P^s is the power assigned to supermode number s. With the product (1.18) from Section 1.1.4 this can be written as $(\boldsymbol{E}^r, \boldsymbol{H}^r; \boldsymbol{E}^s, \boldsymbol{H}^s) = \delta_{rs} P^s$.

The field in the homogeneous coupling section has the form (1.59) with coefficients

$$C_m(z) = \sum_s A^s \frac{1}{\sqrt{P^s}} a_m^s \, \mathrm{e}^{-\mathrm{i}\beta^s z}, \tag{1.78}$$

i.e. a supermode superposition with constant amplitudes A^s:

$$\boldsymbol{\mathcal{E}}(x,y,z,t) = \sum_s \frac{A^s}{\sqrt{P^s}} \boldsymbol{E}^s(x,y) \, \mathrm{e}^{\mathrm{i}\omega t - \mathrm{i}\beta^s z}, \quad \boldsymbol{\mathcal{H}}(x,y,z,t) = \sum_s \frac{A^s}{\sqrt{P^s}} \boldsymbol{H}^s(x,y) \, \mathrm{e}^{\mathrm{i}\omega t - \mathrm{i}\beta^s z}. \tag{1.79}$$

Supermode orthogonality allows us to express the total guided power in the coupling region as $P = \sum_s |A^s|^2$.

Now consider a coupler structure of finite length L with a coupling section extending from $z = 0$ to $z = L$. At $z = 0$, the simulation shall start with the single mode field $\sqrt{P_i^{\mathrm{in}}/P_i}\,(\boldsymbol{E}_i, \boldsymbol{H}_i)$ of one input waveguide (index i), scaled to an input power P_i^{in}. Projection on the supermode fields (1.77) with respect to (1.18) yields the amplitudes

$$A^s = \sqrt{\frac{P_i^{\mathrm{in}}}{P^s}} \sum_m \sigma_{im} a_m^s \,. \tag{1.80}$$

By construction, the total guided power evaluates to the input power $\sum_s |A^s|^2 = P_i^{\mathrm{in}}$ for excitement by one of the coupled modes. In contrast to the theory based on normal modes, the present approach gives no access to radiation loss due to mode mismatch.

Coupling vanishes for $z > L$. Only the modes of the isolated port waveguides remain (the outer waveguides in the example of Figure 1.8), and for these we can assume orthogonality $(\boldsymbol{E}_j, \boldsymbol{H}_j; \boldsymbol{E}_k, \boldsymbol{H}_k) = \delta_{jk} P_k$ due to the waveguide separation. Thus projection on the output mode (index o) yields the output power

$$P_o^{\mathrm{out}} = P_i^{\mathrm{in}} \Big| \sum_s w_{oi}^s \, \mathrm{e}^{-\mathrm{i}\beta^s L} \Big|^2 \quad \text{or} \quad P_o^{\mathrm{out}} = P_i^{\mathrm{in}} \sum_{r,s} w_{oi}^r w_{oi}^s \cos(\beta^r - \beta^s) L \tag{1.81}$$

with

$$w_{oi}^s = \frac{1}{P^s} \Big(\sum_m \sigma_{om} a_m^s \Big) \Big(\sum_m \sigma_{im} a_m^s \Big), \tag{1.82}$$

completely analogous to the expression derived for exact normal modes in Section 1.2, if the sums over m are viewed as products (1.18) between supermode s and the input respectively output field i, o.

2 Planar structures

A slab configuration is called planar if both its permittivity profile and the electromagnetic fields considered for this profile are constant along one of the transverse coordinate axes. Apart from physical waveguides without lateral confinement, the model should be applicable to laterally weakly guiding structures as well. Additionally, planar mode analysis constitutes the basis for a number of both approximate [24] or rigorous [145] methods for calculating two-dimensional modes. In this thesis, the planar model serves for device design (Chapter 7), for numerical assessment of the perturbation theory (Chapter 5), and frequently for judgements on two-dimensional structures in terms of effective indices or in terms of the limiting structures as in Section 1.1.6.

Section 2.1 transfers parts from the preceding chapter to one-dimensional waveguide cross sections; Section 2.2 outlines the mode analysis algorithm for multilayer structures with piecewise constant isotropic refractive index profile. In contrast to the two-dimensional case, planar modes and propagation constants can be calculated analytically up to the solution of a transcendental equation, which provides a sound fundament for subsequent evaluations of perturbational expressions.

2.1 Mode properties

Choosing the x direction to be normal to the planar slabs, the ansatz of vanishing derivatives $\partial_y \boldsymbol{\mathcal{E}}$, $\partial_y \boldsymbol{\mathcal{H}}$, $\partial_y \epsilon$ splits Eqs. (1.7) for isotropic lossless permittivity into two decoupled sets. These combine the mode components H_x, E_y, H_z on the one hand and E_x, H_y, E_z on the other hand.

The solutions of the former constitute mode fields of the form (1.6) without a longitudinal electric component, commonly called transverse electric (TE) modes,

$$\boldsymbol{E} = \begin{pmatrix} 0 \\ E_y \\ 0 \end{pmatrix}, \quad \boldsymbol{H} = \frac{1}{\omega\mu_0} \begin{pmatrix} -\beta E_y \\ 0 \\ \mathrm{i}\partial_x E_y \end{pmatrix}, \tag{2.1}$$

where the electric component E_y satisfies the planar TE mode equation

$$(\partial_x^2 + k^2\epsilon - \beta^2) E_y = 0\,. \tag{2.2}$$

The second subset of Eqs. (1.7) yields transverse magnetic (TM) modes with vanishing longitudinal magnetic component:

$$\boldsymbol{E} = \frac{1}{\omega\epsilon_0\epsilon} \begin{pmatrix} \beta H_y \\ 0 \\ -\mathrm{i}\partial_x H_y \end{pmatrix}, \quad \boldsymbol{H} = \begin{pmatrix} 0 \\ H_y \\ 0 \end{pmatrix}. \tag{2.3}$$

For the single magnetic component H_y, the planar TM mode equation

$$(\epsilon\partial_x \frac{1}{\epsilon} \partial_x + k^2\epsilon - \beta^2) H_y = 0 \tag{2.4}$$

holds. All fields depend on the x-coordinate only.

Power flux and mode orthogonality

The power per lateral unit length $\mathrm{Re}\int \boldsymbol{E}\times\boldsymbol{H}^*\,\mathrm{d}x/2$ associated with a planar mode is

$$P=\frac{\beta}{2\omega\mu_0}\int E_y^2\,\mathrm{d}x\quad\text{(TE)},\qquad\qquad P=\frac{\beta}{2\omega\epsilon_0}\int\frac{1}{\epsilon}H_y^2\,\mathrm{d}x\quad\text{(TM)}. \tag{2.5}$$

With respect to mode orthogonality, for planar problems the identity (1.16) combines the x- and z-derivatives of the involved modes $\boldsymbol{\Phi}_l^{\mathrm{TE,\,TM}}=(\boldsymbol{E}_l,\boldsymbol{H}_l)$. Thus only the integration along x remains in the orthogonality relations for nondegenerate planar modes

$$\frac{\beta_m}{2\omega\mu_0}\int E_{ly}E_{my}\,\mathrm{d}x=\delta_{lm}P_m\quad\text{(TE)},\qquad\qquad\frac{\beta_m}{2\omega\epsilon_0}\int\frac{1}{\epsilon}H_{ly}H_{my}\,\mathrm{d}x=\delta_{lm}P_m\quad\text{(TM)}. \tag{2.6}$$

For the same reason, the restriction of the general bilinear product (1.18) on one-dimensional cross sections

$$(\boldsymbol{\Phi}_l;\boldsymbol{\Phi}_m)=\frac{1}{4}\int(E_{lx}H_{my}-E_{ly}H_{mx}+E_{mx}H_{ly}-E_{my}H_{lx})\,\mathrm{d}x \tag{2.7}$$

allows to write the orthogonality properties in the form

$$(\boldsymbol{\Phi}_l^{\mathrm{TE}};\boldsymbol{\Phi}_m^{\mathrm{TE}})=\delta_{lm}P_m\,,\quad(\boldsymbol{\Phi}_l^{\mathrm{TM}};\boldsymbol{\Phi}_m^{\mathrm{TM}})=\delta_{lm}P_m\,,\quad\text{and}\quad(\boldsymbol{\Phi}_l^{\mathrm{TE}};\boldsymbol{\Phi}_m^{\mathrm{TM}})=0\,. \tag{2.8}$$

Therefore, with the product (1.18) substituted by (2.7), the propagating mode analysis of Section 1.2 applies to planar geometries as well, where the last equality in (2.8) justifies separate simulations for TE and TM polarization in the case of rectangular structures made of isotropic material. Analogously, with the y-integrations skipped in Eqs. (1.62), (1.68) and in related relations, coupled mode theory as formulated in Section 1.5 becomes applicable to planar structures.

Small uniform perturbations

All steps in the derivation of propagation constant shifts due to permittivity perturbations in Section 1.3 can be carried out for the planar configuration as well, provided that the scalar product $\langle\,.\,,\,.\,\rangle$ in the basic functional (1.41) is substituted by $\langle\boldsymbol{F},\boldsymbol{G}\rangle=\int\boldsymbol{F}^*\boldsymbol{G}\,\mathrm{d}x$. This leads to the general perturbational expression for planar modes

$$\delta\beta=\frac{\omega\epsilon_0}{2}\,\frac{\displaystyle\int\boldsymbol{E}^*\,\delta\hat{\epsilon}\boldsymbol{E}\,\mathrm{d}x}{\displaystyle\int(E_xH_y-E_yH_x)\,\mathrm{d}x}\,. \tag{2.9}$$

Note that Eq. (2.9) requires $\delta\hat{\epsilon}$ to be laterally constant.

In the unperturbed planar mode fields, only few components are present. From the nine entries of a general perturbation matrix $\delta\hat{\epsilon}=(\delta\epsilon_{ij})$, only the central element affects the propagation constant of a planar TE mode

$$\delta\beta=\frac{k^2}{2\beta}\,\frac{\displaystyle\int\delta\epsilon_{yy}E_y^2\,\mathrm{d}x}{\displaystyle\int E_y^2\,\mathrm{d}x}\,. \tag{2.10}$$

For TM polarization, the two electric components E_x and E_z give rise to four contributions in the numerator. Written in terms of the basic field H_y, the perturbational expression for TM modes reads

$$\delta\beta=\frac{\beta}{2}\,\frac{\displaystyle\int\left(\frac{\delta\epsilon_{xx}}{\epsilon^2}H_y^2+2\,\mathrm{Im}\frac{\delta\epsilon_{xz}}{\epsilon^2}H_y\frac{1}{\beta}\partial_xH_y+\frac{\delta\epsilon_{zz}}{\epsilon^2}(\frac{1}{\beta}\partial_xH_y)^2\right)\mathrm{d}x}{\displaystyle\int\frac{1}{\epsilon}H_y^2\,\mathrm{d}x}\,, \tag{2.11}$$

where the term $2\,\mathrm{Im}\,\delta\epsilon_{xz}$ has to be replaced by $\mathrm{i}(\delta\epsilon_{zx}-\delta\epsilon_{xz})$ in case of a non-Hermitian perturbation.

Absorption

As in Section 1.3.1, assume an absorbing layer between x_0 and x_1 in the permittivity profile with refractive index n. In bulk form, the material shall damp the intensity of plane waves as $\exp(-\alpha z)$, with a small bulk attenuation constant α. According to Eqs. (2.10), (2.11), the corresponding permittivity perturbation $\delta\epsilon_{\mathrm{abs}} = -\mathrm{i}n\alpha/k$ effects a small imaginary part $\delta\beta_{\mathrm{abs}} = -\mathrm{i}\alpha_{\mathrm{m}}/2$ of the propagation constant, where

$$\alpha_{\mathrm{m}} = \alpha\, n \frac{k}{\beta} \frac{\int_{x_0}^{x_1} E_y^2 \,\mathrm{d}x}{\int E_y^2 \mathrm{d}x} \quad \text{(TE)}, \qquad \alpha_{\mathrm{m}} = \alpha\, n \frac{\beta}{k} \frac{\int_{x_0}^{x_1} \frac{1}{\epsilon^2}\left(H_y^2 + (\frac{1}{\beta}\partial_x H_y)^2\right)\mathrm{d}x}{\int \frac{1}{\epsilon} H_y^2 \,\mathrm{d}x} \quad \text{(TM)} \tag{2.12}$$

is the planar mode power attenuation. These expressions are identical to the results of Ref. [167], which have been derived from a variational principle for planar modes. Obviously, in the limiting case of a plane wave, both expressions yield the correct result $\alpha_{\mathrm{m}} = \alpha$.

Geometry perturbations

Shifts of dielectric boundaries in a layered planar structure correspond to the horizontal boundary displacements investigated in Section 1.4. Figure 2.1 illustrates the relevant geometry.

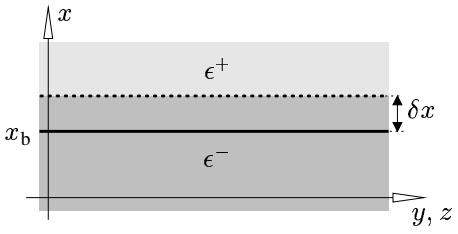

Figure 2.1: Variation of a boundary location in a planar configuration. The dielectric boundary between permittivities ϵ^- and ϵ^+ is shifted by a distance δx from the original position x_b.

A derivation analogously to the two-dimensional case leads to the perturbational expressions

$$\delta\beta = \frac{k^2}{2\beta} \frac{(\epsilon^- - \epsilon^+)\, E_y^2(x_{\mathrm{b}})}{\int E_y^2 \,\mathrm{d}x} \delta x \quad \text{(TE)} \tag{2.13}$$

and

$$\delta\beta = \frac{\beta}{2} \frac{(\epsilon^- - \epsilon^+)\left(\frac{1}{\epsilon^-\epsilon^+} H_y^2(x_{\mathrm{b}}) + \frac{1}{\beta^2}(\frac{1}{\epsilon}\partial_x H_y)^2(x_{\mathrm{b}})\right)}{\int \frac{1}{\epsilon} H_y^2 \,\mathrm{d}x} \delta x \quad \text{(TM)} \tag{2.14}$$

for the propagation constant change $\delta\beta$ due to the shift of a boundary from x_{b} to $x_{\mathrm{b}} + \delta x$.

2.2 Simulation

Provisionally, the discussion of mode calculations shall be restricted to isotropic permittivity profiles. We refer to a geometry as sketched in Figure 2.2, comprising N inner layers (in Chapter 7 structures with N up to 30 will be relevant).

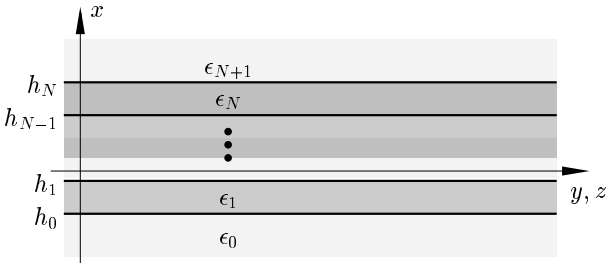

Figure 2.2: General planar multilayer structure. $N+1$ boundaries at x-positions h_0 to h_N separate $N+2$ slabs with constant permittivities $\epsilon_l = n_l^2$, $l = 0, \ldots, N+1$. The outer layers $l = 0$ and $l = N+1$ are unbounded.

For points x inside layer l with constant refractive index n_l, the TE and TM mode equations (2.2), (2.4) reduce to

$$\partial_x^2 \Phi = (\beta^2 - k^2 n_l^2)\Phi\,, \tag{2.15}$$

where Φ represents the basic field E_y for TE and H_y for TM polarization. Its real solutions can be written in the general form

$$\Phi(x) = \begin{cases} A_l \exp(\gamma_l(x - x_l)) + B_l \exp(-\gamma_l(x - x_l)) & \text{if } \beta^2 > k^2 n_l^2 \\ A_l \sin(\gamma_l(x - x_l)) + B_l \cos(\gamma_l(x - x_l)) & \text{otherwise} \end{cases}, \quad \text{for } h_{l-1} < x < h_l\,, \tag{2.16}$$

with h_{-1} and h_{N+1} to be interpreted as $\mp\infty$. The transverse wave vector components are defined as $\gamma_l = \sqrt{|\beta^2 - k^2 n_l^2|}$. Local coordinate offsets $x_l = (h_l + h_{l+1})/2$ with $x_0 = h_0$ and $x_{N+1} = h_{N+1}$ have been introduced to cope with the exponential functions in case of a wide extent $h_N - h_0$.

For guided modes, i.e. fields which are integrable in the sense of Eqs. (2.5), only exponentially decaying parts of ansatz (2.16) are physically relevant on the outer layers. This limits the interval for prospective effective mode indices by $\beta/k > \max\{n_0, n_{N+1}\}$, and amounts to vanishing coefficients B_0 and A_{N+1}.

The continuity requirements for horizontal boundaries from Section 1.1.5 demand a continuous field Φ and continuous normal derivative $\partial_x \Phi$ for TE polarization, while for TM modes Φ and $\epsilon^{-1}\partial_x \Phi$ must be continuous. Inspection of the fields (2.1), (2.3) show that with this choice the continuity conditions for all components are satisfied. Evaluating these conditions for the ansatz (2.16) leads to a linear connection between coefficients on adjacent slabs

$$\begin{pmatrix} A_{l+1} \\ B_{l+1} \end{pmatrix} = \mathsf{T}_l \begin{pmatrix} A_l \\ B_l \end{pmatrix} \tag{2.17}$$

by transfer matrices

$$\mathsf{T}_l = \frac{1}{a_{l+1} q_{l+1} - b_{l+1} p_{l+1}} \begin{pmatrix} q_{l+1} c_l - b_{l+1} r_l & q_{l+1} d_l - b_{l+1} s_l \\ a_{l+1} r_l - p_{l+1} c_l & a_{l+1} s_l - p_{l+1} d_l \end{pmatrix}, \tag{2.18}$$

with entries a_l to s_l as given in Table 2.1.

Consequently, the coefficients belonging to the uppermost layer are related to those of the lowest layer by

$$\begin{pmatrix} A_{N+1} \\ B_{N+1} \end{pmatrix} = \left(\prod_{l=0}^{N} \mathsf{T}_l \right) \begin{pmatrix} A_0 \\ B_0 \end{pmatrix}. \tag{2.19}$$

	a_l	b_l	c_l	d_l
$\beta^2 > k^2 n_l^2$	$\exp(\gamma_l \, \Delta h_{l-1}^l)$	$\exp(-\gamma_l \, \Delta h_{l-1}^l)$	$\exp(\gamma_l \, \Delta h_l^l)$	$\exp(-\gamma_l \, \Delta h_l^l)$
$\beta^2 < k^2 n_l^2$	$\sin(\gamma_l \, \Delta h_{l-1}^l)$	$\cos(\gamma_l \, \Delta h_{l-1}^l)$	$\sin(\gamma_l \, \Delta h_l^l)$	$\cos(\gamma_l \, \Delta h_l^l)$

	p_l	q_l	r_l	s_l
$\beta^2 > k^2 n_l^2$	$\eta_l \gamma_l \exp(\gamma_l \, \Delta h_{l-1}^l)$	$-\eta_l \gamma_l \exp(-\gamma_l \, \Delta h_{l-1}^l)$	$\eta_l \gamma_l \exp(\gamma_l \, \Delta h_l^l)$	$-\eta_l \gamma_l \exp(-\gamma_l \, \Delta h_l^l)$
$\beta^2 < k^2 n_l^2$	$\eta_l \gamma_l \cos(\gamma_l \, \Delta h_{l-1}^l)$	$-\eta_l \gamma_l \sin(\gamma_l \, \Delta h_{l-1}^l)$	$\eta_l \gamma_l \cos(\gamma_l \, \Delta h_l^l)$	$-\eta_l \gamma_l \sin(\gamma_l \, \Delta h_l^l)$

Table 2.1: Definitions for the entries of Eq. (2.18) with l ranging from 0 to N, with elements a_0, b_0, p_0, q_0 and c_{N+1}, d_{N+1}, r_{N+1}, s_{N+1} being obsolete. $\Delta h_l^m = h_l - x_m$ denotes the distance between boundary l and coordinate offset m. Only the quantity η accounts for the polarization discrimination: $\eta_l = 1$ for TE and $\eta_l = 1/n_l^2$ for TM polarization.

A_0 can be chosen as an arbitrary nonzero amplitude, while the integrability condition demands $B_0 = A_{N+1} = 0$. Thus the problem of finding the guided planar modes is reduced to the task to identify the values β, where the first component of $(\prod_{l=0}^{N} \mathsf{T}_l)(1,0)^\mathsf{T}$ vanishes. Note that the trial value β enters all matrices via the transverse wavenumbers γ_l.

Based on the above equations, an algorithm for calculating all modes of a planar multilayer structure can be designed straightforwardly. To find the roots in $A_{N+1}(\beta)$, the variety of applicable techniques [112] may exploit specific nodal properties of the problem [93], for bracketing valid propagation constants. The planar mode solver implemented during this thesis turns out to be efficient and robust.

Therefore, at least for planar isotropic step profiles, perturbational techniques like the geometry perturbation formulas (2.13), (2.14), or coupled mode theory, are of less importance for device design, apart from theoretical considerations. However, this does no longer apply e.g. to structures with anisotropic or absorbing layers. For the former, usually coupling of two TE and two TM mode amplitudes in each layer leads to boundary equations of dimension four, which do not permit the explicit analytical transfer matrix technique as outlined above (an exception are the transversely magnetized magnetooptic waveguides of Chapter 7). For absorbing structures, the root finding routine will be worse in speed and robustness, since the propagation constants have to be searched in the complex plane rather than on the real axis.

3 Wave matching method

Accurate calculation of mode fields and propagation constants is one of the principal tasks of numerically simulating integrated optical devices. Hence a large variety of computational methods have been proposed, Refs. [23, 159] give an overview. There are a few approximative analytical approaches towards the problem (e.g. [155, 133, 118, 120, 58, 18, 24]). While being quite economical with computational resources, their applicability is limited by the approximations they rely on. More versatile, but computationally more expensive methods are usually based on finite element or finite difference approximations of the Maxwell equations (e.g. [114, 115, 19, 139, 140, 119, 1, 64, 143, 88, 44, 102]). Some use beam propagation techniques (e.g. [70, 71, 67, 171, 172]). Others expand the electromagnetic fields into sets of orthogonal functions (e.g. [50, 145, 54, 126]), Ref. [56] suggests a mixture of both.

Waveguides in integrated optics are formed either by a diffusion or by an etching process. In the first case the refractive index varies smoothly in the substrate region, in the second case the guiding profile shows sharp discontinuities with constant permittivity in-between. Most examples in the above mentioned articles refer to waveguides of the second type, but most of the more rigorous methods do not exploit this feature (an exception is the modal transverse resonance technique [145]). Our approach is based on it.

It is motivated by the common strategy for solving the mode problem for multilayer slab waveguides (cf. Section 2.2): First, on each region with constant refractive index a set of plausible solutions to the basic wave equation is selected. Then the boundary conditions for dielectric interfaces combine fields on adjacent regions to a system of linear equations. Finally, its nonvanishing solutions yield propagation constants and mode profiles. Analogously, the approach discussed in the following sections may be regarded as an attempt to establish a similar procedure for two transverse dimensions. Given a reasonable ansatz of trial fields, the algorithm tries to find best solutions in terms of a least squares expression for the remaining mismatch on the dielectric boundaries.

In Section 3.1 suitable fundamental solutions are set up, separately for each region with constant refractive index. Since the number of these trial functions is not limited, one has to select. Therefore the method cannot be expected to give exact results as in the planar case, and the way to connect different regions and the solution method have to be modified. We adopt a least squares method similar to [28], see Section 3.2. The resulting numerical procedure to determine guided modes is the subject of Section 3.3. For the purpose of comparison with results of other methods (Chapter 4), we refer to the present approach as 'wave matching method' WMM. The technique was proposed first for semivectorial mode analysis in Ref. [73] and subsequently extended to fully vectorial simulations [74].

3.1 Trial functions

Consider a longitudinally homogeneous dielectric waveguide described by a piecewise constant rectangular permittivity profile. Figure 3.1 shows a typical example. The cross section consists of $(N_x+2)\times(N_y+2)$ rectangles with real diagonal isotropic permittivity $\epsilon^{lm}=(n^{lm})^2$, $l=0,\ldots,N_x+1$, $m=0,\ldots,N_y+1$, separated by the horizontal lines $x=h_{x,l}$, $l=0,\ldots N_x$ and vertical lines $y=h_{y,m}$, $m=0,\ldots N_y$. A superscript r will be used to shorthand denote a rectangle l,m.

As discussed in Section 1.1, in case of vectorial simulations two basic components have to be calculated directly, while for semivectorial mode analysis one field is sufficient. Let Φ_1, Φ_2 or Φ_1, respectively, denote the basic components. On each rectangle r, these fields are assumed to be linear combinations of J_ν^r trial

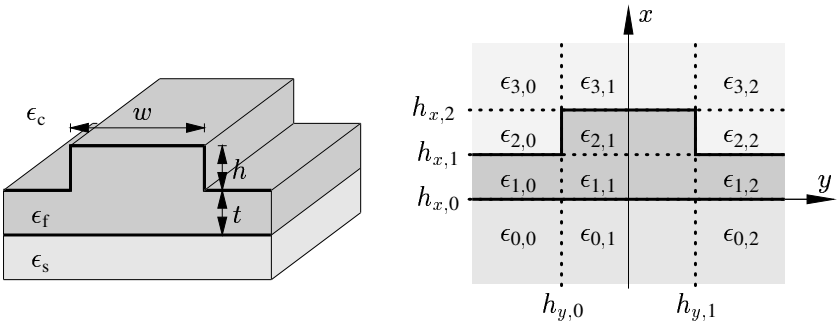

Figure 3.1: Sample structure: The cross section of a rib waveguide can be divided into twelve rectangles with constant permittivity. Note that the first and last rectangles in each horizontal and vertical slice are unbounded.

functions $\phi^r_{\nu j}$:

$$\Phi_\nu(x,y) = \Phi^r_\nu(x,y) \quad \text{if } (x,y) \in \text{rectangle } r, \text{ with } \quad \Phi^r_\nu(x,y) = \sum_{j=0}^{J^r_\nu - 1} a^r_{\nu j} \phi^r_{\nu j}(x,y)\,. \tag{3.1}$$

The unknown amplitudes $a^r_{\nu j}$ will be the subject of the subsequent computation.

According to Section 1.1.5, inside the regions with constant permittivity ϵ^r the fields Φ^r_ν satisfy the Helmholtz wave equation

$$\partial_x^2 \Phi^r_\nu + \partial_y^2 \Phi^r_\nu = (\beta^2 - k^2 \epsilon^r) \Phi^r_\nu. \tag{3.2}$$

Thus we can specialize to an ansatz of functions which factorize with respect to the transverse coordinates

$$\phi^r_{\nu j}(x,y) = c^r_{\nu j}\, F^r_{\nu j}(p^r_{\nu j}(x - x^r_{0,\nu j}))\, G^r_{\nu j}(q^r_{\nu j}(y - y^r_{0,\nu j}))\,, \tag{3.3}$$

where $F^r_{\nu j}$, $G^r_{\nu j}$, are one of the functions sin, cos, or exp. $c^r_{\nu j}$ is a normalization constant and $x^r_{0,\nu j}$ and $y^r_{0,\nu j}$ are introduced as local coordinate offsets (see below). In the remainder of this section, we omit the rectangle label r and the basic component index ν for brevity.

Valid pairs (p_j, q_j) of the transverse wave vector components p_j and q_j lie on curves defined by

$$\pm p_j^2 \pm q_j^2 = \beta^2 - k^2 \epsilon, \tag{3.4}$$

with the signs depending on the choice of F_j and G_j. While in principle all points (p_j, q_j) satisfying Eq. (3.4) yield valid trial functions (3.3), numerically only a suitable discrete set can be implemented.

Therefore a number of points (p_j, q_j) from the curves (3.4) must be selected; each one defines a contribution j to the sum (3.1). There are two constraints: The selected points should cover the entire relevant domain on the curve (3.4), i.e. the space spanned by the corresponding trial functions must be sufficiently large, while at the same time these functions must be as linearly independent as possible.

For this spectral discretization procedure, it is necessary to fix a reasonable set of parameters J, F_j, G_j, p_j, and q_j separately for each rectangle r, component ν, and for a given trial value β. First consider a finite rectangle (indices $1 \le l \le N_x$ and $1 \le m \le N_y$) with β/k larger than the local refractive index. Since $\beta^2 - k^2\epsilon = \pm p_j^2 \pm q_j^2 > 0$, at least one of F_j and G_j must be the exponential function. As shown in Table 3.1(a), the set of trial functions can be divided into twelve subsets. Each is characterized by a choice for F_j and G_j and the signs of p_j and q_j. Possible transverse wave vectors (p_j, q_j) are located on a circle with radius $\sqrt{\beta^2 - k^2\epsilon}$ (for $(F_j, G_j) = (\exp, \exp)$) or a hyperbola (otherwise). Thus they may be defined by discrete values α_j chosen from a single parameter interval (see Table 3.1).

Table 3.1(b) gives the sets of trial functions for a finite rectangle if β/k is smaller than the local refractive index. Since now $k^2\epsilon - \beta^2 = \mp p_j^2 \mp q_j^2 > 0$, at least one of F_j and G_j must be a harmonic function.

The coordinate offsets $x_{0,j}, y_{0,j}$ are introduced to meet symmetry requirements and to handle the exponential functions numerically. For rectangle $r = (l, m)$, if $F_j = \exp$ with $p_j > 0$ ($p_j < 0$) set $x_{0,j} = h_{x,l}$

(a) $\beta^2 - k^2\epsilon > 0, \quad w = \sqrt{\beta^2 - k^2\epsilon}$

F	G	$\alpha \in$	p	q
exp	exp	$]0, \pi/2[$	$w\cos\alpha$	$w\sin\alpha$
exp	exp	$]0, \pi/2[$	$w\cos\alpha$	$-w\sin\alpha$
exp	exp	$]0, \pi/2[$	$-w\cos\alpha$	$w\sin\alpha$
exp	exp	$]0, \pi/2[$	$-w\cos\alpha$	$-w\sin\alpha$
cos	exp	$]0, \infty[$	$w\sinh\alpha$	$w\cosh\alpha$
cos	exp	$]0, \infty[$	$w\sinh\alpha$	$-w\cosh\alpha$
sin	exp	$]0, \infty[$	$w\sinh\alpha$	$w\cosh\alpha$
sin	exp	$]0, \infty[$	$w\sinh\alpha$	$-w\cosh\alpha$
exp	cos	$]0, \infty[$	$w\cosh\alpha$	$w\sinh\alpha$
exp	cos	$]0, \infty[$	$-w\cosh\alpha$	$w\sinh\alpha$
exp	sin	$]0, \infty[$	$w\cosh\alpha$	$w\sinh\alpha$
exp	sin	$]0, \infty[$	$-w\cosh\alpha$	$w\sinh\alpha$

(b) $k^2\epsilon - \beta^2 > 0, \quad w = \sqrt{k^2\epsilon - \beta^2}$

F	G	$\alpha \in$	p	q
cos	cos	$]0, \pi/2[$	$w\cos\alpha$	$w\sin\alpha$
cos	sin	$]0, \pi/2[$	$w\cos\alpha$	$w\sin\alpha$
sin	cos	$]0, \pi/2[$	$w\cos\alpha$	$w\sin\alpha$
sin	sin	$]0, \pi/2[$	$w\cos\alpha$	$w\sin\alpha$
exp	cos	$]0, \infty[$	$w\sinh\alpha$	$w\cosh\alpha$
exp	sin	$]0, \infty[$	$w\sinh\alpha$	$w\cosh\alpha$
exp	cos	$]0, \infty[$	$-w\sinh\alpha$	$w\cosh\alpha$
exp	sin	$]0, \infty[$	$-w\sinh\alpha$	$w\cosh\alpha$
cos	exp	$]0, \infty[$	$w\cosh\alpha$	$w\sinh\alpha$
sin	exp	$]0, \infty[$	$w\cosh\alpha$	$w\sinh\alpha$
cos	exp	$]0, \infty[$	$w\cosh\alpha$	$-w\sinh\alpha$
sin	exp	$]0, \infty[$	$w\cosh\alpha$	$-w\sinh\alpha$

Table 3.1: Trial functions for a finite rectangle.

($x_{0,j} = h_{x,l-1}$). Otherwise, for $F_j = \sin$ or $F_j = \cos$, set $x_{0,j} = (h_{x,l} + h_{x,l-1})/2$. Analogously, $y_{0,j}$ is fixed in terms of $h_{y,m}$, $h_{y,m-1}$ depending on G_j and q_j.

For unbounded rectangles ($l = 0$ or $l = N_x + 1$, $m = 0$ or $m = N_y + 1$), Table 3.1 applies as well. Merely outwards exponentially increasing trial functions must be dropped. This implements the constraint of a square integrable mode field without any further boundary conditions. No spatial computational window is required, the mode functions are defined on the entire waveguide cross section plane.

On corner rectangles, e.g. $l = 0$, $m = 0$, only one subset with outwards exponentially decaying functions remains, provided that β/k is larger than the local refractive index. Otherwise no admissible subset would be left, thus no guided mode is possible. On the contrary, for rectangles unbounded in only one direction, both signs of $\beta^2 - k^2\epsilon$ yield valid subsets. The situation with β/k smaller than the local refractive index occurs frequently, e.g. if a rib has been etched from a guiding film as sketched in Figure 3.1.

Now for each subset a number of discrete values α_j must be selected. Let N_α denote the maximum number. If only one of F_j and G_j is exponential, the parameter interval is not bounded. We introduced a largest admissible value $\alpha_{\max}$, which is set to $\pi/2$ if both F_j and G_j are exponential or harmonic functions. The selected values should be at least spaced by $\alpha_{\max}/N_\alpha$.

The selection starts with an arbitrarily guessed value. We use $\alpha = 1$ if only one of F_j and G_j is exponential and $\alpha = \pi/4$ otherwise. It defines a trial function ϕ_α. The next parameter $\alpha \pm \Delta\alpha$ should yield a function $\phi_{\alpha+\Delta\alpha}$ which differs significantly from ϕ_α. A parameter d will limit this difference. The integrated deviation between the zero function and arbitrary linear combinations of the two functions should be larger than d:

$$\min_{a_1, a_2, a_1^2 + a_2^2 = 1} \iint_r \left(a_1\phi_\alpha + a_2\phi_{\alpha+\Delta\alpha} - 0\right)^2 \mathrm{d}x\,\mathrm{d}y \geq d\,. \tag{3.5}$$

For normalized functions $\iint_r \phi_\alpha^2 \,\mathrm{d}x\,\mathrm{d}y = \iint_r \phi_{\alpha+\Delta\alpha}^2(x,y)\,\mathrm{d}x\,\mathrm{d}y = 1$ — this defines the normalization constants c_j introduced above — Eq. (3.5) reduces to

$$\Gamma_\alpha(\Delta\alpha) = \left| \iint_r \phi_\alpha\,\phi_{\alpha+\Delta\alpha}\,\mathrm{d}x\,\mathrm{d}y \right| \leq 1 - d\,. \tag{3.6}$$

Expansion of Γ_α results in a condition for the admissible parameter difference $\Delta\alpha$:

$$\Delta\alpha \geq \sqrt{\frac{d}{g(\alpha)}}, \quad \text{where} \quad g(\alpha) = -\frac{1}{2}\frac{\mathrm{d}^2\Gamma_\alpha}{\mathrm{d}\Delta\alpha^2}(0)\,. \tag{3.7}$$

g is evaluated as a finite difference expression.

With this condition (3.7) and the constraint $\Delta\alpha \geq \alpha_{\max}/N_\alpha$ the values α_j can be selected, proceeding stepwise towards both ends of the parameter interval. This must be done seperately for each rectangle, each basic component, and each subset of trial functions. One obtains a spectral discretization with nonequidistant step sizes $\Delta\alpha$ on spectral computational windows $]0, \alpha_{\max}[$.

Since the trial value β enters this discretization procedure, it is carried out only once with an average value from each β interval under investigation. The parameter values α_j are stored, and for each trial value β the transverse wave vector components p_j and q_j are evaluated according to Table 3.1.

Many interesting structures show a mirror symmetry with respect to $y \to -y$, and their guided modes have a definite symmetry as well (cf. Section 1.1.3). In these cases the number of unknowns in the WMM calculations can be halved if one drops trial functions with unwanted symmetry in the centered rectangles. Additionally, each pair of corresponding coefficients on both sides must be treated as one unknown.

3.2 Joining the rectangles

Once the systems of trial functions are established on the separate rectangular regions, these regions are to be joined by employing the continuity conditions for electromagnetric fields on dielectric boundaries, as discussed in Section 1.1.5 and summarized in Table 3.2.

	Basic fields	Quantities continuous on horizontal boundaries	Quantities continuous on vertical boundaries
TE	E_y	E_y, $\partial_x E_y$	ϵE_y, $\partial_y E_y$
TM	H_y	H_y, $\epsilon^{-1}\partial_x H_y$	H_y, $\partial_y H_y$
VEC	E_x, E_y, or H_x, H_y, or E_z, H_z	ϵE_x, E_y, E_z, H_x, H_y, H_z	E_x, ϵE_y, E_z, H_x, H_y, H_z

Table 3.2: Basic fields and boundary conditions for semivectorial (TE, TM), and fully vectorial mode analysis (VEC).

Denoting by C_h the horizontal lines $x = h_{x,l}$, $l = 0, \ldots, N_x$, and by C_v the vertical boundaries $y = h_{y,m}$, $m = 0, \ldots, N_y$, on the cross section plane, we establish a least squares expression D for the misfit of the fields on the boundary lines. It is to be considered a function of the trial value β for the propagation constant, and of the vector $\boldsymbol{a}$ of all coefficients $a^r_{\nu j}$ from Eq. (3.1). For semivectorial TE calculations, this reads

$$\begin{aligned} D_\beta(\boldsymbol{a}) &= \int_{C_h} \left\{ \left(E_y^+ - E_y^-\right)^2 + \left(\frac{1}{k}\partial_x E_y^+ - \frac{1}{k}\partial_x E_y^-\right)^2 \right\} \mathrm{d}y \\ &+ \int_{C_v} \left\{ \left(\frac{2\epsilon^+}{\epsilon^+ + \epsilon^-}E_y^+ - \frac{2\epsilon^-}{\epsilon^+ + \epsilon^-}E_y^-\right)^2 + \left(\frac{1}{k}\partial_y E_y^+ - \frac{1}{k}\partial_y E_y^-\right)^2 \right\} \mathrm{d}x\,. \end{aligned} \tag{3.8}$$

The analogous expression for TM polarization is

$$\begin{aligned} D_\beta(\boldsymbol{a}) &= \int_{C_h} \left\{ \left(H_y^+ - H_y^-\right)^2 + \left(\frac{1}{k\epsilon^+}\partial_x H_y^+ - \frac{1}{k\epsilon^-}\partial_x H_y^-\right)^2 \right\} \mathrm{d}y \\ &+ \int_{C_v} \left\{ \left(H_y^+ - H_y^-\right)^2 + \left(\frac{\epsilon^- + \epsilon^+}{2k\epsilon^-\epsilon^+}\partial_y H_y^+ - \frac{\epsilon^- + \epsilon^+}{2k\epsilon^-\epsilon^+}\partial_y H_y^-\right)^2 \right\} \mathrm{d}x\,. \end{aligned} \tag{3.9}$$

For fully vectorial calculations, squared deviations in all six components are summed:

$$\begin{aligned} D_\beta(\boldsymbol{a}) &= \sqrt{\epsilon_0}\int_{C_h} \left\{(\epsilon^+E_x^+ - \epsilon^-E_x^-)^2 + (E_y^+ - E_y^-)^2 + (E_z^+ - E_z^-)^2\right\} \mathrm{d}y \\ &+ \sqrt{\mu_0}\int_{C_h} \left\{(H_x^+ - H_x^-)^2 + (H_y^+ - H_y^-)^2 + (H_z^+ - H_z^-)^2\right\} \mathrm{d}y \end{aligned} \tag{3.10}$$

$$+ \quad \sqrt{\epsilon_0} \int_{C_v} \left\{ (E_x^+ - E_x^-)^2 + (\epsilon^+ E_y^+ - \epsilon^- E_y^-)^2 + (E_z^+ - E_z^-)^2 \right\} \mathrm{d}x$$
$$+ \quad \sqrt{\mu_0} \int_{C_v} \left\{ (H_x^+ - H_x^-)^2 + (H_y^+ - H_y^-)^2 + (H_z^+ - H_z^-)^2 \right\} \mathrm{d}x \,.$$

Here superscripts $+$ and $-$ indicate fields assigned to neighbouring rectangles on opposite sides of the boundary, where the functions are evaluated exactly on the boundary line. The six components in Eq. (3.10) are meant to be expressed by the two basic fields. Obviously, in all three cases vanishing of $D_\beta(\boldsymbol{a})$ guarantees that $\boldsymbol{a}$ and β describe a guided mode exactly.

The square roots of the vacuum permittivity ϵ_0 and permeability μ_0 in Eq. (3.10), and the inverse wavenumbers k and the permittivity averages in Eqs. (3.8), (3.9) have been introduced as weighting factors to adjust the dimensions of the fields and their derivatives and of the electric and magnetic components, and in order to equilibrate contributions from horizontal and vertical boundaries. Note that these factors are chosen somewhat arbitrarily — they may even be functions, but there is no a priori reason why they should. In a numerical calculation only a restricted set of trial functions is available, and the unknown mode function will usually not be included in the function space spanned by the trial functions. Therefore the minimum achievable error and consequently the estimate for the propagation constant depend on the choice of the weighting factors. However, if the set of trial functions is large enough, one can expect these dependence to vanish.

A similar ansatz (Least Squares Boundary Residual Method) has been applied successfully for the simulation of longitudinal waveguide discontinuities [28, 116, 117]. The authors used the freedom in the choice of the weighting factors to improve the conditioning of the resulting matrices (see Section 3.3). We did not exploit this feature because it was not necessary.

There is a particular ambiguity regarding the fully vectorial case. Since we deal with a partial differential equation of second order in both transverse directions, one would expect that four boundary conditions (one for the field and one for the normal derivative of the two basic components) are sufficient. Inspection of the Maxwell equations shows that exact continuity of H_x, H_y, H_z and E_z implies the appropriate behaviour for E_x and E_y, provided that Eq. (3.2) holds for all components. Indeed we have found indications that an expression for D like Eq. (3.10) with the E_x and E_y terms dropped may provide better convergence (see Section 4.2.3). However, in other situations, e.g. for the structure in Section 4.2.2, this modification leads to less reasonable fields where the mismatch is concentrated in the dropped components. Therefore we stick to the original expression (3.10).

With a restricted set of ansatz functions, one cannot expect an exact solution. To compare them with respect to the mismatch on the boundaries, the trial solutions have to be normalized. For this purpose, we adopt the common expressions

$$N_\beta(\boldsymbol{a}) = \iint E_y^2 \,\mathrm{d}x\,\mathrm{d}y \quad \text{(TE)}, \qquad\qquad N_\beta(\boldsymbol{a}) = \iint \frac{1}{\epsilon} H_y^2 \,\mathrm{d}x\,\mathrm{d}y \quad \text{(TM)} \tag{3.11}$$

for semivectorial calculations. Fully vectorial fields are normalized with respect to one of the expressions

$$N_\beta(\boldsymbol{a}) = \iint \left(E_x^2 + E_y^2 + E_z^2\right) \mathrm{d}x\,\mathrm{d}y \quad \text{or} \quad N_\beta(\boldsymbol{a}) = \iint \left(H_x^2 + H_y^2 + H_z^2\right) \mathrm{d}x\,\mathrm{d}y \,. \tag{3.12}$$

The integrals are meant to be evaluated piecewise over the rectangles of the cross section decomposition. Remarks with respect to the arbitrarily chosen error expressions D apply to the normalization N as well. As pointed out in Section 1.1.4, in the fully vectorial case the longitudinal component of the Poynting vector does not yield a positive definite form suitable for normalization.

A consistent theoretical assessment for the WMM is still lacking. Such an assessment should comprise a variational principle as a basis for the numerical error minimization procedure. In particular, it should identify expressions for the least squares error (3.8)–(3.10) and the normalization (3.11)–(3.12) that yield in some way best estimates of the propagation constants for a trial field. However, from our experience we conclude that the definitions given in this section are at least good choices.

3.3 Numerical procedure

With our limited set of trial functions an exact representation of the mode field will not be feasible. But *one can expect the minimum achievable mismatch to be small if β is close to a valid propagation constant*. This assumption forms the basis of the procedure to determine the propagation constants: First, for a given trial value β, an optimum coefficient vector $\boldsymbol{a}$, normalized as $N_\beta(\boldsymbol{a}) = 1$, with corresponding minimum remaining mismatch $\mu_\beta = D_\beta(\boldsymbol{a})$ is calculated. Subsequently, μ_β is minimized with respect to β. The locations of the minima yield approximations to the propagation constants. By insertion of the corresponding eigenvectors into Eq. (3.1), one finally obtains the mode fields.

The implementation of this procedure starts with inserting ansatz (3.1) into Eqs. (3.8)–(3.10) as well as Eqs. (3.11)–(3.12), and analytically evaluating all integrals. This reduces the expressions for the boundary mismatch and norm to quadratic forms

$$D_\beta(\boldsymbol{a}) = \boldsymbol{a}^\mathsf{T}\mathsf{D}_\beta\boldsymbol{a}, \quad N_\beta(\boldsymbol{a}) = \boldsymbol{a}^\mathsf{T}\mathsf{N}_\beta\boldsymbol{a}, \tag{3.13}$$

where D_β and N_β are real sparse symmetric matrices. N_β has block-diagonal form, the sparsity pattern of D_β fits to the block structure of N_β. By construction, both D_β and N_β are positive.

While the latter statement holds mathematically, occasionally N_β turns out to be numerically indefinite: A few negative eigenvalues with small magnitude occur. This is due to an unnecessarily large set of trial functions on at least one rectangle. Some of these are numerically linearly dependent. (The spectral discretization procedure considers only the difference between neighbouring trial functions. Subsets of trial functions with different harmonic and exponential dependence are usually not orthogonal.) To restore positivity, one has to drop some of the trial functions. For each rectangle, we compute the smallest eigenvalue of the relevant part of the normalization matrix N_β. If this value is negative, we drop the trial function with the largest amplitude in the corresponding eigenvector. This procedure is repeated until each block on the diagonal of N_β is positive.

We are left with the following minimization problem: For given β, find $\boldsymbol{a}$ with the smallest $\boldsymbol{a}^\mathsf{T}\mathsf{D}_\beta\boldsymbol{a}$, subject to the condition $\boldsymbol{a}^\mathsf{T}\mathsf{N}_\beta\boldsymbol{a} = 1$. Consequently, solving the generalized eigenvalue equation

$$\mathsf{D}_\beta\boldsymbol{a} = \mu_\beta\mathsf{N}_\beta\boldsymbol{a} \tag{3.14}$$

for the smallest eigenvalue μ_β gives the lowest achievable error for a trial value β. Note that one has to find minima of this quantity μ_β with respect to β, i.e. multiple evaluations of Eq. (3.13) are required.

Two examples illustrating the shape of the μ_β-curves will be given in Sections 4.1.4, 4.2.1. Although they appear to be quite shallow, evaluation of the minima in Figures 4.4 and Figure 4.9 to sufficient precision has never been a problem. However, problems may arise with closely spaced propagation constants. Frequently, splitting the mode set into two subsets of opposite symmetry allows to separate these modes. But at some instances even modes with equal symmetry happen to propagate at almost the same wavenumber. One such case is illustrated in Figure 4.9, where the hybrid first order TE and zeroth order TM modes are almost degenerate. A possible ansatz to handle these structures is to use the freedom in the choice of the normalization expression to identify the parabolic sections in the error function μ_β corresponding to the degenerate modes (cf. the remarks at the end of Section 4.3.4).

An analogous problem occurs e.g. if higher order modes of a rib waveguide are searched for, where the outer regions, regarded as planar waveguides, support guided modes. There should be a continuous transition from a suitable superposition of planar modes of the outer slabs to an almost cut-off mode of the rib waveguide. The high order mode of the rib may be considered as almost degenerate with the continuum of planar modes. Due to the ansatz of decaying fields, the WMM program will probably identify a minimum in μ_β, but how to decide if it corresponds to a physical guided mode? Here the lack of a strict theoretical boundary for admissible effective mode indices becomes apparent. Additionally this problem may coincide with the setting of the slightly etched rib, as sketched at the end of Section 1.1.6. Fortunately, the structures discussed in this thesis do not need such configurations to be analysed exactly.

Remarks on the implementation

To solve Eq. (3.14), we followed a strategy outlined in [112]. Cholesky decomposition of the normalization matrix reduces Eq. (3.14) to an ordinary symmetric eigenvalue problem. The decomposition can be done separately for each diagonal block of N_β. Two subsequent backsubstitution steps take advantage of the block structure and the corresponding sparsity pattern of D_β as well, thus this part of the computation can be performed very efficiently. Afterwards, we used the LAPACK-library [2], or alternatively a simple inverse iteration procedure [112], to find the lowest eigenvalue of the resulting ordinary eigenvalue equation.

Depending on the effort invested in the one dimensional minimization algorithm (see e.g. [112]), only very few evaluations of Eq. (3.14) are required. A good initial estimate for the propagation constant is helpful; we used WMM-calculations with a reduced number of trial functions for that purpose. The mode analysis procedure starts with an initial scanning of the relevant refractive index interval (cf. Section 1.1.6). Using a coarse spectral discretization, on a mesh of typically 10 to 50 points a survey of the μ_β curve is computed. Then each triple of points which bracket a minimum (i.e. a lower value between two larger ones) is further examined, first with the coarse, subsequently with a finer spectral discretization, until the propagation constant is trapped up to sufficient accuracy.

One will note that all benchmark results shown in Sections 4.1 and 4.2 have been calculated with the same spectral discretization parameters (but with quite different total numbers of trial functions, since their number depends on e.g. refractive index values, number and dimension of rectangles, or the propagation constant). The mode indices given are stable with respect to a refinement of the spectral discretization, thus the choice of suitable discretization parameters does not depend crucially on the structure under consideration.

During the work on this thesis, the WMM was developed and implemented in the program language C [63], later in C++ [142]. By now, the code runs on several machines, including the HP workstations of the department, a number of personal computers, and the IBM RS/6000 SP server in the computing center of the University of Osnabrück. For a basic rectangular waveguide, e.g. the square core of Section 4.2.2, a complete run of the vectorial WMM program with accuracy as given takes about 7 minutes on a 99 MHz HP-735 computer, output of all data for Figures 4.11–4.13 included. About 5 MB of memory are needed. Reproducing the benchmarks results of Table 4.4 with state-of-the-art accuracy requires about 9 minutes and also about 5 MB of memory for 10 fundamental semivectorial modes on a current 400 MHz personal computer. Note that both time and memory consumption scale with the number of unknowns in the eigenvalue problem (3.14), where the current programs leave much room for optimization. In terms of computational effort, the method should be competitive with the modal transverse resonance method [145], while the memory requirements of finite element or finite difference methods are an order of magnitude larger.

At present, the WMM has been implemented to handle cross section decompositions as in Figure 3.1 with arbitrary numbers of horizontal and vertical slices. In practice, the computational effort scales strongly with the number of rectangles, if the spectral discretization is not decreased. Therefore discretizing a continuously varying refractive index profile or a profile with not rectangular boundaries is not an option. WMM treatment of such structures would require a major reformulation.

At the same time, many interesting structures consist of only *few* rectangles and boundary lines, with quite different mode profiles and working principles. These are the subject of the subsequent chapters.

4 Numerical WMM assessment

The calculations reported in the following sections intend to characterize the performance of the WMM approach. Due to the lack of available analytical solutions, we necessarily resume to a comparison with published results. The WMM mode fields are to be employed later for evaluating perturbation expressions or in the framework of coupled mode theory. Hence emphasis is put not only on propagation constants, but on mode profiles as well, where comparison of field shapes is the much more sensitive test. Adhering to the continuous development of the method, Section 4.1 starts with semivectorial simulations from Ref. [73]. Fully vectorial mode analysis as in Ref. [74] is the subject of Section 4.2, while Section 4.3 reports on our simulations [80, 81] for a number of less conventional composite structures.

4.1 Semivectorial analysis

The following standard reference examples are semiconductor rib waveguides with comparably large refractive index contrasts between the guiding film and the surrounding air. Due to the prospectively small mode field strength at the rib flanks, violation of continuity conditions becomes less relevant, and the semivectorial approximation can be expected to yield adequate results. This is verified in the next two sections. While these examples deal only with fundamental modes, computing higher order modes allows the characterization of a directional coupler and a multimode waveguide in Sections 4.1.3, 4.1.4.

4.1.1 Benchmark rib waveguides (I)

Table 4.1 summarizes the parameters of three rib waveguide geometries which have been widely used to compare different numerical methods for mode calculations [139, 140, 141, 58, 71, 70, 67, 102]. For Table 4.2, we extended the summary of previously published results from [102] by values from [141, 70, 67] and added a line with the WMM effective mode indices.

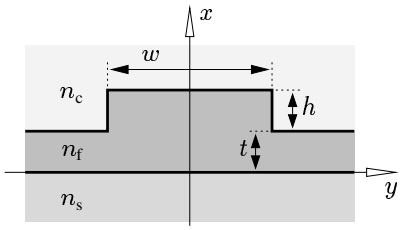

	n_s	n_f	n_c	$w/\,\mu$m	$h/\,\mu$m	$t/\,\mu$m
(i)	3.34	3.44	1.0	2.0	1.10	0.20
(ii)	3.36	3.44	1.0	3.0	0.10	0.90
(iii)	3.435	3.44	1.0	4.0	2.50	3.50

Table 4.1: Sample geometry parameters. The modeled vacuum wavelength is $\lambda = 1.55\ \mu$m.

For waveguides (i) and (ii) the WMM agrees remarkably well with the other approaches, especially with the supercomputer-results FDM_2 from [102], while for geometry (iii) the WMM mode indices are slightly larger. For waveguide (iii), note the perfect agreement between the WMM and the spectral index method SI. According to a remark in [102], a reason may be the limited computational window of the finite difference treatment (width in the y-direction: FDM_1: $12.7\,\mu$m with exponential decay [139], BPM_1, BPM_2, FDM_2: $16\,\mu$m with zero boundary condition [71, 70, 102]). Ref. [70] contains a figure with the corresponding *field* profile on the $16\,\mu$m window. The field looks like being squeezed between the window boundaries. Results from a variety of other vectorial and semivectorial methods concerning structure (i) are collected in

	TE			TM		
	(i)	(ii)	(iii)	(i)	(ii)	(iii)
FDM_1	3.38693	3.39544	3.43681	3.38674	3.39059	3.43677
SI	3.38874	3.39527	3.43690	3.38788	3.39032	3.43684
VM	3.38841	3.39544	3.43674	3.38766	3.39162	3.43668
BPM_1	3.38871	3.39547	3.43680	3.38792	3.39069	3.43677
BPM_2	3.38876	3.39556	3.43681	3.38799	3.39071	3.43677
BPM_3	3.38847	3.3958	3.4360	3.38865	3.3893	3.4367
FDM_2	3.38866	3.39534	3.43678	3.38787	3.39064	3.43674
WMM	3.38866	3.39527	3.43690	3.38780	3.39061	3.43685

Table 4.2: Modal effective indices β/k for the waveguides of Table 4.1. WMM-results are compared with previously published values (in chronological order): FDM_1: finite difference method by Stern [139], SI: spectral index method by Stern, Kendall and McIlroy [141], data from [70], VM: variational approach by Huang and Haus [58], BPM_1, BPM_2, BPM_3: finite difference beam propagation by Liu, Yang, and Yuan [71], by Liu and Li [70], and by Lee and Voges [67], FDM_2: finite difference approach by Noro and Nakayama [102].

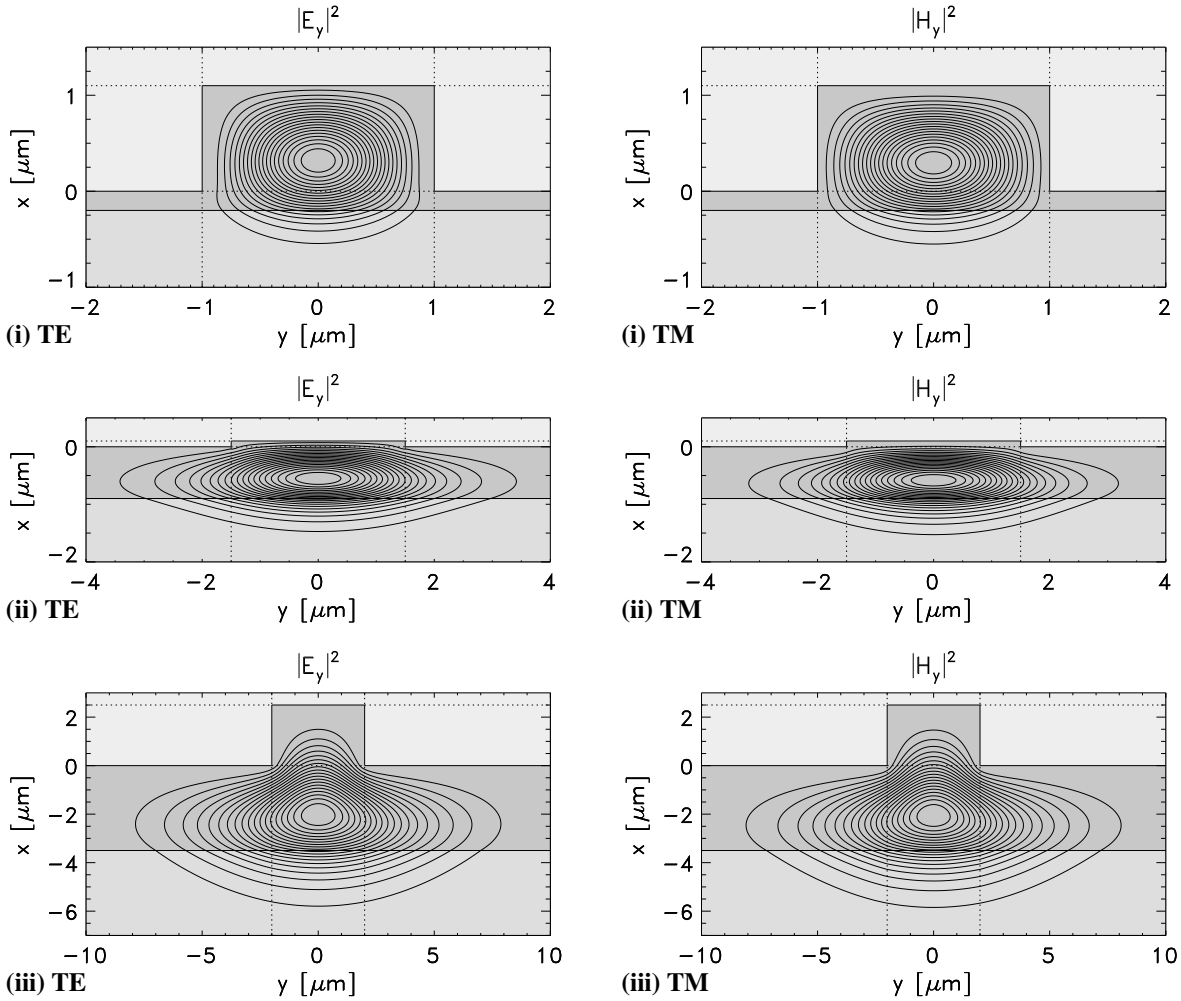

Figure 4.1: Modal field intensities for the sample structures with parameters of Table 4.1. Contour levels are spaced by 5% of the maximum field intensity. Note that the clippings from the waveguide cross section are chosen for displaying purposes only, the WMM fields are defined for the entire x-y-plane. Horizontal and vertical lines indicate the refractive index profile and its splitting into rectangular sections.

[88]. The authors give the value 3.388687 for the TE fundamental effective mode index, obtained by a fully vectorial finite difference calculation on a dense mesh. The WMM result deviates only in the sixth digit.

Figure 4.1 shows intensity contours for the fundamental TE and TM modes. The reader may compare with the plots in [102]. There is good agreement, except for the slightly wider spread WMM contours for guide (iii). The WMM-calculations for these structures were performed with equal parameters for the spectral discretization. We have set $\alpha_{\max} = 3$, $N_\alpha = 30$, and $d = 0.01$, for all rectangles and subsets of trial functions. This resulted in mode fields which are constructed from 887 (888), 890 (897), 854 (852) trial functions, for guides (i), (ii), (iii) and TE (TM) polarization. For test purposes, symmetry with respect to $y = 0$ was *not* imposed by the selection of the trial functions. Coefficients for antisymmetric trial functions in the centered rectangles were computed approximately zero, while corresponding values on both sides of the symmetry plane turned out to be equal, as expected.

4.1.2 Benchmark rib waveguides (II)

Table 4.3 lists mode indices for another frequently investigated rib waveguide geometry [159, 114, 115, 139, 1, 64, 44]. It considers ribs of equal width, etched with varying depth from the same film. Again we find good agreement between the WMM and previous methods, especially with the vectorial approach FDM_2 [44].

$t/\,\mu$m	0.0	0.1	0.2	0.3	0.4	0.5	0.6	0.7	0.8
FEM_1	3.41200	3.41220	3.41235	3.41255	3.41285	3.41315	3.41365	3.41410	3.41475
FDM_1	3.41188	3.41200	3.41217	3.41240	3.41271	3.41310	3.41358	3.41415	3.41484
FEM_2	3.40970	3.40971	3.41003	3.41025	3.41057	3.41097	3.41148	3.41210	3.41298
FEM_3	3.41194	3.41209	3.41224	3.41247	3.41278	3.41312	3.41358	3.41414	3.41480
FDM_2	3.41200	3.41211	3.41226	3.41247	3.41275	3.41311	3.41355	3.41408	3.41472
WMM	3.41204	3.41214	3.41229	3.41250	3.41277	3.41312	3.41356	3.41409	3.41473

Table 4.3: TE mode effective indices β/k for rib waveguides as sketched beside Table 4.1 with parameters $w = 3.0\,\mu$m, $h = 1.0\,\mu\text{m} - t$, $\lambda = 1.15\,\mu$m, $n_s = 3.40$, $n_f = 3.44$, $n_c = 1.0$. FEM_1: vectorial finite element method by Rahman and Davies [115] (data from [44]), FDM_1: semivectorial finite difference method by Stern [139], FEM_2, FEM_3: vectorial finite element methods by Abid et. al. [1] and Koshiba et. al. [64], FDM_2: vectorial finite difference approach by Hadley and Smith [44], WMM: the present method.

Some of the corresponding mode profiles are shown in Figure 4.2. For larger etching depth, slight field irregularities remain close to the artificial rectangle boundaries in the substrate layer (if contours for $|E_y|^2$ were drawn, this would not be visible). Nevertheless, the fields look reasonable, the irregularities disappear with finer spectral discretization. The fields are calculated with parameters $\alpha_{\max} = 3$, $N_\alpha = 30$, and $d = 0.01$. Symmetry with respect to $y = 0$ is explicitely imposed for this and all following examples. For $t = 0.5\,\mu$m, the depicted TE mode function consists of 760 trial functions with 492 independent coefficients.

	TE					TM				
$t/\,\mu$m	0.1	0.3	0.5	0.7	0.9	0.1	0.3	0.5	0.7	0.9
MTRM	0.3019	0.3110	0.3270	0.3512	0.3883	0.2674	0.2751	0.2890	0.3107	0.3455
WMM	0.3024	0.3112	0.3268	0.3508	0.3881	0.2676	0.2759	0.2892	0.3102	0.3451

Table 4.4: Normalized mode effective indices B for rib waveguides with parameters as given for Table 4.3. MTRM: Results from the modal transverse resonance method by Sudbø, from [159].

In a recent review article [159], these ribs with varying etching depth were chosen for a benchmark test. Among a variety of other vectorial and semivectorial approaches, the author considered the Modal Transverse Resonance Method MTRM [145] (Mode Matching Method) to be the most reliable for these waveguides. Table 4.4 compares effective mode indices from [159] with WMM values, normalized as $B = ((\beta/k)^2 - n_s^2)/(n_f^2 - n_s^2)$. Results from other methods regarded in [159] as reliable do not deviate by more than 0.001 from the MTRM. The WMM mode indices, computed with the moderate spectral discretization noted above, fall within this limit as well.

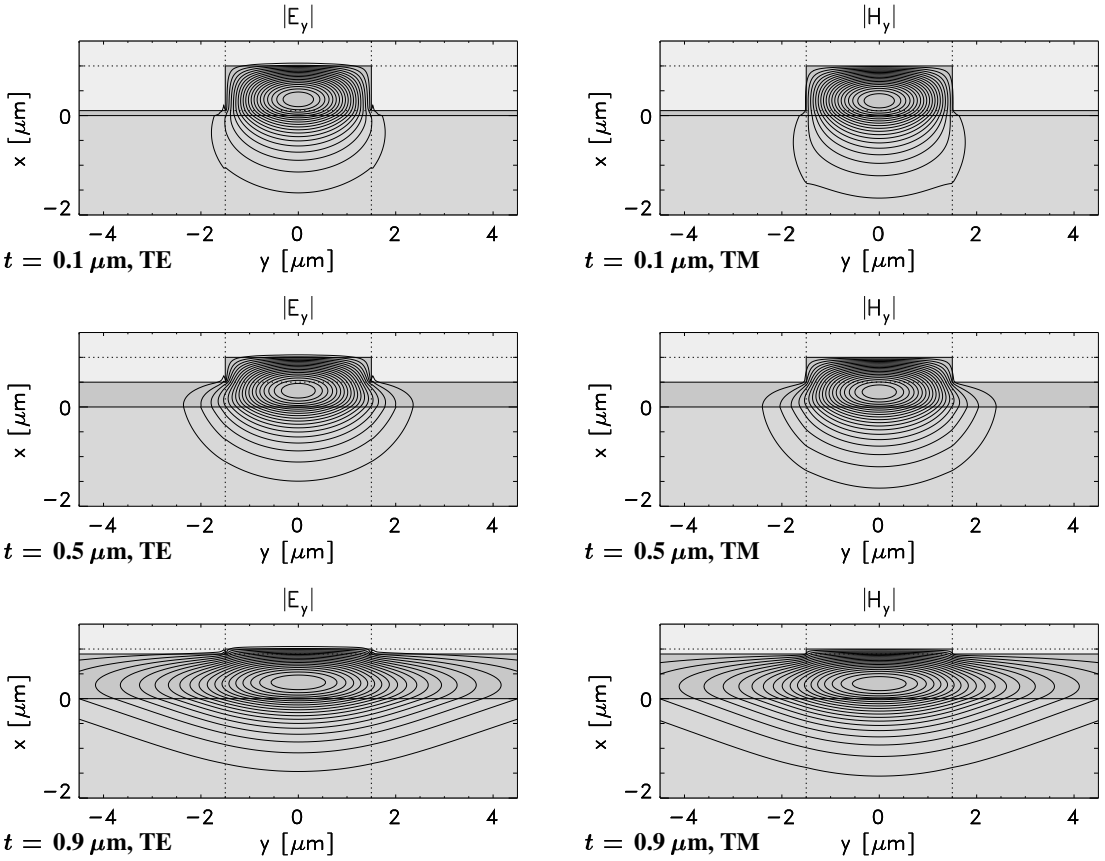

Figure 4.2: Fundamental mode fields for rib waveguides with varying etching depth (t: remaining film thickness) and parameters as given for Table 4.3. The contour levels are spaced by 5% of the maximum field.

4.1.3 Slightly etched coupler

Two parallel rib waveguides on the same film may be regarded as the central part of a directional coupler device. In [102] such a coupler structure made of two waveguides of type (ii) in Table 4.1 has been investigated. Figure 4.3 shows mode intensity contours for the ribs at a distance of $1\,\mu$m.

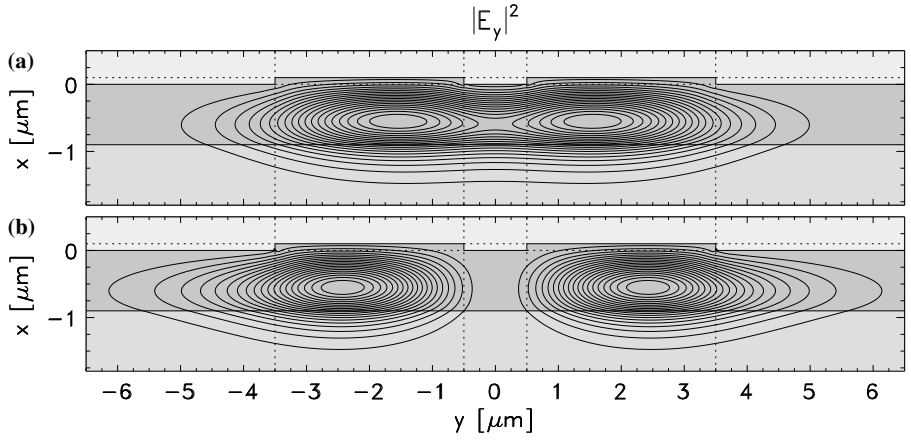

Figure 4.3: Intensity contours for the symmetric (a) and antisymmetric (b) fundamental TE supermode of a directional coupler formed by two waveguides with the parameters of geometry (ii) in Table 4.1. Separation of the ribs is $1\,\mu$m.

The semivectorial WMM program yields $13.76627\,\mu\text{m}^{-1}$ ($13.75944\,\mu\text{m}^{-1}$) and $13.76427\,\mu\text{m}^{-1}$ ($13.76217\,\mu\text{m}^{-1}$) for the propagation constants β_s (β_a) of the symmetric (antisymmetric) supermodes for a waveguide separation of $1\,\mu$m and $3\,\mu$m, respectively. The corresponding coupling lengths $\pi/(\beta_\text{s}-\beta_\text{a})$ are 0.46 mm and 1.49 mm. This agrees well with the values of 0.45 mm and 1.47 mm given in [102].

4.1.4 MMI waveguide

For the design of multimode-interference (MMI) devices [153, 49, 138, 9, 18, 137, 168, 117], a basic task is the exact calculation of propagation constants and mode fields for *all* guided modes of a multimode rib waveguide. Usually the effective index method is used (eventually combined with an approximate analytic expression for the propagation constants of a broad slab [153, 9]), but under certain circumstances deviations from this approximate approach become relevant [18]. To analyze higher order modes of broad rib waveguides with a rigorous finite difference or finite element method, the large waveguide cross section must be covered with a dense mesh, thus these simulations may be relatively expensive. The spectral index method has been employed [18], but it relies on vanishing fields at the rib surface, so it is of limited applicability. We will therefore consider a single multimode rib as the last example. Since the trial functions already exhibit the appropriate sinusoidal dependence in the guiding region, one can expect our method to yield good results with only a small number of unknowns.

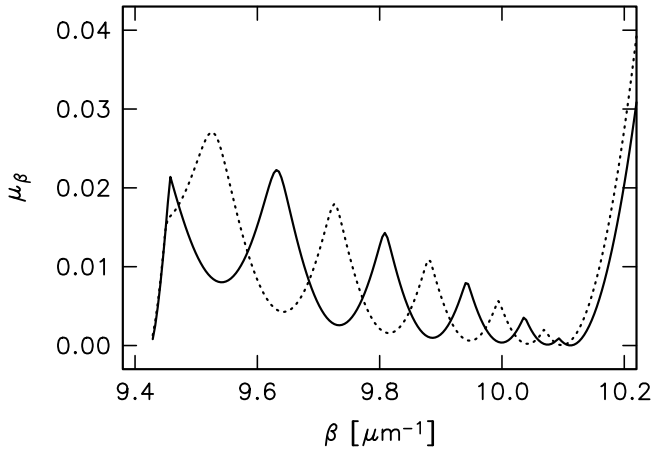

Figure 4.4: Dependence of the optimum field error μ_β on the trial value β for the analysis of a multimode rib waveguide. Each minimum indicates a propagation constant. The continuous (dotted) line corresponds to symmetric (antisymmetric) TM-polarized trial fields. We adopted a typical parameter set for magnetic garnets, a YIG rib on a GGG substrate [126]: $w = 10.0\,\mu$m, $h = 0.5\,\mu$m, $t = 0.0\,\mu$m, $\lambda = 1.3\,\mu$m, $n_s = 1.95$, $n_f = 2.3$, $n_c = 1.0$ (see Table 4.1).

Such a multimode structure serves best to illustrate the behaviour of the WMM error function. Figure 4.4 shows the remaining error $D_\beta(\boldsymbol{a})$ in the field on the rectangle boundaries with the optimum vector $\boldsymbol{a}$ of coefficients inserted for each trial value β. The functions for symmetric and antisymmetric trial fields consist of sections with parabolic appearance, each centered around a propagation constant at its minimum. Thus, after an initial bracketing, the propagation constants can be fixed efficiently with only a very small number of function evaluations [112]. The domain with this piecewise-parabolic behaviour is limited by the propagation constant $10.11653\,\mu\text{m}^{-1}$ of the corresponding planar waveguide. For larger β-parameters, the monotonous increase of both curves (as visible in Figure 4.4) continues. The data is calculated with a spectral discretization given by $\alpha_{\max} = 3$, $N_\alpha = 30$, and $d = 0.01$.

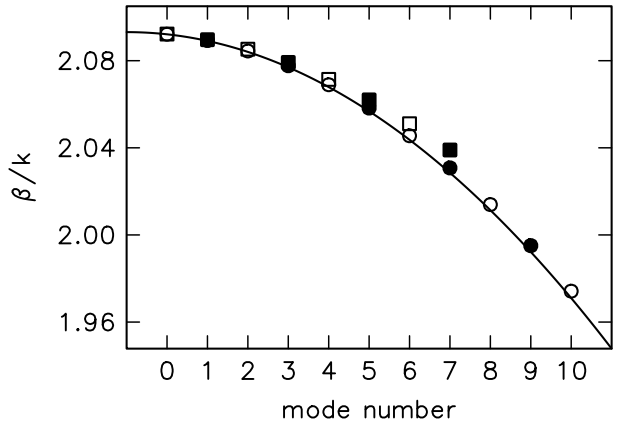

Figure 4.5: TM effective mode indices of two multimode rib waveguides versus the number of zero lines of the mode function in the lateral direction. Circles indicate mode indices for a deeply etched structure with $h = 0.5\,\mu$m, $t = 0.0\,\mu$m, rectangles show values for a less confining waveguide $h = 0.1\,\mu$m, $t = 0.4\,\mu$m; other parameters are as given for Figure 4.4. Open (filled) symbols correspond to symmetric (antisymmetric) modes. The line shows the levels given by Eq. (4.1).

For the totally etched structure ($t = 0$), the WMM finds 11 guided TM-modes. As illustrated by Figure 4.5, the dependence of the propagation constants on the mode number is well approximated [153, 9, 18] by the formula

$$n_\nu = n_\mathrm{p} - \frac{\lambda^2(\nu+1)^2}{8n_\mathrm{p}w^2}, \tag{4.1}$$

where n_ν is the effective mode index of mode number ν and $n_\mathrm{p} = 2.0931$ the effective index of the equivalent planar waveguide.

According to Figure 4.5 this simple expression is no longer valid for a less deeply etched rib. The modes are less confined and some of the higher order modes are cutoff, with the cutoff value given by the planar propagation constant of the outer slab of thickness t. The reader may compare with the more detailed discussion in [18].

Finally, Figure 4.6 shows a series of mode intensity plots for this structure. It should supply some evidence for the ability of the WMM to approximate fundamental as well as higher order modes.

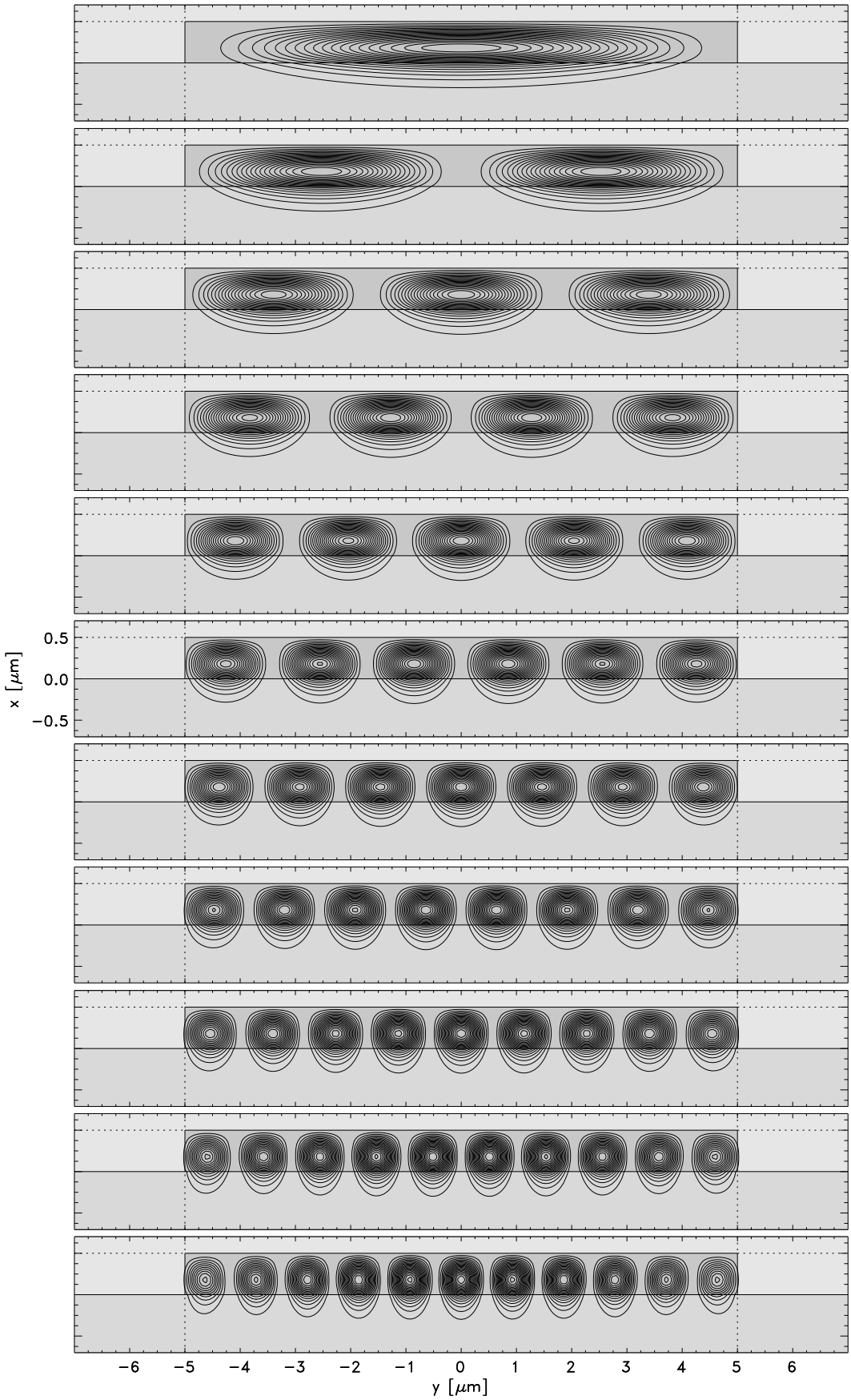

Figure 4.6: Field intensity plots for the guided TM-modes of a broad rib waveguide as prescribed by the parameters of Figure 4.4. The contours correspond to the square $|H_y|^2$ of the transverse magnetic field.

4.2 Fully vectorial analysis

The first two examples of this section have been chosen to characterize the behaviour of the vectorial WMM in situations where a semivectorial simulation tool is definitely insufficient, while the last repeats the simulation of rib waveguide (i) from Section 4.1.1, now without resorting to the semivectorial approximation.

4.2.1 Consistency of fully vectorial calculations

The first example is intended to provide a consistency check for the implemented algorithms. The structure consists of a single rib of increased refractive index on a substrate surface. It is simulated twice, first with the substrate surface parallel to the y-axis of the simulation tool, second with this plane parallel to the x-axis (see Figure 4.7).

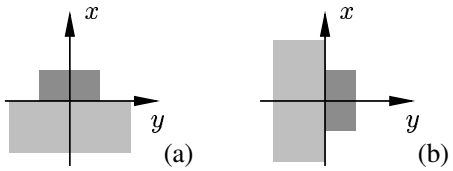

Figure 4.7: Simple strip waveguide, simulated in a horizontal (a) and a vertical configuration (b).

Figure 4.8 shows intensity profiles for the fundamental mode. As expected, the fields from calculations in the two configurations are connected exactly by the rotation $H_x \to H_y$, $H_y \to -H_x$. Note that this result is obtained by exchanging the values for the refractive indices and the layer surfaces only. No parameters have to be adjusted, which assume a different field behaviour in the transverse directions. For the fields displayed, a spectral discretization $d = 0.01$, $\alpha_{\max} = 3.0$, $N_\alpha = 30$ results in a number of 1280 unknown coefficients. Modal symmetry is not imposed, but emerges from the calculations, thus half the coefficients are computed (not set) to be zero.

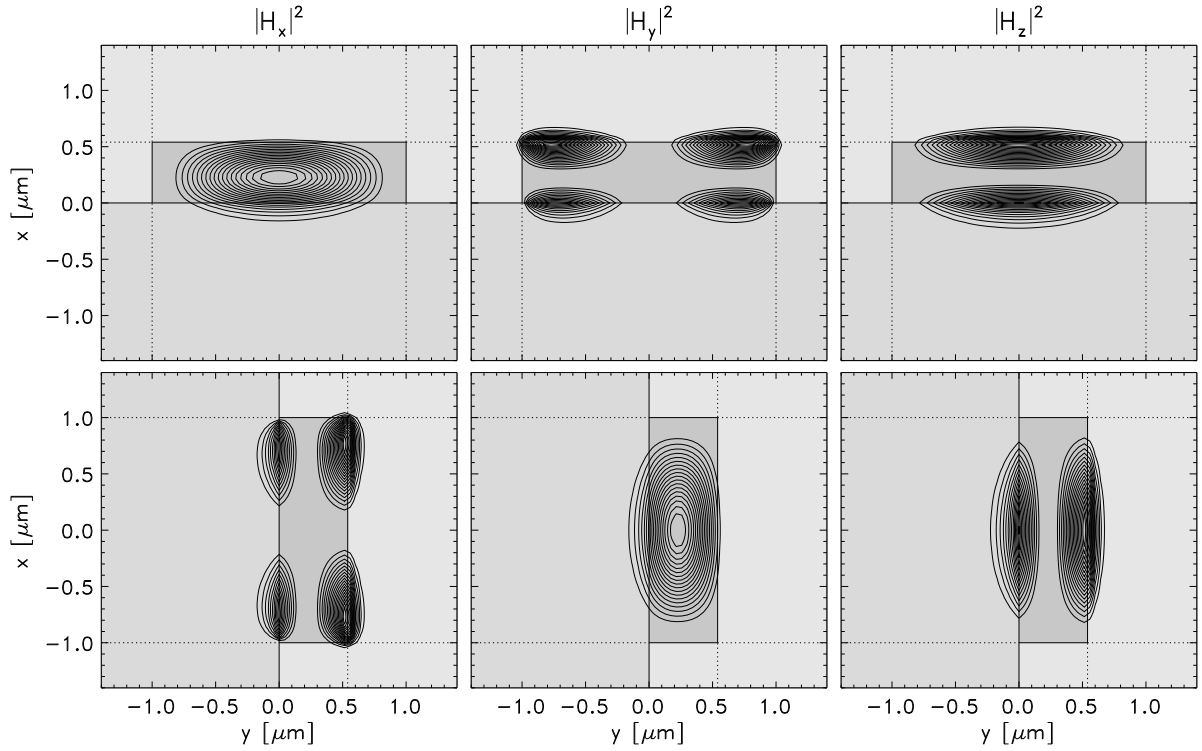

Figure 4.8: Modal intensity profiles for the simulation configurations of Figure 4.7, with parameters $n_s = 1.95$, $n_f = 2.302$, $n_c = 1.0$, $h = 0.54\,\mu$m, $w = 2.0\,\mu$m, $t = 0$, $\lambda = 1.3\,\mu$m (see the inset of Table 4.1).

Figure 4.9 illustrates the behaviour of the least squares error function μ_β in this fully vectorial case. It consists of parabolic sections, each with a valid propagation constant at the minimum. The waveguide supports four guided modes with a definite symmetry with respect to $y \to -y$. A symmetric field ansatz (see Section 1.1.3) yields the hybrid modes TE_0 and TM_1, classified by the dominant components and their vertical nodal lines. An ansatz of odd symmetry gives the lowest order TM and first order TE mode. If no symmetry is prescribed, the least squares error function shows minima corresponding to all four modes.

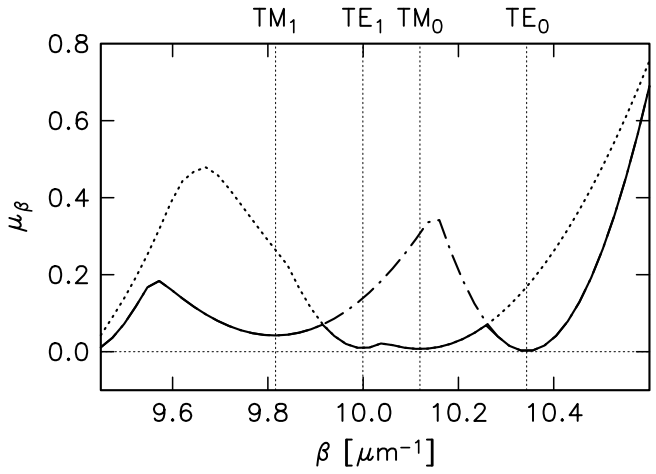

Figure 4.9: For a raised strip waveguide according to Figure 4.8: remaining least squares error μ_β versus the trial value β for the propagation constant. The continuous line corresponds to fields without prescribed symmetry, the dash-dotted and dotted lines (partially shadowed) to fields with even and odd symmetry (see the text). The propagation constants $\beta/\,\mu\mathrm{m}^{-1}$ indicated by the minima locations are 10.3432 (TE_0), 10.1192 (TM_0), 9.9994 (TE_1), and 9.8162 (TM_1).

The propagation constants mentioned in the caption of Figure 4.9 are stable with respect to the choice of the normalization expression (3.12), with respect to the choice of the two basic fields for the vectorial mode problem, and with respect to refinement of the spectral discretization. The calculations with prescribed symmetry involve about 650 unknowns, where identifying the fundamental vectorial mode takes about 10 min and 6 MB of memory on a 99 MHz HP-735 computer. Switching to the semivectorial approximation reduces this to about 1 min and half the number of unknowns, and yields a value of $10.3442\,\mu\mathrm{m}^{-1}$ for the propagation constant.

4.2.2 Square waveguide

From [144] we adopted the second sample structure, a square guiding core surrounded by air as sketched in Figure 4.10.

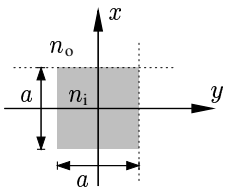

Figure 4.10: Square waveguide cross section. Parameters of the simulated structure are height and width of the core $a = 1.0\,\mu$m, wavelength $\lambda = 1.5\,\mu$m, and core and cladding refractive indices $n_i = 1.5$, $n_o = 1.0$.

The spectral discretization $d = 0.01$, $\alpha_{\max} = 3.0$, $N_\alpha = 30$ leads to a mode function which is a superposition of 554 trial functions. Figure 4.11 shows the corresponding field profiles. We have selected one of the two orthogonal fundamental modes with a field ansatz of proper symmetry. An ansatz with reversed symmetry yields the same propagation constant $\beta = 5.3212\,\mu\mathrm{m}^{-1}$ and identical field profiles, apart from changes due to the transformation $x \to y$, $y \to -x$.

For a more quantitative illustration of the mode shape we have evaluated the mode field on a series of horizontal and vertical lines in the x-y-plane, as displayed in Figures 4.12, 4.13. The maximum amplitudes of the dominant transverse electric and magnetic components E_y, H_x can be read from Figure 4.12. These maximum levels should be kept in mind when examining the fields at the edges of the core. Note that the minor fields E_x, H_y are zero along both transverse coordinate axes due to the prescribed symmetry.

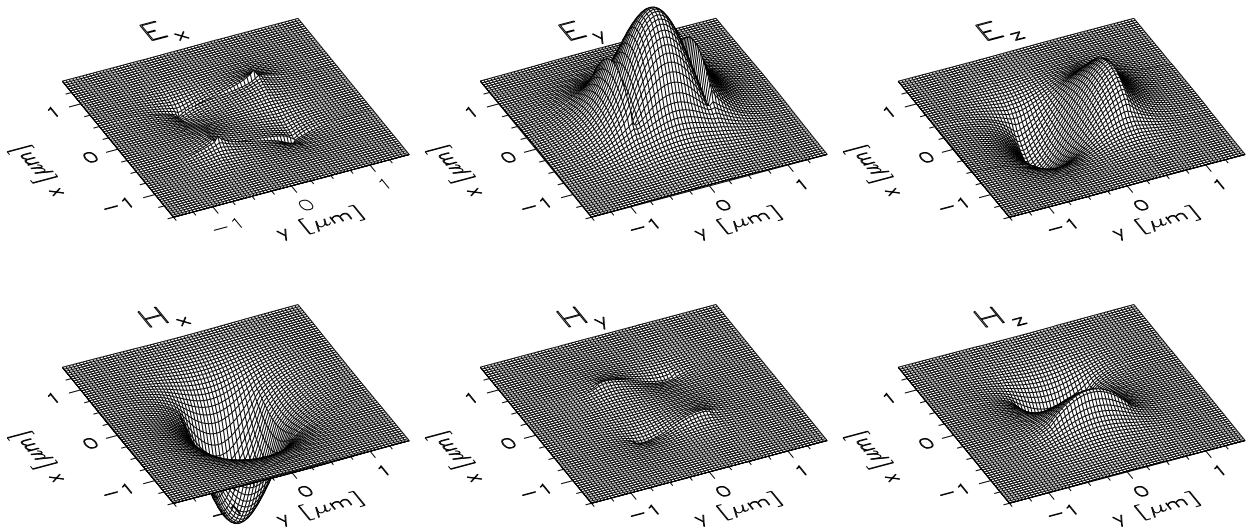

Figure 4.11: Amplitudes of the electric (top row) and magnetic field components (bottom row) plotted versus the cross section plane, for the square waveguide of Figure 4.10. Values are comparable within each row.

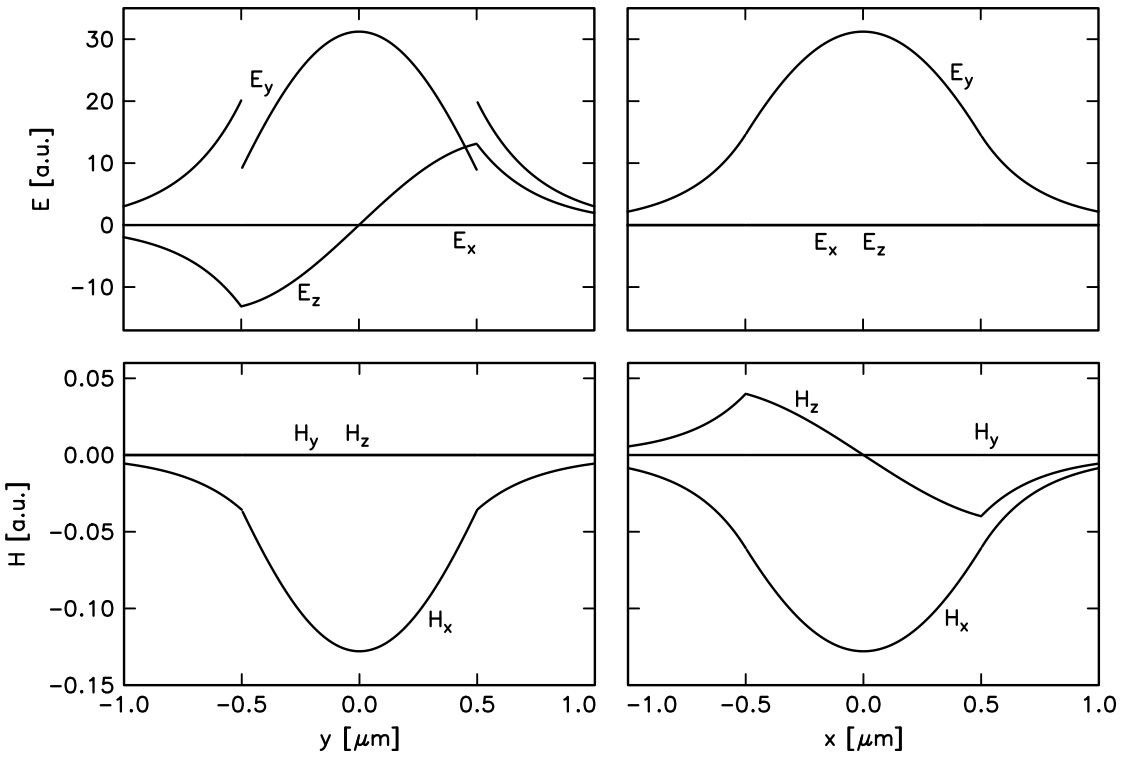

Figure 4.12: For the square waveguide of Figure 4.10: electric (top row) and magnetic (bottom row) field amplitudes evaluated on the y-axis (left column) and on the x-axis (right column).

Figure 4.13 allows for a detailed inspection of the remaining mismatch on the boundaries of the basic rectangular sections. On the lines $x = a/2$ and $y = a/2$ we have plotted two curves for each field component, one where the fields on the core rectangle are evaluated (continuous curves), and one for the field on the adjacent rectangle outside the core (dotted curves). Apart from the normal components of the dielectric displacement, the continuous and dotted curves should always coincide, while for E_x on the horizontal section $x = a/2$, $-a/2 < y < a/2$ and for E_y on the vertical section $y = a/2$, $-a/2 < x < a/2$ the dotted curve should be 2.25 times the level of the continuous curve. As discussed in Section 1.1.5, at the waveguide corners these conditions lead to divergent fields. At least qualitatively, the main features of this behaviour can be approximated with a finite number of exponentials. The reader should compare the upper right quadrant of the top left inset of Figure 4.13 with a corresponding plot in Ref. [144] (note the additional

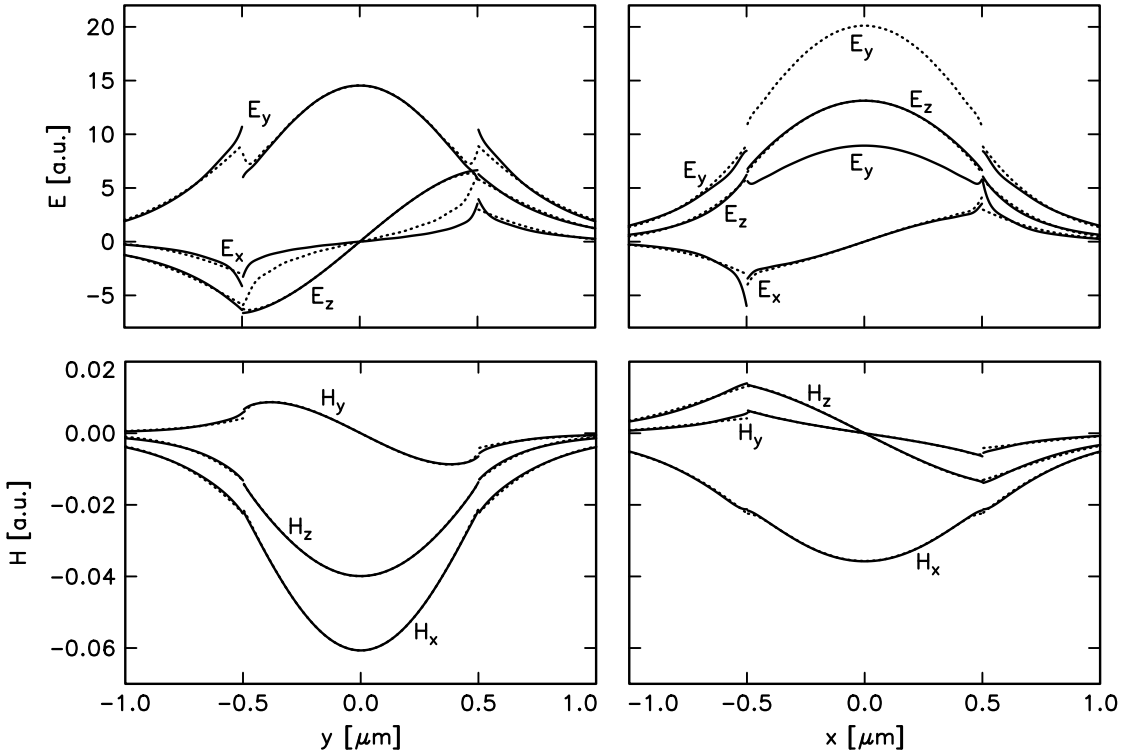

Figure 4.13: For the square waveguide of Figure 4.10: electric (top row) and magnetic (bottom row) field amplitudes evaluated on the horizontal line at the top edge of the core (left column) and the vertical line at the right edge (right column). Continuous curves correspond to locations $(x, y) = (a/2 - \delta, y)$ or $(x, a/2 - \delta)$, respectively, while dotted curves are assigned to coordinates $(a/2 + \delta, y)$ and $(x, a/2 + \delta)$, for a small deviation δ.

boundary conditions). If not necessarily factorizing but numerically applicable divergent solutions of the wave equation in such a corner would be available, it should be possible to incorporate them into the WMM. Approximate analytical solutions may be sufficient, e.g. the fields given in [20].

4.2.3 Benchmark test, fully vectorial

A deeply etched rib, structure (i) of Table 4.1, shall be employed as the last vectorial example. Table 4.5 summarizes effective mode indices for the fundamental mode from a few reference methods and the semivectorial and vectorial WMM. Further results for this waveguide are collected in Table 4.2 and in Refs. [88, 86, 102].

	β/k	B
SFDM	3.388646	0.48278
TRD	3.388690	0.48325
SWMM	3.388659	0.48291
$VFDM_1$	3.388687	0.48319
$VFDM_2$	3.388698	0.48330
MTRM	3.388698	0.48330
VWMM*	3.388669	0.48301
VWMM	3.388573	0.48214

Table 4.5: Effective mode indices β/k and normalized propagation constants $B = ((\beta/k)^2 - n_s^2)/(n_f^2 - n_s^2)$ for the benchmark waveguide. VFDM: vectorial finite difference calculations by P. Lüsse et al. [88] ($VFDM_1$) and [86] ($VFDM_2$); MTRM: vectorial mode transverse resonance method by A. Sudbø[145], data from [86]; TRD: semivectorial transverse resonance diffraction method by T. Rozzi et al. [120]; SFDM: semivectorial finite difference implementation by P. Lüsse et al. [87]; SWMM: our previous semivectorial wave matching program [73]; VWMM: the present vectorial implementation, VWMM: calculation without the E_x and E_y terms in the mismatch expression Eq. (3.10).*

The first three rows of Table 4.5 contain results of semivectorial calculations. They agree up to the third digit in the normalized propagation constant, and there is very good agreement with the vectorial values from the subsequent rows. Thus the semivectorial approximation, i.e. putting E_x zero, is a good approximation for this waveguide. This can also be concluded from the plots in Figure 4.14, where the amplitudes of the

small components E_x and H_y clearly appear to be negligible. The displayed fields correspond to the last row in Table 4.5. They are composed from a trial function set with 879 unknown coefficients, the spectral discretization parameters are $d = 0.01$, $\alpha_{\max} = 3.0$, and $N_\alpha = 30$.

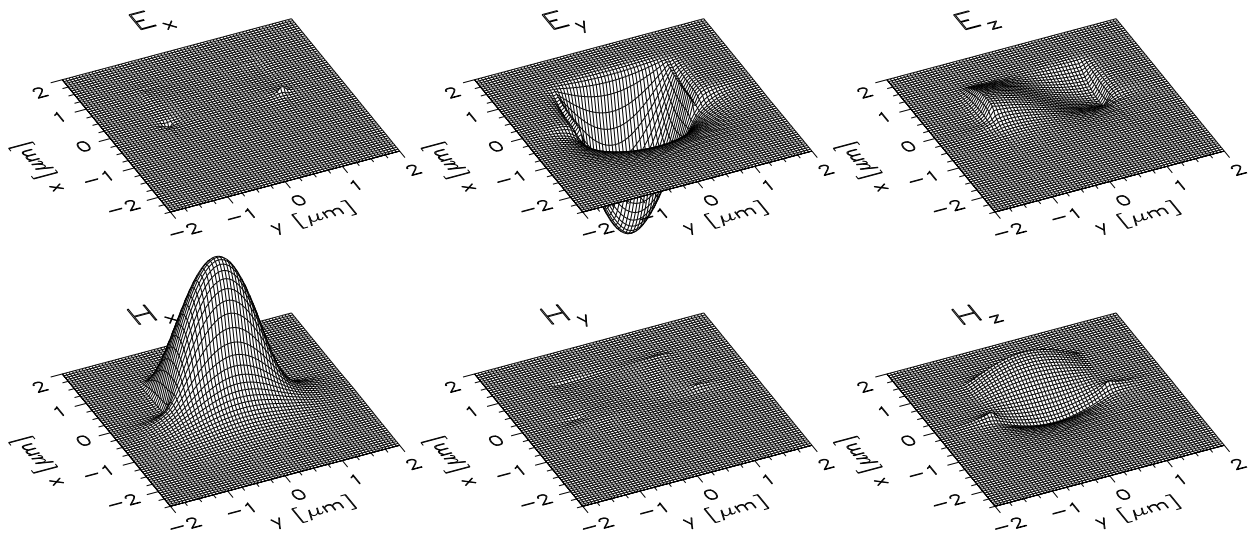

Figure 4.14: Amplitudes of the electric (top row) and magnetic field components (bottom row) plotted versus the cross section plane, for waveguide (i) of Table 4.1. Values are comparable within each row.

Regrettably, there is a noticeable discrepancy between the WMM effective mode index from the last row of Table 4.5 and the previous values. This difference vanishes for the semivectorial WMM program. Therefore a reason may be found in the more irregular shape of the small components, e.g. the divergent peaks at the waveguide edges, where the spectral discretization employed here is less sufficient.

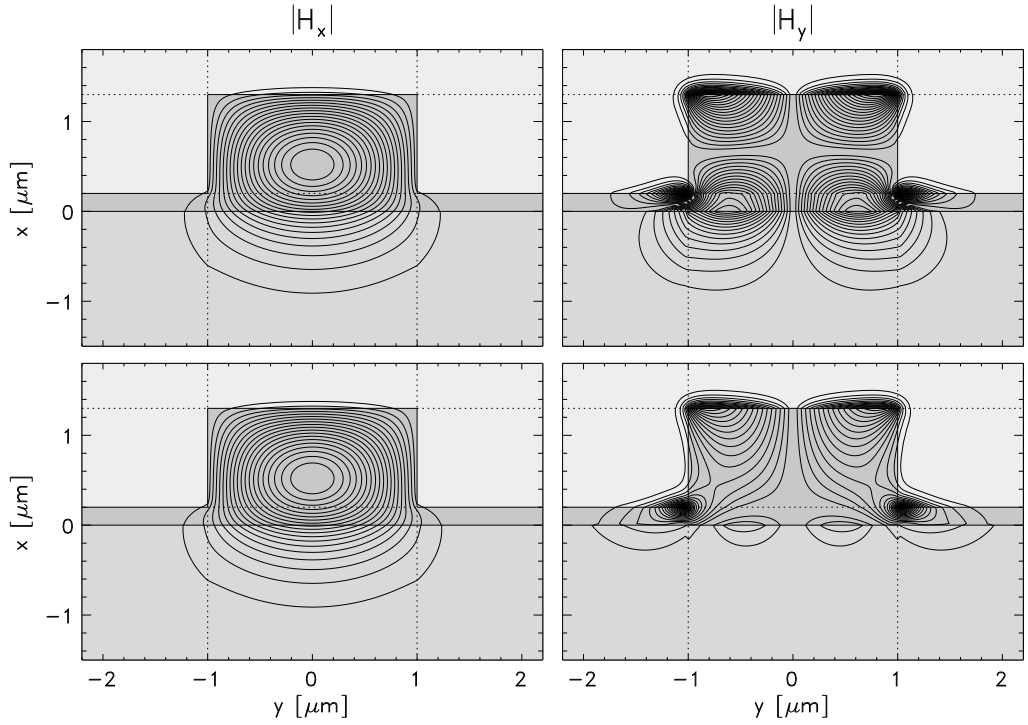

Figure 4.15: Transverse magnetic fields for the waveguide of Table 4.5, from vectorial WMM calculations with error expression (3.10) (top row) and without the E_x and E_y terms in Eq. (3.10) (bottom rom). The contour levels are spaced by 5% of the maximum absolute field, separately for each plot.

As can be seen from the row marked VWMM*, the deviation is significantly reduced, if one modifies the expression for the least squares error in the continuity requirements (cf. Section 1.1.5), such that only continuity of H_x, H_y, H_z, and E_z is explicitely incorporated. Figure 4.15 compares the transverse magnetic components of the corresponding fields. While the dominant component H_x is not visibly influenced, the shape of the minor field H_y changes significantly.

Similar plots in [86] agree well with the bottom row of Figure 4.15. In addition to good agreement of the values for the normalized propagation constants, this recommends the reduced least squares expression as the better choice if one accepts the results taken from [86] as correct. However, there are two reasons to be suspicious about this finding. The finite difference scheme (on which the VFDM_2 value is based) employs the continuity requirements for the three magnetic components and the longitudinal electric component as well. This is correct if the continuity requirements are fulfilled exactly, but probably not in the sense of a balanced approximation of all six fields. Further, for structures with pronounced minor components (e.g. the waveguide of Section 4.2.2), fields computed with the reduced least squares expression show a more irregular appearance, where the error is concentrated in the continuity requirements for the dropped components E_x, E_y.

4.3 Coupler structures

In contrast to the simple raised strip and rib structures discussed before, real integrated optical devices may include more complex cross sections. In this section we therefore investigate applying the WMM to several more involved coupler structures. Due to the need of computing also higher order modes, and due to a usually large relevant part of the waveguide cross section plane, these tasks are difficult for most mode solvers.

4.3.1 Deeply etched coupler

The first example is a conventional two waveguide coupler as sketched in Figure 4.16 with parameters taken from Ref. [113]. Between the two ribs, the film is assumed to be etched less than outside, resulting in strong coupling.

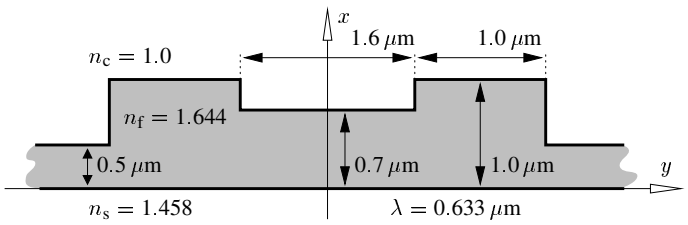

Figure 4.16: Parameters for the two rib waveguide coupler.

The slab waveguide corresponding to the central region (thickness $0.7\,\mu$m, refractive indices 1.458, 1.644, 1.0, wavelength $0.633\,\mu$m) already guides two planar TE and two TM modes, and therefore the rib structure supports more than two modes for each polarization. While in general all these modes contribute to the guided field, only the two fundamental modes will be excited if power is inserted by one single-moded port waveguide. Figure 4.17 illustrates these two modes for TE polarization, each computed with a semivectorial field ansatz of proper symmetry.

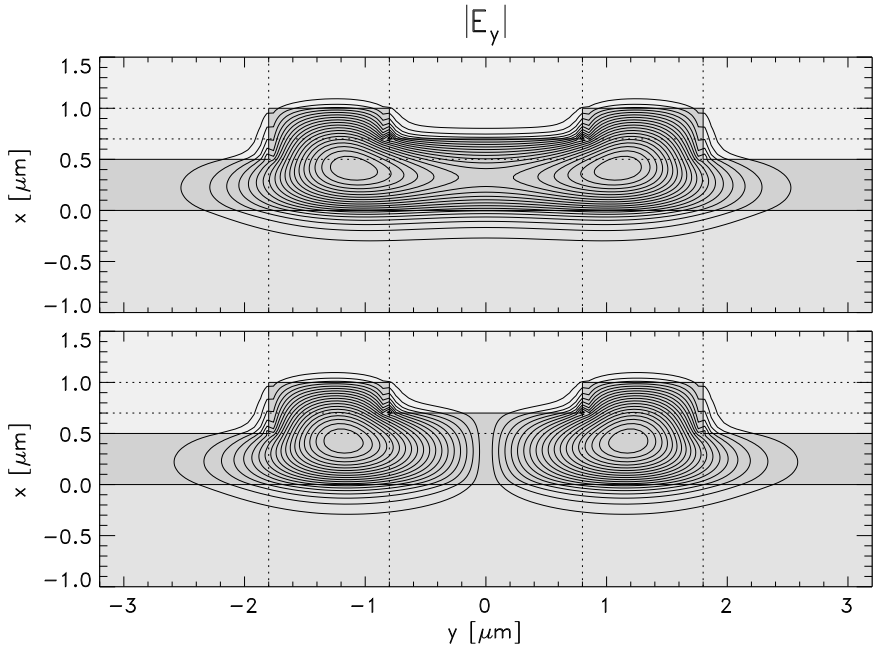

Figure 4.17: Field profiles for the coupler of Figure 4.16. The contours correspond to the dominant component $|E_y|$ of the fundamental modes of even (top) and odd symmetry (bottom).

Their interference results in a periodic transfer of power between the two ribs at a length of $L_c = \pi/(\beta_s - \beta_a)$, where β_s, β_a are the propagation constants of the symmetric and antisymmetric TE supermode. Table 4.6 compares the WMM results with values from Ref. [113].

		EIM	SIM	FEM	WMM
β/k	(s)	1.614021	1.611995	1.611412	1.610794
	(a)	1.612877	1.610369	1.609546	1.609100
$L_c/\,\mu$m		276	194	170	187

Table 4.6: Propagation constants β_s, β_a and coupling length L_c for the coupler of Figure 4.16, computed with the effective index approximation [113] (EIM), with the spectral index method [113] (SIM), a finite element program [113] (FEM), and the semivectorial wave matching method (WMM).

Due to deep etching, the effective index results differ significantly while there is good agreement between the more sophisticated methods. Note that neither the SIM nor the FEM values can be guaranteed to be exact. The former suffer from the assumption of vanishing field at the inner sidewalls of the ribs (cf. Figure 4.17), the latter from a naturally limited mesh (cf. e.g. the benchmark test in Ref. [159]).

4.3.2 ARROW

The second example is not a proper coupler, but has a similar cross section. The dimensions of the antiresonant reflecting optical waveguide (ARROW) [34] as given in Figure 4.18 have been chosen [113] such that for each polarization one of its modes exhibits a large amplitude in the central region between the two small ribs. Figure 4.19 shows the corresponding profiles as computed with the semivectorial WMM.

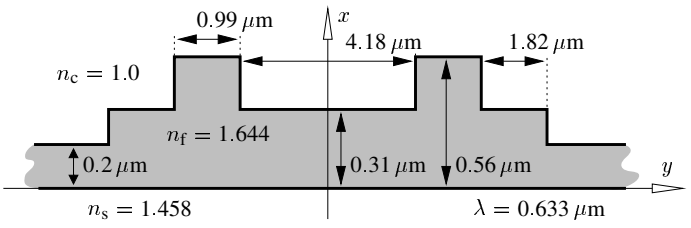

Figure 4.18: ARROW geometry and parameters, data from Ref. [113].

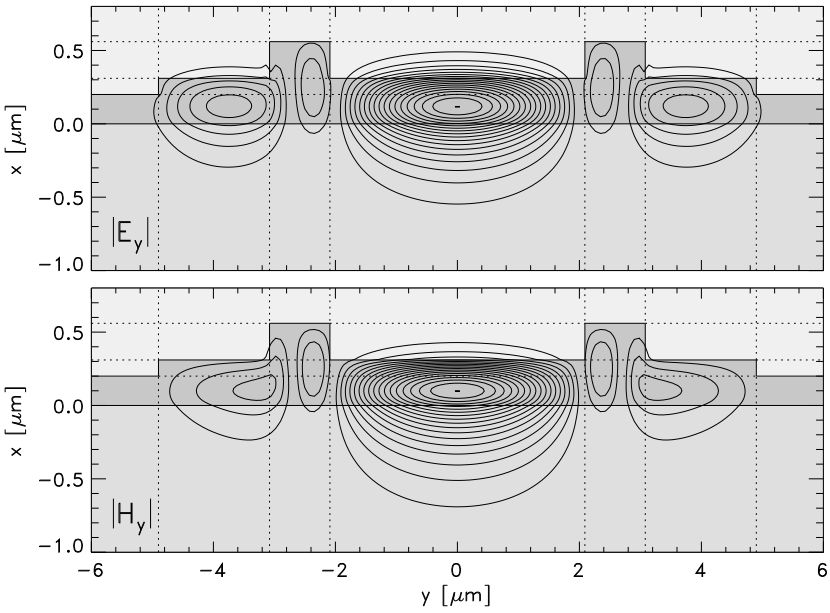

Figure 4.19: Field contours for the dominant components of the relevant TE (top) and TM (bottom) modes for the structure of Figure 4.18.

These modes have propagation constants below the value of the planar waveguide corresponding to the stack of layers in the central region. They are no fundamental modes, but will carry most of the power if the structure is excited e.g. by the field of a fiber focused on the central region.

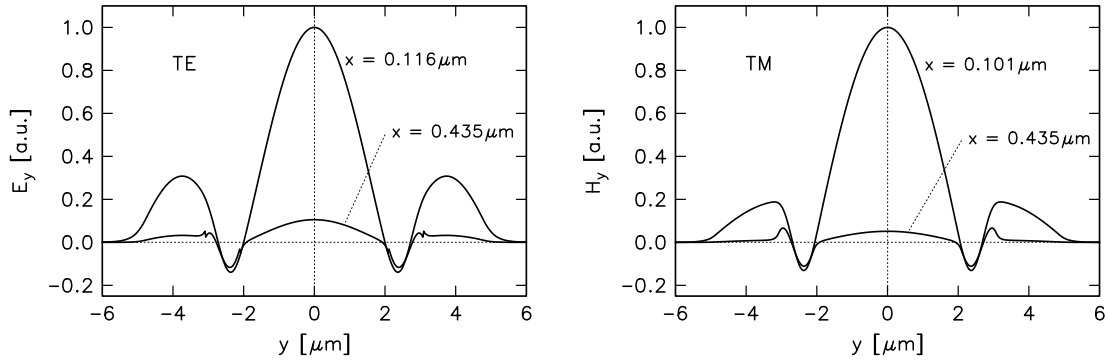

Figure 4.20: Profile cross sections of the dominant field components for the modes of Figure 4.19. E_y (TE mode, left) and H_y (TM mode, right) is evaluated on lines parallel to the y-axis, at the position of the maximum field amplitude ($x = 0.116\ \mu$m for TE, $x = 0.101\ \mu$m for TM) and at half the level of the protruding ribs, at $x = 0.435\ \mu$m.

The mode profile sections shown in Figure 4.20 can be directly compared with analogous plots in Ref. [113]. The good agreement, especially with the fields from the spectral index method, may be explained by the smallness of amplitudes in the regions outside the ribs for $x > 0.31\ \mu$m, where the SIM assumes vanishing fields. The WMM gives access to the correct fields in these regions as well, as shown by the curves in Figure 4.20.

		EIM	SIM	FEM	WMM
β/k	TE	1.534432	1.534115	1.533470	1.534142
	TM	1.507001	1.506904	1.506720	1.506945

Table 4.7: Relevant TE and TM effective mode indices for the ARROW of Figure 4.18. Methods are denoted as in Table 4.6.

Table 4.7 compares propagation constants from different methods. Agreement between the SIM and WMM fields is accompanied by good agreement of the effective mode indices. At the same time, slightly smaller FEM mode indices may be attributed to the limited FEM mesh size (73×109 Points [113]) and to the restriction on a finite computational window.

4.3.3 3D-coupler

Figure 4.21 states the parameters for a three dimensional four waveguide coupler. Details on the proposal, simulation, and fabrication of such a device have been reported in Ref. [41].

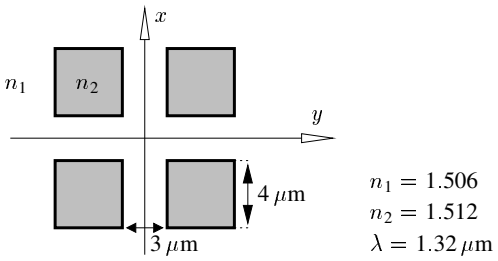

Figure 4.21: 3-D coupler parameters [41].

The cross section may be decomposed into 3×3 inner rectangular regions, therefore the device is fit for a WMM simulation. At the same time, the guiding refractive index is only about 4% higher than the cladding value, and this means somehow extreme conditions for the WMM. Nevertheless, the results are reasonable and agree well with the findings from Ref. [41]. Figure 4.22 shows profiles for the four TE polarized modes of the structure, Table 4.8 compares the corresponding mode indices.

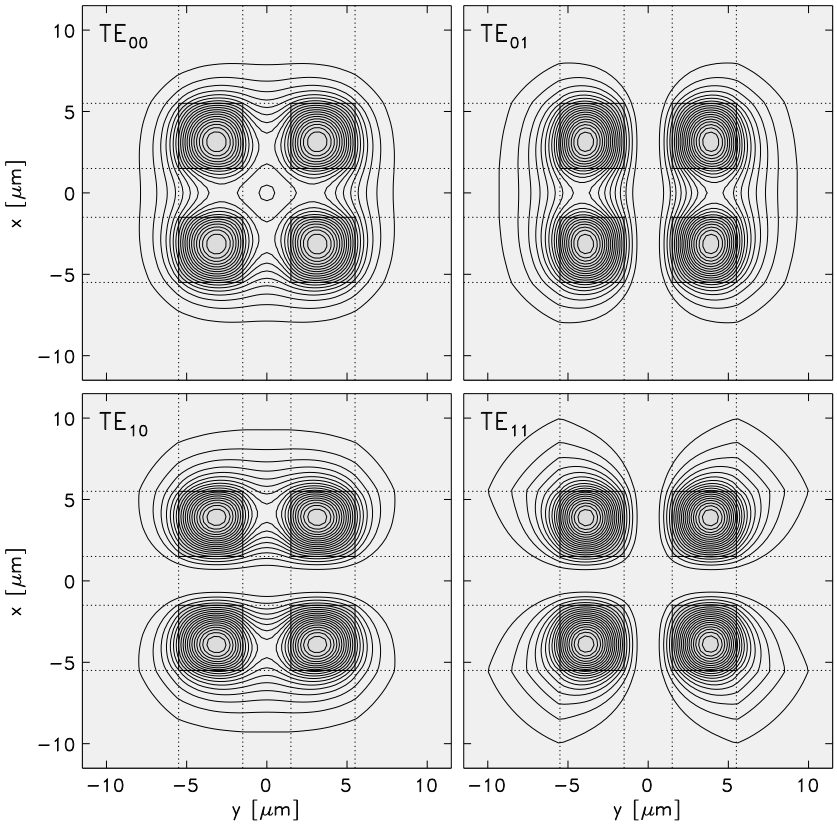

Figure 4.22: Intensity profiles $|E_y|^2$ for the four TE modes of the coupler sketched in Figure 4.21. The mode indices denote the number of horizontal and vertical nodal lines of the dominant E_y component.

The vectorial FEM mode indices are systematically slightly smaller than the values computed with the semivectorial WMM. Explanations may be the remaining error in the WMM field, apparent especially for the lowest order mode in Figure 4.22, or alternatively a narrow FEM computational window. There is also a small qualitative discrepancy: The FEM states exactly equal propagation constants of the two first order TE modes, the WMM predicts slightly different values for the modes with one horizontal respectively vertical nodal line in the dominant component. While due to the symmetry of the problem each TE mode is twofold degenerate with a corresponding TM mode, it is not a priori evident that the first order modes with the nodal line parallel and perpendicular to the direction of the polarization should be degenerate. The latter arguments supports the WMM result.

	β_{00}/k	β_{01}/k	β_{10}/k	β_{11}/k	L_c
VFEM	1.5075807	1.5067966	1.5067966	1.5060266	850 μm
WMM	1.5078966	1.5071085	1.5071092	1.5064697	925 μm

Table 4.8: Effective mode indices β/k and coupling length L_c for the 3-D coupler of Figure 4.21. The line VFEM contains data from a vectorial finite element method [41], WMM are results from our semivectorial calculations.

However, assuming degenerate TE_{01} and TE_{10} modes $\beta_{01} \approx \beta_{10}$ and equal differences $\Delta\beta \approx \beta_{00} - \beta_{10} \approx \beta_{10} - \beta_{11}$, one can define a coupling length $L_c = \pi/\Delta\beta$ for the power transfer between two diagonally opposite waveguides [41]. Values calculated with the corresponding averages are compared in the last column of Table 4.8.

4.3.4 Radiatively coupled waveguides

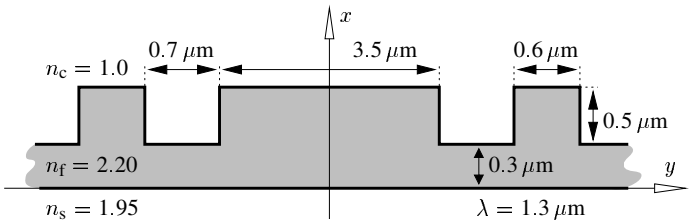

Figure 4.23: Radiatively coupled waveguide structure.

This section covers a three rib waveguide arrangement consisting of two identical outer guides and a broad strip inbetween. Analogous planar configurations and raised strip waveguide based devices will be the subject of Chapter 7. Apart from details of the coupling behaviour, here we focus only on the direct WMM simulation of the coupler as sketched in Figure 4.23. A semivectorial analysis yields the modes shown in Figures 4.24, 4.25.

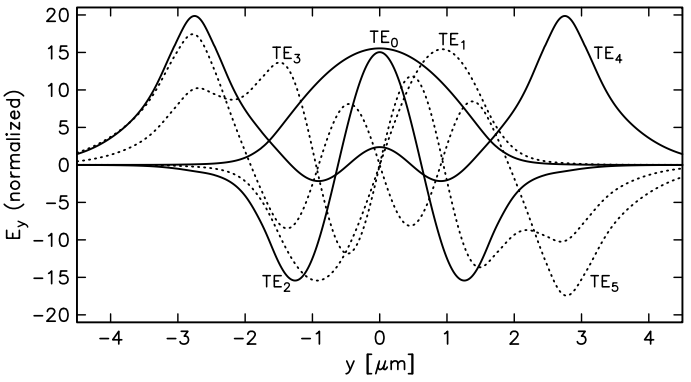

Figure 4.24: Profile cross sections for the six TE modes of the radiatively coupled waveguide structure. E_y is evaluated on a line parallel to the y axis at $x = 0.15$ μm. Continuous lines correspond to modes with even, dotted lines to modes with odd symmetry.

The coupler is to be excited by the single mode of one of the isolated outer waveguides. Figure 4.26 shows its profile. We assume a coupling section of a well defined length L, with the outer waveguides extended to form four input and output ports (cf. Figure 4.28). Let $\phi^a = (\boldsymbol{E}^a, \boldsymbol{H}^a)$ denote the six mode fields of the composed structure, with propagation constants β^a. Analogously ϕ^{l} and ϕ^{r} are the modes of the left and right input respectively output ports, its propagation constant is β_*.

As discussed in Section 1.2, the power transferred to waveguide $j = \mathrm{l}, \mathrm{r}$ at $z = L$ after excitation at $z = 0$ in the left waveguide can be written

$$P_j(L) = \left| \sum_a (\phi^j; \phi^a)(\phi^a; \phi^{\mathrm{l}})\, \mathrm{e}^{-\mathrm{i}\beta^a L} \right|^2 . \tag{4.2}$$

Chiefly those modes with a large overlap with the exciting field contribute to the power transfer. According to Figures 4.25, 4.26, these are the highest order modes, i.e. those with large field amplitudes in the regions

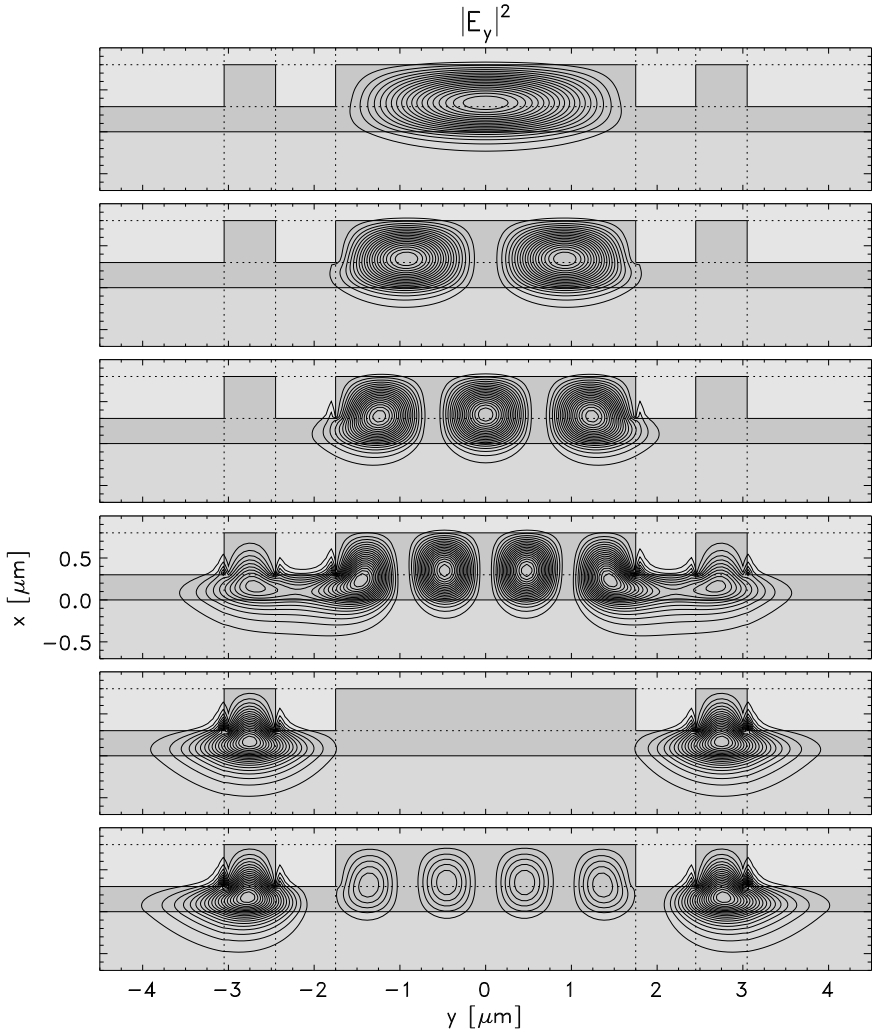

Figure 4.25: Intensity profiles for the TE modes of the coupler prescribed by Figure 4.23. The corresponding propagation constants $\beta/\,\mu\mathrm{m}^{-1}$ are

TE_0: 10.2232,
TE_1: 10.1171,
TE_2: 9.9417,
TE_3: 9.7185,
TE_4: 9.6789,
TE_5: 9.6595,

where the indices denote the number of vertical nodal lines in E_y.

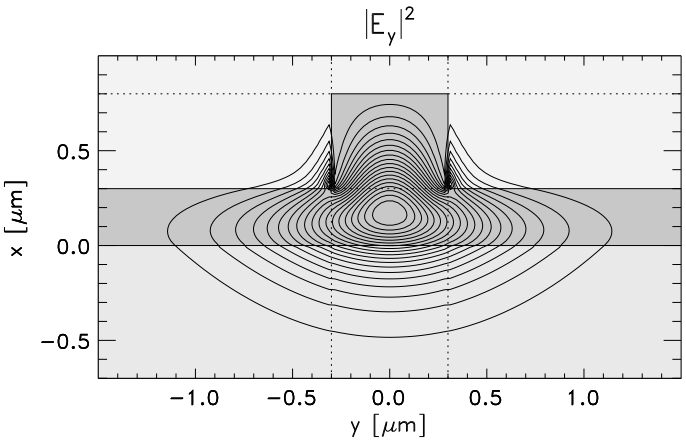

Figure 4.26: Fundamental TE mode of one outer waveguide of the coupler in Figure 4.23. The corresponding propagation constant is $\beta_* = 9.6806\,\mu\mathrm{m}^{-1}$. Note the pronounced discontinuities in E_y at the sidewalls of the deeply etched rib.

of the outer waveguides and with propagation constants close to the level β_*. Together with additional small contributions form the remaining four modes, this results in the beating pattern plotted in Figure 4.27. Coupling between the outer waveguides is a truly multimode interference phenomenon.

For a device length slightly below 1 mm, the power is concentrated in the input waveguide again. Figure 4.28 illustrates the light propagation for this length. For complete power transfer, the device needs a length of about 1.8 mm.

With this structure a problem shows up, which is closely related to that discussed at the end of Section 3.3.

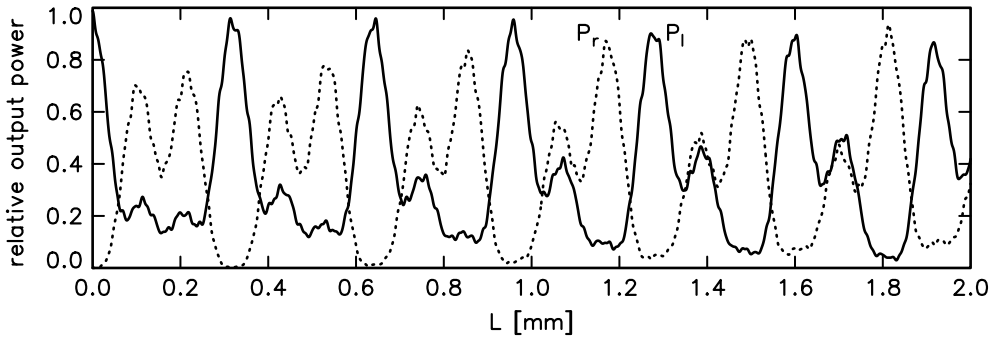

Figure 4.27: For the coupler of Figure 4.23: relative power transfer to the left outer waveguide P_l (continuous line) and to the right outer waveguide P_r (dotted line) versus the length L of the coupling section. The structure is assumed to be excited by the TE mode of the isolated left waveguide.

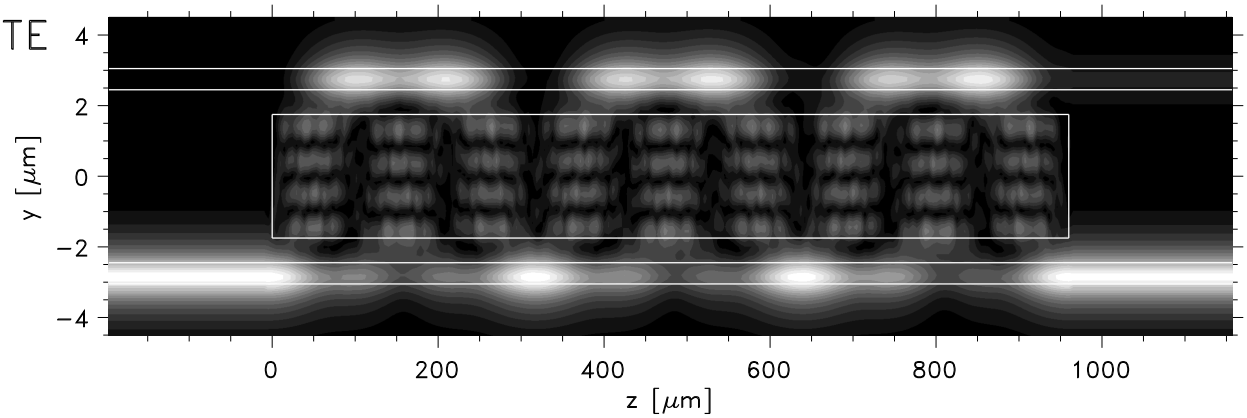

Figure 4.28: TE light propagation through a radiatively coupled waveguide structure with a cross section as given by Figure 4.23, with a coupling section of length $L = 960\ \mu$m. Grey scale levels correspond to the squareroot of the z-component of the Poynting vector, evaluated on the y-z-plane at $x = 0.15\ \mu$m.

Ideally all modes should be orthogonal with respect to the product (1.18) or (1.20). This orthogonality is not enforced by the mode solver, but should emerge if the mode fields are adequately approximated. Indeed, the overlap was zero (for modes with opposite symmetry) or very low (≈ 0.001) for most pairs, with the exception of the combination of the third and fifth order normalized modes (overlap ≈ 0.1). Note that these modes are of the same polarization and symmetry, and both propagation constants are in proximity to the propagation constant β_* of the outer waveguides, i.e. relatively closely spaced. Thus the unphysically large overlap may be understood in the following way. If two modes are exactly degenerate, the WMM will arbitrarily select that superposition of both with the smallest error (3.8). If their propagation constants are farther apart, there may be a remainder of the other one in each calculated field, even if there are two separable parabolic sections in the error function. One cannot expect a discontinuous transition from 'degenerate' to 'nondegenerate'.

To overcome this problem, we followed the hint given at the end of Section 3.3. All results shown for this structure are computed with a normalization expression Eq. (3.11)(TE), where the part concerned with the rectangular regions of the outer waveguides has been multiplied by a factor of 5. This lowered the absolute overlap of the two supermodes in question to a value below 0.005, i.e. to the same order of magnitude as the overlaps of the other pairs. At the same time the properties of the remaining modes were almost unaffected by this modification. This strategy will be applied also for the direct simulation of radiatively coupled waveguide based isolator devices in Section 7.2.2. However, the somehow arbitrary modification must be regarded as an additional uncertanty for the simulation, and as a reason to switch to WMM-based coupled mode theory as in Sections 5.3 and 7.3.2, when such situations are encountered.

5 Applied perturbation theory

Based on numerically exact modes for one dimensional cross sections and on WMM approximations for two transverse dimensions, this chapter collects some numerical examples for different variants of perturbation theory which have been presented in Chapters 1, 2. Waveguides with absorbing regions are the subject of Section 5.1. Section 5.2 deals with the influences of small dielectric boundary shifts on single modes and on devices relying on multimode interference, while Section 5.3 gives some assessment for the coupled mode theory, if applied to a two rib waveguide directional coupler. These techniques will be employed for technologically more relevant structures in the subsequent chapters.

5.1 Lossy waveguides

From Ref. [62] we have taken the example of a slab waveguide with a thin additional cladding. Figure 5.1 explains the relevant geometry.

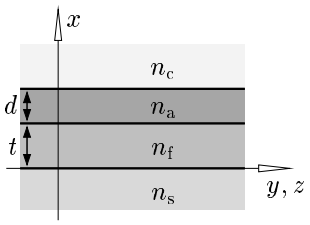

Figure 5.1: Planar four layer waveguide geometry. Parameters are the refractive indices $n_s = 1.515$, $n_f = 1.52$, $n_a = 4.1 - i0.21$, $n_c = 1.0$, the layer thicknesses d and $t = 2.488\ \mu m$ and the wavelength $\lambda = 0.630\ \mu m$ [62].

The upper layer is assumed to be made of a highly refracting absorbing material with complex refractive index $n - i\alpha/(2k)$, where α is the attenuation constant of the medium in bulk form. For modeling in the framework of perturbation theory, only the real part n enters the mode analysis procedure directly.

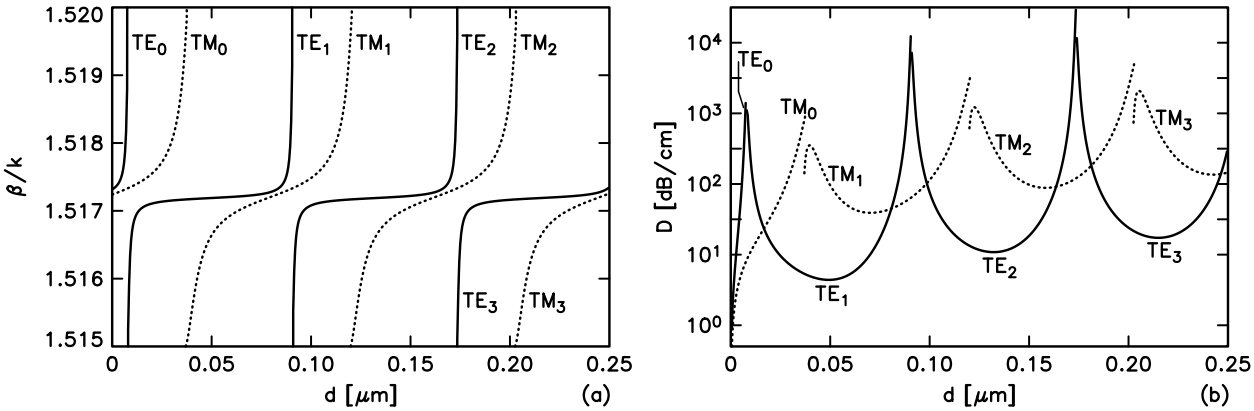

Figure 5.2: For an absorbing four layer waveguide according to Figure 5.1: effective mode indices β/k (a) and mode power attenuation D (b) (see the text) versus the thickness d of the absorbing layer.

Figure 5.2(a) is a plot of the resulting effective mode indices as a function of the cladding thickness. Note that the figure is restricted to the mode index interval between n_s and n_f, which would be relevant for the waveguide without cladding. Modes with β/k above this region have large amplitudes in the absorbing layer; they are subject to large damping and are thus of less interest. The fields corresponding to the mode

indices of Figure 5.2(a) were inserted into the perturbational expressions (2.12) for the mode attenuation constants α_{m}. Figure 5.2(b) shows the attenuation in dezibel units $D = (10 \log_{10} \mathrm{e})\alpha_{\mathrm{m}}$.

The reader should compare with the corresponding plots in Ref. [62] which display the results of a direct mode calculation for the complex refractive index profile. At least for those modes with effective indices in proximity to the levels 1.5173 (TE) and 1.5172 (TM) of the three layer waveguide without cladding, there is good agreement both in the behaviour of the dispersion curves and in the attenuation level. These modes have only small amplitudes in the absorbing region. Note that the poles in (a) and the peaks in (b) are due to the switching of the mode order. In these regions, the perturbation theory yields the correct qualitative behaviour of all curves. But while the perturbational approach naturally transfers the mode order from the nonabsorbing to the attenuating profile, this property is obviously lost by the direct computation. Accordingly, the curves in [62] are continuous. Ref. [154] contains a detailed discussion of the still unsolved mode classification problem in strongly lossy waveguides.

However, for only slightly attenuated modes, we have found a good quantitative agreement between the perturbational and the direct calculations, even for the extremely high bulk attenuation of $\alpha = 20300\,\mathrm{cm}^{-1}$ in the above example (which corresponds to a level $D = 10^{4.945}\,\mathrm{dB/\,cm}$ in Figure 5.2(b)). Typical attenuations for the transparent materials considered in this thesis, e.g. the magnetooptic garnets of Chapter 6, are approximately $0.5\,\mathrm{cm}^{-1}$ to $10\,\mathrm{cm}^{-1}$ [163], four orders of magnitude smaller, and we thus may expect correct results from the perturbational expressions.

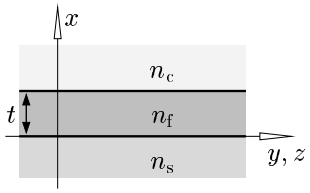

Figure 5.3: Basic three layer dielectric waveguide: a guiding film (refractive index n_f) of thickness t, sandwiched between substrate (refractive index n_s) and cover (refractive index n_c).

If we assume the guiding layer itself to be absorbing, then a planar waveguide as sketched in Figure 5.3 exhibits the power attenuation shown in Figure 5.4 (cf. Figure 5.5 for the effective mode indices).

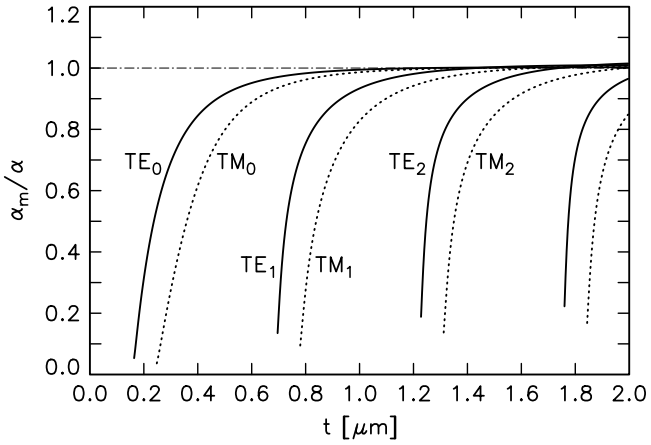

Figure 5.4: Mode power attenuation constants α_m versus film thickness t for the waveguide of Figure 5.3 with parameters $n_s = 1.95$, $n_f = 2.3 - \mathrm{i}\alpha/(2k)$, $n_c = 1.0$, $\lambda = 1.3\,\mu m$, $\alpha = 1\,cm^{-1}$.

According to this plot, modes close to cutoff with considerable amplitudes below and above the absorbing region are subject to low attenuation loss. There are certain configurations with a large difference in the damping of TE and TM polarized guided light. For growing film thickness, along with the effective mode index approaching the refractive index of the film material, the evanescent parts of the mode fields outside the film region become negligible, thus the mode attenuation approaches the bulk value of the film material.

Although hardly visible in Figure 5.4, the mode attenuation α_{m} may *exceed* the bulk value α. Formally, this can be realized by inspecting the two concurrent factors in Eq. (2.12)(TE). The ratio of the mode power on the guiding region over the total mode power is always below one, while the ratio kn/β always exceeds one. For small film thickness the former factor turns out to be significant, for larger thickness the latter

one. Magnification and extension of Figure 5.4 shows that α_{m} approaches α in the limit of large t, but from above, for both TE and TM polarization. Physically, this observation can be undestood by the basic zig-zag or ray model for guided light propagation: Clearly, the path of a frequently reflected ray is longer than the light path of a plane wave propagating along the z direction through the bulk material.

5.2 Geometry variations

This section provides numerical verifications of the geometry perturbation expressions developed in Section 1.4. Sections 5.2.2 and 5.2.3 present the numerical results of Refs. [75, 78] for two series of simple raised strip and rib waveguides. For both series, we show that the theory can be successfully applied to estimate the fabrication tolerances for directional couplers based on these waveguides. Before, the short Section 5.2.1 touches the much simpler case of a series of planar waveguides.

5.2.1 Planar waveguides

The waveguide in Figure 5.3 is specified by one geometry parameter t only. Shifting the cover/film boundary by a distance δx changes the thickness t to $t+\delta x$. In first order, this procedure modifies the propagation constants by small amounts $\delta x \partial_t \beta$. Figure 5.5 compares the exact curves $\beta(t)$ with linear approximations $\beta(t_0) + (t - t_0)\partial_t \beta(t_0)$ for a few thicknesses t_0, where the derivatives $\partial_t \beta$ have been calculated with Eqs. (2.13), (2.14). For this planar configuration the perturbation theory yields numerically exact propagation constant gradients.

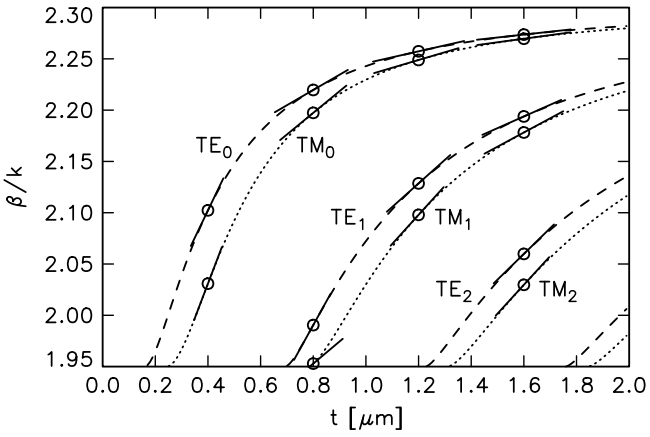

Figure 5.5: Effective mode indices β/k versus the thickness t of the guiding film, for waveguides according to Figure 5.3 with $n_s = 1.95$, $n_f = 2.3$, $n_c = 1.0$, $\lambda = 1.3\,\mu$m. The dashed and dotted lines are the reference dispersion curves, for TE and TM polarization, respectively. At the thicknesses marked by circles, lines with gradients as predicted by the geometry perturbation expressions have been inserted.

5.2.2 Results for raised strip waveguides

As above, for the waveguides investigated in this section we assume parameters typical for magnetooptic garnet materials [165]. The refractive index values are such that the structures can neither be regarded as weakly guiding, nor do the fields at the waveguide/air interfaces almost vanish. Effects due to the jumps of the mode fields and derivatives at the dielectric discontinuities can thus be expected to be large, providing a good test for the perturbation theory.

Single waveguides

Besides the wavelength and the refractive indices, two geometry parameters define the waveguide sketched in Figure 5.6: the rib height h and its width w. Changing these dimensions can be interpreted as shifting the enclosing boundaries. First order effects on the propagation constants, i.e. the gradients in the curves $\beta(h)$ and $\beta(w)$, are given by the perturbational expressions of Section 1.4. For a verification, we have

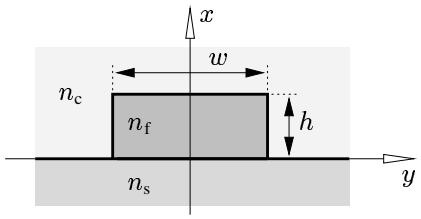

Figure 5.6: Raised strip waveguide geometry. For the subsequent simulations, the refractive indices and wavelength are $n_s = 1.95$, $n_f = 2.3$, $n_c = 1.0$, $\lambda = 1.3\,\mu m$.

calculated the dispersion curves, inserting secants with gradients as predicted by Eqs. (1.51)–(1.57) for a few abscissas. Ideally these secants should be tangents at the evaluation points, and this is almost the case as shown in Figure 5.7 for hybrid mode fields and in Figure 5.8 for fields calculated with the semivectorial approximation.

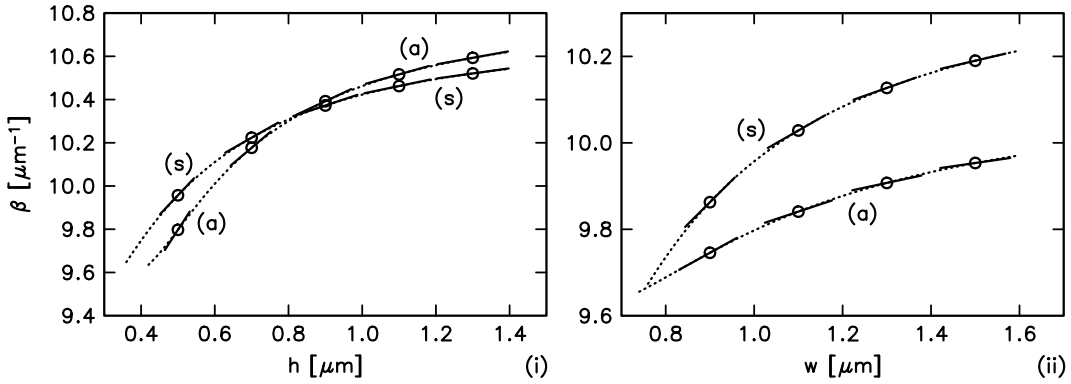

Figure 5.7: Dependence of the hybrid mode propagation constants β on the height h (i) and on the width w (ii) of a raised strip waveguide as sketched in Figure 5.6, for symmetric (s) and antisymmetric (a) trial fields (see Section 1.1.3). The dotted lines correspond to multiple runs of the mode solver for varied parameters, while the continous sections show the tangents predicted by the evaluation of Eqs. (1.51), (1.55), at the points indicated by circles. Parameters are as given for Figure 5.6, with $w = 1.0\,\mu m$ (i), and $h = 0.5\,\mu m$ (ii).

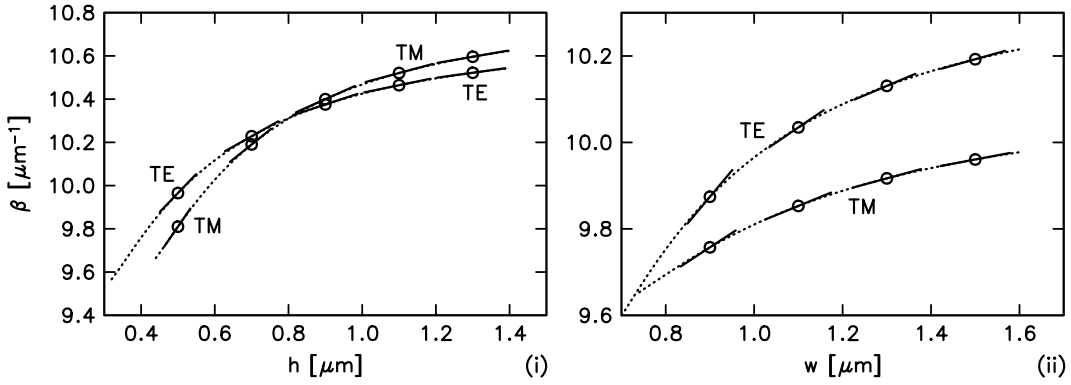

Figure 5.8: Analogon to Figure 5.7, but for the fundamental semivectorial modes of both polarizations with Eqs. (1.52), (1.54) and Eqs. (1.56), (1.57) applied. For symbols and parameters see the caption of Figure 5.7.

In the calculations for Figure 5.7, explicitely imposed mode symmetry with respect to $y = 0$ was used to separate the fundamental hybrid modes of different polarization. Due to opposite symmetry, the two $\beta(h)$-curves do not repel each other. No strong hybridization occurs for the degenerate modes around $h = 0.8\,\mu m$ where the two curves cross.

Usually there are several possibilities to apply the perturbation theory. Enlargement of the rib width can be simulated by evaluating Eqs. (1.55), (1.56), (1.57) on the right or on the left sidewall (with a negative sign), or as an average of both. Likewise, to investigate an extended rib height, the perturbational expressions for horizontal boundary variation may be applied to the top surface or alternatively to the three sections of the

rib baseline, with the results added. While the values for the gradient $\partial_w \beta$ are exactly equal due to mode symmetry, agreement of the values for $\partial_h \beta$ estimated in both ways is not obvious a priory. We have carried out this test by recalculating $\partial_h \beta$ for semivectorial and hybrid fields and found no change with respect to Figures 5.7, 5.8.

Two waveguide couplers

Two parallel waveguides at a small distance form the central part of a directional coupler. Figure 5.9 illustrates mode shapes in a device made up from waveguides of the previous section. Power transfer between them is determined by the interference of these supermodes.

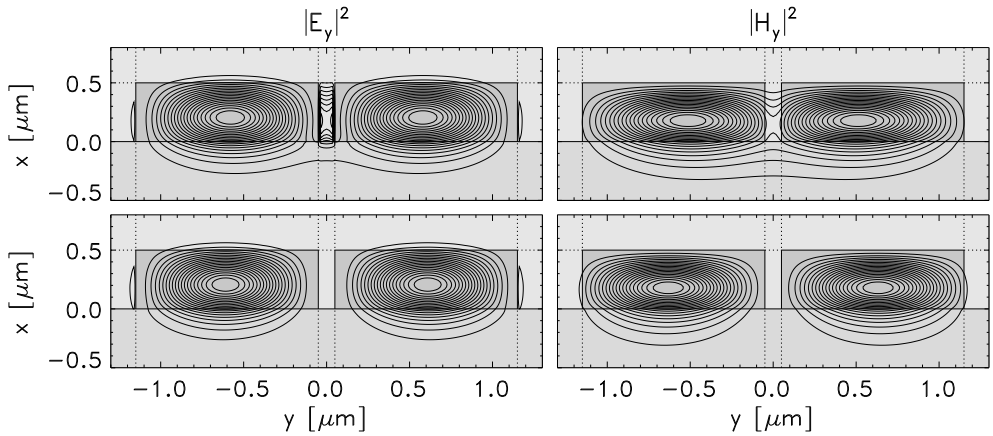

Figure 5.9: Intensity profiles for the symmetric (top) and antisymmetric (bottom) TE- (left) and TM-polarized (right) modes of a directional coupler made of two identical waveguides as sketched in Figure 5.6. Waveguide dimensions are the height and width of the ribs $h = 0.5\,\mu$m, $w = 1.1\,\mu$m, and the spacing $g = 0.1\,\mu$m in-between, with other parameters as given for Figure 5.7. The corresponding propagation constants are $10.0505\,\mu\text{m}^{-1}$ (TE, symm.), $10.0121\,\mu\text{m}^{-1}$ (TE, antis.), $9.9021\,\mu\text{m}^{-1}$ (TM, symm.), $9.8095\,\mu\text{m}^{-1}$ (TM, antis.).

For fixed polarization, let ϕ_l and ϕ_r denote the single modes of the left and right isolated waveguide. ψ_s, ψ_a are the symmetric and antisymmetric supermode of the entire structure. Suppose the coupling section to be excited by the mode of the left waveguide ϕ_l, with unit power input. According to Section 1.2, the relative power coupled out to the mode of the opposite waveguide ϕ_r after propagating along the device length L is

$$P(L) = w_\text{s}^2 + w_\text{a}^2 + 2 w_\text{s} w_\text{a} \cos(\beta_\text{s} - \beta_\text{a}) L \,, \tag{5.1}$$

where the factors w_s, w_a are given by the mode overlaps at input and output: $w_\text{j} = (\phi_\text{r}; \psi_\text{j})\,(\psi_\text{j}; \phi_\text{l})$, $j = $ s,a. All modes involved are meant to be normalized with respect to the product $(\,.\,;\,.\,)$ as defined in Eq. (1.18).

The weights w_s, w_a are real with opposite signs. Hence the guided power in a device of length $L = L_\text{c} = \pi/(\beta_\text{s} - \beta_\text{a})$ or $L = L_\text{c}/2$ is completely transferred to the right waveguide or equally distributed between the two waveguides, respectively. In our example, stronger coupling for TM fields resulted in a shorter coupling length (see the caption of Figure 5.10) and a larger mismatch between the supermodes of Figure 5.9 and the outer waveguide modes. The latter shows up in the maximum power transmission through the untapered structures of $P(L_\text{c}) = 0.999$ for TE and $P(L_\text{c}) = 0.982$ for TM polarization.

If a dimensional parameter in the coupling region is altered, in first order perturbation theory only the propagation constants of the supermodes change, while the mode fields and thus their weights in the power transfer expression (5.1) are not affected. The main contribution to the change in the power troughput will be due to the altered supermode wavenumbers to which the perturbation theory of Section 1.4.2 give direct access. For a verification, Figure 5.10 compares the relative output power $P(L_\text{c})$, $P(L_\text{c}/2)$ from repeated mode calculations for the modified geometries with perturbational results. These were obtained in the following way. With fields from only one mode analysis for the original geometry, the gradients of the

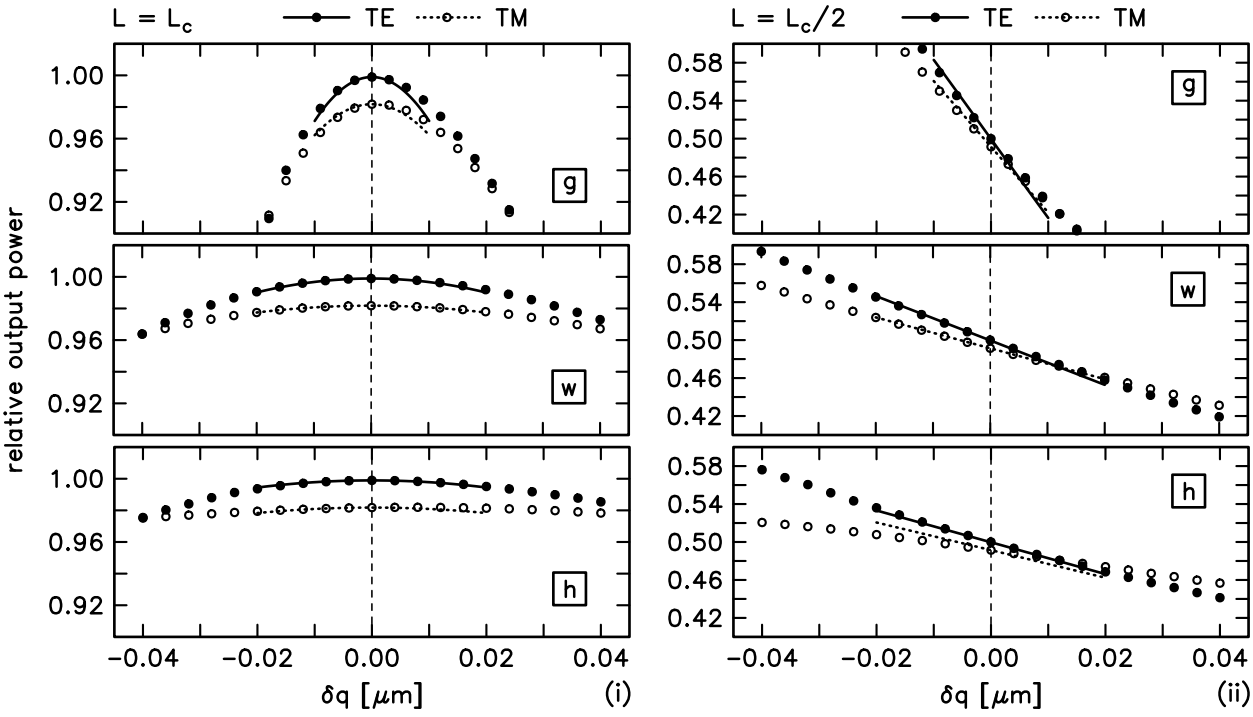

Figure 5.10: Dependence of the relative output power on geometry parameter variations for a directional coupler corresponding to Figure 5.9. Modified parameters are the spacing g (top), the width w (center), and the height h (bottom) of the ribs. Only one parameter $q = g, w, h$ is altered to $q + \delta q$, with q and the remaining dimensions as given for Figure 5.9. Markers correspond to complete semivectorial analysis runs with recalculation of the mode fields for the modified geometry, while the lines show the results of evaluating Eq. (5.1) and the perturbational expressions (1.52), (1.54), (1.56), (1.57) for the original parameter sets. The device length L was set to L_c (i) and $L_c/2$ (ii), with $L_c = 81.8\,\mu$m for TE polarization (filled circles, continuous lines) and $L_c = 33.9\,\mu$m for TM polarization (open circles, dotted lines).

supermode propagation constants $\partial_q\beta_\mathrm{s}$, $\partial_q\beta_\mathrm{a}$ corresponding to the change of one parameter $q = g, w, h$ are computed. Note that usually Eqs. (1.52), (1.56), (1.54), (1.57) must be applied more than once at different boundaries, with the results added or subtracted. Power transmission through the device with dimension $q + \delta q$ is then approximated by Eq. (5.1), with fixed weights, but with the propagation constants replaced by $\beta_{\mathrm{s,a}} + \partial_q\beta_{\mathrm{s,a}}\delta q$.

P depends on β_s and β_a, and therefore on the three geometry parameters $q = g, w, h$. Assuming unaltered weights $|w_\mathrm{s}| = |w_\mathrm{a}| = 1/2$, expanding P with respect to one of these parameters q yields expressions for admissible geometry tolerances Δq for a given maximum deviation ΔP of the transmitted power. Evaluated at $L = L_\mathrm{c}$, this reads

$$\Delta q = \pm\frac{2\sqrt{\Delta P}}{L\,|\partial_q\beta_\mathrm{s} - \partial_q\beta_\mathrm{a}|}, \tag{5.2}$$

and for $L = L_\mathrm{c}/2$, one obtains

$$\Delta q = \pm\frac{2\Delta P}{L\,|\partial_q\beta_\mathrm{s} - \partial_q\beta_\mathrm{a}|}. \tag{5.3}$$

These expressions should be read as follows. Parameter values from $[q-\Delta q, q+\Delta q]$ allow for transmissions above $P - \Delta P$ ($L = L_\mathrm{c}$) or between $P - \Delta P$ and $P + \Delta P$ ($L = L_\mathrm{c}/2$), respectively, if P is the relative power output for the original dimension q. Of course, similar equations can be written for other input/output configurations.

For a more quantitative assessment, the top part of Table 5.1 compares propagation constant gradients from perturbation theory with values obtained by finite difference evaluation of mode analysis results. In the

		g		w		h	
		TE	TM	TE	TM	TE	TM
$\partial_q\beta/\,\mu\mathrm{m}^{-2}$							
(s)	FD	-0.280	-0.565	0.538	0.284	1.738	2.427
	PT	-0.335	-0.636	0.622	0.293	1.768	2.455
(a)	FD	0.075	0.201	0.645	0.475	1.820	2.602
	PT	0.075	0.199	0.737	0.489	1.850	2.559
$\Delta q/\mathrm{nm}$							
$L = L_\mathrm{c}$	NUM	6.4	6.6	22	30	27	50
	PT	6.0	7.0	21	30	30	34
$L = L_\mathrm{c}/2$	NUM	1.4	1.6	4.6	6.3	5.9	11.2
	PT	1.2	1.4	4.3	6.0	6.0	6.7

Table 5.1: Top: Gradients $\partial_q\beta$ of supermode propagation constants for TE and TM polarization and for modes of even (s) and odd (a) symmetry. Modified parameters are the spacing g, the width w, and the height h of the ribs. Values in rows 'FD' are calculated as difference quotients from two mode analysis runs on neighbouring parameter values. Lines 'PT' contain the results of applying Eqs. (1.52), (1.56), (1.54), (1.57). Bottom: Geometry tolerances Δq admissible for a power transmission deviation ΔP less than 1% for device lengths of L_c and $L_\mathrm{c}/2$. 'NUM' indicates the limits read from the marker lines of Figure 5.10, with the smaller difference taken in case of a nonsymmetric curve $P(\delta q)$. 'PT' refers to the results of the perturbational expressions and Eqs. (5.2), (5.3). Parameters are identical to Figure 5.9.

bottom part, the table contrasts geometry tolerances as can be read off from the charts of Figure 5.10 with simple perturbational values according to Eqs. (5.2), (5.3). There is good overall agreement, the largest deviation occurring for the rib height variation in TM polarization. Although the gradients entering Eqs. (5.2), (5.3) are evaluated with a small relative error of about 2%, these are comparably large, almost equal and have to be subtracted. However, since the height h turns out to be the least critical dimension in this case, the tolerance estimate should be still sufficient for practical purposes.

In a realistic device, input and output ports will not be formed by abrupt ending of the waveguides, but by diverging coupler arms, and then the above assumptions are certainly not correct to calculate the exact power transmission. However, we are here interested in estimations for the fabrication tolerances only, and the main influence of a varied dimension on the output power should still arise from the supermode wavenumber shift, even in a more complex geometry. Therefore our analysis can be expected to yield reasonable estimates for devices including coupler arms and tapering.

5.2.3 Results for rib waveguides

While the above calculations were concerned with magnetic garnets, i.e. permittivity profiles of (3.6, 5.3, 1.0), many integrated optics devices are realized with rib waveguides made of semiconductor material with typical refractive index profiles of e.g. (11.6, 11.8, 1.0), that is with a much lower permittivity contrast between substrate and the guiding film, but with a high contrast between the film and the surrounding air. At the relevant dielectric boundaries, either the field strength or the permittivity contrast is small, and it is not obvious a priori whether the perturbational expressions are numerically reliable in this case. To answer this question, we choose a typical benchmark structure [159] for the numerical simulations.

Single waveguides

Figure 5.11 shows intensity profiles for the fundamental modes of both polarizations for one of the waveguides of Section 4.1.2. The corresponding propagation constants are $\beta_*^{\mathrm{TE}} = 18.6481\,\mu\mathrm{m}^{-1}$, $\beta_*^{(\mathrm{s})} = 18.6475\,\mu\mathrm{m}^{-1}$ for TE polarization and $\beta_*^{\mathrm{TM}} = 18.6398\,\mu\mathrm{m}^{-1}$, $\beta_*^{(\mathrm{a})} = 18.6397\,\mu\mathrm{m}^{-1}$ for the TM mode, computed in the semivectorial approximation and fully vectorial, respectively.

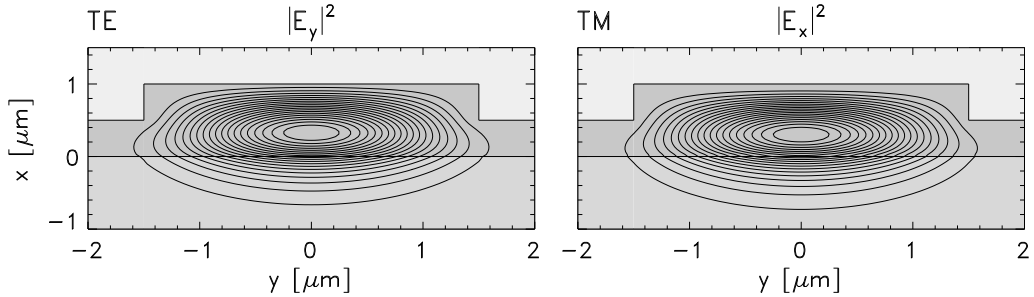

Figure 5.11: Intensity profiles for the dominant components of the TE (left) and TM (right) polarized modes for a rib waveguide according to Figure 1.1 with parameters $h = 0.5\,\mu m$, $w = 3.0\,\mu m$, $t = 0.5\,\mu m$, $\lambda = 1.15\,\mu m$, $n_s = 3.40$, $n_f = 3.44$, and $n_c = 1.0$.

Beginning with the parameter set as stated for Figure 5.11, we have varied separately one of the quantities h, w, t, or λ, and recalculated the propagation constants, keeping all other parameters fixed. Alternatively, applying the perturbational expressions from Section 1.4.2 to the mode profiles of Figure 5.11 or to the corresponding fully vectorial fields should yield propagation constant gradients $\partial_q\beta$, evaluated for the original structure $\delta q = 0$ for parameters $q \in \{h, w, t, \lambda\}$. Figures 5.12, 5.13 compare the corresponding linear approximations $\beta(\delta q) = \beta(0) + \delta q \partial_q \beta$ with the directly computed data.

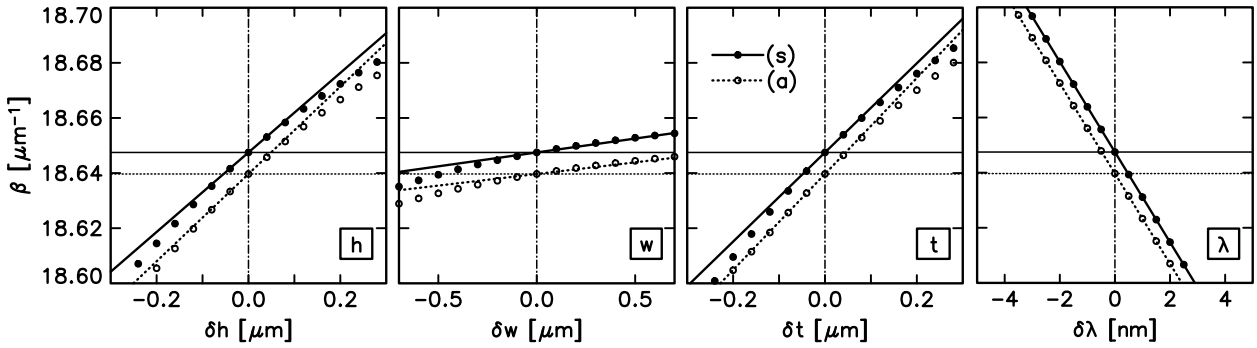

Figure 5.12: Dependence of the propagation constants on variations of the rib height δh, of the rib width δw, of the film thickness besides the rib δt, and of the wavelength $\delta\lambda$, for the fundamental hybrid symmetric (s) and antisymmetric (a) mode of a rib waveguide with parameters as given for Figure 5.11. Marker points indicate values computed directly for the modified structures, lines show the tangents predicted by the perturbation theory.

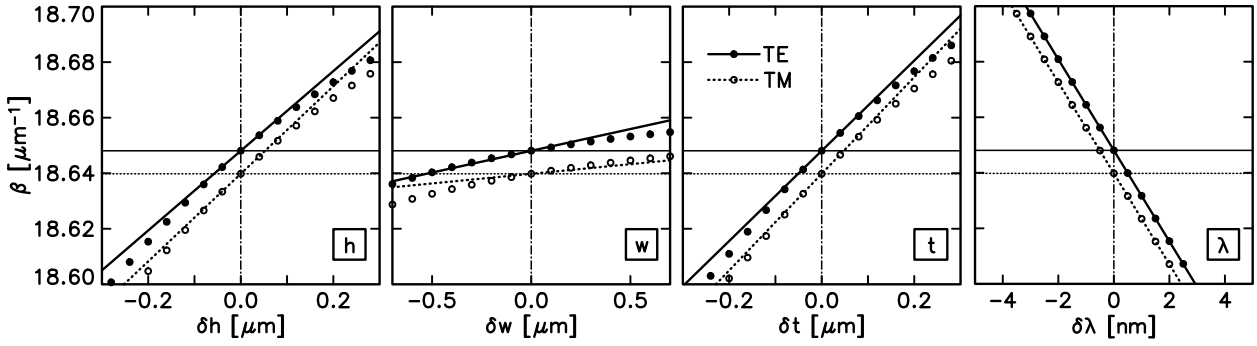

Figure 5.13: Analogon to Figure 5.12 for the fundamental TE and TM modes computed with the semivectorial approximation. Symbols and parameters are as given in the caption of Figures 5.11, 5.12.

Obviously the perturbational secants are almost tangents to the reference curves, the marker lines, as it was intended. As in Section 5.2.2, the good agreement, both for fully vectorial basic fields and for the semivectorial fields, can be regarded as a confirmation of the perturbational expressions.

Among the four parameters, the wavelength has the most pronounced influence on the propagation constants. In contrast to the structures investigated in Section 5.2.2, the wavelength dependence of the propagation constant is given by the inverse wavelength itself. $\partial_\lambda \beta = -\beta/\lambda$ is a good approximation for the present waveguide. Due to either the small field strength on the rib flanks and on the surface (w, h) or to the low refractive index contrast between substrate and film (h, t), the other contributions to Eq. (1.58) remain small ($\approx 0.2\,\mu\mathrm{m}^{-1}$) when compared with the propagation constant ($\approx 18.6\,\mu\mathrm{m}^{-1}$).

Two waveguide couplers

As sketched in Figure 5.14, the central part of a directional coupler made of two of the former rib waveguides is characterized by one additional parameter, the separation g of the ribs.

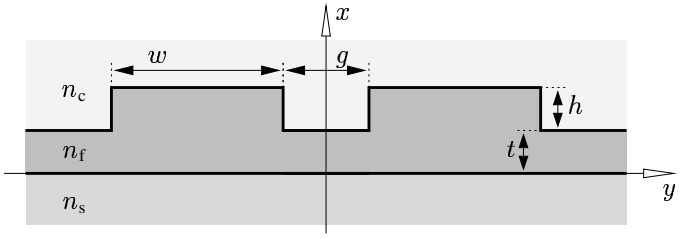

Figure 5.14: Cross section of the two rib waveguide coupler. It is meant to be symmetric with respect to $y \to -y$.

For each polarization, the structure supports one mode of even and one of odd symmetry. Figure 5.15 illustrates the corresponding TE mode profiles; similar plots for TM fields are almost indistinguishable.

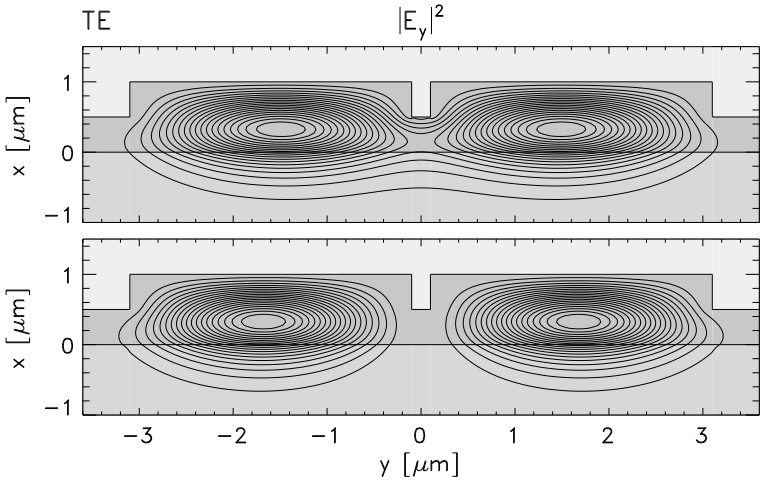

Figure 5.15: Intensity profiles for the semivectorial TE modes of even (top) and odd symmetry (bottom) in a two rib coupler according to Figure 5.14. Parameters are as for Figure 5.11, with a gap spacing $g = 0.2\,\mu$m.

If the device length L is set to $L_\mathrm{c} = \pi/(\beta_\mathrm{s} - \beta_\mathrm{a})$, the transferred power (5.1) is maximal and close to unity, provided that all parameters are kept at their original values. If one of them is slightly detuned, a smaller amount of power will be coupled to the right channel. This dependence is shown in Figure 5.16. For otherwise fixed geometry, we have varied one dimensional parameter and repeated the entire calculation, including mode field composition and overlap integration. The results are indicated by the marker points.

The lines in Figure 5.16 show the results of perturbation theory. For tuned parameters, we have calculated the wavenumber gradients $\partial_q \beta_\mathrm{s}$, $\partial_q \beta_\mathrm{a}$, $q \in \{h, w, t, g, \lambda\}$ using Eqs. (1.52), (1.54), (1.56), (1.57). Then approximations for the transferred power (5.1) were assembled with the unperturbed weights, but with altered propagation constants $\beta_{\mathrm{s,a}} + \delta q \partial_q \beta_{\mathrm{s,a}}$.

At least for the rib height and the outer film thickness, perturbational and reference results agree well. Evaluating the perturbational wavenumber gradients includes integration along lines with comparably large field strength where the relative error in the basic mode field can be assumed to be small. On the other hand, for rib width, gap spacing, and, consequently, wavelength, the field must be integrated along the rib sidewalls, where the mode field is almost vanishing. Nevertheless, the same absolute error in the basic field

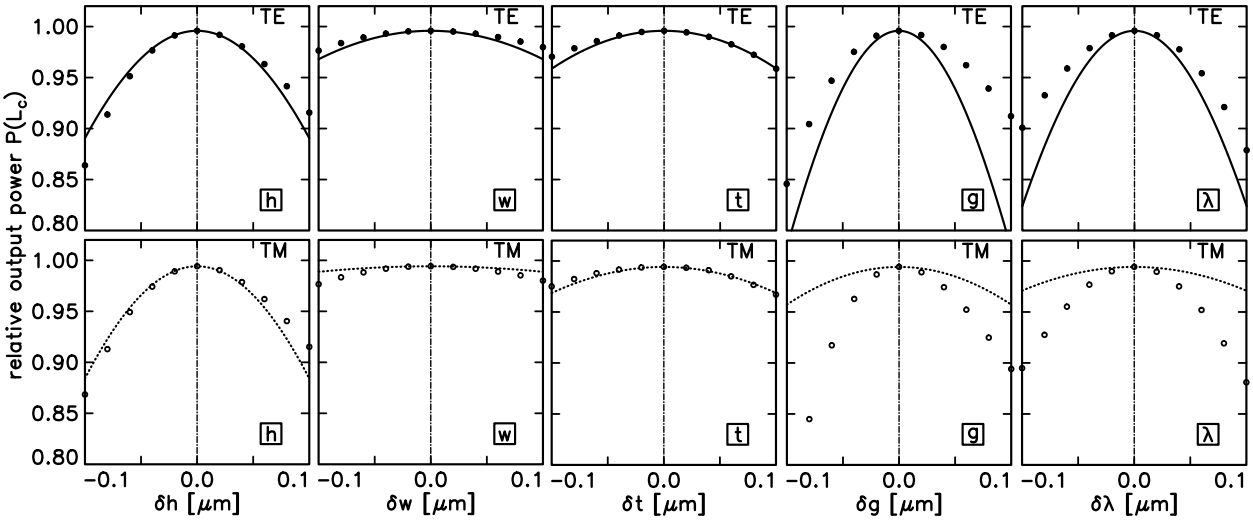

Figure 5.16: Influence of parameter variations on the relative output power $P(L_c)$ of a rib waveguide coupler as sketched in Figure 5.14, for TE (top row) and TM polarization (bottom row). One of $q \in \{h, w, t, g, \lambda\}$ is altered to $q+\delta q$, with the remaining parameters as given for Figure 5.15. Markers correspond to complete semivectorial analysis runs; the lines are perturbational results. $L_c = 650\,\mu$m for TE and $L_c = 599\,\mu$m for TM polarization.

must be assumed, resulting in a higher relative error level of the small wavenumber gradients with respect to these variables.

Another source of error is in the semivectorial approximation. While the continuity conditions on horizontal boundaries are obeyed exactly, the fields violate the conditions on the vertical boundaries, which are directly relevant for the gradients with respect to w and g (cf. the remarks in Section 1.4.2).

		TE	TM	TE	TM	TE	TM	TE	TM	TE	TM
		$\partial_h\beta/\mu\mathrm{m}^{-2}$		$\partial_w\beta/\mu\mathrm{m}^{-2}$		$\partial_t\beta/\mu\mathrm{m}^{-2}$		$\partial_g\beta/\mu\mathrm{m}^{-2}$		$\partial_\lambda\beta/\mu\mathrm{m}^{-2}$	
(s)	FD	0.137	0.151	0.010	0.009	0.168	0.179	−0.006	−0.008	−16.382	−16.383
	PT	0.138	0.151	0.013	0.006	0.167	0.179	−0.009	−0.004	−16.398	−16.384
(a)	FD	0.147	0.162	0.015	0.013	0.162	0.174	0.004	0.004	−16.392	−16.394
	PT	0.148	0.163	0.018	0.008	0.161	0.173	0.005	0.002	−16.411	−16.389
$\Delta P = 1\%$		Δh/nm		Δw/nm		Δt/nm		Δg/nm		$\Delta\lambda$/nm	
NUM		29	28	74	77	52	61	28	23	30	28
PT		30	29	59	135	51	62	21	51	23	64

Table 5.2: For the coupler of Figures 5.14–5.16:
Top: partial derivatives of the supermode propagation constants, for the mode with even (s) and odd symmetry (a), and for TE and TM polarization. Values 'FD' are calculated as difference quotients from two mode analysis runs. 'PT' are the results from using Eqs. (1.52), (1.54), (1.56), (1.57) with the unperturbed modes.
Bottom: Geometry tolerances admissible for a power transfer deviation ΔP of less than 1%, for couplers of length $L = L_c$. 'NUM' gives directly computed limits, 'PT' are values estimated with Eq. (5.2) and the perturbational expressions of Section 1.4.2.

However, as indicated by the top of Table 5.2, the propagation constant derivatives are evaluated correctly up to $0.005\,\mu\mathrm{m}^{-2}$ for all dimensional variables and for both TE and TM polarization. Unfortunately, according to Eq. (5.2) the relevant quantity for tolerance investigations is the difference between the wavenumber gradients of the even and odd supermode. The bottom part of Table 5.2 compares these perturbational tolerances with values read off from the (interpolated) marker curves of Figure 5.16. Obviously, the perturbational wavenumber gradients give good estimates for the rib height and film thickness tolerances. For rib width, gap spacing, and wavelength tolerances, at least the order of magnitude is correct.

5.3 WMM based coupled mode theory

In this section, the by now familiar example of the two waveguide directional coupler will be employed for the last time. Direct WMM simulation of raised strip or rib waveguide based devices is feasible with reasonable effort, thus the structure is well suited to assess the accuracy that can be expected from coupled mode theory as formulated in Section 1.5, if numerical WMM results are supplied as basic fields. As in Ref. [79], the technique will be applied later to the design of radiatively coupled waveguide devices (Chapter 7) for similar dimensional and material parameters, but with a larger number of coupled modes.

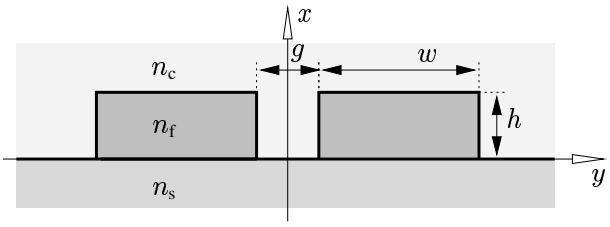

Figure 5.17: Two coupled raised strip waveguides. Fixed parameter values are $n_s = 1.95$, $n_f = 2.2$, $h = 0.7\,\mu m$, $w = 1.2\,\mu m$, and $\lambda = 1.3\,\mu m$.

Figure 5.17 shows the coupler geometry. The propagation constants β_s, β_a of its even and odd mode can be determined by direct mode analysis of the entire structure on the one hand, and by supermode composition via coupled mode theory on the other, according to Section 1.5.2. The latter approach is based on the single, properly polarized modes of the two isolated strips. One WMM simulation is sufficient, with the resulting field shifted to the two core positions. Figure 5.18 compares results for the propagation constants and for the half beat length $L_c = \pi/(\beta_s - \beta_a)$.

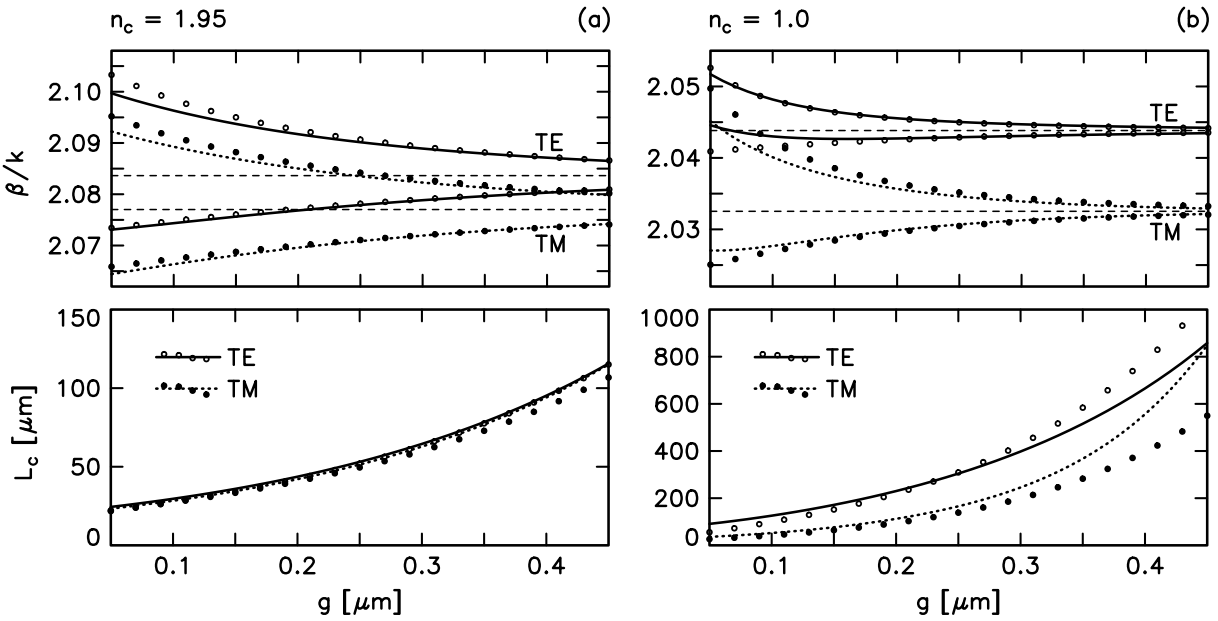

Figure 5.18: Effective mode indices (top) and coupling length L_c (bottom) versus the strip spacing g for two waveguide couplers as in Figure 5.17 with $n_c = n_s$ (a) or $n_c = 1.0$ (b). Lines mark coupled mode theory results, while marker symbols show values from direct calculations. The horizontal lines in the top charts indicate the levels of the single waveguides propagation constants.

Charts (a) correspond to embedded waveguides covered by the substrate material, charts (b) to uncovered waveguides. There is good agreement in the propagation constants, with larger deviations occurring only for increased coupling at smaller gap width. Although the coupling is stronger for the embedded waveguides, as indicated by the shorter coupling length, deviations in the propagation constants are less pronounced due to the lower permittivity contrast between the core and the gap regions. We conclude that the perturbational theory was adequately implemented.

Simulating the embedded, weakly guiding structures is more reliable. However, they are less sensitive to the polarization, thus less suited for e.g. the polarization splitter design in Section 7.3.2. The difference between the levels of TE and TM propagation constants increases with growing contrast between the core and cover permittivities. According to the bottom charts of Figure 5.18, the difference between the TE and TM coupling lengths is also significantly larger for gap refractive index $n_c = 1.0$ than for $n_c = n_s$. Aiming at a short total length, the polarization splitter should be based on structures with high permittivity contrast. Therefore, Section 7.3.2 deals with raised strips rather than embedded or rib waveguides.

The bottom part of Figure 5.18 (b) compares coupled mode theory and rigorous calculations with regard to the coupling length. Results agree best for gap spacings between $0.1\,\mu$m and $0.25\,\mu$m. Deviations for small gaps are due to the larger field strength, and thus larger errors, of the coupled mode fields in the gap region. As illustrated by Figure 5.19, the deviations for L_c at large gap width are accompanied by an excellent agreement of the coupled mode theory mode profiles with rigorously computed fields.

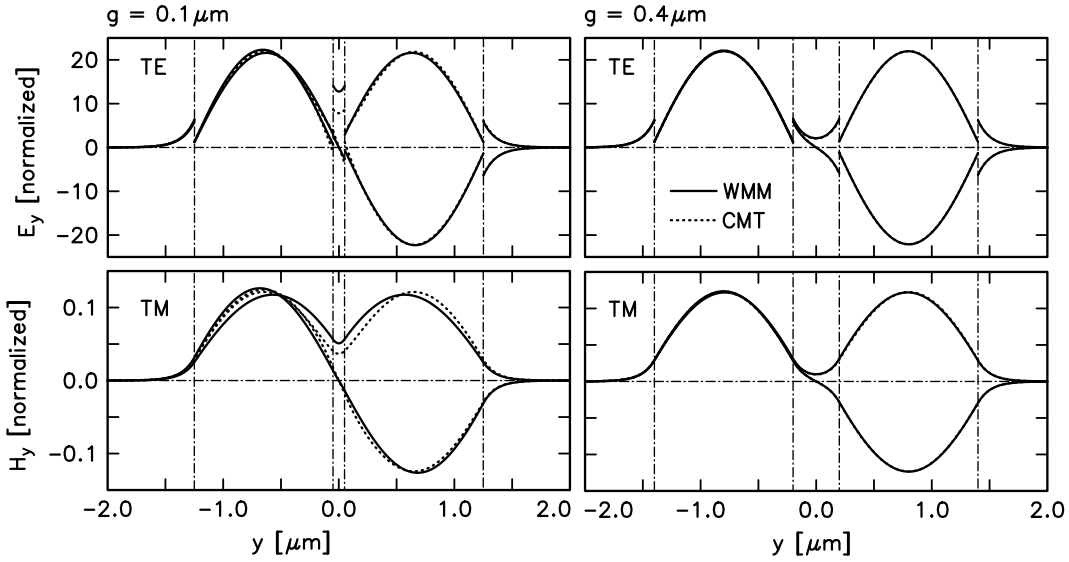

Figure 5.19: Mode profiles for two waveguide couplers evaluated along the horizontal line $x = 0.35\,\mu$m at half the strip height. Parameters are as given for Figure 5.18(b), with the gap size g set to $0.1\,\mu$m (left) and $0.4\,\mu$m (right). Top charts are for TE, bottom charts for TM polarization. The continuous lines show the directly calculated modes, dotted lines correspond to supermode profiles composed by coupled mode theory.

However, for large core separation with large coupling length, the propagation constants of the symmetric and antisymmetric supermodes converge, while we must assume a certain fixed numerical error for both the directly computed values β_s, β_a and the basic profiles for the isolated waveguides. The former affect the accuracy of our reference results, the latter influence coupled mode theory. Obviously one cannot expect an agreement in the limit of large waveguide separation, as it is the case for planar step index waveguides, where analytical solutions are available.

6 Magnetooptic waveguides

Magnetic garnets are promising materials for the realization of nonreciprocal integrated optical components [3, 33]. Reciprocity, or its absence, can be defined quite generally as a global or a local property of optical systems [157, 123]. A passive optical circuit with a symmetric permittivity function $\hat{\epsilon} = \hat{\epsilon}^{\mathsf{T}}$ is called reciprocal. The device allows the connections between its optical ports to be described by a symmetrical scattering matrix, which is constituted by the corresponding transmission and reflection coefficients. For each pair of ports, symmetry of this matrix predicts equal power transmission in both directions of light propagation (where the definition of 'ports' is crucial in the case of optical waveguides). In contrast, the magnetooptic permittivity contributions (6.1) are nonsymmetric. Magnetooptic devices may behave nonreciprocally in the sense that power transmission along a light path depends on the direction of propagation.

Results regarding material properties, fabrication and chracterization of thin garnet films are collected e.g. in Refs. [32, 163]. In this chapter and parts of the subsequent one we focus on selected aspects concerning the numerical modeling of light propagation in magnetooptic waveguides. While the magnetooptic effects themselves may be a means to achieve waveguiding, e.g. for waves traveling along a domain wall [109, 111], we consider them only as small perturbations to the propagation of modes, which are guided by comparably large refractive index contrasts. This is surveyed in Section 6.1. Sections 6.2 and 6.3 are concerned with the application of garnet films for nonreciprocal phase shift and polarization conversion, including numerical results from Refs. [110, 76, 77]. Ref. [10] presents other parts of our recent theoretical work in detail, regarding modeling and optimization of nonreciprocal TM and TE phase shifters [11, 164, 13], interferometers [15, 14, 12], and coupler structures [16] by means of finite element mode analysis and beam propagation simulations.

6.1 Magnetooptic permittivity contribution and nonreciprocal effects

In a region with static or quasistatic magnetization, the permittivity tensor $\hat{\epsilon}$ must be assumed to depend on the magnetization $\boldsymbol{M}$. The discussion shall be restricted to cubic crystals, and to contributions linear in $\boldsymbol{M}$. According to Onsager's relations and to considerations relying on the crystal symmetry [170, 31], the permittivity perturbation related to the magnetooptic effect of first order is

$$\delta\hat{\epsilon}_{\mathrm{mo}} = \begin{pmatrix} 0 & KM_z & -KM_y \\ -KM_z & 0 & KM_x \\ KM_y & -KM_x & 0 \end{pmatrix}. \tag{6.1}$$

A single complex magnetooptic constant K relates the off-diagonal elements and the components of the magnetization. The imaginary part of this constant gives rise to the effects of magnetic circular birefringence, the Faraday rotation, while its real part is responsible for polarization dependent absorption, the magnetic linear dichroism. For optical applications, only materials with relatively low losses are of interest, thus we assume the latter effect to be negligible (some corresponding remarks have been included in Section 6.3.1).

The optical effects of the magnetization depend crucially on the direction to which it is adjusted. Two angles ϑ, φ parametrize this direction as $\boldsymbol{M} = M(\sin\vartheta\cos\varphi, \sin\vartheta\sin\varphi, \cos\vartheta)$. We split the magnetooptic permittivity perturbation

$$\delta\hat{\epsilon}_{\mathrm{mo}} = \sin\vartheta\cos\varphi\,\delta\hat{\epsilon}^{x}_{\mathrm{mo}} + \sin\vartheta\sin\varphi\,\delta\hat{\epsilon}^{y}_{\mathrm{mo}} + \cos\vartheta\,\delta\hat{\epsilon}^{z}_{\mathrm{mo}} \tag{6.2}$$

into contributions related to the three components of the magnetization

$$\delta\hat{\epsilon}^x_{\mathrm{mo}} = \begin{pmatrix} 0 & 0 & 0 \\ 0 & 0 & \mathrm{i}\xi \\ 0 & -\mathrm{i}\xi & 0 \end{pmatrix}, \quad \delta\hat{\epsilon}^y_{\mathrm{mo}} = \begin{pmatrix} 0 & 0 & -\mathrm{i}\xi \\ 0 & 0 & 0 \\ \mathrm{i}\xi & 0 & 0 \end{pmatrix}, \quad \delta\hat{\epsilon}^z_{\mathrm{mo}} = \begin{pmatrix} 0 & \mathrm{i}\xi & 0 \\ -\mathrm{i}\xi & 0 & 0 \\ 0 & 0 & 0 \end{pmatrix}. \tag{6.3}$$

Here the absolute value ξ of the purely imaginary off-diagonal elements is related to the magnetooptic constant K and to the phenomenological constant of the specific Faraday rotation Θ_F by $KM/\mathrm{i} = \xi = \pm n\lambda\Theta_\mathrm{F}/\pi$, where n is the refractive index of the magnetooptic material. While the second equality can be shown by evaluating the propagation of a plane wave along the direction of the magnetization in a bulk crystal, it emerges also from the coupled mode analysis of guided waves as shown below.

If the magnetization is oriented along one of the cartesian axes, only one of the three terms (6.3) is present. According to Ref. [178], setups with the magnetization parallel to the x-axis ($\vartheta = \pi/2$, $\varphi = 0$) and y-axis ($\vartheta = \pi/2$, $\varphi = \pi/2$) are referred to as polar and equatorial configuration, respectively, while a setup with the magnetization adjusted along the z-axis ($\vartheta = 0$) is called the longitudinal configuration. While most of the proposed integrated magnetooptic devices rely on one of these configurattions, intermediate magnetization angles (see Section 6.3) may be interesting as well.

For a classification of the consequences for light propagation, we specialize to a single longitudinally homogeneous waveguide as in Section 1.5.1. Assuming a fixed direction of $\boldsymbol{M}$, the magnetooptic properties are given by a profile ξ and resulting permittivity perturbation $\delta\hat{\epsilon}_\mathrm{mo}$, which are functions of the transverse coordinates. Coupled mode theory predicts coupling coefficients (1.71)

$$\kappa_{lm} = \gamma \iint \boldsymbol{E}_l^* \, \delta\hat{\epsilon}_\mathrm{mo} \boldsymbol{E}_m \, \mathrm{d}x \, \mathrm{d}y \tag{6.4}$$

for modes indexed by l and m, with factors $\gamma = \omega\epsilon_0/(4\sqrt{P_l P_m})$, which include the mode normalization. Without further assumptions, all modes must be suspected to be subject both to phase shifts, given by the diagonal coefficients κ_{ll}, and to mode conversion, caused by the off-diagonal elements κ_{lm} for $l \neq m$. However, frequently the underlying guiding structure is symmetric as considered in Section 1.1.3, and the magnetooptic profile likewise is even or odd with respect to $y \to -y$. Then with the components of the hybrid coupled modes being of definite symmetry as well, half of the coupling coefficients cancel. Table 6.1 summarizes these results. Its rows list the contributions of a single component of Eqs. (6.3) to the coupling coefficient (6.4). For a general orientation of the magnetization, the terms are to be multiplied by the angular factors of Eq. (6.2) and to be summed.

To adopt common notation, we specialize to the case of a single-mode waveguide. According to Section 1.1.3, for a slab like structure the fundamental hybrid symmetric mode turns out to be TE dominant. Likewise, the fundamental hybrid antisymmetric mode is usually dominantly TM polarized. Table 6.2 shows the corresponding entries from Table 6.1. For well polarized modes, or semivectorial basic fields, the terms printed in small letters are negligible or vanish, respectively. Merely one entry remains in each row. Thus each orientation of the magnetization, corresponding to the perturbation terms in one row of Table 6.2, has a singular dominant effect. The polar configuration ($\delta\hat{\epsilon}^x_\mathrm{mo}$) yields phase shifts for TE modes, provided that the magnetooptic structure is antisymmetric. A symmetric ξ-profile in equatorial configuration ($\delta\hat{\epsilon}^y_\mathrm{mo}$) causes TM mode phase shifts. The magnetization adjusted along the longitudinal direction ($\delta\hat{\epsilon}^z_\mathrm{mo}$) drives the TE/TM polarization conversion. Note that polarization conversion also originates from polar and equatorial magnetooptic profiles of even and odd symmetry, respectively.

The most pronounced effect can be expected if the large $E_{\mathrm{TE},y}$ and $E_{\mathrm{TM},x}$ components in the longitudinal configuration are coupled (all other coefficients involve smaller E_z fields). For large core dimension and low transverse refractive index contrast, the corresponding coupling coefficient $-\mathrm{i}\gamma \iint \xi E_{\mathrm{TE},y} E_{\mathrm{TM},x} \mathrm{d}x \, \mathrm{d}y$ reduces to $\kappa = -\mathrm{i}\pi\xi/(n\lambda)$, along with the mode profiles approaching plane waves. According to Section 1.5.1, the resulting length for TE/TM conversion is $L_\mathrm{c} = \pi/(2|\kappa|) = n\lambda/(2\xi)$, which amounts to a polarization rotation of $\Theta_\mathrm{F} = \pi/(2L_\mathrm{c}) = \pi\xi/(n\lambda)$. Thus perturbation theory yields the correct relation between the specific Faraday rotation Θ_F and the simulation parameter ξ in the limit of bulk propagation.

	s_{mo}	(s)–PS, (a)–PS	(s)/(a)–CV	$(\mathrm{s})_j/(\mathrm{s})_k$–CV, $(\mathrm{a})_j/(\mathrm{a})_k$–CV
$\delta\hat{\epsilon}^x_{\mathrm{mo}}$	$+$	0	$-\gamma \iint \xi(E_{\mathrm{s},y}E_{\mathrm{a},z} + E_{\mathrm{s},z}E_{\mathrm{a},y})\,\mathrm{d}x\,\mathrm{d}y$	0
	$-$	$-2\gamma \iint \xi E_y E_z\,\mathrm{d}x\,\mathrm{d}y$	0	$-\gamma \iint \xi(E_{j,y}E_{k,z} + E_{j,z}E_{k,y})\,\mathrm{d}x\,\mathrm{d}y$
$\delta\hat{\epsilon}^y_{\mathrm{mo}}$	$+$	$2\gamma \iint \xi E_x E_z\,\mathrm{d}x\,\mathrm{d}y$	0	$\gamma \iint \xi(E_{j,x}E_{k,z} + E_{j,z}E_{k,x})\,\mathrm{d}x\,\mathrm{d}y$
	$-$	0	$\gamma \iint \xi(E_{\mathrm{s},x}E_{\mathrm{a},z} + E_{\mathrm{s},z}E_{\mathrm{a},x})\,\mathrm{d}x\,\mathrm{d}y$	0
$\delta\hat{\epsilon}^z_{\mathrm{mo}}$	$+$	0	$\mathrm{i}\gamma \iint \xi(E_{\mathrm{s},x}E_{\mathrm{a},y} - E_{\mathrm{s},y}E_{\mathrm{a},x})\,\mathrm{d}x\,\mathrm{d}y$	0
	$-$	0	0	$\mathrm{i}\gamma \iint \xi(E_{j,x}E_{k,y} - E_{j,y}E_{k,x})\,\mathrm{d}x\,\mathrm{d}y$

Table 6.1: Coupling coefficients Eq. (6.4) for different magnetooptic configurations, and for different symmetries of the coupled modes and of the magnetooptic permittivity contribution. s_{mo}: sign in $\delta\hat{\epsilon}_{\mathrm{mo}}(x,y) = s_{mo}\delta\hat{\epsilon}_{\mathrm{mo}}(x,-y)$; (s)–PS, (a)–PS: diagonal coupling coefficients $\kappa_{s,s}$, $\kappa_{a,a}$, with the profile of one hybrid symmetric or hybrid antisymmetric mode inserted; (s)/(a)–CV: off-diagonal coupling coefficient $\kappa_{s,a}$ evaluated for one symmetric and one antisymmetric mode; (s)/(s)–CV, (a)/(a)–CV: off-diagonal coupling coefficient $\kappa_{j,k}$ for two different modes of identical symmetry.

	s_{mo}	TE–PS	TM–PS	TE/TM–CV
$\delta\hat{\epsilon}^x_{\mathrm{mo}}$	$+$	0	0	$-\gamma \iint \xi(E_y^{\mathrm{TE}}E_z^{\mathrm{TM}} + E_z^{\mathrm{TE}}E_y^{\mathrm{TM}})\,\mathrm{d}x\,\mathrm{d}y$
	$-$	$-2\gamma \iint \xi E_y^{\mathrm{TE}}E_z^{\mathrm{TE}}\,\mathrm{d}x\,\mathrm{d}y$	$-2\gamma \iint \xi E_y^{\mathrm{TM}}E_z^{\mathrm{TM}}\,\mathrm{d}x\,\mathrm{d}y$	0
$\delta\hat{\epsilon}^y_{\mathrm{mo}}$	$+$	$2\gamma \iint \xi E_x^{\mathrm{TE}}E_z^{\mathrm{TE}}\,\mathrm{d}x\,\mathrm{d}y$	$2\gamma \iint \xi E_x^{\mathrm{TM}}E_z^{\mathrm{TM}}\,\mathrm{d}x\,\mathrm{d}y$	0
	$-$	0	0	$\gamma \iint \xi(E_x^{\mathrm{TE}}E_z^{\mathrm{TM}} + E_z^{\mathrm{TE}}E_x^{\mathrm{TM}})\,\mathrm{d}x\,\mathrm{d}y$
$\delta\hat{\epsilon}^z_{\mathrm{mo}}$	$+$	0	0	$\mathrm{i}\gamma \iint \xi(E_x^{\mathrm{TE}}E_y^{\mathrm{TM}} - E_y^{\mathrm{TE}}E_x^{\mathrm{TM}})\,\mathrm{d}x\,\mathrm{d}y$
	$-$	0	0	0

Table 6.2: Analogon to Table 6.1, using notational conventions for well polarized or semivectorial fundamental *modes. TE–PS, TM–PS: diagonal coupling coefficients $\kappa_{TE,TE}$ and $\kappa_{TM,TM}$, respectively. TE/TM–CV: off-diagonal coefficients $\kappa_{TE,TM}$.*

Coupling coefficients for planar magnetooptic waveguides emerge from the entries of Table 6.2 if the y-integrations are skipped, and for vanishing E_x, E_z fields for TE modes and E_y components for TM modes, respectively. By definition, the perturbational profile is constant in the y-direction, thus symmetric. Table 6.3 surveys the remaining effects.

In this thesis we adopt the following practical viewpoint for the simulation of nonreciprocal behaviour, i.e. for modeling opposite directions of light propagation. The basic geometries of all simulated magnetooptic devices are longitudinally homogeneous and mirror symmetric with respect to $y \to -y$, thus symmetric with respect to rotating the coordinates by π around the x axis, apart from the magnetooptic permittivity contributions. Assuming the origin to be located in the symmetry plane $y = 0$, this operation reverses the y- and z-components of the static magnetization $(M_x, M_y, M_z)(x,y) \to (M_x, -M_y, -M_z)(x,-y)$.

	TE–PS	TM–PS	TE/TM–CV
$\delta\hat{\epsilon}^{x}_{\mathrm{mo}}$	0	0	$-\gamma \int \xi E_y^{\mathrm{TE}} E_z^{\mathrm{TM}} \,\mathrm{d}x$
$\delta\hat{\epsilon}^{y}_{\mathrm{mo}}$	0	$2\gamma \int \xi E_x^{\mathrm{TM}} E_z^{\mathrm{TM}} \,\mathrm{d}x$	0
$\delta\hat{\epsilon}^{z}_{\mathrm{mo}}$	0	0	$-\mathrm{i}\gamma \int \xi E_y^{\mathrm{TE}} E_x^{\mathrm{TM}} \,\mathrm{d}x$

Table 6.3: Planar magnetooptic coupling coefficients. For notations, see the caption of Table 6.2.

Consequently, light propagation in positive and negative z directions can be modeled with the formalism from Chapter 1 for propagation in $+z$-direction, simply by adjusting $\boldsymbol{M}$ and ξ accordingly. The terms 'forward' and 'backward' refer to simulations with opposite ξ-profiles, where we do not attempt to trace signs consistently. In the relevant cases of even magnetooptic profiles for the equatorial and the longitudinal configuration, and of odd profiles for the polar configuration, this convention leads directly to reverting the sign of ξ for modeling contrarily propagating waves. In all cases we deal only with *positive* propagation constants.

Thus, if a mode with index m is subject to a magnetooptic propagation constant perturbation $\delta\beta_m^{\mathrm{f}} = \kappa_{mm}$ for forward propagation, the propagation constant shift for backward propagation is $\delta\beta_m^{\mathrm{b}} = -\kappa_{mm}$. The magnetooptic phase shift is nonreciprocal. The difference of both perturbations, the difference between the propagation constants $\beta_m^{\mathrm{f}} = \beta_m + \delta\beta_m^{\mathrm{f}}$ and $\beta_m^{\mathrm{b}} = \beta_m + \delta\beta_m^{\mathrm{b}}$ observed in forward and backward directions in the magnetooptic waveguide, is called the 'nonreciprocal phase shift' $\Delta\beta_m = \beta_m^{\mathrm{f}} - \beta_m^{\mathrm{b}} = \delta\beta_m^{\mathrm{f}} - \delta\beta_m^{\mathrm{b}} = 2\kappa_{mm}$, which is the experimentally accessible quantity.

6.2 Nonreciprocal phase shifters

A number of proposals for integrated optical isolators or circulators rely on the nonreciprocal phase shifting properties of magnetooptic waveguides. Among these are Mach-Zehnder interferometers [5, 36] or directional couplers [98, 37]; cf. e.g. Ref. [32, 130] for a more detailed survey. Most work is concerned with analysing and optimizing the phase shift of TM modes, for single and double layer geometries [165]. This effect has been widely experimentally studied as well. Refs. [11, 164] report on recent advances regarding rib waveguide structures. Planar magnetooptic waveguides do not exhibit a phase shift for TE modes, according to Table 6.3. Maybe therefore the TE phase shift has not been considered, until recently two possibilities to realize the required antisymmetric magnetooptic profile in rib geometries have been proposed [110, 13]. There is also some experimental evidence for the effect [40]. Section 6.2.2 deals with this configuration. Usually, integrated lasers emit TE polarized light, hence the TE phase shift may become more important for isolator applications than the TM effect. Provided that both polar and equatorial magnetooptic waveguides can be fabricated side by side on a single substrate, the combination of nonreciprocal TE and TM phase shifters may lead to polarization independent interferometry based isolator devices, as investigated in Ref. [180].

6.2.1 TM phase shifter

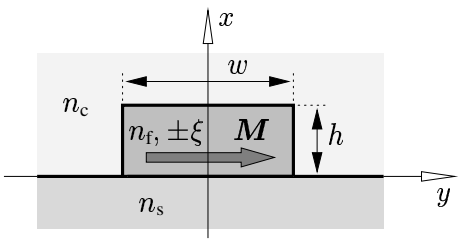

Figure 6.1: Transversely magnetized magnetooptic raised strip waveguide. The parameters of the subsequent computations are $w = 2.0\,\mu$m, $n_s = 1.95$, $n_f = 2.302$, $n_c = 1.0$, $\lambda = 1.3\,\mu$m, $\xi = 0.005$, corresponding to $\Theta_F = 3000°/$ cm.

Figure 6.1 shows an example for a magnetooptic waveguide in equatorial configuration with the magnetization oriented perpendicular to the direction of light propagation, parallel to the substrate surface. Its dominant effect is a shift of TM propagation constants. For a semivectorial basic TM field H_y, the corresponding entry of Table 6.2 evaluates to

$$\delta\beta = -\frac{\iint \frac{\xi}{n^4}\left(H_y - \frac{1}{\beta^2}\partial_y^2 H_y\right)\partial_x H_y \,\mathrm{d}x\,\mathrm{d}y}{\iint \frac{1}{n^2}\left(H_y - \frac{1}{\beta^2}\partial_y^2 H_y\right) H_y \,\mathrm{d}x\,\mathrm{d}y}. \tag{6.5}$$

Further simplification is possible by neglecting the terms $\beta^{-2}\partial_y^2 H_y$, e.g. for the fundamental modes of a slab like waveguide. Assume the cross section to be divided by horizontal boundaries at $x = h_j$, $j = 0, \ldots, N$ into $N+2$ layers with vertically constant permittivities given by $(\xi, n)(x, y) = (\xi_j, n_j)(y)$, if $h_{j-1} < x < h_j$ for $j = 0, \ldots, N+1$, with h_{-1} and h_{N+1} to be interpreted as $\pm\infty$. Then partial x-integration over the piecewise defined fields in the numerator yields the expression

$$\Delta\beta = 2\delta\beta = \frac{\sum_{j=0}^{N} \int \left(\frac{\xi_{j+1}}{n_{j+1}^4}(y) - \frac{\xi_j}{n_j^4}(y)\right) H_y^2(h_j, y)\,\mathrm{d}y}{\iint \frac{1}{n^2} H_y^2 \,\mathrm{d}x\,\mathrm{d}y} \tag{6.6}$$

for the nonreciprocal phase shift $\Delta\beta$ of a slab like semivectorial TM mode [165]. The effect may be viewed to arise from the horizontal discontinuities in the magnetooptic profile, weighted by the local mode intensity. Eq. (6.6) adequately explains the geometry dependencies of the effect; therefore it forms the basis for further optimization of nonreciprocal devices based on TM phase shifts, as exemplified in Section 7.2.1. Note that, in the special case of a planar three layer waveguide employed as a TM phase shifter, a semianalytical optimization procedure can be applied [131], which leads to universal charts for optimized geometry and the resulting phase shift.

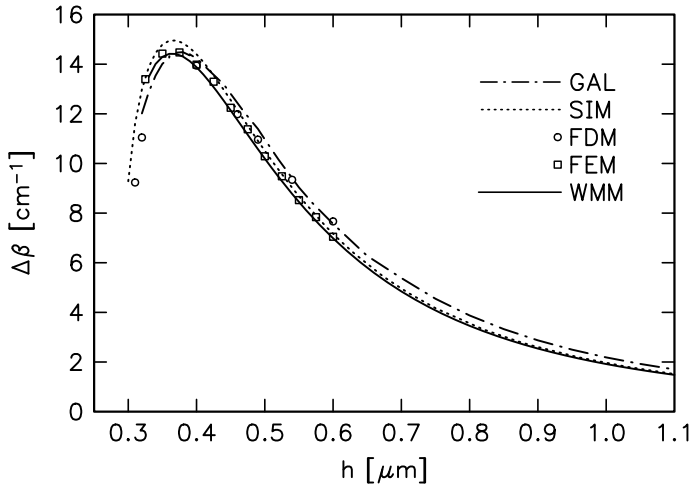

Figure 6.2: Nonreciprocal phase shift $\Delta\beta$ versus the strip height h, for the waveguide of Figure 6.1. GAL: results of the Galerkin method [126], SI: simulations based on the spectral index method [125], FDM: finite difference results [38], FEM: finite element simulations [121], WMM: the mode solver of Chapter 3 (semivectorial).

The structure of Figure 6.1 has been repeatedly investigated in our group, mainly with the purpose of assessing newly implemented modeling approaches. Results for the nonreciprocal phase shift of the fundamental TM mode are summarized in Figure 6.2. We have added a curve with data based on semivectorial WMM mode fields, which obviously matches the previous results well. While the phase shift has been evaluated by employing the full expression (6.5), for this waveguide there is no visible change in Figure 6.2, if the results of the simplified relation (6.6) are plotted.

All simulations shown in Figure 6.2 rely on the semivectorial approximation. Apart from the finite difference calculations of Ref. [38], where the magnetooptic permittivity contribution has been directly incorporated

into the discretization scheme, the methods differ only in the mode solver employed for generating the modes of the corresponding isotropic structure. The magnetooptic effect has been incorporated later via perturbation theory. Thus Figure 6.2 mainly gives evidence for the agreement in the underlying mode profiles.

Unfortunately, these curves must be looked upon with caution. This is revealed by inspecting the effective mode indices plotted in Figure 6.3.

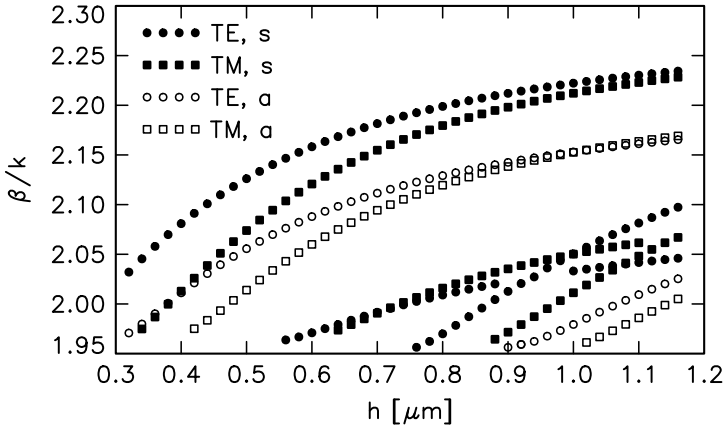

Figure 6.3: For the waveguide of Figure 6.1: effective mode indices β/k versus the strip height h. Results from semivectorial WMM mode simulations, for E_y- (TE) and H_y-fields (TM) of even (a) and odd (s) mirror symmetry with respect to $y = 0$.

The broad waveguide is single-moded for TM polarization up to a height of $0.4\,\mu$m only. Below, in the most interesting region with high nonreciprocal phase shift, the relevant fundamental TM mode is almost degenerate with the first order TE mode; the semivectorial dispersion curves cross. With the corresponding physical hybrid fields being of the same symmetry, this is precisely the situation mentioned in Section 3.3, where the fully vectorial WMM must be suspected to be not reliable. Investigations of analogous configurations have been reported e.g. in Ref. [96]. The almost degenerate modes turn out to be strongly hybrid, and their dispersion curves do not cross, but repel each other. Interference of the two hybrid modes leads to periodical conversion between an x-polarized field of even symmetry $y \to -y$ and an odd, y-polarized electrical field [72]. While this phenomenon can be employed for the design of polarization converters [94], reliable modeling of the promising experiments seems to be difficult [95]. Obviously, semivectorial simulations are not adequate.

6.2.2 TE phase shifter

According to Section 6.1, the nonreciprocal phase shift for TE modes requires a magnetooptic permittivity contribution, which is of odd symmetry with respect to the symmetry plane of the waveguide. Two approaches for a realization with rib waveguides have been proposed: a compensation wall at the rib center [13], and a guiding film with strip domains. Here we focus on the latter configuration. The section reports on numerical simulations related to Ref. [110]. Ref. [40] gives experimental confirmation for the TE phase shift.

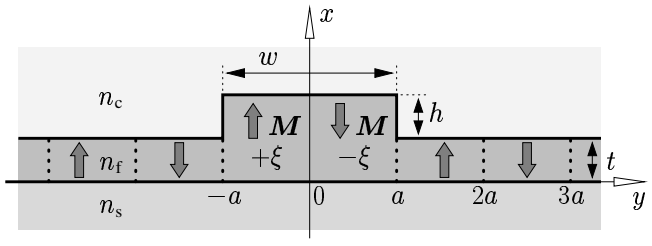

Figure 6.4: Normally magnetized rib waveguide with a domain lattice. The lattice period $2a$ matches the rib width w. The simulations assume permittivity and wavelength parameters of $n_s = 1.9$, $n_f = 2.2$, $n_c = 1.0$, $\lambda = 1.3\,\mu$m, $\xi = \pm 0.005$.

Consider a magnetooptic rib waveguide in the polar configuration, e.g. the geometry of Figure 6.4. The magnetization is oriented perpendicular with respect to the direction of propagation and perpendicular to

the substrate. The asymmetric magnetooptic profile ξ causes mainly a shift of TE propagation constants. With a semivectorial basic field E_y inserted, the related entry of Table 6.2 reads

$$\delta\beta = \frac{k^2}{2\beta^2} \frac{\iint \xi \, \partial_y E_y^2 \, \mathrm{d}x \, \mathrm{d}y}{\iint \left(E_y - \frac{1}{\beta^2} \partial_y^2 E_y \right) E_y \, \mathrm{d}x \, \mathrm{d}y} \,. \tag{6.7}$$

A considerable phase shift may be expected for a mode the intensity profile of which has large y-derivatives. Thus strongly guiding structures with high lateral refractive index contrast, i.e. deeply etched waveguides, are favorable for TE phase shifters.

In contrast to the TM case, it is obviously not adequate to skip the y derivatives in the denominator of Eq. (6.7). Analogously to Section 6.2.1, we specialize to a piecewise constant, vertically sliced permittivity profile. The cross section shall be divided by vertical boundaries at $y = b_j$, $j = 0, \ldots, N$ into $N + 2$ slices with horizontally constant permittivities given by $(\xi, n)(x, y) = (\xi_j, n_j)(x)$, if $b_{j-1} < y < b_j$ for $j = 0, \ldots, N + 1$, with b_{-1} and b_{N+1} to be interpreted as $\pm\infty$. As before, the numerator can be simplified by partial integration, now along the y-direction. However, the piecewise defined basic mode field is discontinuous at the vertical boundaries: $n_j^2(x) E_y^-(x, b_j) = n_{j+1}^2(x) E_y^+(x, b_j) = (\epsilon E_y)(x, b_j)$, where indices $+$ and $-$ indicate appropriate left and right limits, and where the last term defines the (continuous) dielectric displacement. Using this notation, one obtains

$$\Delta\beta = 2\delta\beta = -\frac{k^2}{\beta^2} \frac{\sum_{j=0}^{N} \int \left(\frac{\xi_{j+1}}{n_{j+1}^4}(x) - \frac{\xi_j}{n_j^4}(x) \right) (\epsilon E_y)^2(x, b_j) \, \mathrm{d}x}{\iint \left(E_y - \frac{1}{\beta^2} \partial_y^2 E_y \right) E_y \, \mathrm{d}x \, \mathrm{d}y} \tag{6.8}$$

for the nonreciprocal phase shift $\Delta\beta$ of a semivectorial TE mode, the TE analogon to Eq. (6.6). The vertical discontinuity lines in the magnetooptic profile cause the phase shift, this time weighted by the squared dielectric displacement. Note that the numerator of Eq. (6.8) alternatively reads

$$\sum_{j=0}^{N} \int \left(\xi_{j+1}(x) (E_y^+(x, b_j))^2 - \xi_j(x) (E_y^-(x, b_j))^2 \right) \mathrm{d}x \,. \tag{6.9}$$

Next we refer to the configuration of Figure 6.4. Assume the material and geometry parameters to be adjusted such that the domain walls are parallel to the rib, with the period of the domain lattice $2a$ matching the rib width w. One of the walls shall be located at the symmetry plane at the center of the rib. Then the oppositely directed magnetization in adjacent domains results in a periodical, piecewise constant magnetooptic profile. The domain walls are located at $b_j = ja$, where indices j now extend over the entire integer domain. Using the above notation, the perturbations ξ_j for all slices vanish, except on the magnetooptic film: $\xi_0(x) = +\xi$ and $\xi_1(x) = -\xi$ for $0 < x < t + h$; $\xi_{2m}(x) = +\xi$ and $\xi_{2m+1}(x) = -\xi$ for $0 < x < t$, with nonzero integers m.

According to Table 6.1, all modes in this waveguide are subject to nonreciprocal phase shifts. Figure 6.5 shows propagation constants for the lowest order modes of both polarizations and the corresponding phase shifts, computed with the full perturbation expression from Table 6.2. As expected, the TM phase shifts turn out to be comparably small. For the TE modes, the shape of the curves may be explained with the help of Eq. (6.8). For modes close to cut-off with a widely spread field, the contributions of several domain walls almost cancel in the denominator, and the nonreciprocal effect remains small. For wide ribs, mainly the wall at the rib center is relevant, but the normalized field strength at $y = 0$ decreases with growing w. Inbetween the nonreciprocal phase shift exhibits a maximum. In contrast, the central wall does not contribute to the phase shift of the first order TE mode. Its phase shift is due to the discontinuities at the rib flanks at $y = \pm a$, thus the shift is of of opposite sign. Note that the TE_1 phase shift reaches the same magnitude as the effect for the TE_0 mode.

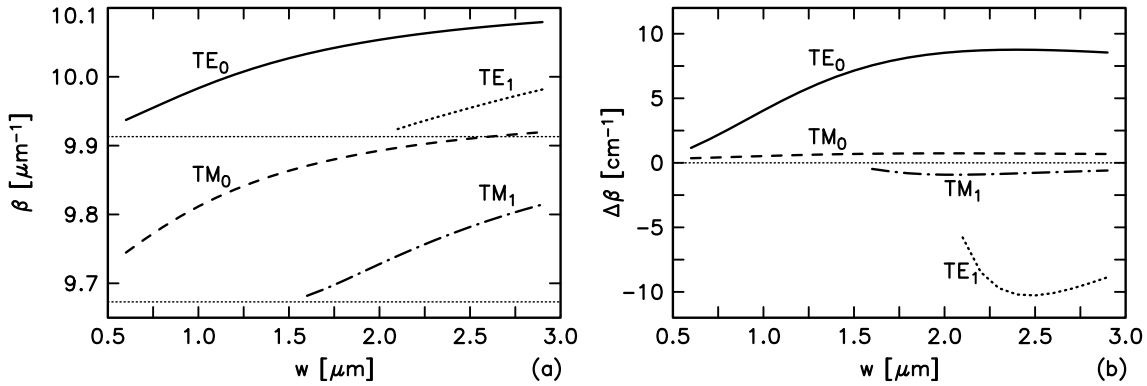

Figure 6.5: Propagation constants β (a) and nonreciprocal phase shift $\Delta\beta$ (b) for the structure of Figure 6.4 with $t = 0.5\,\mu$m, $h = 0.15\,\mu$m, versus the rib width w. The horizontal lines in (a) indicate the propagation constants of the corresponding outer slab waveguides of thickness t.

All data in Figure 6.5 were computed with the semivectorial approximation. Some caution is advisable, since here the configuration discussed at the end of Section 1.1.6 is realized, which must be suspected to be leaky. Additionally, for widths w around $2\,\mu$m, the propagation constants of the fundamental TM and first order TE mode are in close proximity, which may render the semivectorial approximation invalid.

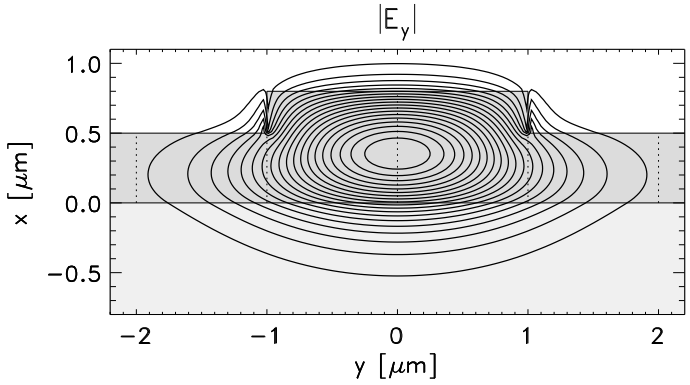

Figure 6.6: E_y field profile of the fundamental TE mode for a waveguide according to Figure 6.4 with dimensions $h = 0.3\,\mu$m, $w = 2.0\,\mu$m, $t = 0.5\,\mu$m. The corresponding effective mode index is $\beta/k = 2.1036$. The dotted lines indicate the locations of the domain walls, leading to a nonreciprocal phase shift of $\Delta\beta = 12.9\,\text{cm}^{-1}$.

However, for an application one will usually focus on the phase shift of the fundamental TE mode. Figure 6.6 illustrates a corresponding field profile. Due to the pronounced discontinuities at the rib flanks, simplified modeling via the effective index method is not well defined. Note that Eq. (6.8) needs the field to be evaluated exactly on these sidewalls.

Eq. (6.8) can be formulated more specifically with respect to Figure 6.4:

$$\Delta\beta = 2\delta\beta = 2\frac{k^2\xi}{\beta^2\mathcal{N}}\left\{\sum_m \int_0^t E_y^2(x,2ma)\,\mathrm{d}x - \sum_m \int_0^t E_y^2(x,(2m+1)a)\,\mathrm{d}x \right. \tag{6.10}$$
$$\left. -\frac{1}{2}\int_t^{t+h}(E_y^+(x,-a))^2\,\mathrm{d}x + \int_t^{t+h} E_y^2(x,0)\,\mathrm{d}x - \frac{1}{2}\int_t^{t+h}(E_y^-(x,a))^2\,\mathrm{d}x\right\},$$

with a normalization factor $\mathcal{N} = \iint (E_y - \beta^{-2}\partial_y^2 E_y)E_y\,\mathrm{d}x\,\mathrm{d}y$. As above, indices $+$, $-$ mean the field to be evaluated at $y = -a + \delta$ or $y = a - \delta$, respectively, for an infinitely small distance δ. The first two sums in Eq. (6.10) represent the strictly periodical structure in the film region below $x = t$, while the latter terms are the contributions of the three discontinuity lines above. At the rib flanks, the jumps in the magnetooptic profile are only half as large as in the center, therefore factors $1/2$ accompany the first and the third term in the second line.

Figure 6.7 shows Eq. (6.10) evaluated for a number of different rib heights h. Especially large etching depths turn out to be advantageous since, with growing confinement, the normalized field strength at the central

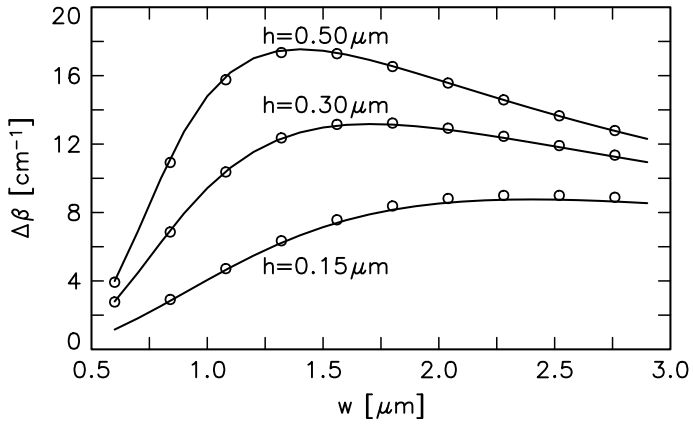

Figure 6.7: Nonreciprocal phase shift $\Delta\beta$ for varying widths w and heights h of rib waveguides as in Figure 6.4, with $t = 0.5\,\mu$m. Lines and markers show results based on semivectorial and fully vectorial WMM simulations, respectively.

wall $y = 0$ increases, while it decreases at the adjacent discontinuities at $y = \pm a$. Both effects raise the nonreciprocal phase shift. At the same time, semivectorial modeling becomes more and more questionable. Hence we have checked the validity of the approximation, using vectorial WMM modes as basic fields and the full perturbational expression from Table 6.1. The coincidence of the markers and lines in Figure 6.7 indicates that semivectorial calculations are appropriate for the fundamental modes of these waveguides.

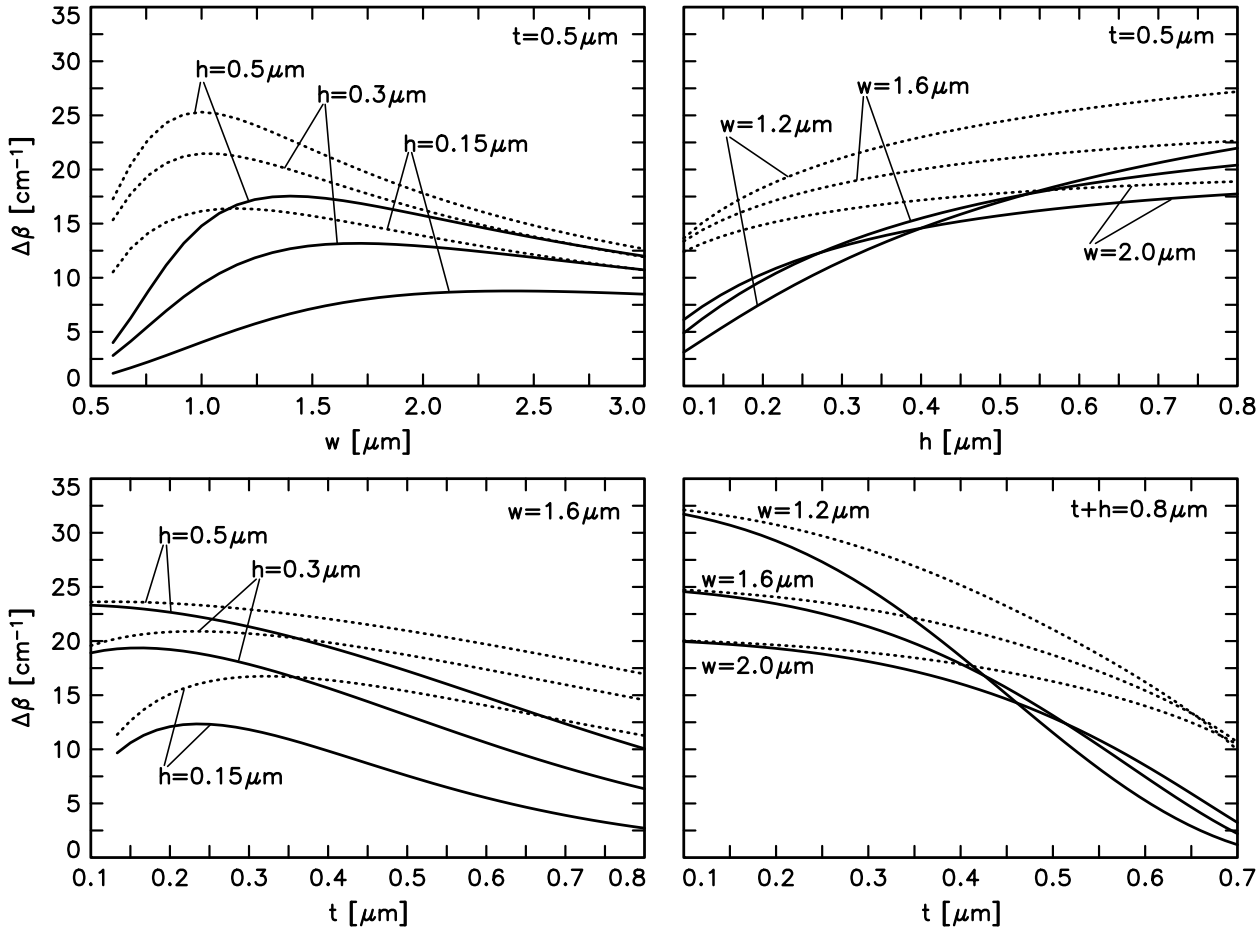

Figure 6.8: Nonreciprocal TE phase shift for waveguides as in Figure 6.4, comprising a domain lattice (continuous lines) or a compensation wall the center of the rib (dotted lines). Varied geomety parameters are the rib height h, width w, and the lateral film thickness t. Material parameters are as given for Figure 6.4.

Analogous semivectorial WMM simulations lead to the plots of Figure 6.8, showing the influence of the geometry parameters h, w, t. The charts compare the nonreciprocal phase shift achievable with a domain

lattice configuration (Figure 6.4, with the lattice period $2a$ adjusted to the rib width w) and the phase shift effected by a compensation wall [13]. For the latter configuration, only the central magnetooptic boundary is present, with additional small contributions to Eq. (6.8) from the rib flanks. In contrast to the domain lattice, the phase shift from the central discontinuity is not diminished by contributions from the adjacent domain walls, thus usually the nonreciprocal effect is larger for a waveguide with a compensation wall, provided that a comparable magnitude of the magnetooptic profile can be achieved. For a more detailed discussion of the geometry dependencies, and for questions regarding the experimental feasibility, we refer to Refs. [10, 39].

The largest effect arises from deeply etched ribs with strong lateral confinement. Thus it is tempting to try the raised strip waveguides from the following section, assuming that the almost square cores can be divided at $y = 0$ into two oppositely Faraday rotating domains, either by a domain or a compensation wall (both have equal effects in this case). For waveguides (i), (ii), (iii), (iv) of Table 6.4, one obtains nonreciprocal TE phase shifts of $\Delta\beta/\,\mathrm{cm}^{-1} = 42, 36, 30, 26$. This should be compared with the highest levels of the phase shift in Figure 6.8 (although the material parameters do not exactly coincide). An application in an interferometric isolator is investigated in Ref. [180].

6.3 Polarization converters

Besides a series of proposals exploiting the nonreciprocal phase shift in magnetooptic waveguides, most theoretical and experimental work on integrated optical isolators was concerned with setups analogous to microoptic devices where the waveguide is used as a nonreciprocal polarization rotator between two polarizers. This corresponds to the longitudinal configuration of Section 6.1 where the direction of light propagation and the orientation of the magnetization are parallel. One of the major problems with this concept in integrated form is to overcome form birefringence: usually the propagation constants for modes of different polarizations are different. This limits the maximum power transfer ratio and thus deteriorates the isolation. To achieve phase-matching for TE- and TM-like modes, a number of techniques were proposed. Among these are the periodic reversal of the magnetization [151], the use of anisotropic top layers [166], of multilayered waveguide structures [99, 108], growth induced birefringence [4], the application of stress [27], Dammann's geometry [26], and thickness tuning for planar [175] and ridged waveguides [176].

In contrast to isotropic planar waveguides, for rib waveguides there are certain configurations where the wavenumbers for modes of both dominant polarizations are exactly equal. This can be realized as follows. For a planar-like raised strip waveguide with a thin and wide core, usually the propagation constant of the fundamental TE mode exceeds that of the fundamental TM mode. If the rib is continuously narrowed and raised, the device becomes a planar-like waveguide again, but with the role of the transverse axes exchanged. Consequently there is an intermediate configuration with almost square core and phase matched modes. Presenting the numerical results of Ref. [76], this section gives a detailed numerical analysis of the effects relevant for isolating performance with emphasis on fabrication tolerances.

We will employ coupled mode theory as formulated in Section 1.5.1, based on the two fundamental vectorial modes of isotropic lossless cores. The magnetooptic effect, linear birefringence, and isotropic absorption are considered as perturbations. Section 6.3.2 states a model for an isolator setup. In Section 6.3.3, first order expansions of the degree of polarization conversion lead to simple perturbational expressions for fabrication tolerances of all structural parameters. These formulas are applied to a series of raised strip waveguides and compared to directly numerically evaluated tolerances in the main part of Section 6.3.4.

Obviously a direct way to achieve phase matching is to use square cores embedded in a homogeneous cladding. Section 6.3.5 reports on our results for such waveguides.

Due to the extreme sensitivity of the phase matching condition, this is one of the few occasions where we have observed the semivectorial approximation to be insufficient. With this approximation the shape of curves for the polarization conversion (e.g. in Figure 6.12(i)) remains, but the positions of the maxima are shifted by amounts exceeding the tolerances to be calculated. Therefore we use only fully vectorial, hybrid

mode fields as a basis for the numerical experiments of Sections 6.3.4, 6.3.5. Although the WMM mode solver is the state of art, the results for waveguide dimensions in Table 6.4 and the limit for the maximum achievable isolation should be looked upon with caution. However, the observed tendencies and estimates for fabrication tolerances seem to be reliable.

6.3.1 Relevant permittivity perturbations

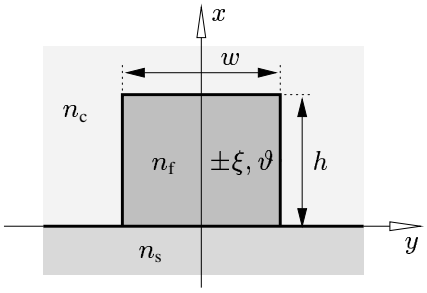

Figure 6.9: Magnetooptic raised strip waveguide. Structural parameters are the height h and width w of the rib, the refractive indices n_s, n_f, n_c of the substrate, the guiding film, and the cover material, respectively. ξ and ϑ correspond to magnitude and orientation of the magnetization in the strip region.

The following simulations are concerned with raised strip waveguides as sketched in Figure 6.9. We assume the substrate and cover to be made of lossless isotropic material with homogeneous permittivities $\epsilon_s = n_s^2$ and $\epsilon_c = n_c^2$. The permittivity tensor $\hat{\epsilon}_f = n_f^2 + \delta\hat{\epsilon}$ of the core region $0 < x < h$, $-w/2 < y < w/2$, in the following indicated by the box symbol $\square$, consists of a lossless isotropic contribution of the refractive index n_f, and a residual $\delta\hat{\epsilon}$. This is again a sum of several terms, which are specified in the next paragraphs.

Magnetooptic core

The magnetooptic core shall be magnetized in the y-z-plane at an angle ϑ with respect to the longitudinal direction. Section 6.1 and Table 6.1 predict the coupling coefficients

$$\kappa_{jj}^{\mathrm{mo}} = \xi \sin\vartheta \frac{\omega\epsilon_0}{2P_j} \iint_{\square} E_{jx} E_{jz} \,\mathrm{d}x\,\mathrm{d}y \tag{6.11}$$

and

$$\kappa_{jk}^{\mathrm{mo}} = \mathrm{i}\xi \cos\vartheta \frac{\omega\epsilon_0}{4\sqrt{P_j P_k}} \iint_{\square} (E_{jx} E_{ky} - E_{jy} E_{kx}) \,\mathrm{d}x\,\mathrm{d}y \quad \text{for} \quad j \neq k\,, \tag{6.12}$$

where indices $j, k =$ TE, TM indicate the two basic hybrid modes of opposite symmmetry, or different dominant polarization, respectively.

Eq. (6.11) is the nonreciprocal phase shift for the TM-like mode. This shift remains small since the integrated product of the E_x- and E_z-fields almost vanishes. For the TE-like mode the phase shift is two orders of magnitude smaller due to its tiny E_x-component. The off-diagonal coupling coefficients $\kappa = \kappa_{\mathrm{TE,TM}} = \kappa_{\mathrm{TM,TE}}^*$ (6.12) drive the mode coupling. They combine only those parts of the fields which are in the core area; thus the conversion length in the waveguide exceeds the length $L_c^{\mathrm{bulk}} = n_f\lambda/2\xi = \pi/2\Theta_F$ for plane waves in a bulk medium. According to Table 6.1, an inclination of the magnetization with respect to the y-z-plane adds a tiny contribution to the coupling coefficient, but it does not lead to a phase shift. We will therefore restrict the simulations to $\varphi = \pi/2$ (cf. Eq. (6.2)).

Anisotropy

For a typical YIG-film grown on a (111)-oriented GGG-substrate, growth- and stress-induced anisotropies cause the diagonal component at the x-position of the permittivity tensor to be different from the elements

on y- and z-positions [43]. This effect is accounted for by a dimensionless anisotropy parameter a in the corresponding permittivity perturbation:

$$\delta\hat{\epsilon}_{\text{anis}} = \frac{a}{2}\begin{pmatrix} -1 & 0 & 0 \\ 0 & 1 & 0 \\ 0 & 0 & 1 \end{pmatrix} . \tag{6.13}$$

While $\delta\hat{\epsilon}_{\text{anis}}$ does not contribute to the coupling coefficients κ due to mode symmetry, it is responsible for additional phase shifts

$$\kappa_{jj}^{\text{anis}} = \frac{a}{2}A_j \quad \text{with} \quad A_j = \frac{\omega\epsilon_0}{4P_j}\iint_{\square}(-E_{jx}^2 + E_{jy}^2 + E_{jz}^2)\,\mathrm{d}x\,\mathrm{d}y\,. \tag{6.14}$$

Absorption

If the core material attenuates the intensity of a plane wave as $\sim \exp(-\alpha z)$ with a small attenuation constant α, this causes an imaginary permittivity perturbation $\delta\epsilon_{\text{abs}} = -\mathrm{i}n_{\text{f}}\alpha/k$. According to Section 1.3.1, the propagation constants β_j get imaginary parts

$$\kappa_{jj}^{\text{abs}} = -\mathrm{i}\alpha_j/2\,, \quad \text{with} \quad \alpha_j = \alpha\sqrt{\frac{\epsilon_0}{\mu_0}}\frac{n_{\text{f}}}{2P_j}\iint_{\square}|\boldsymbol{E}_j|^2\mathrm{d}x\,\mathrm{d}y\,. \tag{6.15}$$

If we adopt the approximation of equal attenuation for both modes, the propagation equations (1.73) carry over to the lossy system. Both amplitudes C_j must be multiplied by a factor $\exp(-\bar{\alpha}z/2)$, where $\bar{\alpha} = (\alpha_{\text{TE}} + \alpha_{\text{TM}})/2$ is the average attenuation, and the device of length L shows an additional power loss $\sim \exp(-\bar{\alpha}L)$.

This approximation amounts to neglecting terms $(\alpha_{\text{TE}} - \alpha_{\text{TM}})/4|\kappa|$ and $\sim \Delta\beta'(\alpha_{\text{TE}} - \alpha_{\text{TM}})/|\kappa|^2$. The latter vanish for phase matched waveguides. The former should have an effect comparable to a phase difference $\Delta\beta'/2|\kappa|$. If one can tolerate an error in the polarization conversion η (Eq. (1.75)) up to 10^{-3}, then $(\alpha_{\text{TE}} - \alpha_{\text{TM}})/4|\kappa|$ must not exceed 0.03. This condition is indeed fulfilled, as we will show in Section 6.3.4.

However, for larger differences in the mode attenuations α_{TE} and α_{TM}, Eqs. (1.73) have to be modified. This will be necessary for materials with higher losses if the relevant mode fields differ considerably, or if the damping must be assumed anisotropic. The latter may be the case if the absorption related to the Faraday rotation (magnetic circular dichroism) turns out to be non-negligible. Note that the type of damping introduced here models the intrinsic material absorption only.

6.3.2 Simulation of an experimental setup

The isolator setup employs a magnetooptic polarization rotating waveguide of total length $L = L_{\text{c}}/2$ which is set between a front polarizer adjusted to the TE-position and a back polarizer at an angle of 45° with respect to the y-direction.

Simulation of forward propagating light starts with a TE-polarized Gaussian beam (input power P_{in}) the diameter and maximum location of which has been adjusted to the mode profile average. It passes the front polarizer without modification. Overlap (1.74) with the mode profiles yields the initial amplitudes for coupled mode propagation along a distance $L = L_{\text{c}}/2$. The output power $P_{\text{out}}^{\text{f}}$ is then determined by projecting $\boldsymbol{\mathcal{E}}$ on a unit vector $\boldsymbol{n} = (\sin\alpha_{\text{o}}, \cos\alpha_{\text{o}}, 0)$ in the direction of the back polarizer at $\alpha_{\text{o}} = 45^\circ$,

$$P_{\text{out}}^{\text{f}} = \frac{1}{2}\sqrt{\frac{\epsilon_0}{\mu_0}}\iint|\boldsymbol{\mathcal{E}}(x, y, L, t)\cdot\boldsymbol{n}|^2\mathrm{d}x\,\mathrm{d}y\,. \tag{6.16}$$

We assume that the total power after the polarizer is detected.

Backward light propagation starts with a -45° polarized Gaussian beam of equal shape and input power (the sign reflects the convention for backward propagation, see Section 6.1) and ends with the projection (6.16) on a unit vector according to the front polarizer at $\alpha_\mathrm{i} = 0$. With the backward output power $P^\mathrm{b}_\mathrm{out}$, isolation and transmission loss are defined as $\mathrm{IS} = -10\log(P^\mathrm{b}_\mathrm{out}/P^\mathrm{f}_\mathrm{out})$ and $\mathrm{LO} = -10\log(P^\mathrm{f}_\mathrm{out}/P_\mathrm{in})$. The simulations described in the subsequent sections are within the limits of this model.

There are at least two effects that may limit the achievable isolation. Ideally, in the backward direction, the light that has passed the back polarizer should excite the modes of both polarizations with equal amplitudes. But in the case of non-embedded waveguides the profiles of TE- and TM-like modes differ slightly, and the initial amplitudes will be different as well, resulting in a small amplitude of the TE-like mode at the front polarizer. Additionally, the hybrid TM-like mode has a small E_y component, and consequently at the front polarizer its contribution cannot be completely suppressed. Both causes will be investigated in Sections 6.3.4 and 6.3.5.

The significant refractive index contrasts of the materials under consideration cause these simulations to be somewhat questionable. Neither is the input Gaussian profile a valid electromagnetic field in the waveguide region, nor are the mode fields solutions of the Maxwell equations in the homogeneous region behind the waveguide end. With the simple overlap model, no realistic estimation of the power transition, or the loss LO, respectively, can be expected since the amounts of reflection, transmission, and radiation at input and output are not known with sufficient precision. However, these quantities cancel in the expression for the isolation IS, and we will obtain more realistic results.

From the viewpoint of modeling, these difficulties arise in the following way. To evaluate the input power P_in consistently, one has to provide a refractive index value for the homogeneous material that supports the Gaussian beam, since both the electric and the magnetic part of the input field are required for the overlap integral. With values between the two plausible choices ($n = 1.0$, a beam focussed in air, and $n = n_\mathrm{f}$, most of the power is concentrated in the core region) the power $P = |C_\mathrm{TE}|^2 + |C_\mathrm{TM}|^2$ inside the waveguide typically changes by a factor of $n_\mathrm{f} \approx 2$. The same problem arises at power output, where according to our model even with a perfectly adjusted polarizer power is diminished by the factor n_f, if the field profile is transferred from the guiding core to free space without change.

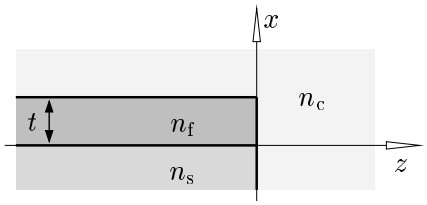

Figure 6.10: End facet of a planar three layer waveguide.

A way out may be advanced modeling of the waveguide/air-transitions e.g. by means of semianalytical approaches as attempted in [21, 122, 161]. As an example, what is to be expected for waveguide end facets with typical garnet parameters, consider a planar waveguide as sketched in Figure 6.10. We assume the nomalized fundamental guided mode to be incident from the left on the facet at $z = 0$ and are interested in the mode reflectivity, i.e. the reflected mode amplitude. Figure 6.11 shows some corresponding results.

The simplest approach would be to view the mode as a plane wave, traveling in the film medium, perpendicularly incident on the dielectric boundary between refractive indices n_f and n_c. Fresnel's law for perpendicular incidence evaluates to the reflectivity levels indicated by the horizontal lines. Parts of the mode fields penetrate in the substrate region, thus the contrast n_s, n_c may be relevant also.

Better agreement with the numerical curves can be found if one recalls the basic zig-zag model for mode propagation, which associates a mode with interfering plane waves propagating at an angle α with respect to the z-axis, where $\cos\alpha = \beta/(kn_\mathrm{f})$. With this angle of incidence and refractive indices n_f, n_c, Fresnel's equations yield the curves marked as FE(β). These become reasonable for small mode angles and plane mode profiles at large waveguide thicknesses where the modes are well confined in the film region. For modes close to cutoff, the mode angle exceeds the limit of total reflection at the interface at $z = 0$ for

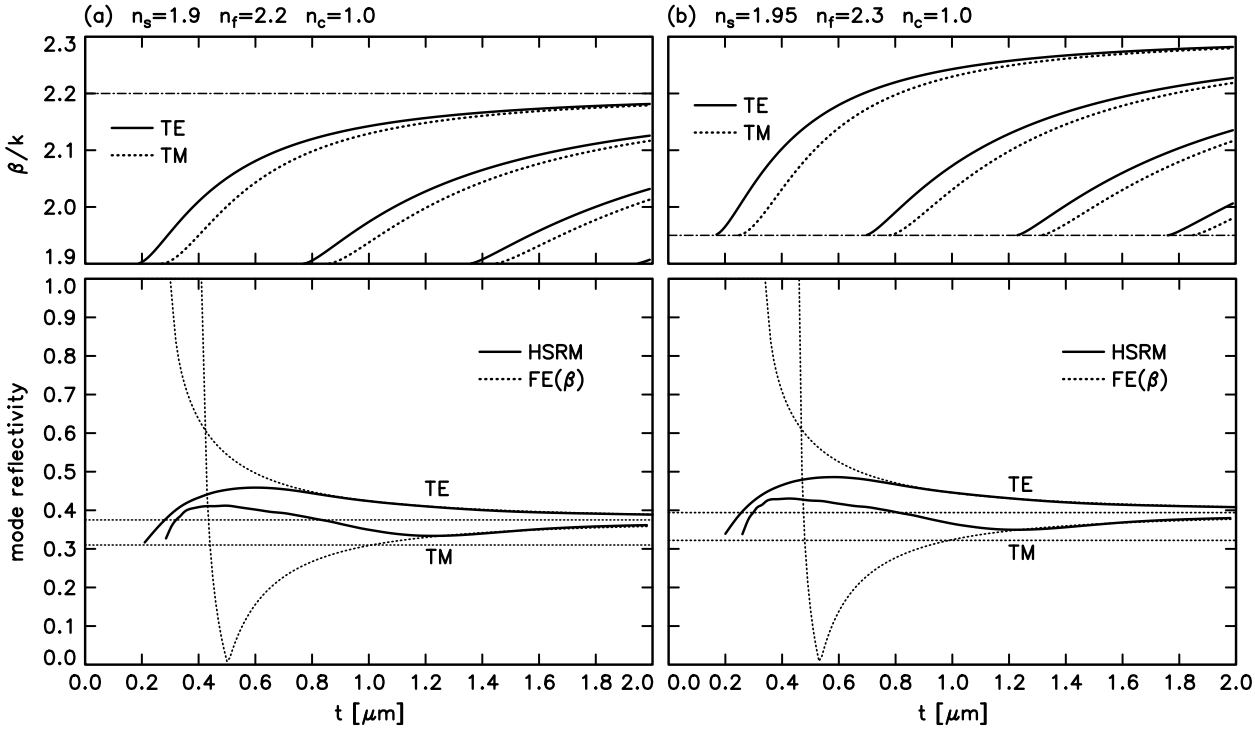

Figure 6.11: Effective mode indices (top) and reflectivities (bottom, for the fundamental modes) versus the film thickness for a waveguide facet as sketched in Figure 6.10. Refractive index values are as given on top of the charts; the wavelength parameter is $\lambda = 1.3\,\mu$m. HSRM: numerical calculated data according to Ref. [162, 160], FE(β): Fresnel's equation for appropriate polarization, for plane waves with incidence angle as prescribed by the propagation constant (see the text). Horizontal lines in the bottom charts indicate the reflectivity levels $(n_f - n_c)/(n_f + n_c)$ (upper line) and $(n_s - n_c)/(n_s + n_c)$ (lower line) according to Fresnel's equation for perpendicular incidence.

small t. For slightly larger thicknesses, the Fresnel equation predicts vanishing TM reflectivity for a mode incident at Brewster's angle. Both phenomena should have been noticed experimentally; obviously the zig-zag reflectivity model fails here.

Semianalytical modeling with the Half-Space-Radiation Method [162, 160] predicts curves which somehow interpolate between the perpendicular incidence of plane waves in the substrate for modes close to cutoff at small t, and the zig-zag estimate for large t. Note the pronounced difference between the TE and TM reflectivities. The HSRM model takes the large permittivity jump at the film surface explicitely into account. Some caution is required with the results, since the method relies on a small transverse refractive index contrast between substrate and film (the ratio $(n_\mathrm{f} - n_\mathrm{s})/n_\mathrm{f}$ should be below 10 % [122, 160]; the parameters of Figure 6.11 yield 14 % and 15 %, respectively). Unfortunately, up to now no experiments with garnet waveguides have been carried out which could give access to the reflectivity values directly. The reflectivity loss is always mixed up with insertion loss, attenuation loss, uncertainties related to varying incoupling conditions for TE and TM, etc.

For the deeply etched raised strip waveguides of Section 6.3.4, because of similar mode profiles, the reflectivity difference between TE and TM polarized modes may be expected to be smaller. The difference vanishes exactly in case of the square embedded waveguides of Section 4.2.2. However, in this thesis the problem is not elaborated further. Besides, exact modelling of the rather artificial setup sketched above is not useful for a Faraday rotator in an integrated optical chip, e.g. in hybrid form [146].

6.3.3 Fabrication tolerances

For estimating the fabrication tolerances of a setup as described above, an idealized treatment should be sufficient. Assuming the final mode amplitudes of the forward analysis to be equal to the initial amplitudes of the backward simulation, the combined light paths are equivalent to a coupled mode propagation over twice the device length $2L$. In the forward direction no power is lost, $P_{\text{in}} = P^{\text{f}}_{\text{out}} = |C_{\text{TE}}(0)|^2$, while the power transmission in the backward direction is given by the final amplitude of the TE-like mode as $P^{\text{b}}_{\text{out}} = |C_{\text{TE}}(2L)|^2 = P^{\text{f}}_{\text{out}}(1 - \eta(2L))$, with TE and TM substituted for the mode indices in Eqs. (1.73)–(1.75). Thus the deviation $\Delta\eta = 1 - \eta(2L)$ of the polarization conversion from unity becomes relevant. The effects mentioned in the last section contribute another small fraction $rP^{\text{f}}_{\text{out}}$ of the power input to the backward output power, such that the total isolation is $\text{IS} = -10\log(\Delta\eta + r)$.

Our model structures are formulated first in terms of parameters n_{s}, n_{f}, n_{c}, h, w, λ which determine the wavenumbers and the shape of the basic modes. Then there are the quantities ξ and ϑ which are responsible for mode coupling and related to the length parameter L. Finally, perturbations like the diagonal anisotropy a must be checked. We will separately consider the influence of each of these parameters q, while all other quantities are kept fixed to their optimum values. If q is optimally adjusted as well, we have a phase matched waveguide of length $L_{\text{c},q}/2$ with $\eta_q(L_{\text{c},q}) = 1$. Changing q to $q + \delta q$ results in a lower conversion $\eta_{q+\delta q}(L_{\text{c},q})$. The maximum deviation Δq for a given limited conversion degradation $\Delta\eta = 1 - \eta_{q+\Delta q}(L_{\text{c},q})$ is defined as the tolerance of the parameter q.

Basic mode parameters

Assume q to be one of h, w, n_{s}, n_{c}, or n_{f} (where we keep ξ constant). In first order perturbation theory, a variation δq does not affect the shape of the basic mode fields and the coupling coefficient κ (6.12). At the same time, small propagation constant shifts $(\partial_q\beta_j)\delta q$ detune the phase matching according to $\Delta\beta'_{q+\delta q} = (\partial_q\beta_{\text{TE}} - \partial_q\beta_{\text{TM}})\delta q$. Expanding $\eta_{q+\delta q}(L_{\text{c},q})$ up to first order in δq^2 gives $\eta_{q+\delta q}(L_{\text{c},q}) \approx 1 - (\partial_q\beta_{\text{TE}} - \partial_q\beta_{\text{TM}})^2\delta q^2/4|\kappa|^2$. For this quantity to be larger than $1 - \Delta\eta$, the parameter q may vary by no more than

$$\Delta q = \pm\frac{2|\kappa|\sqrt{\Delta\eta}}{|\partial_q\beta_{\text{TE}} - \partial_q\beta_{\text{TM}}|}\,. \tag{6.17}$$

Obviously, along with κ, the tolerances for rib height, rib width and the refractive indices scale linearly with the off-diagonal permittivity ξ, i.e. linearly with the specific Faraday rotation Θ_{F}. Thus, materials with improved magnetooptic effect will not only lead to shorter devices, but also to relaxed tolerance requirements.

For an evaluation of Eq. (6.17), expressions must be supplied for the gradients of the propagation constant. What concerns the refractive indices, Eq. (1.44) is to be applied with a diagonal permittivity perturbation $2n_{\text{s,f,c}}\delta n_{\text{s,f,c}}$ and with the integration extending over the substrate, core, and cover regions. For the rib dimensions h and w, the continuity requirements of the electromagnetic fields at dielectric boundaries must be taken into account explicitely. Expressions for the variation of the propagation constant due to the shift of boundary locations have been investigated in Sections 1.4 and 5.2. According to these formulas, Δh and Δw are approximately inversely proportional to the relevant permittivity differences.

The coupling coefficient can be written as $|\kappa| = 2n_{\text{f}}\Theta_{\text{F}}R$ with a dimensionless factor R. Therefore, if we neglect, in R, the variation of the mode shape with respect to a wavelength alteration, κ remains fixed in first order, and Eq. (6.17) applies to the wavelength parameter λ as well. Derivatives of the propagation constants with respect to the wavelength can be expressed in terms of the h- and w-gradients, see Section 1.4.3.

Device length and magnetooptic parameters

The optimum length for a phase matched device is given by $L = \pi/4|\kappa|$. An alteration δL changes the power transfer ratio at the end of the relevant light path to $\eta(2(L+\delta L)) \approx 1 - (\pi\delta L/4L)^2$. Thus the tolerance for the device length is

$$\Delta L = \pm\frac{1}{2|\kappa|}\sqrt{\Delta\eta} = \pm\frac{1}{\pi}L_\mathrm{c}\sqrt{\Delta\eta}\,. \tag{6.18}$$

ΔL is the only tolerance that turns out to be reciprocal to the Faraday constant.
With regard to Θ_F itself, an expansion of $\eta_{\xi+\delta\xi}(L_{\mathrm{c},\xi}) = \sin^2(\pi(1+\delta\xi/\xi)/2)$ leads to the tolerances

$$\Delta\xi = \pm\frac{2}{\pi}\xi\sqrt{\Delta\eta} \quad \text{or} \quad \Delta\Theta_\mathrm{F} = \pm\frac{2}{\pi}\Theta_\mathrm{F}\sqrt{\Delta\eta}. \tag{6.19}$$

Assuming the specific Faraday rotation to be the parameter with the most pronounced temperature dependence $\partial_T\Theta_\mathrm{F}$, an otherwise optimally tuned device should operate properly in a temperature range of

$$\Delta T = \pm\frac{2}{\pi}\frac{\Theta_\mathrm{F}}{\partial_T\Theta_\mathrm{F}}\sqrt{\Delta\eta}\,. \tag{6.20}$$

By evaluating $\eta_{\delta\vartheta}(L_{\mathrm{c},0}) = \sin^2(\pi\cos(\delta\vartheta)/2)$, the magnetization angle ϑ can be shown to be the least critical quantity:

$$\Delta\vartheta = \pm\frac{2}{\sqrt{\pi}}(\Delta\eta)^{1/4}\,. \tag{6.21}$$

If one admits $\Delta\eta = 0.001$ (0.01), ϑ may deviate from the optimum 0° position by $\pm11^\circ$ ($\pm20^\circ$). While formally the nonreciprocal phase shift at an angle $\vartheta \neq 0$ must be considered as well, it turns out to be negligible when compared to the phase mismatch due to a detuned geometry (cf. the corresponding paragraph in Section 6.3.4).

Anisotropy

Changing the anisotropy parameter by δa shifts the propagation constants by $\delta a A_j/2$. Consequently, a must be known with a tolerance of

$$\Delta a = \pm\frac{4|\kappa|\sqrt{\Delta\eta}}{|A_\mathrm{TE} - A_\mathrm{TM}|}\,. \tag{6.22}$$

Compared to a device with isotropic core and dimensions w and h, a waveguide with anisotropic core achieves phase matching with slightly modified geometry, e.g. for parameters w and $h + \delta h$ where

$$\delta h = -\frac{a(A_\mathrm{TE} - A_\mathrm{TM})}{2(\partial_h\beta_\mathrm{TE} - \partial_h\beta_\mathrm{TM})}\,. \tag{6.23}$$

6.3.4 Results for raised strip waveguides

Device design starts with identifying suitable geometries where the fundamental modes are degenerate. For four arbitrarily chosen values of the waveguide width, the top left inset of Figure 6.12 shows the rib height dependence of the fundamental effective mode indices. The curves for TE- and TM-like modes cross at a height h which is slightly smaller than the specified width w. Analogous curves can be drawn for the variation of the width for given rib height (top right inset).

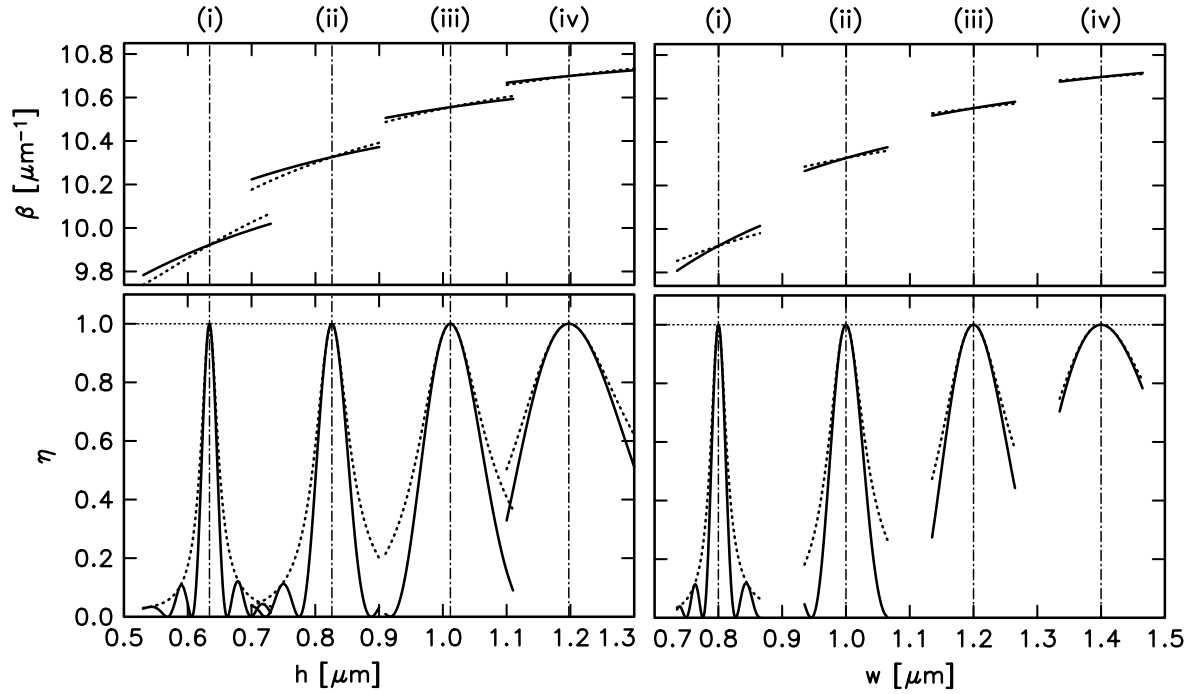

Figure 6.12: Propagation constants β (top) and polarization conversion η (bottom) versus the rib height h (left) and the rib width w (right) for waveguides as sketched in Figure 6.9. For the four fixed values of the rib width (left) and rib height (right) see Table 6.4. In the top charts, continuous lines correspond to hybrid TE-like modes, dotted lines to modes with dominant TM polarization. Continuous lines in the bottom chart show the polarization conversion $\eta(L_c)$ at the fixed lengths L_c as given in Table 6.4, while the dotted lines indicate the maximum achievable conversion η_{max} at a length adjusted to the detuned height or width. The remaining parameters are as given for Table 6.4.

Table 6.4 summarizes the geometry data for the phase matched waveguides indicated by the crossing points. The tolerances for applications in an isolator setting can be evaluated by directly calculating the mode fields for a detuned geometry. Figures 6.12 (bottom insets) and 6.13 show the dependences of the power transfer ratio η on rib height and width and wavelength variations. In the bottom parts of Table 6.4 these results are contrasted with perturbational values estimated with Eq. (6.17). There is good overall agreement, with the most pronounced differences occurring for the wavelength parameter λ. While the relevant derivatives $\partial_\lambda \beta_j$ can be accurately evaluated by Eq. (1.58) with a deviation below 1%, they are large (compared to $\partial_w \beta_j$, $\partial_h \beta_j$) and nearly equal. Therefore Eq. (6.17) with $q = \lambda$ gives the correct order of magnitude only, which should be sufficient since the wavelength turns out to be an uncritical parameter. This is a promising result with respect to the bandwidth dependences of the isolator concept. Note that the limiting values for the polarization conversion $\Delta\eta$ can be translated into limits for the isolation $\mathrm{IS} = -10\log(\Delta\eta)$ of 30 dB, 20 dB, 13 dB, 10 dB.

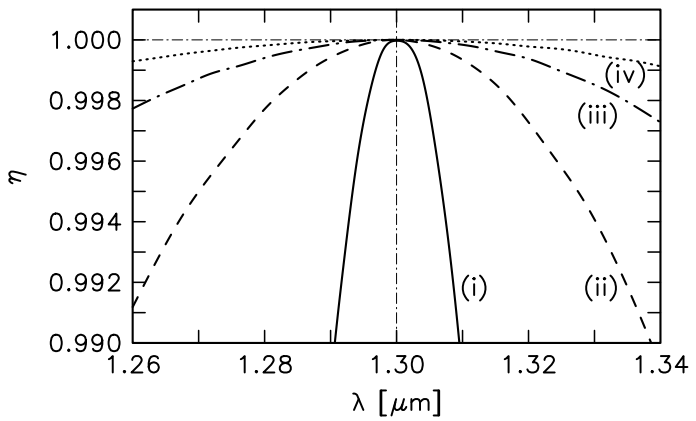

Figure 6.13: Polarization conversion η versus the operation wavelength λ for waveguides (i) to (iv) of Table 6.4. The degree of conversion η is evaluated at the fixed conversion lengths L_c corresponding to a wavelength of $\lambda = 1.3\,\mu$m. See Table 6.4 for parameters.

	(i)		(ii)		(iii)		(iv)	
w/μm	0.8		1.0		1.2		1.4	
h/μm	0.6340		0.8260		1.0118		1.1975	
L_c/μm	357		325		315		309	
$\Delta\eta = 0.001$								
Δh/nm		*0.5*		*1.2*		*2.2*		*3.9*
Δw/nm		*0.4*		*1.0*		*2.1*		*3.8*
$\Delta\lambda$/nm	3	*2*	12	*4*	25	*10*	>40	*21*
$\Delta n_s/10^{-3}$		*1*		*2*		*4*		*7*
$\Delta n_f/10^{-3}$		*1*		*3*		*5*		*8*
$\Delta L/\mu$m		*4*		*3*		*3*		*3*
$\Delta\eta = 0.01$								
Δh/nm	1.5	*1.7*	3.2	*3.7*	6.3	*7.0*	11.2	*12.2*
Δw/nm	1.5	*1.4*	3.5	*3.3*	6.8	*6.6*	12.1	*11.9*
$\Delta\lambda$/nm	9	*6*	38	*16*	>40	*34*	>40	*66*
$\Delta n_s/10^{-3}$	4	*4*	9	*8*	16	*14*	25	*23*
$\Delta n_f/10^{-3}$	3	*4*	10	*8*	17	*15*	26	*26*
$\Delta L/\mu$m		*11*		*10*		*10*		*10*
$\Delta\eta = 0.05$								
Δh/nm	3.5	*3.9*	7.3	*8.3*	14.2	*15.7*	25.1	*27.3*
Δw/nm	3.4	*3.1*	7.9	*7.3*	15.3	*14.7*	27.1	*26.6*
$\Delta\lambda$/nm	19	*14*	>40	*35*	>40	*76*	>40	*149*
$\Delta n_s/10^{-3}$	8	*8*	21	*17*	36	*31*	56	*52*
$\Delta n_f/10^{-3}$	7	*8*	22	*18*	37	*34*	58	*58*
$\Delta L/\mu$m		*25*		*23*		*22*		*22*
$\Delta\eta = 0.1$								
Δh/nm	5.2	*5.4*	10.6	*11.7*	20.5	*22.2*	36.0	*38.6*
Δw/nm	5.0	*4.4*	11.3	*10.4*	22.1	*20.9*	38.7	*37.7*
$\Delta\lambda$/nm	>20	*20*	>40	*49*	>40	*108*	>40	*210*
$\Delta n_s/10^{-3}$	11	*11*	29	*24*	51	*44*	80	*74*
$\Delta n_f/10^{-3}$	11	*11*	31	*26*	52	*48*	80	*82*
$\Delta L/\mu$m		*36*		*33*		*32*		*31*

Table 6.4: Optimum dimensions h, w, conversion length $L_c = 2L$ and fabrication tolerances for raised strip waveguides as sketched in Figure 6.9 used as nonreciprocal polarization converters. Tolerances printed in italic style are determined by perturbational expressions, while the roman numbers have been read off from curves $\eta(q)$, with $q = h, w, \lambda, n_{f,s}$ as in Figure 6.12, with the smaller difference taken in case of a nonsymmetric curve. See the text for a concise interpretation of the tolerances. Parameters not listed are the refractive indices $n_s = 1.95$, $n_f = 2.302$, $n_c = 1.0$, the nondiagonal permittivity element $\xi = 0.005$, magnetization angle $\vartheta = 0$, anisotropy $a = 0$, absorption $\alpha = 0$, and the vacuum wavelength $\lambda = 1.3\,\mu$m.

For the parameters not listed in Table 6.4, we have observed the following tendencies. The influence of the cover refractive index is less significant. Due to the small field amplitudes at the rib/air-interface and to the low refractive index ($\delta\epsilon = 2n\delta n$), the tolerances Δn_c are roughly six times the values for the substrate refractive index.

If the magnetization offset-angle ϑ is regarded as a perturbational parameter, the polarization coupling is not affected in first order, while the TE/TM phase difference $\Delta\beta$ is slightly altered. This alteration turns out to be very small: for the four waveguides of Table 6.4, the nonreciprocal TM phase shift for a maximum angle of 10° can compensate the phase mismatch for a geometry deviation of about 1Å only. In the limit of a transversely adjusted magnetization the phase shift difference is equivalent to a geometry deviation still below 1 nm. Thus, varying the direction of the magnetization cannot be used for tuning phase matching (which can be achieved for one direction of propagation only, and is therefore less useful in the current setting; cf. Section 6.4). On the other hand, precise adjustment of this direction is less important. A larger deviation from the longitudinal direction will show up mainly in a conversion length alteration, where, for waveguides (i) to (iv), values $\Delta L_c = 2\Delta L$ below 6 μm (20 μm) are tolerable. According to Figure 6.14, ϑ must be adjusted to $\pm 11^\circ$ ($\pm 20^\circ$) to guarantee $\Delta\eta \leq 0.001$ ($\Delta\eta \leq 0.01$). The same result can be obtained with the perturbational formula (6.21).

For $\Delta\eta$ below 0.001 (0.01), the nondiagonal permittivity element must be kept at $\xi = 0.005$ with tolerances of $\pm 1.0 \cdot 10^{-4}$ ($\pm 3.2 \cdot 10^{-4}$). This corresponds to tolerances for the Faraday constant $\Theta_F = 3000^\circ/\text{cm}$ of $\pm 60^\circ/\text{cm}$ ($\pm 191^\circ/\text{cm}$). For a typical temperature coefficient $\partial\Theta_F/\partial T = 3.19^\circ/\text{cmK}$ at room temperature

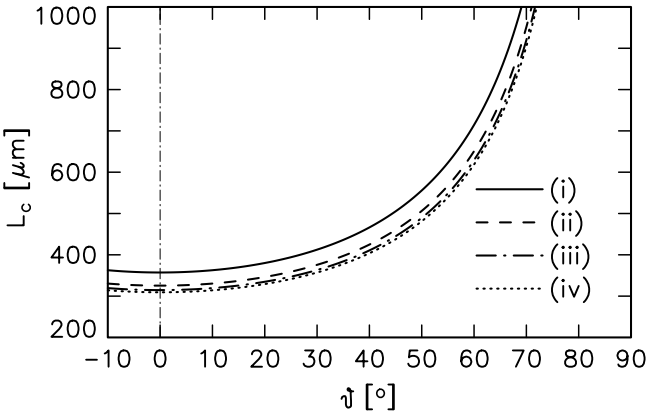

Figure 6.14: Conversion length L_c versus the angle ϑ of the magnetization with respect to the longitudinal direction, for the four waveguides of Table 6.4.

[164], the temperature should deviate by no more than 19 K (60 K), if the temperature coefficients of all other material parameters are neglected.

In contrast to the phase shifts induced by refractive index changes, the shifts (6.13) due to a variation of the anisotropy parameter a have different signs for the modes of different dominant polarizations. Thus a must be known with accuracy one order of magnitude higher. According to Eq. (6.22), $\Delta a/10^{-4}$ evaluates to 3, 10, 22, 31, for given $\Delta\eta$ of 0.001, 0.01, 0.05, 0.1, and uniformly for waveguides (i) - (iv). To compensate for anisotropy, the basic geometry must be significantly changed. From Eq. (6.23), we obtain values for $(\delta h/a)/\mu$m of 1.8, 3.8, 7.1, and 12.3 for waveguides (i) to (iv). For an anisotropy $a = 0.01$, the rib height of device (iv) should change by 123 nm from the value given in Table 6.4 to restore phase matching. In this case, consideration of anisotropy is indispensable.

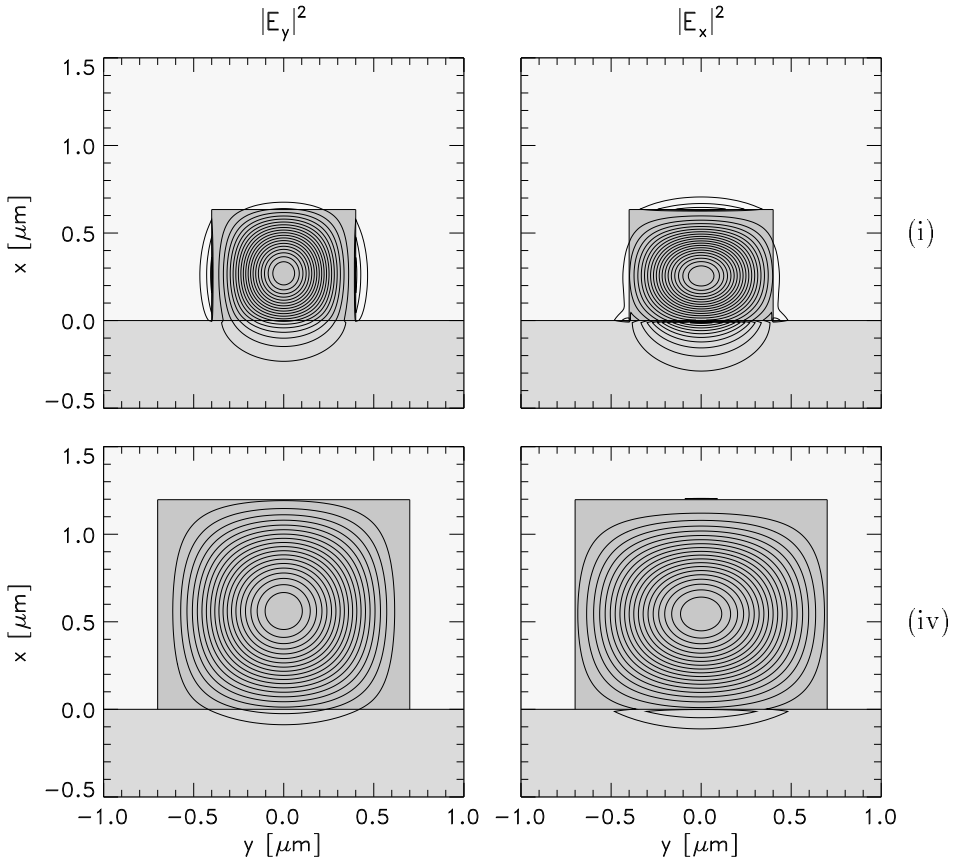

Figure 6.15: Mode intensity profiles for the dominant field components of the fundamental modes for waveguides (i) (top) and (iv) (bottom) in Table 6.4. The contours show the squared E_y-components of symmetric, TE-like modes (left) and the squared E_x-component of the antisymmetric, TM-like modes (right).

Figures 6.15 and 6.16 illustrate the relevant components of the normalized fundamental modes in waveguides (i) and (iv). The E_x-components of TM-like solutions appear almost equal in magnitude and shape to the E_y-components of the TE-like modes, with only small deviations caused by dielectric discontinuities. There the field strength and thus the absolute difference is more pronounced for the small core of waveguide (i). As can be seen by inspecting Eqs. (1.44), (6.17), this results in larger differences of the wavenumber derivatives, and thus in the tight tolerances, of (i) compared to (iv).

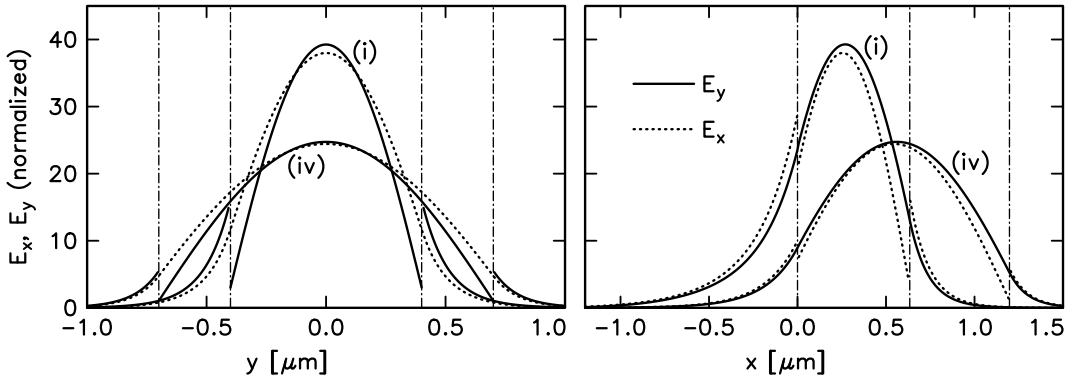

Figure 6.16: Profile sections of the dominant field components of the fundamental modes for waveguides (i) and (iv) in Table 6.4. Continuous lines correspond to E_y-components of symmetric, TE-like modes, dotted lines to the E_x-component of the fundamental antisymmetric, TM-like modes. For the left chart, fields have been evaluated on horizontal lines at $x = 0.26\,\mu$m (i) and $x = 0.55\,\mu$m (iv), close to the amplitude maxima. The right chart shows the mode amplitudes along the waveguide symmetry plane at $y = 0$.

According to Figure 6.15, even for device (i) almost all of the mode power is concentrated in the core region. Thus, by Eq. (6.15), the attenuation constants α_j/α evaluate close to unity, with differences of about 5% (i) and 1% (iv) between TE- and TM-like modes. With typical values for α as low as $1\,\mathrm{cm}^{-1}$ [33], for waveguides (i) to (iv) the relevant quantity $(\alpha_{\mathrm{TE}} - \alpha_{\mathrm{TM}})/4|\kappa|$ remains below 10^{-4}. Attenuation of both fundamental modes is almost equal and will not deteriorate the isolation.

Because of to the similar mode profiles, an initial field that has passed a polarizer at an angle of 45° excites both modes with equal amplitudes. For backward propagation, the amplitude ratio $|C_{\mathrm{TE}}/C_{\mathrm{TM}}|^2$ is indeed below 10^{-5} in the numerical simulations of setups for waveguides (i) to (iv).

Nevertheless, we obtained numerical upper limits for the isolation of about 25 dB, 30 dB, 32 dB, and 35 dB for these devices. The limits are due to the hybrid nature of the modes. In backward direction, at the position of the front TE-adjusted polarizer, almost all of the inserted power is carried by the TM mode. In our model, the polarizer blocks its large E_x-part, but the power in the small E_y component passes. As it should be, the ratios $\iint |E_y|^2 \mathrm{d}x\,\mathrm{d}y / \iint |E_x|^2 \mathrm{d}x\,\mathrm{d}y$ for the TM modes of the four waveguides evaluate to the above given limits for the maximum isolation. Note that these values depend crucially on the model for the waveguide-air transition. For the TE modes we have observed ratios of the powers assigned to x- and y-components that are almost reciprocal to the ratios given above, thus changing to TM input will not enlarge the peak isolation.

(i) and (ii) are single-mode waveguides. For (iii) and (iv), both rib height and width are enlarged, thus they support a total of six modes, one additional mode with a horizontal and one with a vertical nodal line for each polarization. Due to their asymmetric shape and differences of propagation constants, coupling with the fundamental modes will not occur. If higher order modes are excited, about half of the power passes the device in both directions and degrades the isolation. However, by means of properly focused input beams (or tapers) it should be possible to suppress this phenomenon. With circular Gaussian fields adjusted to the fundamental mode shape, the power fraction assigned to higher order modes could be kept well below 10^{-3} in our simulations.

If a polarization rotating waveguide is to be used in an integrated isolator device, e.g. in a hybrid setup [146], the relative adjustment of the components will be important. The effects of the two polarizer angles

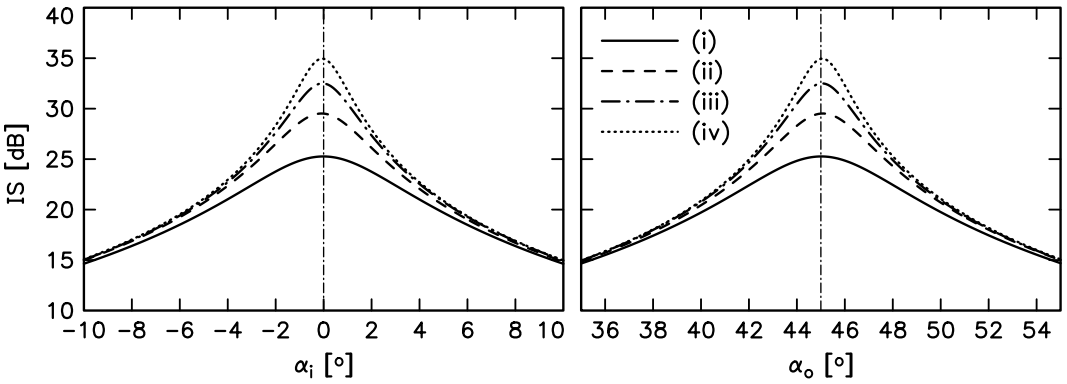

Figure 6.17: Isolation IS versus the angles α_i, α_o, of the polarizers at input (left) and (output) of an isolator setting employing the Faraday rotating waveguides of Table 6.4. An angle of $0°$ corresponds to linear polarization in the y-direction.

are easily accessible from our model. Figure 6.17 shows their influence on the isolation. For an isolation larger than 20 dB, both polarizers may not deviate by more than $\pm 5°$ from the optimum $0°$ and $45°$ positions, respectively. Both charts show the maximum levels of the isolation. Due to the small difference between the shapes of TE and TM modes, the locations of the maxima are slightly shifted from the $0°$ and $45°$ positions. Obviously this effect can well be neglected even for strongly guiding cores.

6.3.5 Results for embedded waveguides

For square embedded waveguides surrounded by a homogeneous cladding the phase matching condition is realized if, apart from the magnetooptic effect, the core material is isotropic. Figure 6.18 summarizes results for a series of such waveguides with varying core dimension and for parameters as in Section 6.3.4.

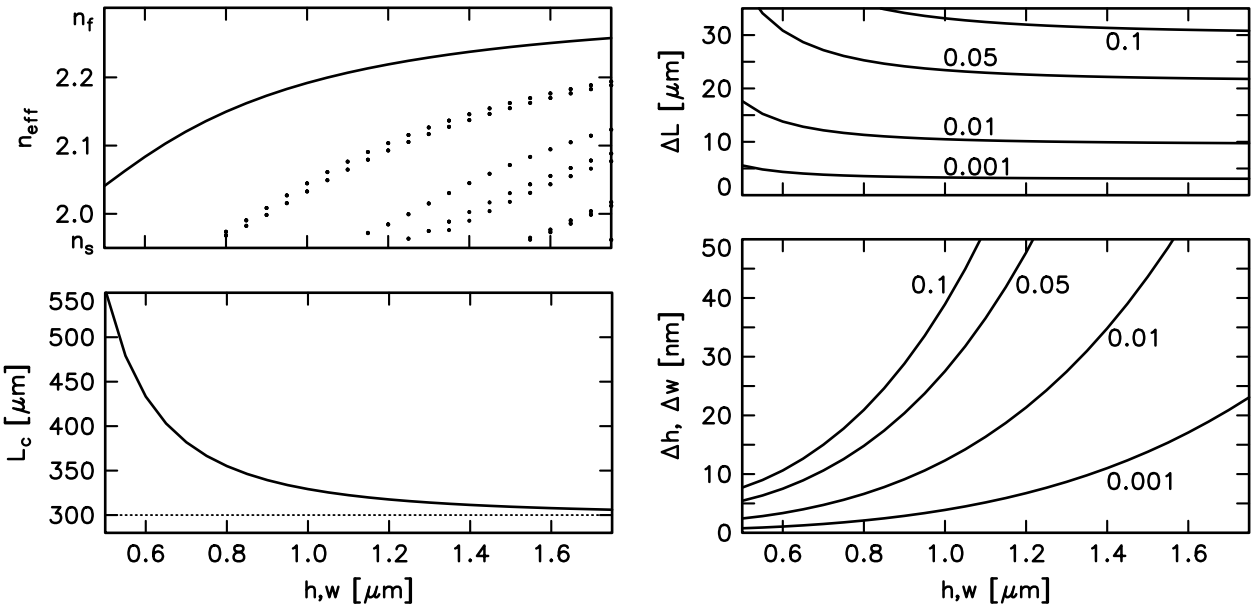

Figure 6.18: Effective mode indices n_{eff}, conversion length L_c (left) and geometry tolerances Δh, Δw, ΔL (right) versus the height and width h, w of the core for embedded waveguides of square shape. Parameters are $n_s = n_c = 1.95$, $n_f = 2.302$, $\xi = 0.005$, $\lambda = 1.3\ \mu$m (see Figure 6.9). The allowed polarization conversion deviation $\Delta\eta$ is the curve parameter in the charts on the right.

According to Figure 6.18, up to a width of about $0.8\ \mu$m the waveguides support only one mode for each polarization. For larger cores higher modes appear, all are twofold degenerate. The closely spaced dotted

lines correspond to four first order modes with one nodal line in the dominant electric component, in a direction parallel or perpendicular to the polarization. Therefore they are not fourfold degenerate.

For smaller cores less power is guided inside the magnetooptic region. Thus the mode coupling weakens, the conversion length L_c increases. The bigger cores convert the polarization along a distance already close to the length $L_c^{bulk} = 300\,\mu$m for plane waves in a magnetooptic bulk medium.

Since we have kept constant the value of the Faraday constant, the conversion length tolerances ΔL_c are also similar to the results for the uncovered strips. At the same time, the lower permittivity contrast relaxes the tolerance requirements Δh, Δw significantly. Core height and width alterations have equal effects. Scaling the waveguide does have little influence on the polarization conversion, a deviation of the core shape from a square matters. The tolerances give the maximum allowed absolute difference between the core width and height.

Due to the symmetry of the problem, in the lowest relevant order the dependence of the polarization conversion on refractive index and wavelength variations vanishes. Thus these tolerances are much larger than those worked out in Section 6.3.4.

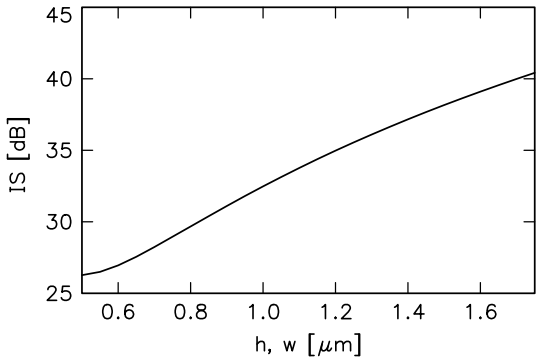

Figure 6.19: Limit for the achievable isolation IS for square embedded magnetooptic wavguides versus height and width h, w of the core. Parameters are as in Figure 6.18.

For the embedded waveguides one can again evaluate the isolation limits caused by the small mode components. As shown in Figure 6.19, these values do not deviate much from those for the raised strip waveguides of comparable height and width.

6.4 Unidirectional polarization converters

Due to the need for a 45° polarizer, integrated optical realization of the polarization converting isolator discussed in the last section will be difficult. While success with a hybrid setup has been reported in Ref. [146], a monolithically integrated device would have to be designed with polarization splitters which discriminate modes of different polarization, rather than with abitrarily orientable polarizers. Input and output are to be restricted to the TE and TM states. This may be achieved with an additional reciprocal polarization converting element, i.e. an optical active or proper anisotropic waveguide, as proposed and realized for microoptic devices [61, 123], but integration of the probably totally different materials (e.g. quartz) into the garnet basis must be suspected to raise problems. However, in contrast to the bulk configuration, for waveguide based devices there is a way to achieve the exact effect of a 45° Faraday rotator in line with a 45° optical active element *without* the latter. This proposal [77] is elaborated in the current section.

In the preceding section, the phase matching condition has been shown to be highly sensitive. A small difference in the relevant propagation constants is sufficient to diminish the achievable polarization conversion considerably. We will therefore introduce an additional nonreciprocal phase shift to the polarization converters. By means of slight geometry alterations, it should be possible to adjust phase matching for one direction of propagation. With proper length, the waveguide completely converts TE polarized light to TM polarization. Between two polarization splitters which are transparent for TE light, the input power

gets blocked in this backward direction. At the same time, oppositely propagating TE light is converted incompletely, with the remaining TE fraction passing the device in forward direction. As shown below, it is possible to design an ideally performing isolator which transmits the entire forward input.

Similar concepts have been proposed and experimentally demonstrated in Refs. [134, 135]. They rely on unidirectional mode conversion between the fundamental TM mode and the first order TE mode [134] or between the TM_0 mode and the set of TE polarized radiation modes [135], caused by a magnetization in equatorial orientation. Table 6.1 predicts phase shifts and mode conversion for two modes of equal symmetry for a symmetric perturbation $\delta\hat{\epsilon}^{y}_{\mathrm{mo}}$. While both concepts may be less critical with respect to fabrication tolerances due to wider, slightly etched waveguides (the dispersion curves of the relevant TM and TE modes versus waveguide width cross at a smaller angle), they pose problems with respect to integration, since one has to deal either with multimode waveguides or with radiated power. The concepts are not suitable for the realization of circulator devices. Additionally, a sound numerical analysis is difficult. For the first proposal, one has to calculate almost degenerate TM_0 and TE_1 modes, which are of the same symmetry, thus not separable with the current formulation of the vectorial mode problem (cf. the remarks in Section 3.3). Semivectorial modeling can be tried, but will be questionable. Simulation of the investigations of Ref. [135] would require a rigorous description of the spectrum of radiation modes. In both cases, three-dimensional vectorial beam propagation modeling of the magnetooptic structures [72] may be an alternative. However, these problems do not show up with the present proposal.

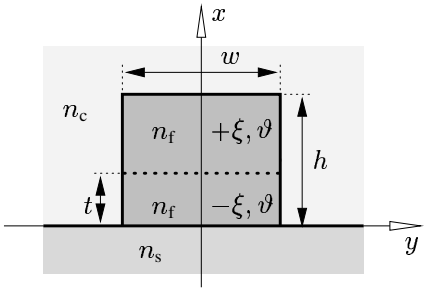

Figure 6.20: Magnetooptic double layer waveguide. The strip of height h and width w consists of two magnetooptic layers with opposite Faraday rotation ($\pm\xi$), with the in-plane magnetization oriented at an angle ϑ with respect to the z-direction. t denotes the thickness of the bottom layer, n_s, n_f, n_c are the refractive indices of the substrate, the guiding film, and the cover, respectively.

We refer to the phase matched raised strip waveguides investigated in Section 6.3, this time etched from a composite magnetooptic film where the Faraday rotation in the two layers has opposite signs (see Figure 6.20). The magnetization shall be adjusted in the y-z-plane, at an angle ϑ with respect to the z-axis. This magnetooptic profile yields both nonreciprocal phase shifts, mainly for TM modes, and polarization conversion. As we have found in Section 6.3.4, the phase shift remains negligible small for single layer waveguides. In contrast, for the double layer configuration the maximum TM phase shift, achievable in the equatorial configuration, and the TE/TM coupling coefficient in the longitudinal configuration are of equal order of magnitude. This allows to balance both effects. Figure 6.21 shows corresponding plots, for the off-diagonal coupling coefficent κ and the larger diagonal coefficient $\kappa_{\mathrm{TM,TM}} = \delta\beta_{\mathrm{TM}}$.

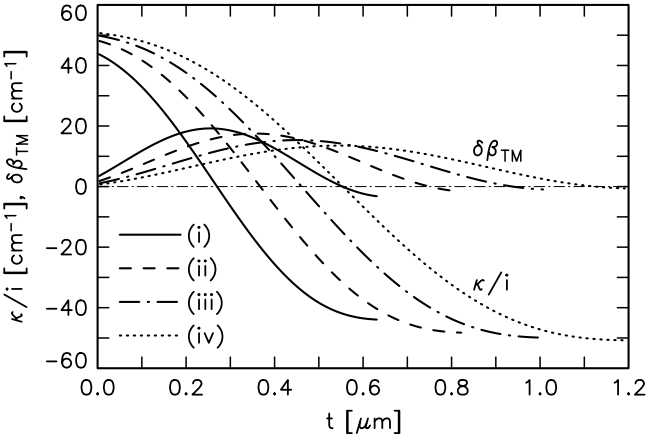

Figure 6.21: Maximum TE/TM coupling coefficient κ ($\vartheta = 0$) and maximum TM phase shift ($\vartheta = \pi/2$) for double layer waveguides, as sketched in Figure 6.20, versus the bottom layer thickness t. (i) to (iv) denote the waveguides of Table 6.5.

Eq. (6.6) explains the shape of the curves for the TM phase shift $\delta\beta_{\mathrm{TM}}$, which is approximately proportional to the mode intensity at the central boundary between the magnetooptic layers. With growing thickness t, the coupling coefficient κ changes from the maximum value, for a totally positively rotating waveguide, to zero, where the contributions from the bottom and the top layer compensate, and back to the maximum absolute value, for a totally negatively rotating waveguide.

The final device will have geometry parameters very close to the dimensions of a phase matched waveguide. The magnetooptic profile, determined by the bottom layer thickness t and by the magnetization angle ϑ, causes different propagation constants, or phase mismatch values $\Delta\beta'_{\mathrm{b}} = (\beta_{\mathrm{TE}} + \delta\beta_{\mathrm{TE}}) - (\beta_{\mathrm{TM}} + \delta\beta_{\mathrm{TM}})$ and $\Delta\beta'_{\mathrm{f}} = (\beta_{\mathrm{TE}} - \delta\beta_{\mathrm{TE}}) - (\beta_{\mathrm{TM}} - \delta\beta_{\mathrm{TM}})$ for forward and backward propagation, respectively. Demanding a backward phase matched waveguide $\Delta\beta'_{\mathrm{b}} = 0$, the mismatch for forward propagating light is $\Delta\beta'_{\mathrm{f}} = 2(\delta\beta_{\mathrm{TM}} - \delta\beta_{\mathrm{TE}})$.

The constraint of complete polarization conversion in backward direction fixes the device length to one conversion length $L_{\mathrm{c}}^{\mathrm{b}}$. In forward direction, besides a reduction of the maximum conversion, the additional phase mismatch leads to a shorter conversion length $L_{\mathrm{c}}^{\mathrm{f}}$. The forward conversion does not reach pure TM polarization, but after propagating over a distance of an even multiple of $L_{\mathrm{c}}^{\mathrm{f}}$, the light is purely TE polarized again. Thus for optimal isolator performance the magnetooptic profile is to be adjusted such that

$$L_{\mathrm{c}}^{\mathrm{b}} = \frac{\pi}{2|\kappa|} = 2mL_{\mathrm{c}}^{\mathrm{f}} = \frac{m\,\pi}{\sqrt{(\Delta\beta'_{\mathrm{f}}/2)^2 + |\kappa|^2}} \tag{6.24}$$

holds, with a natural number m. Increasing the phase mismatch $|\Delta\beta'_{\mathrm{f}}|/2 \approx |\delta\beta_{\mathrm{TM}}|$ by adjustment of t implies reduction of $|\kappa|$, or lengthening the device, respectively (cf. Figure 6.21). Therefore, $m = 1$ is the proper choice for Eq. (6.24). This amounts to a condition for ideal isolation and loss

$$|\kappa| = \frac{1}{2\sqrt{3}}\,|\Delta\beta'_{\mathrm{f}}| \quad \text{or} \quad |\kappa| = \frac{1}{\sqrt{3}}\,|\delta\beta_{\mathrm{TM}} - \delta\beta_{\mathrm{TE}}|\,, \tag{6.25}$$

in addition to the constraint of backward phase matching $\Delta\beta'_{\mathrm{b}} = 0$.

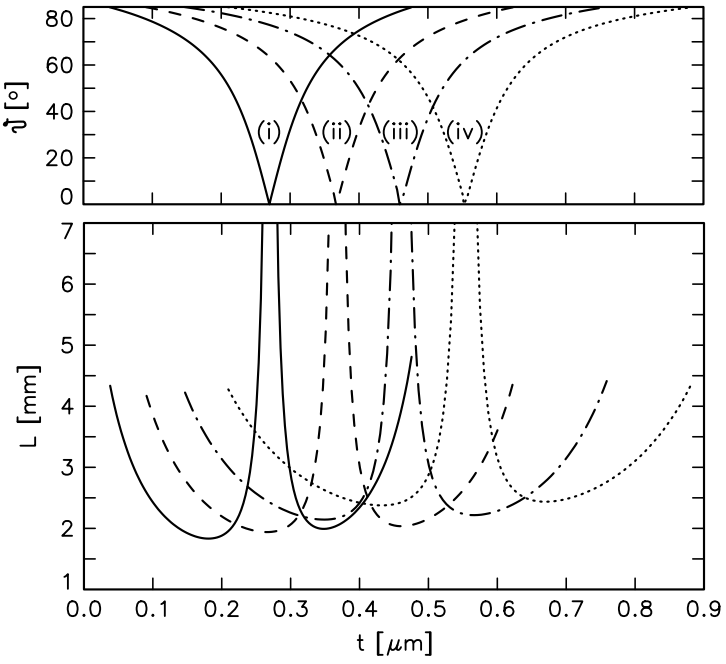

Figure 6.22: Optimum angle for isolator performance ϑ (top) and resulting isolator device length L versus the thickness t of the lower layer, for phase shifting and polarization converting waveguides as sketched in Figure 6.20, with parameters of Table 6.5.

According to Figure 6.22, the condition (6.25) can be met for most configurations t with a properly selected angle ϑ of the magnetization. The lower part of the figure shows the resulting length $L = L_{\mathrm{c}}^{\mathrm{b}} = \pi/(2|\kappa|)$. Aiming at short devices, the magnetooptic profile should be adjusted to the parameters given by the minima

	(i)	(ii)	(iii)	(iv)
$h/\,\mu$m	0.634	0.826	1.012	1.198
$w/\,\mu$m	0.798	0.995	1.191	1.387
$t/\,\mu$m	0.181	0.264	0.349	0.431
$\vartheta/^\circ$	63	65	66	68
$L/$ mm	1.83	1.94	2.14	2.38

Table 6.5: Parameters for isolating waveguides, according to Figure 6.20. Other quantities are as assumed for Section 6.3.4, $n_s = 1.95$, $n_f = 2.302$, $n_c = 1.0$, $\lambda = 1.3\,\mu$m, $\xi = \pm 0.005$, corresponding to $\Theta_F = \pm 3000^\circ/$ cm.

of these curves. Table 6.5 summarizes parameters for backward phase matched, polarization converting and phase shifting isolator waveguides.

In contrast to Section 6.3, only part of the magnetooptic effect is available for polarization conversion, and the device length must match a complete conversion length, instead of its half. Therefore the waveguides are to be about six times as long as those for the conventional setup. While a total length of 2 mm is still tolerable, according to Eq. (6.17) one has to deal with tolerances which are about six times as strict as those given in Section 6.3.4 (where we do not go into details again). This price has to be paid for the change of input and output from TE/45° polarized light to TE and TM modes, and the possibility of monolithic integration, where the difficulties mentioned in Section 6.3.2 do not occur.

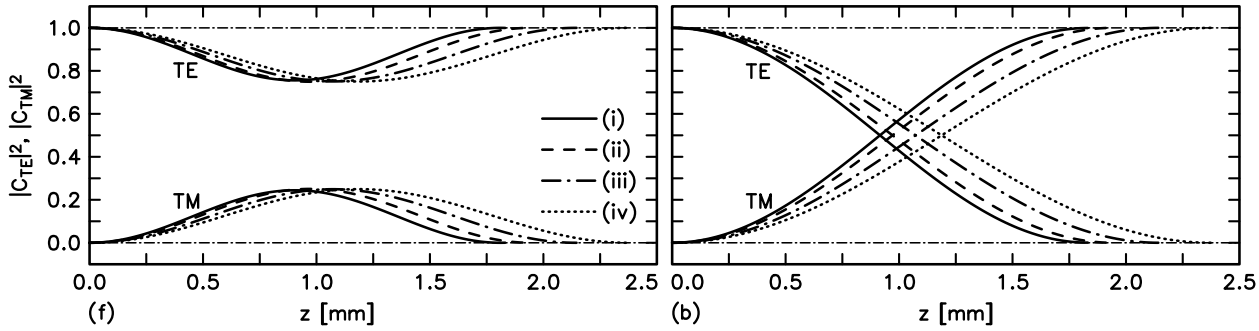

Figure 6.23: Relative mode power $|C_{TE}|^2$, $|C_{TM}|^2$ for light propagation in the waveguides of Table 6.5 versus the propagation distance z, for forward (f) and backward propagation (b). The TE mode is launched at $z = 0$.

Finally, Figure 6.23 illustrates the light propagation. While in forward direction the TE input is transformed to TE output, TE input leaves the device as TM polarized light in backward direction. Note that the waveguide works exactly analogously for TM input. In combination with polarization splitters, this enables the design of a polarization independent isolator, the simulation of which is the subject of Section 7.4.

7 Radiatively coupled waveguide devices

Many applications of integrated optics rely on directional couplers as basic components. Conventionally two waveguides are coupled by the evanescent mode fields between them. Since these fields decrease exponentially with the waveguide distance, branching sections must be added to obtain optically well separated input and output channels. Such sections necessarily contain long waveguide bends, which usually introduce losses and are difficult both to manufacture and to simulate. With the concept of radiative coupling [92, 85] these bends may be avoided, at least for directional couplers.

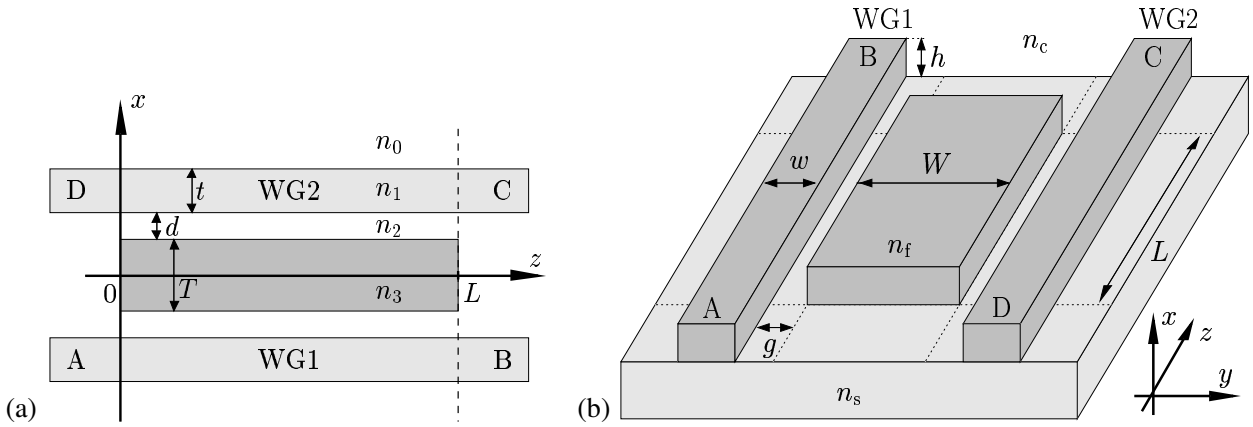

Figure 7.1: Planar (a) and three-dimensional (b) coupler geometries. The central layer or strip, respectively, couples the two identical outer waveguides WG1 and WG2 along a distance L. The structures are to be considered four port devices with input and output channels A to D.

Figure 7.1 illustrates the relevant geometries. Coupling of two parallel remote waveguides is achieved by insertion of a third thick guiding layer or a third broad strip inbetween. In the planar case, the waveguides can be considered as two leaky waveguides on opposite sides of a substrate. Power radiated into the central coupling layer by one waveguide is caught by the other one, and vice versa; a periodic coupling process develops. This motivates the term radiative coupling.

Other ways to achieve power transfer between remote waveguides include e.g. grating assisted couplers [90, 147], leaky modes of anisotropic waveguides [107], or antiresonant reflecting optical waveguides (ARROWs) [34, 7, 89, 66, 113]. In particular the latter exhibit coupling characteristics which are very similar to those of radiatively coupled waveguides, although the refractive index profiles are not comparable. As mentioned in Section 4.3.2, ARROW structures are intended to adapt the field profiles of optical fibers. In contrast, radiatively coupled waveguides usually need only a smaller number (five) of layers, or three ribs, respectively, and do not require a resonance condition to be met. In rib waveguide form, integration with other components should be easily feasible since rib waveguides are already used as input and output channels. These features distinguish them from ARROW structures of both A and B types [6].

The devices of Figure 7.1 may alternatively be viewed as three waveguide couplers with a central guide, which is very thick or broad, respectively, thus multimode. While planar three waveguide couplers were studied e.g. for use as power dividers and for power transfer (cf. e.g. [29, 22] and references cited therein), or for the purpose of wavelength filtering [47], these investigations deal with single-mode central guides only, or with central waveguides that are identical to the outer ones. There seems to be no previous investigation of three-dimensional etched rib- or strip waveguide based devices, apart from effective index approximations.

A recently published analysis [100] indicates that the subject is of current interest. Based on the spectral index method [118], the investigation is concerned with the TE power transfer characteristics of three rib waveguide couplers with single-mode central ribs made of semiconductor material.

Subsequently to a survey of the coupling features in Section 7.1, this chapter reports on our simulations of both planar and three-dimensional radiatively coupled waveguides for use as integrated optical isolators or circulators (Section 7.2) and for polarization splitting (Section 7.3). These sections include material from Refs. [129, 84, 82, 79]. Section 7.4 proposes a polarization independent isolator device, composed of radiatively coupled polarization splitters and magnetooptic polarization converters as introduced in Section 6.4. While the formerly mentioned investigations deal with linear devices, an analysis of nonlinear planar couplers has been published in [128].

The following simulations employ the propagating mode analysis technique outlined in Section 1.2, based either on directly calculated modes or on supermodes generated by coupled mode theory (cf. Section 1.5.2). An alternative is perturbational modeling using leaky modes [85, 129], which directly adapts to the viewpoint of radiative coupling. However, a theory for calculating mode leakage is established for planar structures only. Applied to systems of radiatively coupled waveguides, its accuracy deteriorates for growing central layer thicknesses, as shown in [129], although this may be partially corrected. In particular, the leaky mode approach is not capable to deal with configurations where three supermodes are relevant, which turn out to be the most interesting. We thus do not further dwell on this theory.

7.1 Coupling characteristics

Provisionally, the discussion shall be restricted to planar couplers as sketched in Figure 7.1(a). Sections 7.2.2 and 7.3.2 show that analogous features apply to three-dimensional devices.

Each of the two identical outer waveguides (refractive indices n_0, n_1, n_2, film thickness t) supports one mode with propagation constant β_*, for fixed polarization state. To achieve remote coupling between the outer waveguides, n_3 has to be larger than the effective index β_*/k, such that the isolated central waveguide (refractive indices n_2, n_3, n_2, film thickness T) supports modes beyond this level. We assume the materials, outer waveguide geometry t and gap width d to be fixed, and choose the central layer thickness T as a tuning parameter. Figure 7.2 depicts the dependence of the propagation constants β of the entire structure on T. The dispersion curves resemble the lines expected for the isolated central guide, apart from the anomaly around the effective mode index β_*/k, magnified in the second chart. Since remote coupling is intended, we are interested in large thicknesses T, thus in modes of high order.

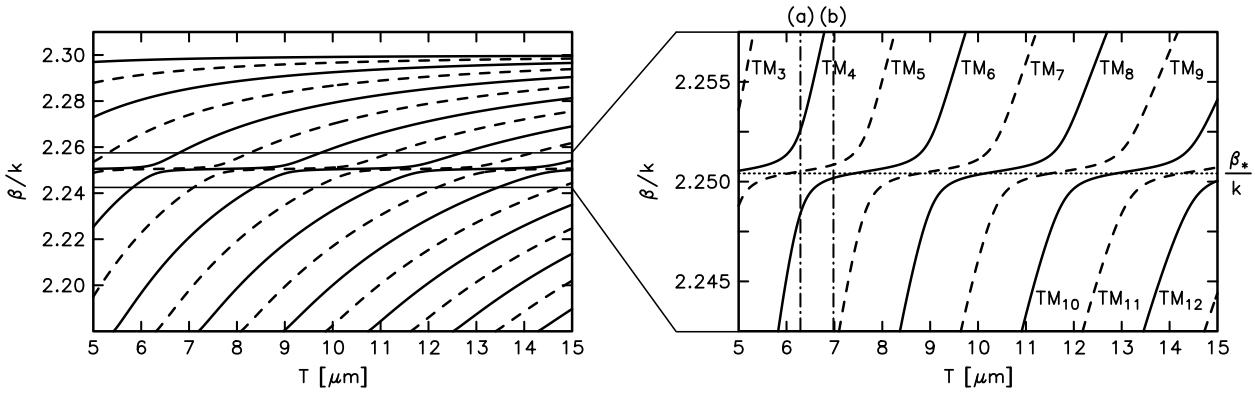

Figure 7.2: Effective mode indices for TM-polarized modes versus the thickness of the central layer. Remaining parameters are: $\lambda = 1.3\,\mu$m, $n_0 = n_2 = 2.18$, $n_1 = n_3 = 2.30$, $t = 0.8\,\mu$m, $d = 0.8\,\mu$m. Symmetric modes are indicated by continuous lines, antisymmetric modes by dashed lines. The dotted line in the right inset shows the level $\beta_*/k = 2.25041$.

Dispersion curves $\beta(T)$ for modes of different order are tightly connected. Assume that the structure with thickness $T = T_0$ supports a mode with propagation constant β. In the central layer, the mode function varies sinusoidally along the x coordinate with a spatial period of $2\pi/\sqrt{k^2 n_3^2 - \beta^2}$, see Eq. (2.16). Therefore, modes with the same propagation constant β exist in a set of waveguides with thicknesses $T_j = T_0 + j\pi/\sqrt{k^2 n_3^2 - \beta^2}$ ($j = 1, 2, \ldots$), too. These modes are of equal (even j) or opposite symmetry (odd j) with respect to the reflection $x \to -x$. The shape of the mode function remains unchanged apart from the sine or cosine term inserted on a distance $T_j - T_0$. Note that this reasoning is applicable both to single planar waveguides and to composite structures if the thickness of one guiding layer is varied. In particular, it explains the approximate periodicity of the curves in the magnifying inset of Figure 7.2 for a small β-interval, and the decreasing gradient of the dispersion curves with growing T (this property should be incorporated, if the perturbation theory of Refs. [85, 129] is to be applied for large waveguide separation).

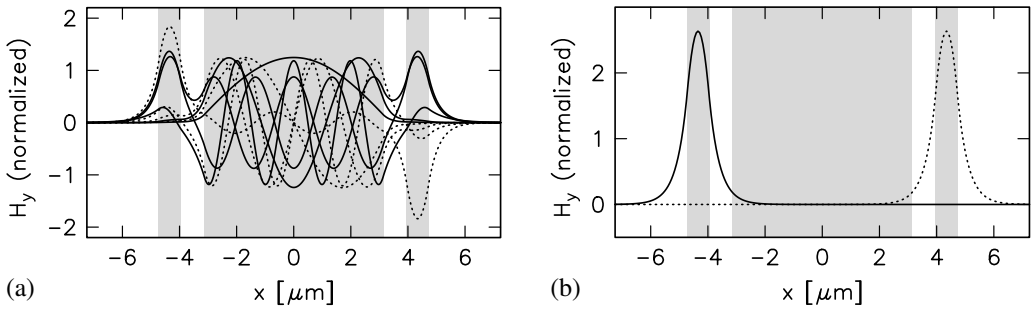

Figure 7.3: Coupling section supermodes (a) and outer waveguides modes (b), for a coupler marked (a) in Figure 7.2, $T = 6.29\,\mu$m. The structure supports 9 TM modes. Shading indicates the guiding regions.

Figure 7.3 surveys the mode profiles. For a distinction between the relevant mode sets, in the following the modes of the entire three waveguide structure as depicted in (a) are occasionally named 'supermodes', analogously to Section 1.5.2. Most of these functions exist on the central core only, with small amplitudes in the regions of the outer waveguides. In contrast, a few selected modes have large amplitudes on the outer cores and lower field strength on the central waveguide, along with their propagation constants beeing close to the level β_*. These modes will be relevant, if the structure is excited by the outer waveguides modes, plotted in Figure 7.3(b).

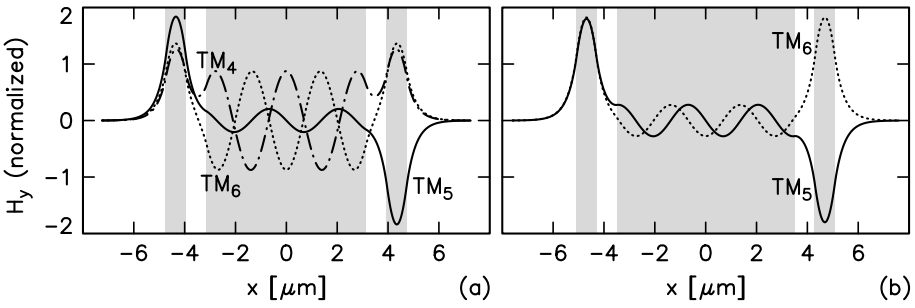

Figure 7.4: Mode field profiles for coupling layer thicknesses $T = 6.29\,\mu$m (a) and $T = 6.98\,\mu$m (b), corresponding to the three- (a) and two-mode regimes (b) marked in Figure 7.2.

With respect to the variation of the propagation constants with T, there are two extreme configurations, examples of which are marked (a) and (b) in Figure 7.2. In (a), one supermode propagation constant matches β_*, with two equally spaced adjacent wavenumbers. In (b), two supermode propagation constants are in close proximity to each other, slightly above and below β_*. Figure 7.4 shows the corresponding mode functions.

Addition of the two profiles in (b) yields a field which is localized in the left outer waveguide. These two modes will carry about half of the power inserted in waveguide WG1 each. Figure 7.5 illustrates that the mode profiles of the outer waveguides can be obtained by proper superposition of the three most relevant supermodes in the three mode regime as well. Here, power from input port A is distributed chiefly among these three modes. Hence we call configurations (a) and (b) the three and two mode regime, respectively.

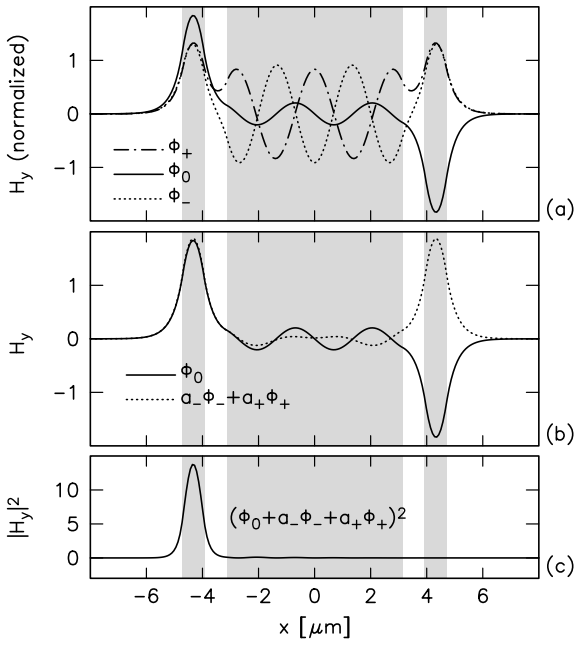

Figure 7.5: (a) Mode functions ϕ_-, ϕ_0, ϕ_+ (TM_6, TM_5, TM_4) for the structure with parameters as in Figure 7.2 and $T = 6.261\,\mu$m. Corresponding propagation constants are $\beta_- = 10.8660/\,\mu$m, $\beta_0 = 10.8772/\,\mu$m, $\beta_+ = 10.8864/\,\mu$m. The linear combination of ϕ_- and ϕ_+ with coefficients $a_- = 0.671$ and $a_+ = 0.754$ is similar to ϕ_0 in the outer waveguide regions, apart from the reversed symmetry (b). The mode function of one outer waveguide can be approximated by a superposition of all three modes (c).

Light propagation is to be discussed in the framework of the formalism of Section 1.2. Letters A to D of the coupler ports indicate the properly polarized modes of the outer waveguides. According to Eqs. (1.33), (1.34), a device of length L transmits the relative power $P_{io} = P_o^{\text{out}}/P_i^{\text{in}}$ from port $i = \text{A, D}$ to port $o = \text{B, C}$. Assuming normalized modes, and skipping the segment indices of Section 1.2, this reads

$$P_{io}(L) = \Big| \sum_m w_{oi}^m \, \mathrm{e}^{-\mathrm{i}\beta_m L} \Big|^2 \quad \text{with} \quad w_{oi}^m = (\phi_o; \phi_m)(\phi_m; \phi_i)\,, \tag{7.1}$$

where $(\,.\,;\,.\,)$ denotes the products (1.18) or (2.7), respectively.

According to Figure 7.3, only a few supermodes must be suspected to be relevant for the power transfer. For a more quantitative statement, we have restricted the sum in Eq. (7.1) to two and three modes with the largest amplitudes $|w_{\text{BA}}^m|$, and computed the power throughput for zero device length, i.e. only the overlap integrals are evaluated. The results are plotted in Figure 7.6.

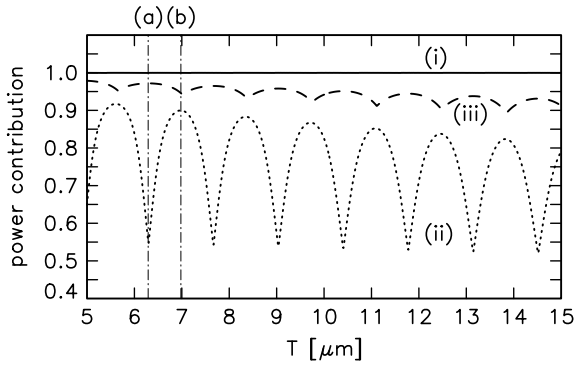

Figure 7.6: Contributions of different mode sets to the power transfer for zero device length versus the thickness of the central layer. (i): power transfer $P_{AB}(0)$ of the entire mode spectrum, (iii): contribution $\mathcal{P}_{AB}(0)$ of the three most exited modes, (ii): power transferred by the two most exited modes. Parameters are as in Figure 7.2. Note that the power contribution of the three modes in the three mode regime (maxima of curve (iii)) is larger than the contribution of two modes in the two mode regime (maxima of curve (ii)).

$P_{\text{AB}}(0)$ always exceeds 0.999, indicating that representing the propagating fields as superpositions of guided modes is a very good approximation for the current parameter set. As assumed in Section 1.2, radiation loss and reflection at the longitudinal discontinuities should be negligible, since the supermode superpositions match the input respectively output fields well.

While considering only two modes is unsufficient, with an approximation that takes three modes into account about 90% of the input power can be controlled. Admittedly, this approximation is somewhat crude, and

hence the simulations of the subsequent sections always employ Eq. (7.1) with the entire mode set. However, for the purpose of finding promising points in a multi-dimensional parameter space, this three mode approximation serves quite well. In particular, it justifies the introdcution of a kind of coupling length.

To elaborate it further, we consider the three supermodes ϕ_-, ϕ_0, ϕ_+, with increasingly ordered propagation constants β_-, β_0, β_+, with largest absolute weights w^-_{BA}, w^0_{BA}, w^+_{BA}. Usually, these are the modes with wavenumbers closest to β_*. They effect the power transmission

$$\mathcal{P}_{io}(L) = \Big| \sum_{-,0,+} w^m_{oi}\, \mathrm{e}^{-\mathrm{i}\beta_m L} \Big|^2 . \tag{7.2}$$

Because of the symmetry of the entire structure and with the subsequent selection of propagation constants, ϕ_0 and ϕ_-, ϕ_+ have opposite parities with respect to the reflection $x \to -x$. Therefore, on choosing $\phi_{\mathrm{A}}(x) = \phi_{\mathrm{B}}(x) = \phi_{\mathrm{C}}(-x) = \phi_{\mathrm{D}}(-x)$, the overlaps with the outer waveguide modes are related by $(\phi_{\mathrm{A}};\phi_m) = \pm(\phi_{\mathrm{D}};\phi_m)$, for $\phi_m(x) = \pm\phi_m(-x)$. If the three modes are supposed to represent the outer waveguide modes exactly, i.e. if $\mathcal{P}_{\mathrm{AB}}(0) = 1$, $\mathcal{P}_{\mathrm{AC}}(0) = 0$, their mode weights satisfy the equations $w^0_{\mathrm{BA}} + w^-_{\mathrm{BA}} + w^+_{\mathrm{BA}} = 1$, and $w^0_{\mathrm{BA}} = w^-_{\mathrm{BA}} + w^+_{\mathrm{BA}}$. If β_0 is closer to β_- than to β_+, define

$$\Delta\beta = \beta_0 - \beta_- , \quad \gamma = (\beta_+ - \beta_0 - \Delta\beta)/\Delta\beta , \quad r = w^-_{\mathrm{BA}}/w^0_{\mathrm{BA}} , \tag{7.3}$$

otherwise

$$\Delta\beta = \beta_+ - \beta_0 , \quad \gamma = (\beta_0 - \beta_- - \Delta\beta)/\Delta\beta , \quad r = w^+_{\mathrm{BA}}/w^0_{\mathrm{BA}} . \tag{7.4}$$

$\Delta\beta$ denotes the smallest difference between the propagation constants of neighbouring modes. It defines a characteristic coupling length $L_{\mathrm{c}} = \pi/\Delta\beta$. Additionally one amplitude ratio r and the asymmetry parameter γ are sufficient to characterize the power contained in the input waveguide, as we shall see.

With the above definitions the power transfer function $\mathcal{P}_{\mathrm{AB}}$ reads

$$\mathcal{P}_{\mathrm{AB}}(L) = \frac{1}{4}\Big| 1 + r\,\mathrm{e}^{\mathrm{i}\pi L/L_{\mathrm{c}}} + (1-r)\,\mathrm{e}^{-\mathrm{i}(1+\gamma)\pi L/L_{\mathrm{c}}} \Big|^2 . \tag{7.5}$$

Obviously, the conditions for the transmission to be complete — $\mathcal{P}_{\mathrm{AB}}(L) = 1$ — are

$$L = 2mL_{\mathrm{c}} \quad \text{and} \quad \gamma = j/m. \tag{7.6}$$

Likewise the transmission vanishes — $\mathcal{P}_{\mathrm{AB}}(L) = 0$ — if

$$L = (2m+1)L_{\mathrm{c}} \quad \text{and} \quad \gamma = 2j/(2m+1) \tag{7.7}$$

hold. In both cases m and j must be nonnegative integer numbers. Recall that Eqs. (7.6), (7.7) refer to the 'three closest modes' approximation. Parameters determined in this manner may serve as starting values for an optimization procedure which takes all modes into account.

The transferred power is minimal or maximal if the device length is an odd or even multiple of L_{c}, respectively. In contrast to the superposition of only two modes, the propagation constants must additionally satisfy the conditions (7.6) and (7.7) with γ as given by Eqs. (7.3), (7.4). Defining the usual coupling length L_{c} makes sense for three mode interference, even for nonequidistant propagation constants ($\gamma \neq 0$).

The corresponding expressions for the two mode regime result for grossly unequally weighted modes ϕ_-, ϕ_+, i.e. for $r \to 1$. In this case the conditions (7.6) and (7.7) loose their significance, and maximum or minimum power transfer occurs at each multiple of the coupling length. This situation was investigated in Ref. [129].

A variation of the parameter T alters both L_{c} and γ. In Figure 7.7 we have marked points (T, L_{c}) where the condition (7.6) for total power transfer is met. These points occur rather frequently, thus justifying the continuous curve $L_{\mathrm{c}}(T)$ for design considerations.

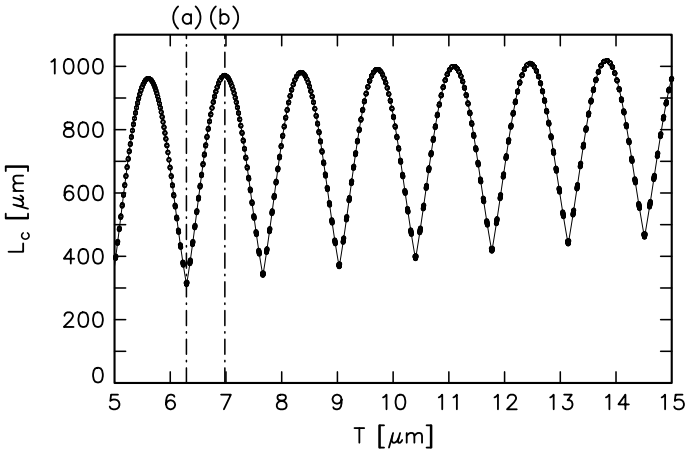

Figure 7.7: Coupling length L_c for different thicknesses T of the central layer, for the structures of Figure 7.2. The line represents L_c according to Eqs. (7.3), (7.4). Regions for T with $\mathcal{P}_{AB}(2L_c(T)) = 1$ according to the three mode approximation are marked. At such points Eq. (7.6) holds approximately with $m = 1$, i.e. $m\gamma(T)$ deviates from the next natural number by less than 0.1.

Finally, Figure 7.8 illustrates the effects of multimode interference, in terms of power transmission. In general, P_{AB} and P_{AC} do not add to one, since a sizeable amount of power may be contained in the central region at $z = L$. If present, this power adds to the intrinsic losses of the system.

With growing central layer thickness T, more and more supermodes take part in the power transfer (cf. Figure 7.6), leading to an increasingly irregular beating pattern. The geometries in (a) are selected such that the estimated coupling length is always $L_{\mathrm{c}} = 1\,\mathrm{mm}$, and this trend is clearly visible even for the largest separation. Figure 7.8(b) shows approximations to the power transmission (7.1), with the sum restricted to the two, three, and four most excited supermodes. The charts correspond to the configuration $T \approx 20\,\mu\mathrm{m}$ of the last inset in (a). Two mode interference in the upper right plot yields the general trend only. The second inset shows the result of the three mode approximation. The four mode interference pattern is already very close to the exact curves in (a). Note that for this figure parameters from Refs. [85, 129] were chosen, which differ from the preceding geometries in this section.

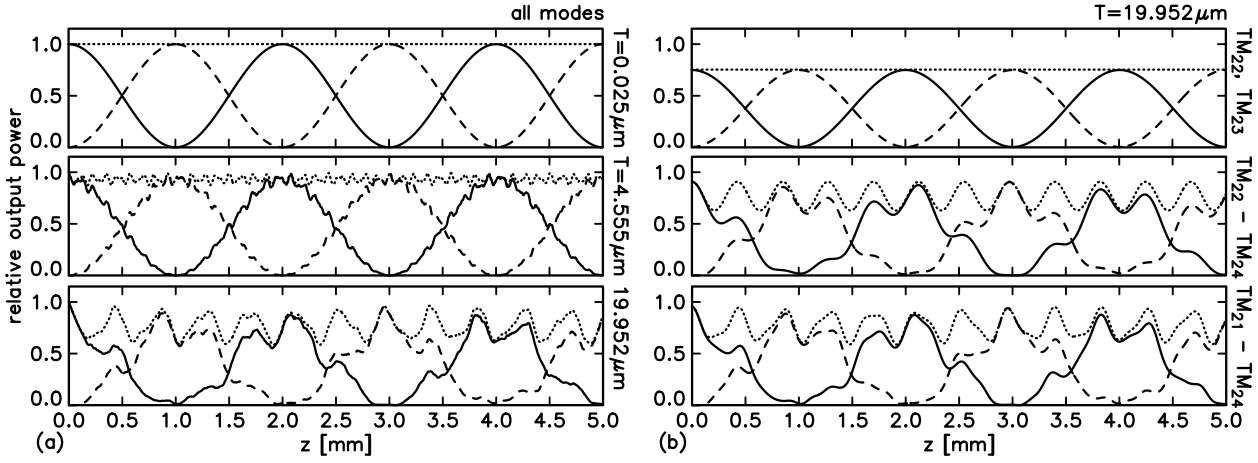

Figure 7.8: Relative output power P_{AB} (solid lines), P_{AC} (dashed lines), and the total power $P_{AB} + P_{AC}$ (dotted lines) of TM waves versus the propagation distance z (or the device length L). Chart (a) shows curves for different thicknesses of the central layer, where the given values of T correspond to $L_{\mathrm{c}} = 1\,\mathrm{mm}$. The structures support 15, 32 and 87 TM-modes, respectively. For (b), the power transmission is evaluated with different numbers of modes taken into account. These are the two (top), three (center), and four (bottom) supermodes with largest initial amplitudes, for $T = 19.952\,\mu\mathrm{m}$. Parameters are as in Refs. [85, 129]: $n_0 = 1$, $n_1 = 1.49$, $n_2 = 1.46$, $n_3 = 1.52$, $t = 1.35\,\mu\mathrm{m}$, $d = 0.8\,\mu\mathrm{m}$, $\lambda = 0.6328\,\mu\mathrm{m}$.

7.2 Isolators / circulators

The majority of integrated optical isolator configurations have two waveguide ports, which are connected for light propagation in the direction of transmission. In the opposite direction, the power is either damped by a polarizer or radiated into the surrounding. In contrast, the concept of the nonreciprocal coupler [98] is suitable for the realization of circulator devices since the blocked power remains well confined in its own output waveguide. Recent proposals are based on the nonreciprocal phase shift in magnetooptic waveguides [97, 68, 37, 177, 16]. The difference of the mode interference patterns in forward and backward directions allows to spatially separate forward and backward propagating waves. Unfortunately, the conventional X-coupler as simulated e.g. in Ref. [37] has the drawback of a large total length. For current magnetooptic materials with limited specific Faraday rotation, this leads not only to undesirably high optical losses, but also to very strict fabrication tolerances (cf. Eqs. (5.2), (5.3)). Design concepts have to be developed which aim at short device lengths.

An application of radiatively coupled waveguides for optical isolators and circulators has been proposed in [127, 123], further elaborated for planar structures in [84] and for raised strip geometries in [82]. Sections 7.2.1, 7.2.2 cover material from the latter references. The special form of the relevant modes can be used for optimizing the nonreciprocal phase shift with respect to the device length. In particular, devices operating in the three mode regime turn out to be interesting.

7.2.1 Planar nonreciprocal devices

We first focus on planar devices as sketched in Figure 7.1(a), assuming that one or more layers have a first order magnetooptic effect, with the static magnetization adjusted in the film plane, perpendicular to the direction of propagation (equatorial configuration). In these layers a magnetooptic permittivity perturbation $\delta\hat{\epsilon}^y_{\mathrm{mo}}$ in the form of Eq. (6.3) is present. We adopt the notation of Section 6.2.1 for the piecewise constant dielectric profile, with all y-dependencies skipped.

The planar gyrotropic multilayer structures can be analysed with the formalism outlined in Section 2.2. Scalar equations for TE and TM polarized modes may be derived just as for isotropic media. In first order, gyrotropy does not affect the propagation of TE polarized light, so our further analysis concentrates on TM modes. For the latter, the off-diagonal permittivity element ξ does not enter the wave equaton (2.15), but now the quantities H_y and $n^{-2}\partial_x H_y + \xi\beta n^{-4} H_y$ are required to be continuous at the layer interfaces. This leads to modified entries for the transfer matrices (2.18) according to Table 7.1.

	p_l	q_l
$\beta^2 > k^2 n_l^2$	$\eta_l\gamma_l \exp(\gamma_l \Delta h^l_{l-1}) + \zeta_l \exp(\gamma_l \Delta h^l_{l-1})$	$-\eta_l\gamma_l \exp(-\gamma_l \Delta h^l_{l-1}) + \zeta_l \exp(-\gamma_l \Delta h^l_{l-1})$
$\beta^2 < k^2 n_l^2$	$\eta_l\gamma_l \cos(\gamma_l \Delta h^l_{l-1}) + \zeta_l \sin(\gamma_l \Delta h^l_{l-1})$	$-\eta_l\gamma_l \sin(\gamma_l \Delta h^l_{l-1}) + \zeta_l \cos(\gamma_l \Delta h^l_{l-1})$

	r_l	s_l
$\beta^2 > k^2 n_l^2$	$\eta_l\gamma_l \exp(\gamma_l \Delta h^l_{l}) + \zeta_l \exp(\gamma_l \Delta h^l_{l})$	$-\eta_l\gamma_l \exp(-\gamma_l \Delta h^l_{l}) + \zeta_l \exp(-\gamma_l \Delta h^l_{l})$
$\beta^2 < k^2 n_l^2$	$\eta_l\gamma_l \cos(\gamma_l \Delta h^l_{l}) + \zeta_l \sin(\gamma_l \Delta h^l_{l})$	$-\eta_l\gamma_l \sin(\gamma_l \Delta h^l_{l}) + \zeta_l \cos(\gamma_l \Delta h^l_{l})$

Table 7.1: Definitions for the elements of Eq. (2.18), for a transversely magnetized multilayer magnetooptic waveguide. $\zeta_l = \xi_l\beta/n_l^4$; the remaining definitions are as stated in Table 2.1.

According to Table 6.3, the gyrotropy in equatorial orientation affects TM propagation constants to be different for opposite directions of propagation. These nonreciprocal TM phase shifts $2\delta\beta$ can be calculated by subtracting exact solutions for opposite signs of ξ, or alternatively, by perturbation theory. Eq. (6.6) is to be applied, without arguments y and without the y-integrations.

If the layers of radiatively coupled waveguides are made of magnetooptic material, usually the coupling lenghts $L_{\mathrm{c}}^{\mathrm{f}} = \pi/\Delta\beta^{\mathrm{f}}$ for forward and $L_{\mathrm{c}}^{\mathrm{b}} = \pi/\Delta\beta^{\mathrm{b}}$ for backward light propagation differ. An isolator

results if the device length L_{is} can be adjusted such that $L_{\mathrm{is}} = lL_{\mathrm{c}}^{\mathrm{f}} = (l \pm 1)L_{\mathrm{c}}^{\mathrm{b}}$ holds for a positive integer number l,

$$L_{\mathrm{is}} = \frac{\pi}{|\Delta\beta^{\mathrm{f}} - \Delta\beta^{\mathrm{b}}|}. \tag{7.8}$$

If l is even and light is injected at port A, it will leave the device at port B (see Figure 7.1); if light is injected at port B, it will leave the device at port D. Likewise, if l is odd and light is injected at port A, it will leave the device at port C; if injected at C, it will leave at D.

Eq. (7.8) specifies the dependence of L_{is} on the tuning parameter T, the thickness of the central layer. L_{is} is the length of an isolator only if $L_{\mathrm{is}}(T)/L_{\mathrm{c}}^{\mathrm{f}}(T)$ turns out to be an integer. Moreover, the conditions (7.6) and Eq. (7.7) with multiplicities l and $l \pm 1$, respectively, must hold for both $L_{\mathrm{c}}^{\mathrm{f}}$ and $L_{\mathrm{c}}^{\mathrm{b}}$, at least approximately. With regard to isolator (not circulator) performance, Eq. (7.8) is unnecessarily rigid, since complete power transfer is required only in forward direction.

Using the notation of Section 7.1, Eq. (7.8) may be rewritten as

$$L_{\mathrm{is}} = \frac{\pi}{2|\delta\beta_{\pm} - \delta\beta_0|}. \tag{7.9}$$

To realize a short device, not only large nonreciprocal phase shifts are required, but also the *difference* between the phase shifts $2\delta\beta_{\pm}$ and $2\delta\beta_0$ of the two most relevant modes (with indices $+$ or $-$, and 0) must be as large as possible. Note that this is the weak point of the conventional coupler. Its two squared supermodes appear very similar, thus the difference in the nonreciprocal phase shifts remains small (unless a more elaborated magnetooptic structure is realized, as we have proposed in Ref. [16]).

Eq. (6.6) suggests to insert boundaries between regions with different Faraday rotation at locations x, where the difference in the absolute values of the mode fields is maximal. The modes ϕ_0 and ϕ_+ or ϕ_-, respectively, are of opposite symmetry with respect to $x = 0$. In the central layer their absolute field values are periodic in x with a period of $2a \approx \pi/\sqrt{k^2 n_3^2 - {\beta_*}^2}$. Therefore ξ should jump at $x = \pm ja$, with $j = 1, 2, \ldots, |x| < T/2$.

If the coupling region is made of layers of thickness a with alternating Faraday rotation, the magnetooptic phase shifts $\delta\beta_0$ and $\delta\beta_+$ or $\delta\beta_-$, respectively, differ not only strongly in magnitude, but are of different signs. L_{is} can be further reduced if the outer waveguides are fabricated from double magnetooptic layers as well. In this case the two layers must be ordered properly to enhance the nonreciprocal phase shift caused by the magnetic grating in the central layer. These concepts are illustrated in Figure 7.9.

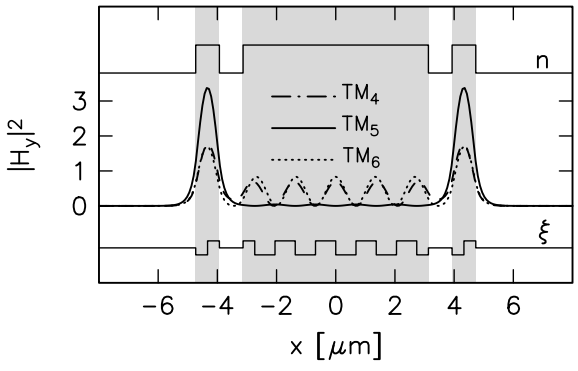

Figure 7.9: Absolute field values of the modes from Figure 7.5. The refractive index profile is sketched above. The magnetooptic profile shown below is adjusted to the shape of the mode functions to obtain optimal nonreciprocal phase shifts.

The following discussion assumes two different media. A nonmagnetic medium with smaller refractive index $n_0 = n_2$ is used for the cladding and gap layers. The guiding regions are made of magnetooptic material (refractive index $n_1 = n_3$) which can be properly doped to exhibit positive and negative Faraday rotation of equal magnitude (off-diagonal elements $\pm\xi$). These assumptions are realistic, see Ref. [165]. Figure 7.10 compares potential device lengths of isolators based on radiatively coupled waveguides with

identical refractive index profile. The values are estimated with the aid of Eq. (7.9). Clearly, shortest devices can be expected in the regions of the three mode regime, for periodically occurring values T.

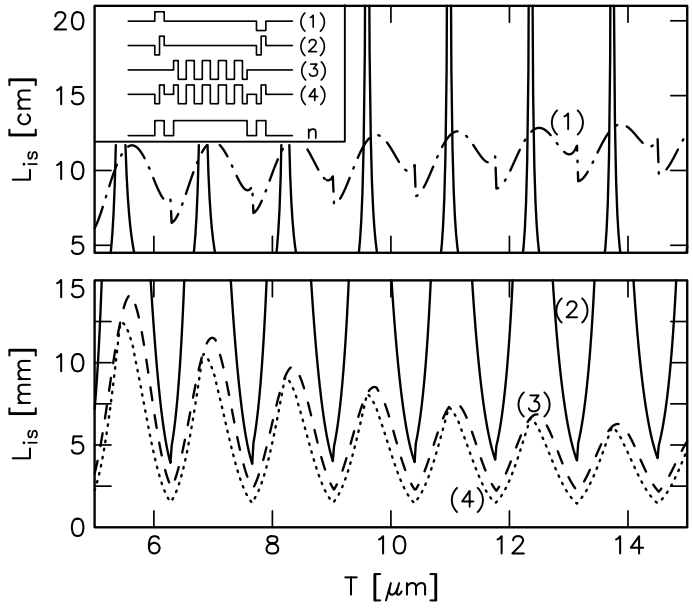

Figure 7.10: Isolator device length L_{is} versus the thickness T of the coupling layer. Different parts of the multilayer structures have been modeled to be magnetooptic: (1 – dash-dotted line) only the outer waveguides: single layers with opposite faraday rotation on both sides, (2 – continuous line) the outer waveguides: double layers of equal thickness with opposite Faraday rotation, (3 – dashed line) the central region: magnetic grating with alternating Faraday rotation, (4 – dotted line) the outer waveguides: double layers, additionally alternating Faraday rotation in the coupling layer. Parameters are as in Figure 7.2, $|\xi| = 0.005$. Example profiles of Faraday rotation and refractive index for $T = 6.261\,\mu$m are sketched in the inset.

If the outer waveguides are made of two layers, the total length can be shortened by a factor of 10 as compared to magnetooptic single layer outer waveguides provided that T is choosen within the three mode regime. In the case of only two relevant modes, both propagation constants are shifted in the same way because of approximately equally large amplitudes in the outer waveguides. This is the reason for the poles in curve (2) of Figure 7.10. Such large variations vanish if the coupling layer is a magnetic grating. In the three mode regime, the device is half as long as compared to the double layer stuctures. It is further diminished by a factor of $3/4$ if both the central region and the outer waveguides consist of magnetooptic layers. The following paragraphs refer to such structures.

The available material ($n_0 = n_2, n_1 = n_3, \xi$), the light wavelength λ and the height t of the outer waveguides are assumed to be fixed, the gap width d and the coupler thickness T have to be optimized. We observed the following tendencies:

If d decreases, the modes of the outer waveguides deviate more and more from the modes of the entire structure which leads to larger coupling losses at input and output. If d increases, the coupling length increases in both regimes. In the three mode regime the minimal isolator length depends but weakly on d while gradients in $L_{\mathrm{is}}(T)$ increase for larger d. We are looking for values T for which $L_{\mathrm{c}}^{\mathrm{f}}(T)$, $L_{\mathrm{c}}^{\mathrm{b}}(T)$, and $L_{\mathrm{is}}(T)$ simultaneously have their proper meaning as coupling or isolator length. Such values occur less frequently with increasing gap width d.

For given gap width d, regions with promising thicknesses T can be selected from charts like Figure 7.10. In these regions points T are likely to be found which guarantee a proper isolation at a device length L close to $L_{\mathrm{is}}(T)$. These simulations have to consider all guided modes of the coupler structure to give reliable results. Larger T improves the separation of the input and output waveguides, but the number of magnetic layers, hence the structuring effort, increases. The relevant propagation constants are more closely spaced, therefore coupling lengths increase, while the total length does not significantly change. Tolerance requirements for L and T become less strict. At the same time, additional modes contribute to the coupling process, thus the conditions of all of them being properly in phase are met less frequently.

Table 7.2 presents three example parameter sets which correspond to well performing isolator devices. We have calculated the interference of all guided modes, with the magnetooptic anisotropy included directly into the planar modesolver by means of the transfer matrices of Table 7.1. The isolation is defined by $\mathrm{IS} = 10\log P_{\mathrm{AB}}^{\mathrm{f}}/P_{\mathrm{AB}}^{\mathrm{b}}$, the (forward transmission) loss by $\mathrm{LO} = -10\log P_{\mathrm{AB}}^{\mathrm{f}}$. Reflections at power input or output and losses due to material absorption are neglected. The tolerance Δq of a length parameter q

	$T/\,\mu$m	$L/\,\mu$m	IS [dB]	LO [dB]	$\Delta T/$ nm	$\Delta d/$ nm	$\Delta t/$ nm	$\Delta L/\,\mu$m
(i)	6.261	1512	38	0.15	5	16	3	35
(ii)	10.352	1558	55	0.15	7	16	3	40
(ii)	18.719	1504	38	0.27	12	20	3	35

Table 7.2: Example parameters and tolerances for isolators based on planar radiatively coupled waveguides. The remaining parameters are $\lambda = 1.3\,\mu$m, $t = 0.8\,\mu$m, $d = 0.8\,\mu$m, $n_0 = n_2 = 2.18$, $n_1 = n_3 = 2.30$, $|\xi| = 0.005$ (see Figure 7.1).

is declared as follows. If all other parameters remain fixed, then $[q - \Delta q, q + \Delta q]$ is an interval of values such that isolation better than 20 dB *and* forward transmission loss below 0.5 dB are guaranteed. Parameters t and d have been varied for one of the outer waveguides only. The coupling region of structures (i), (ii), and (iii) is made up of 10, 16, and 28 layers of alternating Faraday rotation. Figure 7.11 illustrates light propagation in structure (i).

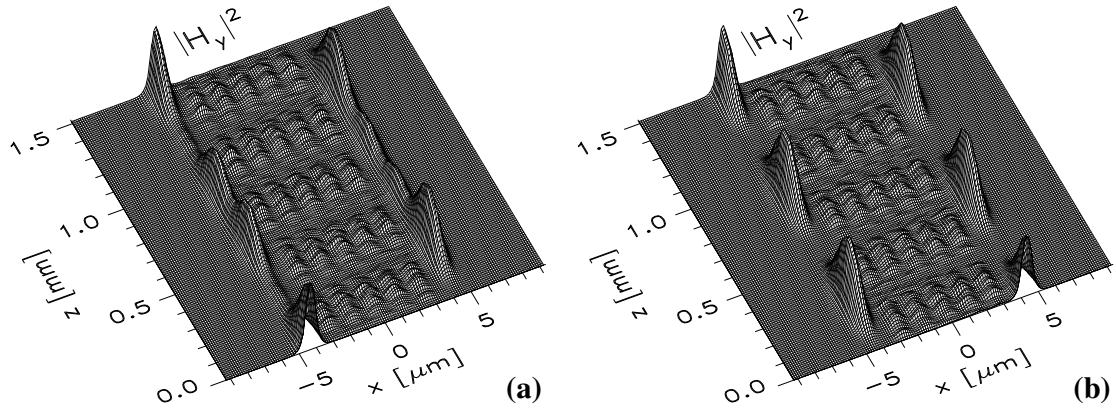

Figure 7.11: Light propagation in structure (i) of Table 7.2. The TM-polarized mode function of one outer waveguide is used as an initial field in $z = 0$ (a) and $z = 1.5$mm (b). In the direction of transmission the power remains in the input waveguide (a), while in the opposite direction the power is guided to the other waveguide (b). Due to $\gamma^b \approx 0$ an almost periodic interference pattern emerges in the backward direction (b).

The three sample devices may be analyzed by the three mode approximation outlined in Section 7.1. Conditions (7.8) and (7.6), (7.7) for good isolator performance are met, at least approximately, as demonstrated in Table 7.3. The ratios of device to coupling lengths should be integer numbers (4, 4, 2, 5, 3, and 3 in our case). Likewise, the asymmetry parameters γ turn out to be close to fractions of two small integers ($1/2$, 0, 1, 0, $2/3$, and 0).

	(i)	(ii)	(iii)
$L_c^f/\,\mu$m	381	391	739
L/L_c^f	3.97	3.98	2.04
γ^f	0.504	0.012	1.015
$L_c^b/\,\mu$m	309	507	522
L/L_c^b	4.89	3.07	2.88
γ^b	0.003	0.671	0.002

Table 7.3: Values characterizing the coupling behaviour for the structures of Table 7.2. The values listed here are the subject of Eqs. (7.6)–(7.8) for good isolator performance according to the three mode approximation. See the text for further explanation.

For comparison, a conventional nonreciprocal coupler (no central layer in Figure 7.1) made from the same materials ($n_0 = n_2$, n_1, $|\xi|$) with the same geometry of the coupled waveguides (λ, t) must be longer than 2.75 mm. This length results for a gap width $d = 0$ and double layer waveguides. It is further enlarged by bends which are necessary for separating input and output ports. A gap width $d = 0$ corresponds to a coupling length of $11.7\,\mu$m, and a tolerance below $0.7\,\mu$m for the total device length is required. The device length increases to 10.5 mm for a gap of width $2d = 0.8\,\mu$m. Conventional coupler isolators are highly

sensitive to alterations of the waveguide separation. The optimal value of $0.8\,\mu$m must be maintained with a tolerance better than $\pm 0.4\,$nm as can be estimated from the sinusoidal form of the power transfer and the dependence of the coupling length on d.

7.2.2 Concepts based on raised strip waveguides

Analogous mode patterns appear in more realistic three-dimensional structures. Figure 7.12 illustrates the supermodes of a rib coupler in the three mode regime. Geometry and cross section are sketched in Figures 7.1, 1.8. The three most relevant modes corresponding to the planar profiles in Figure 7.4(a) can be clearly identified. However, the sound basis of semianalytic planar mode solutions is replaced by numerical approximations. The plotted modes are generated by the semivectorial wave matching program of Chapter 3, with the penalty factor technique mentioned in the last paragraph of Section 4.3.4 applied.

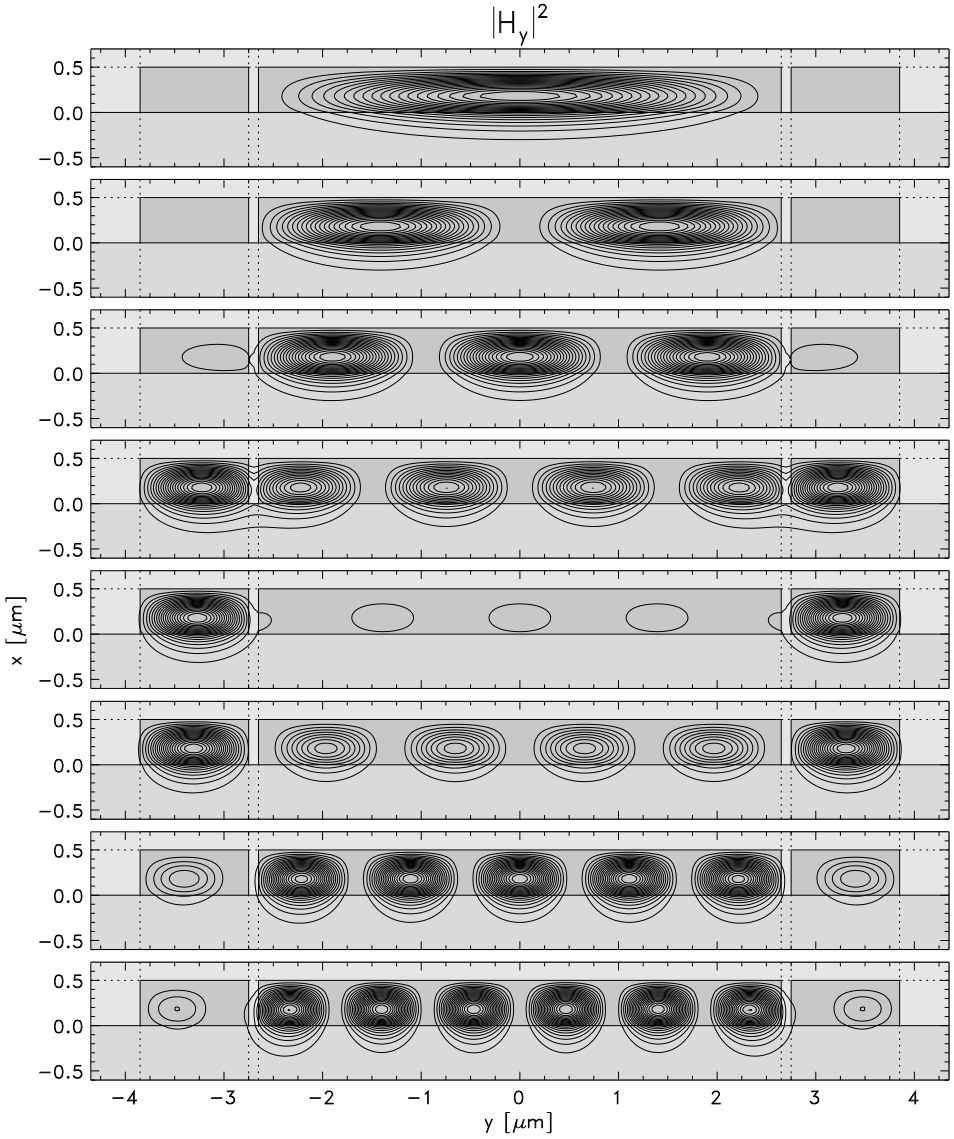

Figure 7.12: Mode intensity profiles for the eight TM polarized modes of a radiatively coupled waveguide structure given by the following parameters: $W = 5.3\,\mu$m, $w = 1.1\,\mu$m, $g = 0.1\,\mu$m, $h = 0.5\,\mu$m, $n_f = 2.3$, $n_s = 1.95$, $n_c = 1.0$, $\lambda = 1.3\,\mu$m.

One can expect similar intensity profiles for the three mode regime of TE polarization, for slightly varied geometry parameters. The mode shape inspires isolator configurations as shown in Figure 7.13. As before, we assume the guiding strips to be made of magnetooptic material. (a) is the straightforward extension

of the planar multilayer concept of Section 7.2.1 to the two-dimensional cross section, obtained by a 90° rotation. It applies to TE polarized light, with the magnetization adjusted in the polar configuration to effect nonreciprocal TE phase shifts. The positions of the walls separating regions with opposite Faraday rotation are subject to design considerations analogous to Section 7.2.1, with Eq. (6.6) substituted by Eq. (6.8). For a fabrication of these periodic magnetooptic profiles, both proposals of domain or compensation walls may be considered.

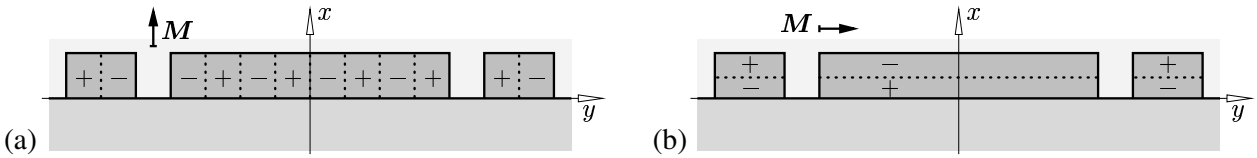

Figure 7.13: Concept for isolators/circulators based on radiatively coupled raised strip waveguides, for TE (a) and TM polarized light (b). Dotted lines indicate boundaries between stripes or layers, respectively, with opposite Faraday rotation, where the signs indicate the signs of the magnetooptic profile ξ.

In contrast to concept (a), which relies on the different mode symmetry, concept (b) for TM polarization takes advantage of the strongly differing amplitudes of the relevant supermodes. Here the guiding strips are fabricated from two magnetooptic layers with opposite Faraday rotation, in equatorial configuration. The nonreciprocal phase shifts of the central and the neighbouring modes must be as unequal as possible, therefore the outer waveguides should have a magnetooptic profile with reverted signs. The central magnetooptic boundary is to be adjusted to the vertical mode field maximum.

With the central layer thickness T replaced by the width W of the central rib, the dispersion characteristic of the three-dimensional devices is similar to the planar case, as confirmed by Figure 7.14. Here the slight shift of the region of the anomaly, i.e. the level of the central mode wavenumber in case of three propagation constants at two equal distances, above the level β_* is more pronounced than in the planar case.

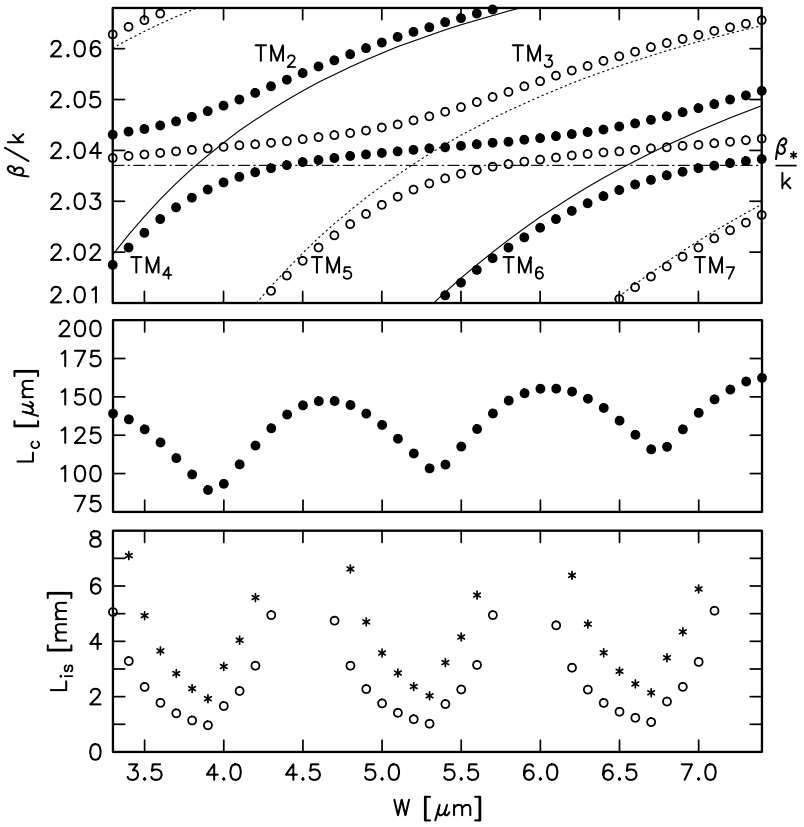

Figure 7.14: Propagation constants β (top), coupling length L_c (center), and the estimated isolator device length L_{is} (bottom) for TM-polarized light versus the central rib width W of the three rib waveguide coupler. Only part of the region allowed for propagation constants is displayed. Thin lines in the top inset indicate propagation constants of the isolated outer waveguides, the level β_*/k, and of the modes of the central strip (continuous and dotted lines for modes of even and odd symmetry). Parameters are as given for Figure 7.12, with an off-diagonal permittivity element $\xi = \pm 0.005$. Circles in the bottom chart correspond to a device with isotropic outer guides but a double layer magnetooptic central waveguide, while the stars indicate the total length for a device with both central and outer waveguides made of magnetooptic material as sketched in Figure 7.13(b), with a thickness of the bottom magnetooptic layers of $0.18\ \mu$m.

According to the bottom inset, evaluation of Eqs. (6.5), (7.9) yields an estimate for the minimum achievable device length of $1.02\,\mathrm{mm}$. This is one order of magnitude smaller than the value of $10\,\mathrm{mm}$ given in [37] for a conventional two-waveguide nonreciprocal coupler of comparable materials and geometry. If only the central waveguide is made of magnetooptic material, for a device with isotropic outer waveguides one can still expect a minimum total length below $2\,\mathrm{mm}$.

7.3 Polarization splitters

The coupling length of radiatively coupled waveguides depends strongly and periodically on the thickness of the coupling layer or the width of the center waveguide, respectively. In general, the periodicity is different for light of both polarizations. Provided that the device length can be adjusted to an even multiple of the coupling length for TE polarization and to an odd multiple of the length for TM polarization (or vice versa), light of different polarizations propagates from the same input towards different output ports. Thus the concept of radiatively coupled waveguides [124] is among the number of recent proposals for integrated optical polarization splitting devices [132, 35, 150, 149, 152, 69]. We have simulated both planar [129] and three-dimensional [79] couplers for use as polarization splitters. These investigations are the subject of the following sections.

7.3.1 Planar devices

For the following planar simulations, the material parameters (glass waveguides) have been selected similar to Ref. [149], such that a direct comparison is possible. Figure 7.15 shows a pronounced difference in the coupling lengths for TE and TM polarization, with a ratio of $5/4$ of the maximum lengths. The current parameter set yields only a slight variation of the maximum level with the central layer thickness T.

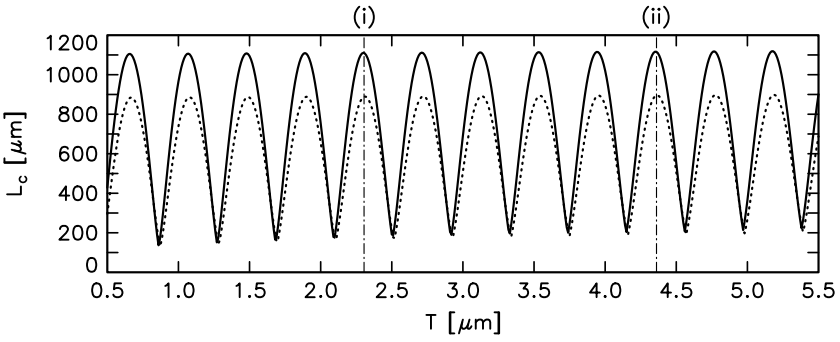

Figure 7.15: Coupling length L_c for TE (continuous line) and TM polarized light (dotted curve) versus the thickness T of the central layer for planar radiatively coupled waveguides with parameters as given for Table 7.4. Marks (i) and (ii) correspond to rows (i) and (ii) in the table.

We have selected regions with the coupling lengths close to the maximum level, and searched for thicknesses T and device lengths L with proper polarization splitting performance. Since the coupling lengths vary almost periodically with T, there is also an almost periodical set of possible values of T, where the polarization discrimination occurs. Table 7.4 summarizes three sets of sample parameters, while Figure 7.16 illustrates the light propagation in device (iii). Due to operation in the two mode regime, there is an almost regular beating pattern for both polarizations. After 4 half beat lengths for TE or 5 half beat lengths for TM polarization, the input power leaves the device at different output ports.

Strict fabrication tolerances with respect to the geometry parameters are a general property of all polarization splitting devices [152]. The polarization splitting performance and the fabrication tolerances are characterized by the extinction ratios $\mathrm{ER}_1 = 10\log_{10}(P_{\mathrm{AB}}^{\mathrm{TM}}/P_{\mathrm{AB}}^{\mathrm{TE}})$ and $\mathrm{ER}_2 = 10\log_{10}(P_{\mathrm{AC}}^{\mathrm{TE}}/P_{\mathrm{AC}}^{\mathrm{TM}})$, as in [149, 152]. Figure 7.17 shows the variation of these quantities with the propagation distance z or the device length, respectively. For a good polarization discrimination, the device length should be chosen in such a

	$T/\,\mu$m	$L/\,\mu$m	$\Delta T/$ nm	$\Delta t/$ nm	$\Delta d/$ nm	$\Delta L/\,\mu$m
(i)	2.305	4428	20	9	8	40
(ii)	4.361	4464	17	11	11	40
(iii)	10.108	4548	15	11	10	40

Table 7.4: Geometry parameters and tolerances for planar radiatively coupled waveguide based polarization splitters. See the text for the interpretation of the tolerances. Remaining geometry and material parameters are $n_0 = 1.51065$, $n_1 = 1.52$, $n_2 = 1.512$, $n_3 = 1.7$, $t = 1.50\,\mu$m, $d = 0.77\,\mu$m, $\lambda = 0.6328\,\mu$m.

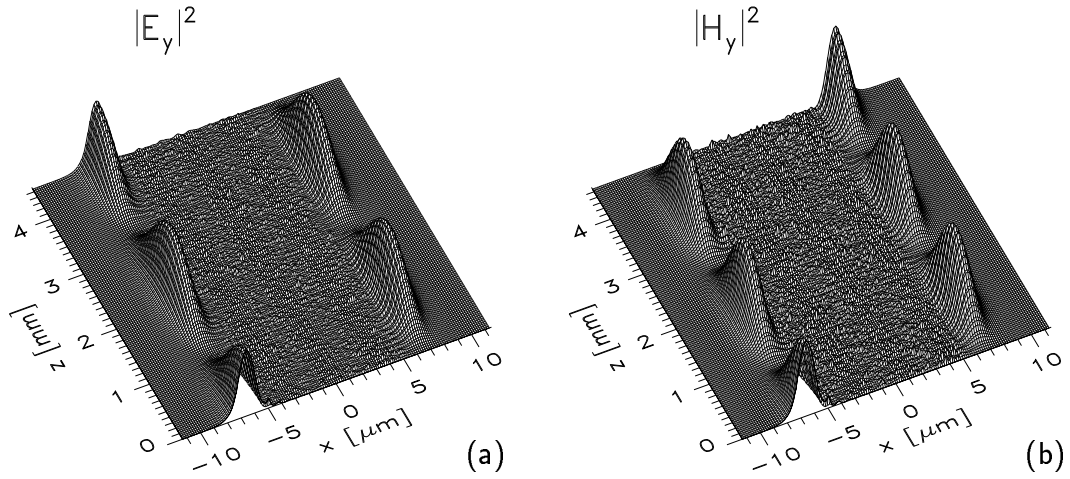

Figure 7.16: Propagation of TE polarized light (a) and TM polarized light (b) in device (iii) of Table 7.4. The properly polarized mode of a basic slab waveguide is launched into WG1 at $z = 0$. Accordingly to the theoretical prediction, light with different polarization states is directed towards different output channels.

way that both extinction ratios are below -20 dB, or above $+20$ dB [152]. These levels are shown by dashed lines.

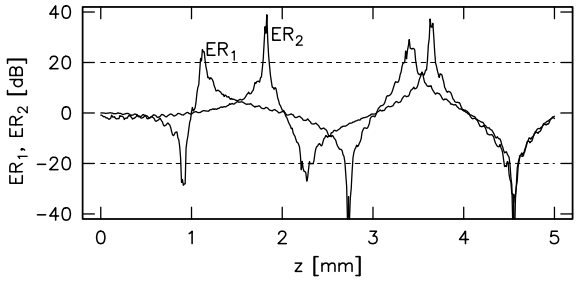

Figure 7.17: Extinction ratios ER_1, ER_2 versus the propagation distance z for structure (iii) of Table 7.4.

The couplers (i) to (iii) of Table 7.4 achieve an optimum performance $\min\{\mathrm{ER}_1, \mathrm{ER}_2\}$ of -28.5 dB, -32.7 dB, and -34.2 dB, respectively. The fabrication tolerances are determined such that both extinction ratios are below the level of -20 dB if the parameter is enlarged or diminished by at most the tolerance. Values for structure (iii) can be read off from Figure 7.18. If compared to other recent planar design proposals, these tolerances are much less critical (± 1 nm in Ref. [149] for a three waveguide coupler with high refracting, thin intermediate layer) or comparable (± 15 nm in Ref. [152] for a multilayer ARROW configuration).

However, the above simulations were carried out with leaky mode perturbation theory in mind [129], and restricted to the two mode regime. Aiming at a short device length, future designs should operate in the two mode regime for TE and in the three mode regime for TM polarization (or vice versa), such that the entire range of the coupling length variations is exploited. For the above parameter set this concept is not useful, since the curves for the coupling lengths of both polarizations are almost 'in phase' on the T-axis in Figure 7.15. But it can be realized with raised strip waveguides, as exemplified in the next section.

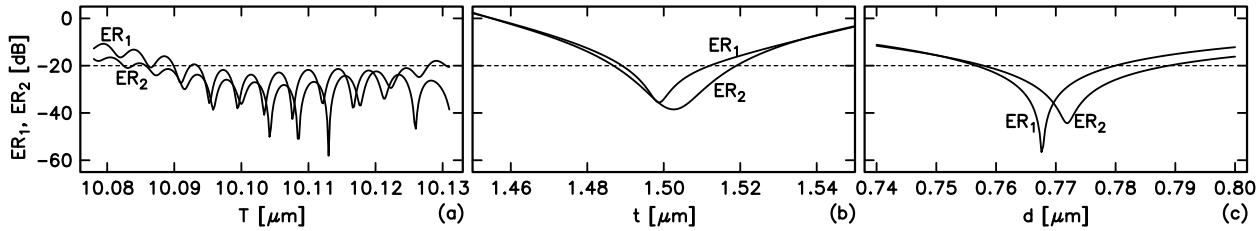

Figure 7.18: (a) Extinction ratios ER_2, ER_2 versus the thickness of the central layer T (a), the outer film thickness t (b), and the thickness d of the buffer layers (c). In each chart, the remaining parameters are as for coupler (iii) of Table 7.4.

7.3.2 Three-dimensional couplers

This section refers again to the cross section of Figure 1.8, with typical garnet parameters. As we shall see, these configurations exhibit a pronounced polarization dependence, enabling a polarization splitter design with short device length. This time the structures are to be modeled by means of the coupled mode theory formalism of Section 1.5.2. As we have demonstrated in Section 7.2.2, an analysis based on directly computed supermodes is feasible as well which avoids the approximations introduced by the coupled mode theory. However, for a complete design usually a large number of simulations are required. Besides a prohibitive demand of computing power, the direct procedure becomes unreliable due to the need to calculate higher order modes with closely spaced propagation constants. At least this difficulty can be overcome with the considerably faster coupled mode theory approach.

Our simulations start with the computation of the guided mode sets for a series of isolated central waveguides, for varying width W. With the two additional modes of the outer waveguides with fixed geometries and gap width, the coupled mode analysis for the three waveguide coupler yields supermode dispersion curves as shown in Figure 7.19.

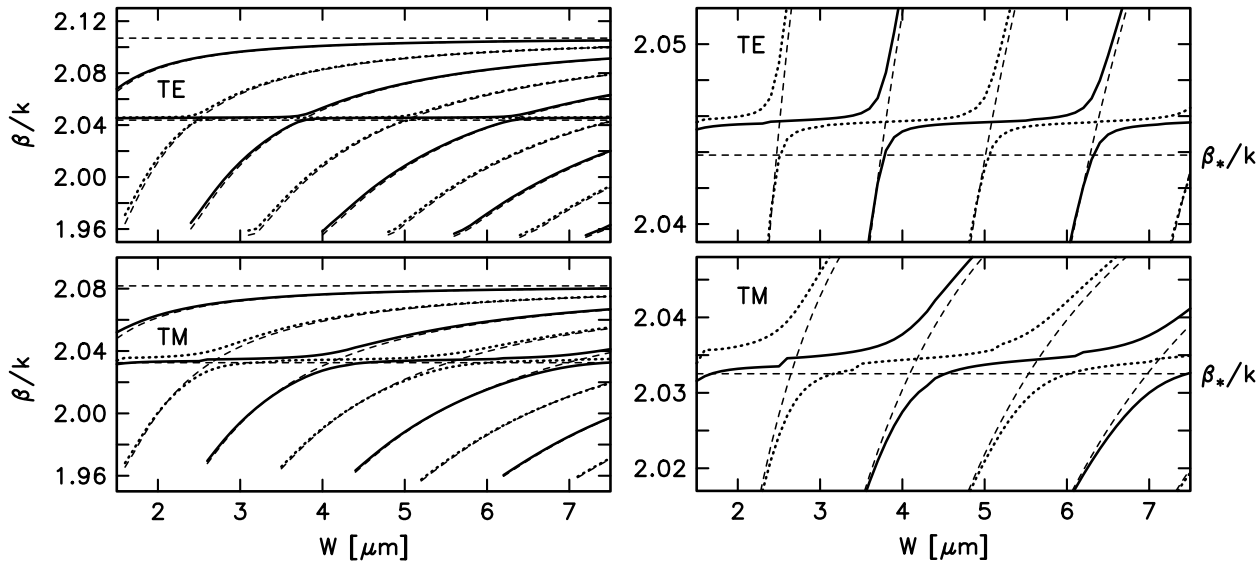

Figure 7.19: Effective mode indices β/k for the supermodes of the three waveguide coupler, for TE (top) and TM polarization (bottom), and for supermodes of even (continuous lines) and odd symmetry (dotted lines), versus the width W of the central waveguide. The thin dashed lines indicate the effective mode indices of the corresponding planar waveguide (top line), the levels β_*/k of the modes of the isolated outer waveguides (center line) and the mode indices of the isolated center guide of proper width. Parameters are $h = 0.7\,\mu m$, $w = 1.2\,\mu m$, $g = 0.1\,\mu m$, $n_s = 1.95$, $n_f = 2.2$, $n_c = 1.0$, $\lambda = 1.3\,\mu m$.

The supermode propagation constants exhibit the expected asymptotic behaviour. For proper polarization and height, the wavenumbers of the corresponding planar, three layered waveguides constitute upper limits. The propagation constant β_* of the isolated outer waveguides is indicated by the central thin horizontal line. Outside the region around this level, the supermode dispersion curves resemble the lines for the isolated central waveguide of the same width.

The corresponding mode profiles exist on the central core only, with small amplitudes on the outer core regions, as illustrated by the mode profiles in Figure 7.20. In contrast, the supermodes with propagation constants close to β_* have only small amplitudes on the core region of the central waveguide, but larger field strength on the outer cores. In the example of Figure 7.20, these are the three supermodes of order 4, 5, and 6 for TE polarization and those of 4th and 5th order for TM polarization.

All these findings agree with expectations from our investigations on planar structures, and with the results of rigorous supermode calculations. At the same time, from planar simulations one would expect β_* to match the region of almost horizontal tangents in the supermode dispersion curves. As shown by the magnifications in the right part of Figure 7.19, these regions turn out to be shifted upwards from the levels β_*. This observation is confirmed by the rigorous treatment of Section 7.2.2.

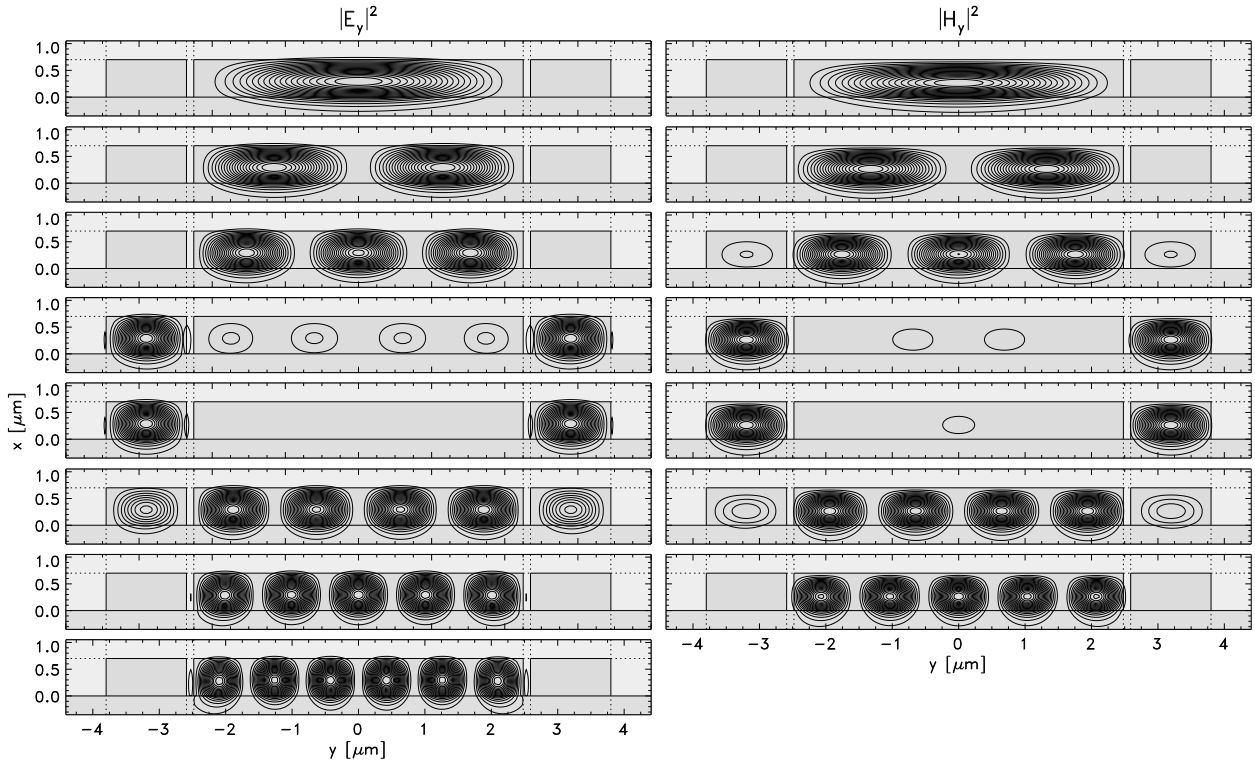

Figure 7.20: Mode intensity profiles for a three waveguide coupler, for TE (left) and TM polarization (right). Parameters are $h = 0.7\,\mu$m, $w = 1.21\,\mu$m, $g = 0.11\,\mu$m, $W = 4.96\,\mu$m, remaining values as stated for Figure 7.19.

If the structure is excited by the single waveguides modes, the supermodes with large amplitudes on the outer cores, i.e. those with propagation constants close to β_*, will carry the main part of the inserted power. According to the reasoning of Section 7.1, this allows to define a characteristic coupling length as $L_c = \pi/|\beta^s - \beta^a|$, where β^s, β^a are the wavenumbers of the symmetric (s) and antisymmetric (a) supermodes with largest initial weights (1.80). Constructive interference of the two modes is at least a necessary condition for the power transfer between the outer waveguides. This condition covers the distribution of the largest part of the guided power. Note that for complete power transfer the remaining modes must add properly to the two most dominant, and this additional constraint is not included in the definition of L_c.

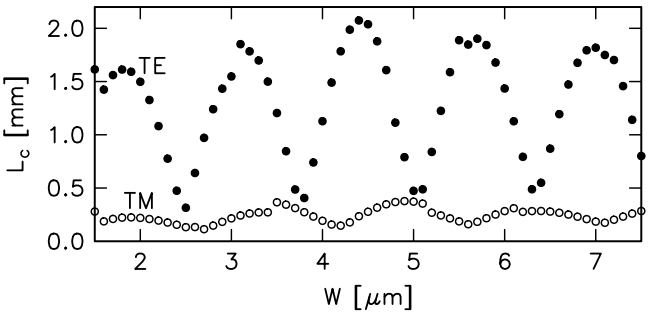

Figure 7.21: Coupling length for the couplers of Figure 7.19, for TE (filled circles) and TM polarized light (open markers) versus width W of the central waveguide.

For our series of couplers L_c evaluates to the curves of Figure 7.21. The figure confirms the pronounced difference between the TE and TM coupling behaviours as predicted in Section 5.3. The curves are not smooth due to two reasons. First, in the locations of the minima, the supermodes change, which enter the expression for L_c.

The second reason for the discontinuity becomes apparent if Figures 7.21 and 7.19 are compared. With increasing width W, the basic set of coupled modes is enlarged by newly appearing modes of the central rib. These are identified by the mode solver only if there is a certain distance between the trial propagation constant and the background value, given by the substrate refractive index. If a guided mode is identified, its field distribution (which enters the coupled mode theory integrals) becomes more and more unreliable for a mode approaching cutoff. Even if the accuracy can be increased, with numerically calculated basic modes there will never be a smooth transition to enlarged mode sets. We regard this as a fundamental problem for the application of coupled mode theory to such multimode structures. However, while a quantitative accuracy better than the discontinuities in $L_c(W)$ cannot be guaranteed, the qualitative behaviour of these curves is correct.

For the following design we stay away from the discontinuities for both TE and TM. We have assumed the waveguide height, wavelength and refractive indices to be fixed, and calculated a series of central waveguide mode sets with $4.5\,\mu\text{m} < W < 5.1\,\mu\text{m}$. Then coupled mode theory simulations with parameters varying around $w = 1.2\,\mu\text{m}$, $g = 0.1\,\mu\text{m}$ lead to a parameter set for a well performing polarization splitter as summarized in Table 7.5.

	W	w	g	h	λ	L
q	$4.96\,\mu$m	$1.21\,\mu$m	$0.11\,\mu$m	$0.70\,\mu$m	$1.30\,\mu$m	$850\,\mu$m
Δq	± 10 nm	± 1 nm	± 2 nm	± 20 nm	± 1 nm	$\pm 25\,\mu$m

Table 7.5: Parameters and tolerances for a three waveguide polarization splitter according to Figures 7.1(b) and 1.8. See the text for the interpretation of the tolerances and the caption of Figure 7.19 for refractive index values.

The device achieves polarization splitting ratios of $\text{ER}_1 = 10\log_{10}(P_{\text{AB}}^{\text{TM}}/P_{\text{AB}}^{\text{TE}}) = 27\,\text{dB}$ and $\text{ER}_2 = 10\log_{10}(P_{\text{AC}}^{\text{TE}}/P_{\text{AC}}^{\text{TM}}) = 26\,\text{dB}$. For otherwise tuned parameters, the geometry tolerances are determined such that both ER_1 and ER_2 exceed the level 20 dB if a parameter deviates from its optimum q by no more than the value Δq given in the table. The tolerances are roughly estimated with the help of the perturbational expressions of Section 1.4 for the derivatives of propagation constants due to geometry variations, based on the supermode profiles of Figure 7.20. For each parameter $q \in \{W, h, w, g, \lambda\}$, we have calculated curves $P_{\text{AB,AC}}^{\text{TE,TM}}(\delta q)$ and the extinction ratios by Eq. (1.81), with original mode profiles, but with the propagation constants changed by $\partial_q \beta^s \delta q$, and read off the tolerance values. Unfortunately the short device length has its price: the tolerances for the widths of the gaps and of the outer waveguides are very strict. At the same time, due to similar supermode profiles along the vertical direction, the waveguide height turns out to be an uncritical parameter.

The optimum device length, its tolerance and the peak performance are indicated by the curves of Figure 7.22. From Figure 7.21, at $W = 4.96\,\mu$m one expects a coupling length for TE beeing about twice as long as that for TM, corresponding to the superposition of the dominant modes. Despite the interference

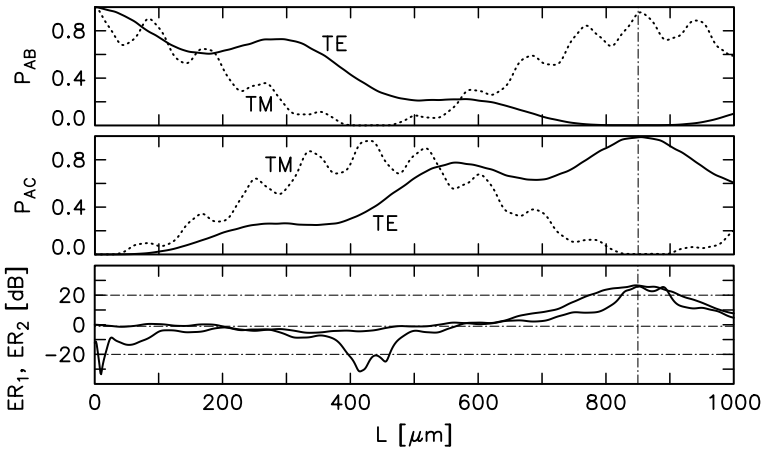

Figure 7.22: Relative output power for TE (continuous lines) and TM polarization (dotted lines) for waveguide WG1 (top) and waveguide WG2 (center) and extinction ratios ER_1, ER_2 (bottom) versus the length of the coupling section L. The vertical line indicates the proper length for the polarization splitter of Table 7.5.

of 8 TE and 7 TM modes, this sinusoidal trend is clearly visible in the power versus propagation distance curves of Figure 7.22.

Finally, Figure 7.23 shows the light propagation in the polarization splitter. Note that for most positions $0 < z < L$ part of the power is carried in the center core region, therefore $P_{\mathrm{AB}}^{\mathrm{TE/TM}}$ and $P_{\mathrm{AC}}^{\mathrm{TE/TM}}$ usually do not add to one.

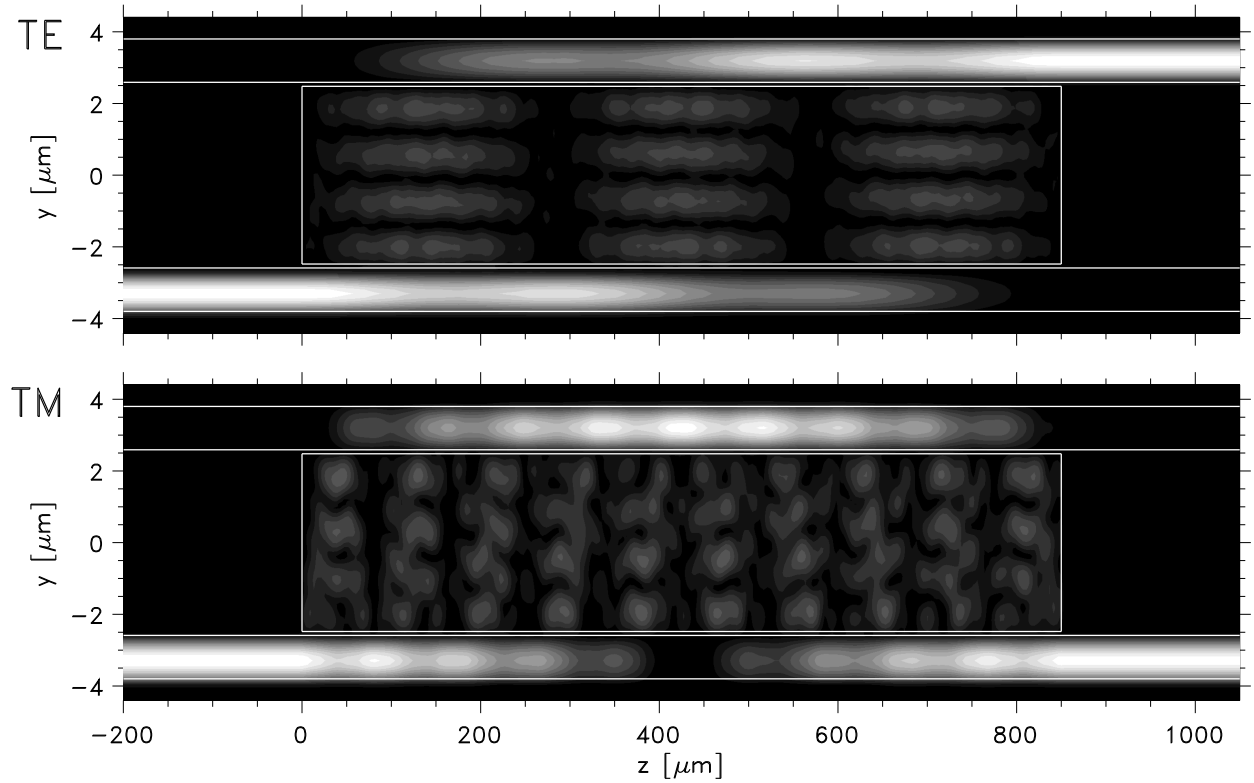

Figure 7.23: TE (top) and TM light propagation (bottom) for the three waveguide coupler as prescribed by the parameters of Table 7.5. The length of the coupling section is $L = 850\,\mu$m. The grey scale levels correspond to the squareroot of the z-component of the Poynting vector, evaluated in the y-z-plane at half the waveguide height $x = h/2$.

7.4 Polarization independent isolator/circulator

Protection of an optical circuit from backscattered light is the most prominent application of optical isolators. In general, the attached optical network does not preserve polarization, hence arbitrarily polarized reflected light must be blocked. For a light source that is restricted to a single polarization, combination of a single polarization isolator and a properly adjusted polarizer or polarization splitter yields the desired protection. If, in contrast, the circuits output is not of a specific polarization, e.g. because part of it is constructed by pieces of circular optical fiber, the task requires an isolator with polarization independent performance.

In an integrated optical setting, we thus have to demand proper isolation for both TE and TM input light. The straightforward way to achieve this is to line up a TE and a TM isolator, provided that each device is transparent for the other polarization (note that this is a critical additional constraint for most single polarization concepts). The conventional polarization rotator setup of Section 6.3 cannot be used, since it involves polarizers.

Alternatively, one may think of one isolator for TE light and one for TM light in parallel, connected to single input and output waveguides by two polarization splitters. Both have to be manufactured side by side on the same substrate, requiring in close proximity different materials and perpendicularly directed outer bias fields for proper adjustment of the magnetization (cf. Section 7.2.2). Similar difficulties arise with the first concept for a non-composite integrated polarization independent isolator, as proposed recently in Ref. [180]. The device consists of a Mach-Zehnder interferometer where one branch is designed as a nonreciprocal phase shifter for TE modes, the other a phase shifter for TM modes. Both branches are of almost square shape and made with a compensation wall, or from a double layer waveguide, respectively, such that two regions of opposite Farady rotation exist. The magnetization has to be adjusted perpendicularly to the substrate surface in one branch, and parallel to the substrate in the other branch.

As another alternative, it is tempting to employ the unidirectional polarization converters of Section 6.4 [77]. Almost square magnetooptic double layer waveguide segments of proper length are placed between two polarization splitters, where we can use the radiatively coupled waveguide design of Section 7.3.2, with the shape of the outer waveguides adjusted to the polarization converters. Figure 7.24 sketches the concept.

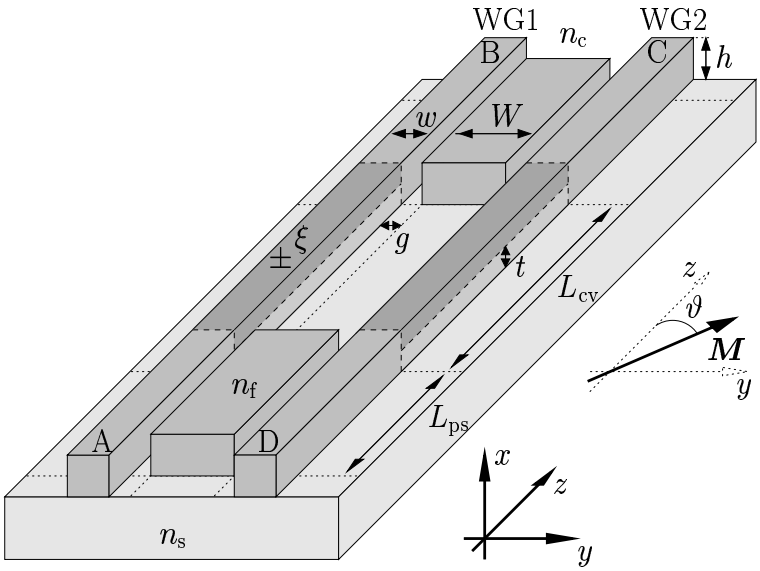

Figure 7.24: Geometry of the polarization independent circulator. The composite device consists of two polarization splitters, each of length L_{ps}, with two polarization converting double layer waveguides of length L_{cv} in-between.

Table 7.6 collects a set of suitable parameters. The analysis of the composite device employs semivectorial WMM based coupled mode theory for the polarization splitters, and the vectorial coupled mode formalism for the magnetooptic polarization converters. The simulation proceeds stepwise along the five longitudinally homogeneous segments, with the output amplitudes of the four port modes from one waveguide segment used as input amplitudes for the subsequent one. For simplicity, we assume an isotropic material and pos-

itively and negatively rotating magnetooptic materials with the same refractive index. Then the port waveguide geometry h, w, the length of the polarization converters L_{cv}, and the magnetooptic profile ξ, t, ϑ, are dictated by the unidirectional phase matching condition (6.25), and by the requirement of backward phase matched waveguides. Table 7.6 shows parameters for waveguide (i) of Table 6.5. The planar waveguide (n_{s}, n_{f}, n_{c}, h) corresponding to the strips is still single-mode, thus the polarization splitter design procedure of Section 7.3.2 can be applied, leading to the remaining dimensional parameters W, g, and L_{ps}. For a rough estimation of fabrication tolerances we refer to Sections 6.4 and 7.3.2.

$h/\,\mu$m	$w/\,\mu$m	$t/\,\mu$m	$\vartheta/\,^\circ$	$g/\,\mu$m	$W/\,\mu$m	$L_{\mathrm{ps}}/\,\mu$m	$L_{\mathrm{cv}}/\,\mu$m	n_{s}	n_{f}	n_{c}	$\pm\xi$	$\lambda/\,\mu$m
0.634	0.798	0.181	63	0.103	3.616	492	1832	1.95	2.302	1.0	0.005	1.3

Table 7.6: Parameters enabling isolator performance of the device of Figure 7.24. The polarization converters and two polarization splitters add up to a total device length of 2.816 *mm.*

The simulation of the device serves best to explain its behaviour. Previously one should recall the function of the polarization splitters and of the unidirectional polarization converters. TM light injected in one of the polarization splitter ports leaves the splitter in the same waveguide straight ahead, while TE light changes the waveguide. This applies to both directions of light propagation. Waves propagating in the polarization converters in forward direction regain their input polarization at the output. In backward direction, TE input polarization is converted to TM output light, and vice versa. Combination of these functions leads to the light paths depicted in Figure 7.25. Charts (a) and (b) show a straight transmission from port A to B in forward direction for both input polarizations. In backward direction, illustrated in insets (c) and (d), port B is connected to D for TE and TM polarized light. Mirrored beating patterns appear for forward transmission from D to C and for the backward connection between C and A. This is the functionality of an isolator for the two straight light paths A $\leftrightarrow$ B and D $\leftrightarrow$ C.

An assessment of the device performance has to consider the polarization splitters first. The characteristic quantities are the relative power transmissions P_{s} for straight connections (WG1 $\rightarrow$ WG1, WG2 $\rightarrow$ WG2) and P_{x} for cross light paths (WG1 $\rightarrow$ WG2, WG2 $\rightarrow$ WG1) for TE and TM polarized light. Our analysis predicts extiction ratios of $10\log_{10}(P_{\mathrm{s}}^{\mathrm{TM}}/P_{\mathrm{s}}^{\mathrm{TE}}) = 26.3\,\mathrm{dB}$ for the polarization discrimination in straight paths and $10\log_{10}(P_{\mathrm{x}}^{\mathrm{TE}}/P_{\mathrm{x}}^{\mathrm{TM}}) = 26.7\,\mathrm{dB}$ for the cross connections. Losses due to mode mismatch at the waveguide junctions in the polarization splitters evaluate to $-10\log_{10}(P_{\mathrm{x}}^{\mathrm{TE}}) = 0.34\,\mathrm{dB}$ for TE light and to $-10\log_{10}(P_{\mathrm{s}}^{\mathrm{TM}}) = 0.07\,\mathrm{dB}$ for TM polarization.

In principle, properly adjusted parameters of the polarization converters enable ideal conversion. Then only the limited splitting ratios of the two polarization splitters bound the isolator performance. In backward direction, all power fractions pass a polarization splitter once in the TE and once in the TM polarization state. Hence the total relative backward power transmission from port B to A, $P_{\mathrm{BA}} = P_{\mathrm{s}}^{\mathrm{TE}}P_{\mathrm{s}}^{\mathrm{TM}} + P_{\mathrm{x}}^{\mathrm{TE}}P_{\mathrm{x}}^{\mathrm{TM}}$, is independent from the input polarization. In forward direction, the power passes two polarization splitters in the input polarization state. The relative transmission is slightly polarization dependent. One obtains $P_{\mathrm{AB}} = \alpha((P_{\mathrm{s}}^{\mathrm{TE}})^2 + (P_{\mathrm{x}}^{\mathrm{TE}})^2) + (1-\alpha)((P_{\mathrm{s}}^{\mathrm{TM}})^2 + (P_{\mathrm{x}}^{\mathrm{TM}})^2)$, where α is the ratio of TE over TM forward power input. If the device is employed as an isolator for the A-B connection, the simulation yields isolation levels $10\log_{10}(P_{\mathrm{AB}}/P_{\mathrm{BA}})$ of $23.3\,\mathrm{dB}$ and $23.7\,\mathrm{dB}$ and losses $-10\log_{10}(P_{\mathrm{AB}})$ of $0.67\,\mathrm{dB}$ and $0.14\,\mathrm{dB}$ for TE and TM forward input polarization.

It depends on the definition of 'ports', whether the device can be regarded as a circulator. If the ports are defined in terms of modes, thus to be specified by a spatial outlet A to D and the mode polarization TE or TM, we obtain the two separate transmission cycles $\mathrm{A_{TE}} \rightarrow \mathrm{B_{TE}}$, $\mathrm{B_{TE}} \rightarrow \mathrm{D_{TM}}$, $\mathrm{D_{TM}} \rightarrow \mathrm{C_{TM}}$, $\mathrm{C_{TM}} \rightarrow \mathrm{A_{TE}}$, and $\mathrm{A_{TM}} \rightarrow \mathrm{B_{TM}}$, $\mathrm{B_{TM}} \rightarrow \mathrm{D_{TE}}$, $\mathrm{D_{TE}} \rightarrow \mathrm{C_{TE}}$, $\mathrm{C_{TE}} \rightarrow \mathrm{A_{TM}}$. There is no circulator functionality with respect to the four waveguides if only modes of equal polarization are admitted. If one considers input and output power only, the device performs as a polarization independent four port circulator with the transmission cycle A $\rightarrow$ B, B $\rightarrow$ D, D $\rightarrow$ C, C $\rightarrow$ A.

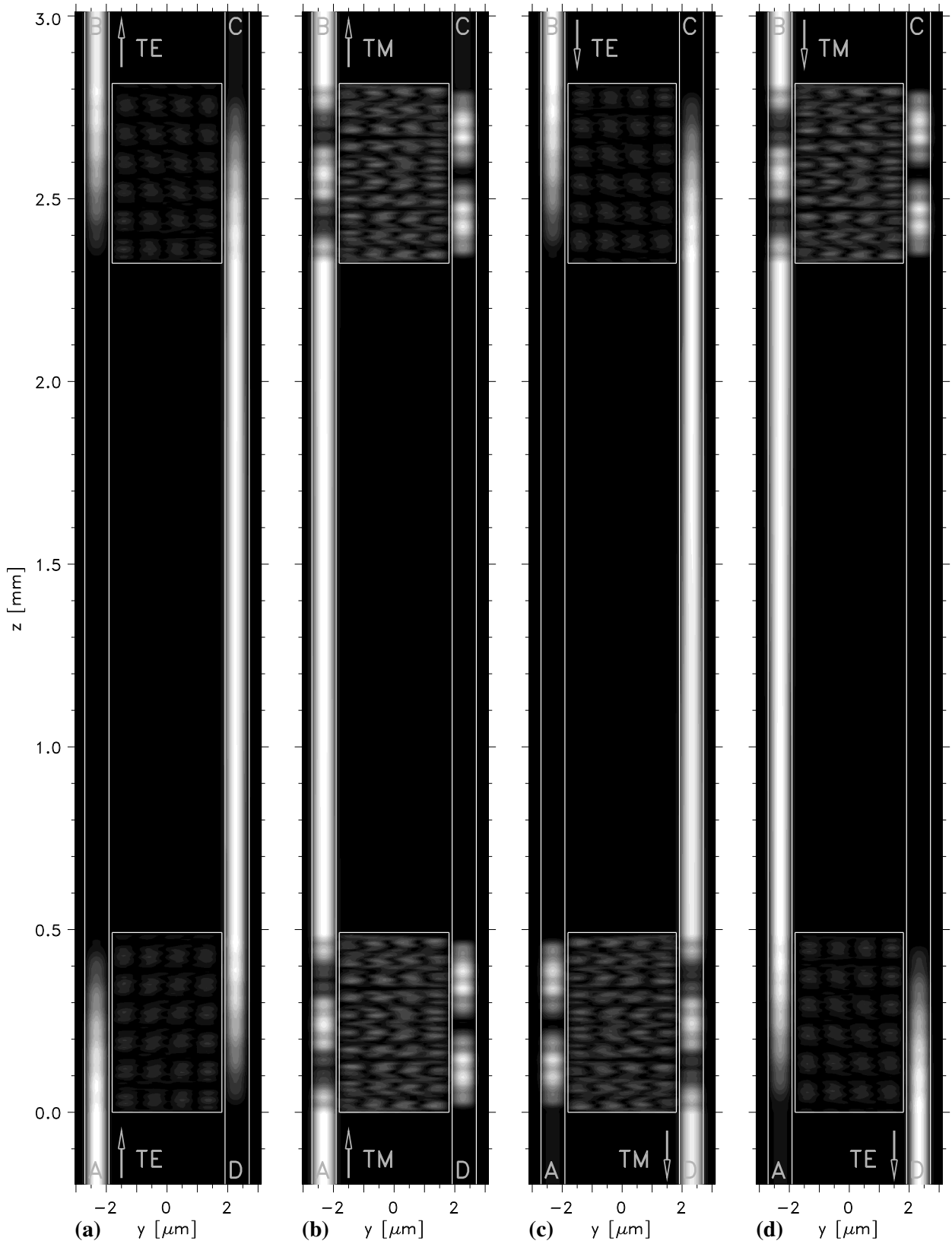

Figure 7.25: Light propagation through the device of Figure 7.24, with parameters as in Table 7.6. Grey scale levels indicate the squareroot of the local intensity (TE and TM part) in the y-z-plane in the center of the guiding film at $x = h/2$. Arrows indicate the excited port, either TE or TM light is launched.

Let us stop here with further details. Improving the design reliability, e.g. by employing fully vectorial and/or direct mode calculations for the polarization splitters, optimizing the device performance with regard to isolation and loss, and estimating the fabrication tolerances will be left for future work. The preceding chapters provide suitable theoretical and numerical tools for this task.

Summary

Touching the fields of general waveguide theory, of numerical simulation tools, and of concrete design considerations, this work has gone through a course from the fundamental Maxwell equations towards concepts for integrated magnetooptic devices. Results of this thesis include:

Proposal, implementation, and assessment of the WMM mode solver (Chapters 3, 4; Refs. [73, 74, 80, 81])

For waveguides with piecewise constant, rectangular permittivity profiles, a simple local expansion into factorizing exponential or harmonic trial functions forms a promising ansatz for the calculation of guided modes. This function space turns out to be large enough to approximate the unknown mode fields well. Inside the homogeneous rectangles the trial functions solve the Maxwell equations exactly. A least squares expression for the mismatch in the continuity conditions at dielectric boundaries connects the fields on neighbouring regions. Minimization of this error allows to identify propagation constants and to compute the mode fields.

The procedure has been implemented both for semivectorial simulations and for fully vectorial mode analysis, where each of the common formulations for the vectorial mode problem may be employed. The vectorial WMM performs truly vectorial calculations in the sense that both transverse directions are treated alike. The piecewise defined trial fields are well suited to deal with field discontinuities or discontinuous derivatives. At the corners of dielectric waveguides, the method yields correct qualitative features of the divergent field behaviour.

For widely established benchmark problems we observed excellent agreement between the WMM and several previously published methods. While in principle the current implementation allows to simulate cross sections with an arbitrary rectangular decomposition, the method turns out to be effective especially for structures described by few rectangles and boundary lines only. This class includes single rib and raised strip waveguides as well as coupler geometries constructed from these waveguides. For the composite structures investigated in this thesis, the results are reasonable and accurate. At the same time, the WMM shows to be quite economic both in computational time and memory consumption. This qualifies the method for larger simulation tasks, i.e. as the basis of a more extensive tool for integrated optics design. Inclusion of the programs into a commercial simulation environment [17] is intended.

Unlike methods based on finite differences or finite elements, the WMM yields semianalytical mode field representations which are defined on the entire plane of the waveguide cross section, including the dielectric discontinuities explicitely and accurately. The fields are therefore perfectly suited for further processing, for instance in the framework of propagating mode analysis, coupled mode theory, or for the evaluation of perturbation theory integrals. Chapters 5–7 of this thesis rely on these features.

Perturbational geometry tolerancing procedure (Sections 1.4, 5.2; Refs. [75, 78])

Shifting the location of a dielectric boundary in the cross section of a waveguide with piecewise constant refractive index profile results in a permittivity perturbation in a layer along the discontinuity line. On the basis of these thin layer perturbations, we discussed perturbational expressions for the derivatives of the propagation constants with respect to geometry parameters, both for fully vectorial, hybrid and for semivectorial approximations to the basic modes.

These derivatives can be estimated by line integrals of the mode fields along the relevant dielectric interfaces. The expressions provide direct access to the wavelength dependence. We verified the approach numerically

by comparison with rigorously calculated data on single rib and raised strip waveguides. These comparisons provide a good test not only for the perturbation formulas, but for the accuracy of the underlying mode solver.

The accuracy actually achieved is sufficient to yield reasonable tolerance estimates for realistic integrated optical devices. This was demonstrated by the examples of directional couplers. Complete tolerancing needs one mode analysis run only, even for a more complex device defined by N dimensional parameters, where at least $N + 1$ calculations are necessary to evaluate the wavenumber gradients in a conventional way by difference quotients.

The perturbational approach allows to establish and to quantify guidelines for geometry tolerant devices. The total length should be kept short, intensities on dielectric boundaries must be low, and only modes with almost equal intensity profiles should interfere.

Numerical assessment of nonreciprocal wave propagation (Chapter 6; Refs. [76, 110, 77])

The coefficients of coupled mode theory for the magnetooptic permittivity contribution allow a classification of the influences of gyrotropy on guided wave propagation. For mirror symmetric waveguides with well polarized fundamental modes, one identifies the dominant effects of TE phase shift, TM phase shift, and TE/TM polarization conversion, for polar, equatorial, and longitudinal magnetooptic configurations, respectively.

Layered equatorial magnetooptic profiles lead to phase shifters for TM modes. The nonreciprocal phase shift can be written as a sum of integrals along the horizontal magnetooptic discontinuities, multiplied with the squared transversal magnetic mode field. Analogously, sliced asymmetric polar magnetooptic profiles yield phase shifts for TE polarized modes. Here the nonreciprocal phase shift arises from vertical magnetooptic discontinuities, this time weighted by the squared dielectric displacement. We gave an explicit expression for the nonreciprocal TE phase shift of a rib waveguide with a magnetooptic domain lattice. Exact recognition of the discontinuities in the dominant electric mode field is indispensable. For comparable magnetooptic profiles, the effect reaches the same order of magnitude as the phase shift for TM modes.

Polarization conversion is the dominant effect in magnetooptic waveguides with longitudinally directed magnetization. Phase matching as a condition for complete polarization rotation can be realized with selected geometries of raised strip waveguides or embedded square waveguides. Based on coupled mode theory for the vectorial modes of rectangular isotropic waveguides, we simulated the performance of such devices in an isolator setting, including birefringence and optical absorption. Fabrication tolerances with respect to all relevant parameters can be evaluated by simple perturbational expressions. Numerical verification shows that these formulas are accurate enough for practical purposes.

Unfortunately, most tolerances turn out to be very strict. Ab initio fabrication of a waveguide with 30 dB isolation in a conventional experimental setup is difficult. However, even the tight tolerances qualify the traditional polarization rotator setup as competitive to recent proposals for integrated optical isolators based on nonreciprocal interferometry.

A magnetooptic waveguide which is magnetized at a certain angle with respect to the longitudinal direction may perform as a unidirectional polarization converter. The term specifies a device that converts TE light to TM light for one direction of propagation, while it maintains the polarization state for the opposite direction. This requires to balance the gyrotropic effects of nonreciprocal phase shift and of polarization coupling. We proposed and simulated a setup with double layer waveguides, which are composed of magnetooptic films of opposite Faraday rotation. The concept is a monolithic substitute for the conventional, usual hybrid configuration, where a nonreciprocal 45° polarization converter and a reciprocal 45° rotator are placed in line.

Designs of three waveguide couplers for applications as isolators/circulators and polarization splitters (Chapter 7; Refs. [129, 84, 82, 79])

Three-guide couplers with multimode central waveguides allow for remote coupling between optical channels. A simple three mode approximation turns out to be sufficient for a rough description. One can identify

two different regimes where either two or three supermodes determine the coupling behaviour. The conventionally defined coupling length is still useful, although here the power transfer is a truly multimode interference process.

We found good agreement between the main features of light propagation in planar radiatively coupled waveguides and in more realistic three dimensional structures. In case of the multimode and multiwaveguide raised strip structures, analysis via coupled mode theory offers an attractive alternative. Comparison with rigorously computed results for two waveguide couplers prove that the coupled mode model is adequate.

The specific form of the relevant modes suggests the design of integrated optical isolators and circulators. Aiming at a short device length, the differing shapes of the relevant mode intensity profiles in the three mode regime turn out to be advantageous. In the planar case, an effective TM circulator can be designed if the central region consists of a stack of magnetooptic layers with alternating Faraday rotation. While the planar concept directly inspires a design for a three dimensional circulator for TE polarized light, a three dimensional circulator for TM polarization may be much simpler. For a raised strip coupler consisting of magnetooptic double layer waveguides, our design enables standard isolating performance with a total length of about one millimeter.

Polarization separation in a directional coupler at a short device length requires the TE and TM coupling lengths to be as different as possible. Hence a radiatively coupled waveguide polarization splitter should operate in the two mode regime for TE polarization and in the three mode regime for TM polarization, or vice versa, such that the entire dynamic range of the coupling length variations is exploited. This is easily possible with a three dimensional raised strip configuration.

Finally, combination of two magnetooptic unidirectional polarization converters and two radiatively coupled waveguide based polarization splitters leads to a design for a polarization independent isolator. If defined in terms of input/output power rather than in terms of mode amplitudes, this is a concept for a polarization independent integrated four port circulator device, up to our knowledge the first ever proposed and simulated. Our simulation predicts a total length of about three millimeters.

Bibliography

[1] Z.-E. Abid, K. L. Johnson, and A. Gopinath. Analysis of Dielectric Guides by Vector Transverse Magnetic Field Finite Elements. *Journal of Lightwave Technology*, 11(10):1545–1549, 1993.

[2] E. Anderson, Z. Bai, C. Bischof, J. Demmel, J. Dongarra, J. Du Croz, A. Greenbaum, S. Hammarling, A. McKenney, S. Ostrouchov, and D. Sorensen. *LAPACK Users' Guide, 2nd ed.* Society for Industrial and Applied Mathematics, Philadelphia, 1995.

[3] K. Ando. Nonreciprocal devices for integrated optics. *SPIE Proceedings*, 1126:58–65, 1989.

[4] K. Ando, N. Takeda, N. Koshizuka, and T. Okuda. Annealing effects on growth induced optical birefringence in liquid-phase-epitaxial-grown Bi-substituted iron garnet films. *Journal of Applied Physics*, 57:1277–1281, 1985.

[5] F. Auracher and H. H. Witte. A new design for an integrated optical isolator. *Optics Communications*, 13(4):435–438, 1975.

[6] T. Baba and Y. Kokubun. New Polarization-Insensitive Antiresonant Reflecting Optical Waveguide (ARROW-B). *IEEE Photonics Technology Letters*, 1:232–234, 1989.

[7] T. Baba and Y. Kokubun. Dispersion and radiation loss characteristics of antiresonant reflecting optical waveguides — numerical results and analytical expression. *IEEE Journal of Quantum Electronics*, 28:1689–1700, 1992.

[8] J. Bach Andersen and V. V. Solodukhov. Field Behaviour near a Dielectric Wedge. *IEEE Transactions on Antennas and Propagation*, 29(4):598–602, 1978.

[9] M. Bachmann, P. A. Besse, and H. Melchior. General self-imaging properties in N×N multimode interference couplers including phase relations. *Applied Optics*, 33(18):3905–3911, 1994.

[10] N. Bahlmann. *Finite element simulations of integrated optical isolators and circulators in magnetic garnet films*. Universität Osnabrück, Osnabrück, 1999. Dissertation.

[11] N. Bahlmann, V. Chandrasekhara, A. Erdmann, R. Gerhardt, P. Hertel, R. Lehmann, D. Salz, F. Schröteler, M. Wallenhorst, and H. Dötsch. Improved design of magneto-optic rib waveguides for optical isolators. *Journal of Lightwave Technology*, 16(5):818–823, 1998.

[12] N. Bahlmann, M. Lohmeyer, H. Dötsch, and P. Hertel. Integrated magneto-optic Mach-Zehnder interferometer isolator for TE-modes. *Electronics Letters*, 34(22):2122–2123, 1998.

[13] N. Bahlmann, M. Lohmeyer, H. Dötsch, and P. Hertel. Finite-Element Analysis of Nonreciprocal Phase Shift for TE Modes in Magnetooptic Rib Waveguides with a Compensation Wall. *IEEE Journal of Quantum Electronics*, 35(2):250–253, 1999.

[14] N. Bahlmann, M. Lohmeyer, M. Wallenhorst, H. Dötsch, and P. Hertel. A comparison of an improved design for two integrated optical isolators based on nonreciprocal Mach-Zehnder interferometry. In K. Rubin, J. A. Bain, T. Nolan, D. Bogy, B. J. H. Stadler, M. Levy, J. P. Lorenzo, M. Mansuripur, Y. Okamura, and R. Wolfe, editors, *High-Density Magnetic Recording and Integrated Magneto-Optics: Materials and Devices*, volume 517 of MRS Symposium Proceedings Series, pages 513–518, 1998.

[15] N. Bahlmann, M. Lohmeyer, M. Wallenhorst, H. Dötsch, and P. Hertel. An improved design of an integrated optical isolator based on nonreciprocal Mach-Zehnder interferometry. *Optical and Quantum Electronics*, 30:323–334, 1998.

[16] N. Bahlmann, M. Lohmeyer, O. Zhuromskyy, H. Dötsch, and P. Hertel. Nonreciprocal coupled waveguides for integrated optical isolators and circulators for TM-modes. *Optics Communications*, 161(4-6):330–337, 1999.

[17] 2D Mode Solver 'Selene'. BBV Software BV, Hengelosestraat 705, 7521 PA Enschede, The Netherlands; http://www.bbv-software.com.

[18] G. M. Berry and S. V. Burke. Analysis of optical rib self-imaging multimode interference (MMI) waveguide devices using the discrete spectral index method. *Optical and Quantum Electronics*, 27:921–934, 1995.

[19] K. Bierwirth, N. Schulz, and F. Arndt. Finite-Difference Analysis of Rectangular Dielectric Waveguide Structures. *IEEE Transactions on Microwave Theory and Techniques*, MTT-34(11):1104–1113, 1986.

[20] M. Bressan and P. Gamba. Analytical Expressions of Field Singularities at the Edge of Four Right Wedges. *IEEE Microwave and Guided Wave Letters*, 4(1):3–5, 1994.

[21] J. Buus, M. C. Farries, and D. J. Robbins. Reflectivity of Coated and Tilted Semiconductor Facets. *IEEE Journal of Quantum Electronics*, 27(6):1837–1842, 1991.

[22] K. L. Chen and S. Wang. The Crosstalk in Three-Waveguide Optical Directional Couplers. *IEEE Journal of Quantum Electronics*, 22(7):1039–1041, 1986.

[23] K. S. Chiang. Review of numerical and approximate methods for the modal analysis of general optical dielectric waveguides. *Optical and Quantum Electronics*, 26:S113–S134, 1994.

[24] K. S. Chiang. Analysis of the Effective-Index Method for the Vector Modes of Rectangular-Core Dielectric Waveguides. *IEEE Transactions on Microwave Theory and Techniques*, 44(5):692–700, 1996.

[25] S. L. Chuang. A Coupled Mode Formulation by Reciprocity and a Variational Principle. *Journal of Lightwave Technology*, 5(1):5–15, 1987.

[26] H. Dammann, E. Pross, G. Rabe, and W. Tolksdorf. 45° waveguide isolators with phase mismatch. *Applied Physics Letters*, 56:1302–1304, 1990.

[27] H. Dammann, E. Pross, G. Rabe, W. Tolksdorf, and M. Zinke. Phase matching in symmetrical single-mode magneto-optic waveguides by application of stress. *Applied Physics Letters*, 49:1755–1757, 1986.

[28] J. B. Davies. A Least Squares Boundary Residual Method for the Numerical Solution of Scattering Problems. *IEEE Transactions on Microwave Theory and Techniques*, MTT-21(2):99–104, 1973.

[29] J. P. Donelly. Limitations on Power Transfer Efficiency in Three-Guide Optical Couplers. *IEEE Journal of Quantum Electronics*, 22(5):610–616, 1986.

[30] H. Dötsch. Integrierte Optik. Skript zur Vorlesung an der Universität Osnabrück, 1995.

[31] H. Dötsch. Magnetooptik. Skript zur Vorlesung an der Universität Osnabrück, 1994.

[32] H. Dötsch, A. Erdmann, M. Fehndrich, R. Gerhardt, P. Hertel, B. Lührmann, M. Shamonin, H. P. Winkler, and M. Wallenhorst. Application of magnetic garnet films in optical communications. In R. Marcelli and S. A. Nikitov, editors, *Nonlinear Microwave Signal Processing: Towards a New Range of Devices*, pages 411–465, Dordrecht, Boston, London, 1996. Kluwer Academic Publishers.

[33] H. Dötsch, P. Hertel, B. Lührmann, S. Sure, H. P. Winkler, and M. Ye. Applications of Magnetic Garnet Films in Integrated Optics. *IEEE Transactions on Magnetics*, 28(5):2979–2984, 1992.

[34] M. A. Duguay, Y. Kokubun, and T. L. Koch. Antiresonant reflecting optical waveguides in SiO_2–Si multilayer structures. *Applied Physics Letters*, 49:13–15, 1986.

[35] M. Eisenmann and E. Weidel. Single-mode fused biconical coupler optimized for polarization beamsplitting. *Journal of Lightwave Technology*, 9:853–858, 1991.

[36] A. Erdmann and P. Hertel. Beam-Propagation in Magnetooptic Waveguides. *IEEE Journal of Quantum Electronics*, 31(8):1510–1516, 1995.

[37] A. Erdmann, P. Hertel, and H. Dötsch. Nonreciprocal coupling effects in gyrotropic waveguide structures. *Optical and Quantum Electronics*, 26:949–955, 1994.

[38] A. Erdmann, M. Shamonin, P. Hertel, and H. Dötsch. Finite difference analysis of gyrotropic waveguides. *Optics Communications*, 102:25–30, 1993.

[39] M. Fehndrich. *Entwicklung integrierter optischer Isolatoren und Modulatoren*. Universität Osnabrück, Osnabrück, 1999. Dissertation.

[40] M. Fehndrich, A. Josef, L. Wilkens, J. Kleine-Börger, N. Bahlmann, M. Lohmeyer, P. Hertel, and H. Dötsch. Experimental Investigation of the Nonreciprocal Phase Shift of a TE-Mode in a Magneto-Optic Rib Waveguide. *Applied Physics Letters*, 74(20):2918–2920, 1999.

[41] L. Friedrich, P. Dannberg, C. Wächter, Th. Hennig, A. Bräuer, and W. Karthe. Directional coupler device using a three-dimensional waveguide structure. *Optics Communications*, 137:239–243, 1997.

[42] G. J. Gabriel and M. E. Brodwin. The Solution of Guided Waves in Inhomogeneous Anisotropic Media by Perturbation and Variational Methods. *IEEE Transactions on Microwave Theory and Techniques*, MTT-13:364–370, 1965.

[43] R. Gerhardt, S. Sure, H. Dötsch, T. Linkewitz, and W. Tolksdorf. Optical properties of bismuth and gallium substituted thulium iron garnet films. *Optics Communications*, 102:31–35, 1993.

[44] G. R. Hadley and R. E. Smith. Full-Vector Waveguide Modeling Using an Iterative Finite-Difference Method with Transparent Boundary Conditions. *Journal of Lightwave Technology*, 13(3):465–469, 1995.

[45] D. G. Hall and B. J. Thompson, editors. *Selected Papers on Coupled-Mode Theory in Guided-Wave Optics*, volume MS 84 of *SPIE Milestone Series*. SPIE Optical Engineering Press, Bellingham, Washington USA, 1993.

[46] A. Hardy and W. Streifer. Coupled Mode Theory of Parallel Waveguides. *Journal of Lightwave Technology*, LT-3(5):1135–1146, 1985.

[47] A. Haus and C. G. Fonstad. Three-Waveguide Couplers for Improved Sampling and Filtering. *IEEE Journal of Quantum Electronics*, 17(12):2321–2325, 1981.

[48] H. A. Haus, W. P. Huang, S. Kawakami, and N. A. Whitaker. Coupled Mode Theory of Optical Waveguides. *Journal of Lightwave Technology*, LT-5(1):16–23, 1987.

[49] J. M. Heaton, R. M. Jenkins, D. R. Wight, J. T. Parker, J. C. H. Birbeck, and K. P. Hilton. Novel 1-to-N way integrated optical beam splitters using symmetric mode mixing in GaAs/AlGaAs multimode waveguides. *Applied Physics Letters*, 61(15):1754–1756, 1992.

[50] C. H. Henry and B. H. Verbeek. Solution of the Scalar Wave Equation for Arbitrarily Shaped Dielectric Waveguides by Two-Dimensional Fourier Analysis. *Journal of Lightwave Technology*, 7(2):308–313, 1989.

[51] P. Hertel. Dielektrische Wellenleiter. Skript zur Vorlesung an der Universität Osnabrück, WS 95/96.

[52] P. Hertel. Lineare und nichtlineare Antwort auf Störungen des thermodynamischen Gleichgewichtes durch zeitveränderliche elektrische Felder. Skript zur Vorlesung an der Universität Osnabrück, 1992.

[53] P. Hertel. Numerische Behandlung Partieller Differentialgleichungen. Skript zur Vorlesung an der Universität Osnabrück, WS 92/93.

[54] S. J. Hewlett and F. Ladouceur. Fourier Decomposition Method Applied to Mapped Infinite Domains: Scalar Analysis of Dielectric Waveguides Down to Modal Cutoff. *Journal of Lightwave Technology*, 13(3):375–383, 1995.

[55] R. C. Hewson-Browne, P. C. Kendall, and D. A. Quinney. Roughness scattering into substrate radiation modes of rib waveguides. *IEE Proceedings, Pt. J*, 136(5):281–286, 1989.

[56] H. J. W. M. Hoekstra. An Economic Method for the Solution of the Scalar Wave Equation for Arbitrarily Shaped Optical Waveguides. *Journal of Lightwave Technology*, 8(5):789–793, 1990.

[57] H. J. W. M. Hoekstra. On beam propagation methods for modelling in integrated optics. *Optical and Quantum Electronics*, 29:157–171, 1997.

[58] W. Huang and H. A. Haus. A Simple Variational Approach to Optical Rib Waveguides. *Journal of Lightwave Technology*, 9(1):56–61, 1991.

[59] W. P. Huang. Coupled mode theory for optical waveguides: an overview. *Journal of the Optical Society of America A*, 11(3):963–983, 1994.

[60] R. G. Hunsperger. *Integrated Optics: Theory and Technology, Fourth Edition*. Springer Verlag, Berlin, 1995.

[61] H. Iwamura, S. Hayashi, and H. Iwasaki. A compact optical isolator using a $Y_3Fe_5O_{12}$ crystal for near infra-red radiation. *Optical and Quantum Electronics*, 10:393–398, 1978.

[62] W. Karthe and R. Müller. *Integrierte Optik*. Akademische Verlagsgesellschaft Geest & Portig K.-G., Leipzig, 1991.

[63] B. W. Kernighan and D. M. Ritchie. *The C Programming Language (Second Edition)*. Prentice-Hall, Englewood Cliffs, New Jersey, 1988.

[64] M. Koshiba, S. Maruyama, and K. Hirayama. A Vector Finite Element Method With the High-Order Mixed-Interpolation-Type Triangular Elements for Optical Waveguiding Problems. *Journal of Lightwave Technology*, 12(3):495–502, 1994.

[65] G. Krijnen. *All-Optical Switching in Nonlinear Integrated Optic Devices*. University of Twente, Enschede, The Netherlands, 1992. Ph.D. Thesis.

[66] F. Lederer, L. Leine, M. Mann, T. Peschel, U. Muschall, U. Trutschel, C. Wächter, C. Carigan, M. A. Duguay, and F. Ouelette. Linear mode beating and nonlinear mode coupling in resonant optical waveguides. In G. Wegner, W. Karthe, and W. Ehrfeld, editors, *Integrated Optics and Micro Optics with Polymers*, pages 301–331. Teubner Verlagsgesellschaft, Stuttgart, 1993. Teubner Texte zur Physik, Nr. 27.

[67] P.-C. Lee and E. Voges. Three Dimensional Semi-Vectorial Wide-Angle Beam Propagation Method. *Journal of Lightwave Technology*, 12(2):215–224, 1994.

[68] M. Levy, I. Ilic, R. Scarmozzino, R. M. Osgood, R. Wolfe, C. I. Guiterrez, and G. A. Prinz. Thin-film-magnet magnetooptic waveguide isolator. *IEEE Photonics Technology Letters*, 5:198–200, 1994.

[69] X. Li and R. T. Deck. Light polarizer based on antiresonant reflecting layers in a directional coupler. *Applied Physics Letters*, 66:130–132, 1995.

[70] P.-L. Liu and B.-J. Li. Semivectorial Helmholtz Beam Propagation by Lanczos Reduction. *IEEE Journal of Quantum Electronics*, 29(8):2385–2389, 1993.

[71] P.-L. Liu, S. L. Yang, and D. M. Yuan. The Semivectorial Beam Propagation Method. *IEEE Journal of Quantum Electronics*, 29(4):1205–1211, 1993.

[72] M. Lohmeyer. Ausbreitungsrechungen für integrierte magnetooptische Wellenleiter — Methode der finiten Differenzen, 1995. Diplomarbeit, Fachbereich Physik der Universität Osnabrück.

[73] M. Lohmeyer. Wave-matching method for mode analysis of dielectric waveguides. *Optical and Quantum Electronics*, 29:907–922, 1997.

[74] M. Lohmeyer. Vectorial wave-matching mode analysis of integrated optical waveguides. *Optical and Quantum Electronics*, 30:385–396, 1998.

[75] M. Lohmeyer, N. Bahlmann, and P. Hertel. Geometry tolerance estimation for rectangular dielectric waveguide devices by means of perturbation theory. *Optics Communications*, 163(1-3):86–94, 1999.

[76] M. Lohmeyer, N. Bahlmann, O. Zhuromskyy, H. Dötsch, and P. Hertel. Phase-matched rectangular magnetooptic waveguides for applications in integrated optics isolators: numerical assessment. *Optics Communications*, 158:189–200, 1998.

[77] M. Lohmeyer, N. Bahlmann, O. Zhuromskyy, H. Dötsch, and P. Hertel. Unidirectional magnetooptic polarization converters. *Journal of Lightwave Technology*, 1999. Submitted.

[78] M. Lohmeyer, N. Bahlmann, O. Zhuromskyy, and P. Hertel. Perturbational estimation of geometry tolerances for rectangular integrated optics devices. In G. C. Righini and S. I. Najafi, editors, *Integrated Optics Devices III*, volume 3620 of SPIE Proceedings, pages 311–319, 1999.

[79] M. Lohmeyer, N. Bahlmann, O. Zhuromskyy, and P. Hertel. Radiatively coupled waveguide polarization splitter simulated by wave-matching based coupled mode theory. *Optical and Quantum Electronics*, 1999. Accepted for publication.

[80] M. Lohmeyer, N. Bahlmann, O. Zhuromskyy, and P. Hertel. Wave-matching-simulations of integrated optical coupler structures. In G. C. Righini and S. I. Najafi, editors, *Integrated Optics Devices III*, volume 3620 of SPIE Proceedings, pages 68–78, 1999.

[81] M. Lohmeyer, N. Bahlmann, O. Zhuromskyy, and P. Hertel. Wave-matching-simulations of integrated optical coupler structures. *Fiber and integrated optics*, 1999. Submitted (invited).

[82] M. Lohmeyer, M. Shamonin, N. Bahlmann, P. Hertel, and H. Dötsch. Radiatively coupled waveguide concept for an integrated magneto-optic circulator. In K. Rubin, J. A. Bain, T. Nolan, D. Bogy, B. J. H. Stadler, M. Levy, J. P. Lorenzo, M. Mansuripur, Y. Okamura, and R. Wolfe, editors, *High-Density Magnetic Recording and Integrated Magneto-Optics: Materials and Devices*, volume 517 of MRS Symposium Proceedings Series, pages 519–524, 1998.

[83] M. Lohmeyer, M. Shamonin, and P. Hertel. Boundary Conditions for the Finite Difference Beam Propagation Method Based on Plane Wave Solutions of the Fresnel Equation. *IEEE Journal of Quantum Electronics*, 33(2):279–285, 1997.

[84] M. Lohmeyer, M. Shamonin, and P. Hertel. Integrated Optical Circulator based on Radiatively Coupled Waveguides. *Optical Engineering*, 36(3):889–895, 1997.

[85] S. M. Loktev, V. A. Sychugov, and B. A. Usievich. Propagation of light in a system of two radiatively coupled waveguides. *Sov. Journal of Quantum Electronics*, 24(5):435–438, 1994.

[86] P. Lüsse. *Numerische Entwurfswerkzeuge für optische Wellenleiterbauelemente*. VDI - Verlag, Düsseldorf, 1997. Dissertation, VDI Fortschritts-Berichte, Reihe 20: Rechnerunterstützte Verfahren, Nr. 239.

[87] P. Lüsse, K. Ramm, and H.-G. Unger. Comparison of a vectorial and new semivectorial finite-difference approach for optical waveguides. *Optical and Quantum Electronics*, 29:115–120, 1997.

[88] P. Lüsse, P. Stuwe, J. Schüle, and H.-G. Unger. Analysis of Vectorial Mode Fields in Optical Waveguides by a New Finite Difference Method. *Journal of Lightwave Technology*, 12(3):487–493, 1994.

[89] M. Mann, U. Trutschel, C. Wächter, L. Leine, and F. Lederer. Directional coupler based on antiresonant reflecting optical waveguide. *Optics Letters*, 16:805–807, 1991.

[90] D. Marcuse. Directional Coupler Made of Nonidentical Asymmetric Slabs: Part II: Grating-Assisted Couplers. *Journal of Lightwave Technology*, 5:268–273, 1987.

[91] R. März. *Integrated Optics — Design and Modeling*. Artech House, Boston, London, 1994.

[92] V. L. Maslennikov, V. A. Sychugov, A. V. Tishchenko, and B. A. Usievich. Light generation in a system of two coupled waveguides. *Sov. Journal of Quantum Electronics*, 22:1041–1044, 1992.

[93] H.-P. Menzler. *Planare dielektrische Wellenleiter: Analytische und numerische Verfahren*. Universität Osnabrück, Osnabrück, 1989. Dissertation.

[94] K. Mertens. Vorrichtung zur Polarisationskonversion in passiven integriert optischen Streifen-, Rippen-, streifenbelasteten Film-Wellenleitern o.ä. aus isotropen Materialien. Deutsches Patentamt, Patentanmeldung, Akz. 195 05 996.4 51, 22.08.1996.

[95] K. Mertens. *Entwicklung von integriert-optischen Bauelementen auf Indiumphosphid-Basis*. Shaker Verlag, Aachen, 1996. Dissertation.

[96] K. Mertens, B. Scholl, and H. J. Schmitt. New Highly Efficient Polarization Converters Based on Hybrid Supermodes. *Journal of Lightwave Technology*, 13(10):2087–2092, 1995.

[97] T. Mizumoto, S. Mashimo, T. Ida, and Y. Naito. In-plane magnetized rare earth iron garnet for a waveguide optical isolator employing nonreciprocal phase shift. *IEEE Transactions on Magnetics*, 29:3417–3419, 1993.

[98] T. Mizumoto, K. Oochi, T. Harada, and Y. Naito. Measurement of Optical Nonreciprocal Phase Shift in a Bi-Substituted $Gd_3Fe_5O_{12}$ Film and Application to Waveguide-Type Optical Circulator. *Journal of Lightwave Technology*, 4(3):347–352, 1986.

[99] M. Monerie, A. Leclert, P. Anizan, G. Moisan, and P. Auvray. Dispositifs magnetooptiques en couches minces a accord de phase: utilisation d'une double heteroepitaxie de grenats ferromagnetiques. *Optics Communications*, 19:143–146, 1976.

[100] W.-C. Ng, M. S. Stern, and S.-J. Chua. The Design of Triple Rib Waveguide Couplers by the Discrete Spectral Index Method. *Journal of Lightwave Technology*, 17(3):475–482, 1999.

[101] W. Nolting. *Grundkurs Theoretische Physik, Bd. 3: Elektrodynamik*. Verlag Zimmermann - Neufang, Ulmen, 1990.

[102] H. Noro and T. Nakayama. A New Approach to Scalar and Semivector Mode Analysis of Optical Waveguides. *Journal of Lightwave Technology*, 14(6):1546–1556, 1996.

[103] A. Oliner, S.-T. Peng, T.-I. Hsu, and A. Sanchez. Guidance and Leakage Properties of a Class of Open Dielectric Waveguides: Part II — New Physical Effects. *IEEE Transactions on Microwave Theory and Techniques*, MTT-29(9):855–869, 1981.

[104] F. P. Payne and J. P. R. Lacey. A theoretical analysis of scattering loss from planar optical waveguides. *Optical and Quantum Electronics*, 26:977–986, 1994.

[105] S.-T. Peng and A. Oliner. Guidance and Leakage Properties of a Class of Open Dielectric Waveguides: Part I — Mathematical Formulations. *IEEE Transactions on Microwave Theory and Techniques*, MTT-29(9):843–854, 1981.

[106] P. S. Pershan. Magneto-Optical Effects. *Journal of Applied Physics*, 38(3):1482, 1967.

[107] D. V. Petrov. Directional Coupler Using a Leaky Wave of an Anisotropic Waveguide. *IEEE Photonics Technology Letters*, 8:381–383, 1996.

[108] S. P. Pogossian. Phase-matching in magneto-optic waveguides with W-shaped refractive index profile. *Optics Communications*, 96:52–54, 1993.

[109] A. F. Popkov. Wave properties of a domain wall in a transparent magnetic material. *Sov. Phys. Solid State*, 19(8):1339–1343, 1977.

[110] A. F. Popkov, M. Fehndrich, M. Lohmeyer, and H. Dötsch. Nonreciprocal TE-mode phase shift by domain walls in magnetooptic rib waveguides. *Applied Physics Letters*, 72(20):2508–2510, 1998.

[111] A. F. Popkov, M. Fehndrich, O. Zhuromskyy, and H. Dötsch. Nonreciprocal light channeling in a film by a magnetic nonuniformity akin to a néel domain wall. *Journal of Applied Physics*, 84(6):3020–3025, 1998.

[112] W. H. Press, S. A. Teukolsky, W. T. Vetterling, and B. P. Flannery. *Numerical Recipes in C, 2nd ed.* Cambridge University Press, 1992.

[113] J. R. Pujol Pola, W. Biehlig, and F. Lederer. A Generalization of the Spectral Index Method Toward Multiple Rib Waveguides. *Journal of Lightwave Technology*, 14(3):454–460, 1996.

[114] B. M. A. Rahman and J. B. Davies. Finite-Element Solution of Integrated Optical Waveguides. *Journal of Lightwave Technology*, 2:682–687, 1984.

[115] B. M. A. Rahman and J. B. Davies. Vector-H Finite-Element Solution of GaAs/GaAsAs Rib Waveguides. *IEE Proceedings*, 132(6):349–353, 1985.

[116] B. M. A. Rahman and J. B. Davies. Analysis of Optical Waveguide Discontinuities. *Journal of Lightwave Technology*, 6(1):52–57, 1988.

[117] M. Rajarajan, B. M. A. Rahman, T. Wongcharoen, and K. T. V. Grattan. Accurate Analysis of MMI Devices with Two-Dimensional Confinement. *Journal of Lightwave Technology*, 14(9):2078–2084, 1996.

[118] P. N. Robson and P. C. Kendall. *Rib Waveguide Theory by the Spectral Index Method.* Wiley, New York, 1990.

[119] U. Rogge and R. Pregla. Vectorial Method of Lines for the Analysis of Strip-Loaded Optical Waveguides. *Journal of the Optical Society of America B*, 8:459–463, 1991.

[120] T. Rozzi, G. Cerri, M. N. Husain, and L. Zappelli. Variational Analysis of the Dielectric Rib Waveguide Using the Concept of "Transition Function" and Including Edge Singularities. *IEEE Transactions on Microwave Theory and Techniques*, 39(2):247–257, 1991.

[121] R. Schoppenhauer. Berechnung magnetooptischer Streifenwellenleiter mit der Methode der Finiten Elemente, 1994. Diplomarbeit, Fachbereich Physik der Universität Osnabrück.

[122] P. Sewell, M. Reed, T. M. Benson, and P. C. Kendall. Full Vector Analysis of Two-Dimensional Angled and Coated Optical Waveguide Facets. *IEEE Journal of Quantum Electronics*, 33(12):2311–2318, 1997.

[123] M. Shamonin. *Nonreciprocal mode propagation in magnetooptic waveguides.* Verlag Shaker, Aachen, 1995. Dissertation.

[124] M. Shamonin, A. Erdmann, and P. Hertel. Properties of TE/TM polarized-mode propagation in a system of two radiatively coupled waveguides. In *European Optical Society, Annual Meetings Digest Series, Photonics '95*, volume 2A, pages 170–173, Prague, Czechoslovakia, 1995. Czech and Slovak Society for Photonics.

[125] M. Shamonin and P. Hertel. Analysis of non-reciprocal mode propagation in magneto-optic rib-waveguide structures with the spectral-index method. *Applied Optics*, 33(27):6415–6421, 1994.

[126] M. Shamonin and P. Hertel. Analysis of nonreciprocal phase shifters for integrated optics by the Galerkin method. *Optical Engineering*, 34(3):849–852, 1995.

[127] M. Shamonin, M. Lohmeyer, and P. Hertel. Radiatively coupled magneto-optic waveguides. In S. I. Najafi and M. N. Armenise, editors, *Functional Photonic and Fiber Devices*, volume 2695 of SPIE Proceedings, pages 355–361, 1996.

[128] M. Shamonin, M. Lohmeyer, and P. Hertel. Analysis of Power-Dependent Switching Between Radiatively Coupled Planar Waveguides. *Journal of Lightwave Technology*, 15(6):983–989, 1997.

[129] M. Shamonin, M. Lohmeyer, and P. Hertel. Directional coupler based on radiatively coupled waveguides. *Applied Optics*, 36(3):635–641, 1997.

[130] M. Shamonin, M. Lohmeyer, P. Hertel, and H. Dötsch. Magneto-optic waveguides: modeling and applications. In S. I. Najafi and M. N. Armenise, editors, *Functional Photonic and Fiber Devices*, volume 2695 of SPIE Proceedings, pages 344–354, 1996.

[131] M. Shamonin, M. Lohmeyer, P. Hertel, and H. Dötsch. Optimization of a nonreciprocal phase shifter comprising a magneto-optic slab waveguide. *Optics Communications*, 131:37–40, 1996.

[132] Y. Shani, C. H. Henry, R. C. Kistler, and K. J. Orlowsky. Four-port integrated optic polarization splitter. *Applied Optics*, 29:337–339, 1990.

[133] A. Sharma, P. K. Mishra, and A. K. Ghatak. Single-Mode Optical Waveguides and Directional Couplers with Rectangular Cross Section: A Simple and Accurate Method of Analysis. *Journal of Lightwave Technology*, 6(6):1119–1125, 1988.

[134] T. Shintaku. Integrated optical isolator based on nonreciprocal higher order mode conversion. *Applied Physics Letters*, 66(21):2789–2791, 1995.

[135] T. Shintaku. Integrated optical isolator based on efficient nonreciprocal radiation mode conversion. *Applied Physics Letters*, 73(14):1946–1948, 1998.

[136] A. W. Snyder and J. D. Love. *Optical Waveguide Theory*. Chapman and Hall, London, New York, 1983.

[137] L. B. Soldano and E. C. M. Pennings. Optical Multi-Mode Interference Devices Based on Self-Imaging: Principles and Applications. *Journal of Lightwave Technology*, 13(4):615–627, 1995.

[138] L. B. Soldano, F. B. Veerman, M. K. Smit, B. H. Verbeek, A. H. Dubost, and E. C. M. Pennings. Planar Monomode Optical Couplers Based on Multimode Interference Effects. *Journal of Lightwave Technology*, 10(12):1843–1849, 1992.

[139] M. S. Stern. Semivectorial polarised finite difference method for optical waveguides with arbitrary index profiles. *IEE Proceedings, Pt. J*, 135(1):56–63, 1988.

[140] M. S. Stern. Semivectorial polarised H field solutions for dielectric waveguides with arbitrary index profiles. *IEE Proceedings, Pt. J*, 135(5):333–338, 1988.

[141] M. S. Stern, P. C. Kendall, and P. W. A. McIlroy. Analysis of the spectral index method for vector modes of rib waveguides. *IEE Proceedings, Pt. J*, 137:21–26, 1990.

[142] B. Stroustrup. *The C++ Programming Language — 3rd.ed.* Addison-Wesley, 1997.

[143] J.-Y. Su, P.-K. Wei, and W.-S. Wang. A New Iterative Method for the Analysis of Longitudinally Invariant Waveguide Couplers. *Journal of Lightwave Technology*, 12(12):2056–2065, 1994.

[144] A. S. Sudbø. Why Are Accurate Computations of Mode Fields in Rectangular Dielectric Waveguides Difficult? *Journal of Lightwave Technology*, 10(4):418–419, 1992.

[145] A. S. Sudbø. Film mode matching: a versatile numerical method for vector mode fields calculations in dielectric waveguides. *Pure and Applied Optics*, 2:211–233, 1993.

[146] N. Sugimoto, H. Terui, A. Tate, Y. Katoh, Y. Yamada, A. Sugita, A. Shibukawa, and Y. Inoue. A Hybrid Iintegrated Waveguide Isolator on a Silica-Based Planar Lightwave Circuit. *Journal of Lightwave Technology*, 14(11):2537–2546, 1996.

[147] V. A. Sychugov, A. V. Tishchenko, and B. A. Usievich. Radiatively coupled corrugated waveguides. *Quantum Electronics*, 21:442–444, 1994.

[148] T. Tamir. *Integrated Optics*. Springer Verlag, Berlin, 1979.

[149] K. Thyagarajan and S. Pilevar. Resonant tunneling three-waveguide polarization splitter. *Journal of Lightwave Technology*, 10:1334–1337, 1992.

[150] K. Thyagarajan, S. D. Seshadri, and A. K. Ghatak. Waveguide polarizer based on resonant tunneling. *Journal of Lightwave Technology*, 9:315–317, 1991.

[151] P. K. Tien, R. J. Martin, R. Wolfe, R. C. Le Craw, and S. L. Blank. Switching and modulation of light in magneto-optic waveguides of garnet films. *Applied Physics Letters*, 21:394–396, 1972.

[152] U. Trutschel, F. Ouelette, V. Delisle, M. A. Duguay, G. Fogarty, and F. Lederer. Polarization splitter based on antiresonant reflecting optical waveguides. *Journal of Lightwave Technology*, 13:239–243, 1995.

[153] R. Ulrich and G. Ankele. Self-imaging in homogeneous planar optical waveguides. *Applied Physics Letters*, 27(6):337–339, 1975.

[154] M. J. N. van Stralen, K. F. I. Haak, and H. Blok. On the classification of discrete modes in lossy planar waveguides: the modal analysis revisited. *Optical and Quantum Electronics*, 29:243–262, 1997.

[155] R. K. Varshney and A. Kumar. A Simple and Accurate Modal Analysis of Strip-Loaded Optical Waveguides with Various Index Profiles. *Journal of Lightwave Technology*, 6(4):601–606, 1988.

[156] C. Vassallo. About Coupled Mode Theories for Dielectric Waveguides. *Journal of Lightwave Technology*, 6(2):294–303, 1988.

[157] C. Vassallo. *Optical Waveguide Concepts*. Elsevier, Amsterdam, 1991.

[158] C. Vassallo. Reformulation for the Beam Propagation Method. *Journal of the Optical Society of America A*, 10(10):2208–2216, 1993.

[159] C. Vassallo. 1993-1995 Optical mode solvers. *Optical and Quantum Electronics*, 29:95–114, 1997.

[160] A. Vukovic, 1999. Private communication.

[161] A. Vukovic, P. Sewell, T. M. Benson, and P. C. Kendall. Facet reflectivity of waveguides buried at realistic depth. In G. C. Righini and S. I. Najafi, editors, *Integrated Optics Devices III*, volume 3620 of SPIE Proceedings, pages 98–108, 1999.

[162] A. Vukovic, P. Sewell, T. M. Benson, and P. C. Kendall. Novel half space radiation mode method for buried waveguide analysis. *Optical and Quantum Electronics*, 31:43–51, 1999.

[163] M. Wallenhorst. *Herstellung und Charakterisierung magnetooptischer Granatfilme für nichtreziproke Wellenleiter und magnetooptische Sensoren*. Verlag Shaker, Aachen, 1998. Dissertation.

[164] M. Wallenhorst, V. Backherms, A. Josef, N. Bahlmann, M. Lohmeyer, H. Dötsch, and P. Hertel. Optimized nonreciprocal rib waveguides for integrated magneto-optic isolators. In K. Rubin, J. A. Bain, T. Nolan, D. Bogy, B. J. H. Stadler, M. Levy, J. P. Lorenzo, M. Mansuripur, Y. Okamura, and R. Wolfe, editors, *High-Density Magnetic Recording and Integrated Magneto-Optics: Materials and Devices*, volume 517 of MRS Symposium Proceedings Series, pages 463–468, 1998.

[165] M. Wallenhorst, M. Niemöller, H. Dötsch, P. Hertel, R. Gerhardt, and B. Gather. Enhancement of the nonreciprocal magneto-optic effect of TM modes using iron garnet double layers with opposite Faraday rotation. *Journal of Applied Physics*, 77(7):2902–2905, 1995.

[166] J. Warner. Nonreciprocal magnetooptic waveguides. *IEEE Transactions on Microwave Theory and Techniques*, MTT-23:70–78, 1975.

[167] W. H. Weber, S. L. McCarthy, and G. W. Ford. Perturbation theory applied to gain or loss in an optical waveguide. *Applied Optics*, 13:715–716, 1974.

[168] C. M. Weinert and N. Agrawal. Three-Dimensional Finite Difference Simulation of Coupling Behaviour and Loss in Multimode Interference Devices. *IEEE Photonics Technology Letters*, 7:529–531, 1995.

[169] R. F. Werner. Quantentheorie. Skript zur Vorlesung an der Universität Osnabrück, WS 95/96.

[170] W. Wettling. Magneto-Optics of Ferrites. *Journal of Magnetism and Magnetic Materials*, 3:147–160, 1976.

[171] F. Wijnands, H. J. W. M. Hoekstra, G. J. M. Krijnen, and R. M. de Ridder. Modal Fields Calculation Using the Finite Difference Beam Propagation Method. *Journal of Lightwave Technology*, 12(12):2066–2072, 1994.

[172] F. Wijnands, T. Rasmussen, H. J. W. M. Hoekstra, J. H. Povlsen, and R. M. de Ridder. Efficient Semivectorial Mode Solvers. *IEEE Journal of Quantum Electronics*, 33(3):367–374, 1997.

[173] J. Willems, J. Haes, and R. Baets. The bidirectional mode expansion method for two-dimensional waveguides: the TM case. *Optical and Quantum Electronics*, 27:995–1007, 1995.

[174] G. Winkler. *Magnetic Garnets*. Vieweg, Braunschweig/Wiesbaden, 1981.

[175] R. Wolfe, V. J. Fratello, and M. McGlashan-Powell. Thin-film garnet materials with zero linear birefringence for magneto-optic waveguide devices. *Journal of Applied Physics*, 63(8):3099–3103, 1988.

[176] R. Wolfe, R. A. Lieberman, V. J. Fratello, R. E. Scotti, and N. Kopylov. Etch-tuned ridged waveguide magneto-optic isolator. *Applied Physics Letters*, 56(5):426–428, 1990.

[177] R. Wolfe, W.-K. Wang, D. J. DiGiovanni, and A. M. Vengsarkar. All-fiber magneto-optic isolator based on the nonreciprocal phase shift in asymmetric fiber. *Optics Letters*, 20:1740–1742, 1995.

[178] S. Yamamoto and T. Makimoto. Circuit theory for a class of anisotropic and gyrotropic thin-film optical waveguides and design of non-reciprocal devices for integrated optics. *Journal of Applied Physics*, 45:882, 1974.

[179] D. Yevick. A guide to electric field propagation techniques for guided-wave optics. *Optical and Quantum Electronics*, 26:185–197, 1994.

[180] O. Zhuromskyy, M. Lohmeyer, N. Bahlmann, H. Dötsch, and P. Hertel. Analysis of Polarization Independent Mach-Zehnder Type Integrated Optical Isolator. *Journal of Lightwave Technology*, 17(7):1200–1205, 1999.

Thanks . . .

to all the persons who have supported my way to this thesis, in particular

. . . to Prof. Dr. Peter Hertel,

. . . to Dipl. Phys. Norbert Bahlmann and Dipl. Phys. Oleksandr Zhuromskyy,

. . . to Prof. Dr. Horst Dötsch, Dipl. Phys. Martin Fehndrich, Dipl. Phys. Reinald Gerhardt, Dr. Michael Wallenhorst, to all other members of the applied magnetooptics group, and to Prof. Dr. A. F. Popkov,

. . . to Dipl. Ing. Ana Vukovic, University of Nottingham, UK, and to Dr. Jan Bos, BBV Software BV, NL,

. . . to Dr. Ekaterina Shamonina and Dr. Mikhail Shamonin,

. . . to my parents,

. . . and to Barbara.

Die vorliegende Arbeit ist im Rahmen des Sonderforschungsbereiches 225 *Oxidische Kristalle für elektro- und magnetooptische Anwendungen* mit finanzieller Unterstützung der Deutschen Forschungsgemeinschaft im Fachbereich Physik der Universität Osnabrück entstanden.